



**HAL**  
open science

# Elastodynamic design and optimization of architected materials

Saad El Ouafa

► **To cite this version:**

Saad El Ouafa. Elastodynamic design and optimization of architected materials. Mechanics [physics]. Université Gustave Eiffel, 2023. English. NNT : 2023UEFL2083 . tel-04830332

**HAL Id: tel-04830332**

**<https://theses.hal.science/tel-04830332v1>**

Submitted on 11 Dec 2024

**HAL** is a multi-disciplinary open access archive for the deposit and dissemination of scientific research documents, whether they are published or not. The documents may come from teaching and research institutions in France or abroad, or from public or private research centers.

L'archive ouverte pluridisciplinaire **HAL**, est destinée au dépôt et à la diffusion de documents scientifiques de niveau recherche, publiés ou non, émanant des établissements d'enseignement et de recherche français ou étrangers, des laboratoires publics ou privés.

**Université Gustave Eiffel**  
École doctorale Sciences, Ingénierie et Environnement

**Thèse**  
Pour obtenir le grade de  
**DOCTEUR de l'Université Gustave Eiffel**  
Spécialité : Mécanique.

Présentée et soutenue par :  
**Saad EL OUAFA**

---

**Elastodynamic design and  
optimization of architected  
materials**

---

Pour une soutenance le 22 septembre 2023 devant le jury composé de:

|                       |  |              |
|-----------------------|--|--------------|
| Claude Boutin         | Professeur des universités, Ecole Nationale des Travaux Publics de l'Etat                      | Rapporteur   |
| Marc François         | Professeur des universités, GeM - Nantes université  | Rapporteur   |
| Camille Perrot        | Professeur des universités, MSME - Université Gustave Eiffel                                   | Examineur    |
| Christelle Combescure | Maîtresse de conférences, Université Bretagne Sud - Académie Militaire de Saint Cyr Coëtquidan | Examinatrice |
| Claire Lestringant    | Maîtresse de conférences, d'Alembert - Sorbonne université                                     | Examinatrice |
| Nicolas Auffray       | Professeur des universités, d'Alembert - Sorbonne université                                   | Directeur    |
| Giuseppe Rosi         | Maître de conférences, MSME - Université Paris-Est Créteil                                     | Encadrant    |
| Rémi Cornaggia        | Maître de conférences, d'Alembert - Sorbonne université  | Encadrant    |



# Contents

|          |     |
|----------|-----|
| Notation | xii |
|----------|-----|

## Part I : Modelling of Periodic Architected Materials xiii

|          |   |           |
|----------|---|-----------|
| <b>1</b> | <b>Architected material : a brief state of art</b>                    | <b>5</b>  |
| 1.1      | INTRODUCTION  | 6         |
| 1.2      | DEFINITION OF ARCHITECTED MATERIALS                                   | 8         |
| 1.3      | SPATIAL ORGANIZATION OF THE MATTER                                    | 10        |
| 1.4      | OVERVIEW OF DESIGN AND MANUFACTURING TECHNIQUES                       | 12        |
| 1.5      | MECHANICAL PROPERTIES OF ARCHITECTED MATERIALS                        | 17        |
| 1.6      | MODELLING AND CHARACTERIZATION OF ARCHITECTED MATERIALS BEHAVIOUR     | 19        |
| 1.7      | SYNTHESIS   | 20        |
| <b>2</b> | <b>Mathematical modelling of periodic architected materials</b>       | <b>21</b> |
| 2.1      | FROM GEOMETRY TO MATHEMATICS  | 22        |
| 2.1.1    | SYMMETRY IN THE PLANE   | 22        |
| 2.1.2    | LATTICES  | 25        |
| 2.1.3    | POINT GROUPS  | 29        |
| 2.1.4    | SPACE GROUP   | 31        |
| 2.2      | THE SPACE OF BIDIMENSIONAL CLASSIC ELASTICITY TENSORS                 | 36        |
| 2.2.1    | CONSTITUTIVE EQUATIONS  | 36        |
| 2.2.2    | MATERIAL AND PHYSICAL SYMMETRIES                                      | 37        |
| 2.2.3    | REPRESENTATION OF THE ELASTICITY TENSOR SPACE                         | 41        |
| 2.2.4    | SYMMETRY CLASSES AND INVARIANTS OF $\mathbb{E}LA$                     | 45        |
| 2.3      | ELASTODYNAMICS OF ARCHITECTED MATERIALS                               | 50        |
| 2.3.1    | PERIODIC MEDIA : SOME ELEMENTS OF THEORY                              | 50        |
| 2.3.2    | FLOQUET-BLOCH ANALYSIS  | 53        |
| 2.4      | EFFECTIVE GENERALIZED CONTINUUM : FROM ELASTOSTATIC TO ELASTODYNAMICS | 58        |
| 2.4.1    | INTRODUCTION TO GENERALIZED CONTINUUM                                 | 58        |
| 2.4.2    | MICROMORPHIC ELASTICITY   | 59        |
| 2.4.3    | COSSERAT ELASTICITY IN 2D   | 61        |
| 2.4.4    | STRAIN-GRADIENT ELASTICITY IN 2D                                      | 64        |
| 2.5      | SYNTHESIS   | 69        |

|  |            |
|--|------------|
| <b>Part II : Towards elastodynamic approaches for the design and characterization of the overall behavior of Architected Materials</b> | <b>71</b>  |
| <b>3 From periodic lattices to overall homogeneous continuum</b>   | <b>73</b>  |
| 3.1 INTRODUCTION . . . . .   | 73         |
| 3.2 EXPLICIT PARAMETERISATION OF A FAMILY OF LATTICES . . . . .  | 74         |
| 3.3 DETERMINATION OF THE ELASTODYNAMIC SIGNATURES . . . . .  | 83         |
| 3.3.1 FLOQUET-BLOCH COMPUTATIONAL SIGNATURE . . . . .  | 84         |
| 3.3.2 INVESTIGATION OF ANISOTROPIC INERTIA CONTRIBUTION . . . . .  | 105        |
| 3.4 DETERMINATION OF THE APPROPRIATE KINEMATICS EXTENSION . . . . .  | 108        |
| 3.5 SYNTHESIS . . . . .  | 110        |
| <b>4 Christoffel tensor based elastodynamic identification approach : LW-LF asymptotics</b>  | <b>111</b> |
| 4.1 INTRODUCTION . . . . .   | 111        |
| 4.2 THEORETICAL FRAMEWORK . . . . .  | 112        |
| 4.2.1 HOMOGENEOUS EQUIVALENT MODEL IN LW-LF APPROXIMATION . . . . .  | 112        |
| 4.2.2 CHRISTOFFEL TENSOR REVISITED . . . . .   | 114        |
| 4.3 ELASTODYNAMIC IDENTIFICATION APPROACHES OF APPARENT PROPERTIES . . . . .   | 116        |
| 4.3.1 POLARISATION-VELOCITY BASED APPROACH (PVBA) . . . . .  | 117        |
| 4.3.2 VELOCITY-BASED APPROACHES (VBA) . . . . .  | 118        |
| 4.4 NUMERICAL VALIDATION . . . . .   | 122        |
| 4.4.1 METHODOLOGY . . . . .  | 122        |
| 4.4.2 RESULTS . . . . .  | 122        |
| 4.5 SYNTHESIS . . . . .  | 127        |
| 4.6 APPENDIX: ELASTOSTATIC HOMOGENIZATION . . . . .  | 129        |
| 4.6.1 INTRODUCTION . . . . .   | 129        |
| 4.6.2 REPRESENTATIVE ELEMENTARY VOLUME . . . . .   | 129        |
| 4.6.3 LOCALIZATION PROBLEM . . . . .   | 131        |
| 4.6.4 AVERAGING FIELDS . . . . .   | 132        |
| <b>5 Asymptotic homogenization: Application to strain-gradient elasticity</b>  | <b>135</b> |
| 5.1 INTRODUCTION . . . . .   | 136        |
| 5.2 TWO-SCALE HOMOGENIZATION FRAMEWORK . . . . .   | 137        |
| 5.2.1 SCALE SEPARATION . . . . .   | 137        |
| 5.2.2 GOVERNING EQUATIONS . . . . .  | 139        |
| 5.2.3 TWO-SCALE ASYMPTOTIC EXPANSIONS . . . . .  | 139        |
| 5.2.4 HOMOGENIZATION PROCEDURE . . . . .   | 140        |
| 5.3 SECOND ORDER HOMOGENIZATION OF THE 2D WAVE EQUATIONS . . . . .   | 141        |
| 5.3.1 COMPUTATION OF $\tilde{\mathbf{u}}_0$ . . . . .  | 142        |
| 5.3.2 COMPUTATION OF $\tilde{\mathbf{u}}_1$ AND FIRST CELL PROBLEM . . . . .   | 143        |
| 5.3.3 COMPUTATION OF FIRST-ORDER HOMOGENIZED TENSORS . . . . .   | 144        |
| 5.3.4 COMPUTATION OF $\tilde{\mathbf{u}}_2$ AND SECOND CELL PROBLEM . . . . .  | 146        |
| 5.3.5 COMPUTATION OF THE SECOND-ORDER HOMOGENIZED COUPLING TENSORS . . . . .   | 147        |

|          |  |            |
|----------|--|------------|
| 5.3.6    | COMPUTATION OF $\tilde{\mathbf{u}}_3$ AND THIRD CELL PROBLEM . . . . .                                 | 149        |
| 5.3.7    | COMPUTATION OF SECOND-ORDER HOMOGENIZED TENSORS . . . . .  | 151        |
| 5.4      | RECIPROCITY RELATIONSHIPS . . . . .  | 152        |
| 5.4.1    | RELATIONSHIP BETWEEN TENSORS $\boldsymbol{\rho}_1^H$ AND $\mathbf{C}_1^H$ . . . . .                    | 153        |
| 5.4.2    | RELATIONSHIP BETWEEN TENSORS $\boldsymbol{\rho}_1^H$ , $\mathbf{C}_1^H$ AND $\mathbf{C}_2^H$ . . . . . | 154        |
| 5.5      | MEAN FIELDS, HOMOGENIZED EQUATIONS AND LINK WITH STRAIN-GRADIENT ELASTICITY . . . . .                  | 157        |
| 5.5.1    | DERIVATION OF A FOURTH-ORDER EFFECTIVE TIME-HARMONIC WAVE EQUATION . . . . .                           | 157        |
| 5.5.2    | TRANSIENT FOURTH-ORDER EFFECTIVE WAVE EQUATION . . . . .   | 160        |
| 5.6      | SYNTHESIS . . . . .  | 160        |
| <b>6</b> | <b>Computation of high-order homogenized tensors : numerical examples</b> . . . . .                    | <b>161</b> |
| 6.1      | NUMERICAL VALIDATION . . . . .   | 161        |
| 6.1.1    | CONVERGENCE OF THE HOMOGENIZATION SCHEME . . . . .   | 165        |
| 6.1.2    | INFLUENCE OF THE HETEROGENITIES/UNIT-CELL SIZE . . . . .   | 168        |
| 6.1.3    | TRANSLATION INVARIANCE . . . . .   | 169        |
| <b>7</b> | <b>Conclusion and Perspectives</b> . . . . .   | <b>173</b> |



# List of Figures

|      |   |    |
|------|---|----|
| 1.1  | The different scales of materials . . . . .   | 6  |
| 1.2  | Material property charts (Ashby diagrams) of strength $\sigma_f$ versus mass density $\rho$ for materials known in 1945 and 2010 [Fleck et al., 2010] Ashby diagrams compare two or three properties of different material classes, and each bubble represents a distinct type of material. . . . . | 7  |
| 1.3  | Examples of architected materials with differing configurations and connectivities. [Ashby, 2013] . . . . .   | 8  |
| 1.4  | Examples of architected materials with differing configurations and connectivities. [Faure, 2017] . . . . .   | 9  |
| 1.5  | Examples of periodic architected materials . . . . .  | 10 |
| 1.6  | Examples quasi-periodic structures . . . . .  | 11 |
| 1.7  | Examples quasi-periodic structures . . . . .  | 11 |
| 1.8  | Examples additive manufacturing methods . . . . .   | 13 |
| 1.9  | Examples non-additive manufacturing methods . . . . .   | 15 |
| 1.10 | Two different optimisation modellings (a) Mono-scale modelling [Amstutz and Andrä, 2006] and (b) Multi-scale modelling [Amstutz et al., 2010] . . . . .   | 16 |
| 1.11 | Example of auxetic behaviour : (a) unloaded configuration, (b) loaded configuration . . . . .   | 17 |
| 1.12 | . . . . .   | 17 |
| 1.13 | Time transient Finite Elements simulation of energy propagation in a hexagonal lattice at a given instant for shear pulses of different central frequency [Rosi and Auffray, 2016] . . . . .  | 18 |
| 1.14 | Example of concept of an invisibility cloak [Bückmann et al., 2015] . . . . .   | 18 |
| 1.15 | Example of a multistable lattice for trapping elastic strain energy [Shan et al., 2015] . . . . .   | 19 |
| 2.1  | Translation of the point $M$ and $P$ respectively by vectors $\mathbf{a}$ and $3\mathbf{a}$ . . . . .   | 23 |
| 2.2  | Rotation around a given $M$ . . . . .   | 23 |
| 2.4  | Glide reflection across the horizontal axis $\mathbf{e}_1$ and displacement $\mathbf{a}$ . . . . .  | 25 |
| 2.5  | The equivalence of material points $\mathbf{x}$ and $\mathbf{x}'$ under the action of $\mathcal{R}$ . . . . .   | 26 |
| 2.6  | Example of bidimensional periodic medium . . . . .  | 27 |
| 2.7  | Definition of an elementary cell . . . . .  | 28 |
| 2.8  | Bravais lattices in 2D space and their unit cell shapes (coloured area) . . . . .   | 28 |
| 2.9  | Examples of $k$ -sided chiral polygons; . . . . .   | 30 |
| 2.10 | Examples of $k$ -sided regular polygons; . . . . .  | 30 |
| 2.11 | Lattice diagrams of the 17 wallpaper groups . . . . .   | 33 |
| 2.12 | Examples of periodic architected materials of the 17 wallpaper groups . . . . .   | 34 |
| 2.13 | A microstructure $\mathcal{M}(P)$ attached to a given material point $P$ . . . . .  | 37 |

|      |  |    |
|------|--|----|
| 2.14 | Active transformation on the left figure: a new vector is obtained; Passive transformation on the right figure, in which only the basis is changed. . . . .  | 38 |
| 2.15 | Graphical presentation of the harmonic bouquet, within the bases $\mathcal{K}^2$ and $\mathcal{K}^4$ . . . . .   | 45 |
| 2.16 | Harmonic normal form of a generic elasticity tensor . . . . .  | 46 |
| 2.17 | Harmonic normal form of non generic elasticity tensors . . . . .   | 46 |
| 2.18 | (a): Semi-algebraic variety of elastic materials with respect to $(i_2, j_2, i_3)$ , (b): Transitions between symmetry classes . . . . .   | 49 |
| 2.19 | A 2D example of hexagonal unit cell. Left-hand figure : the Wigner-Seitz unit cell $\mathcal{T}_0$ in $\mathcal{R}$ . Right-hand figure : FBZ $\mathcal{T}^*$ associated with $\mathcal{T}_0$ in the reciprocal space $\mathcal{R}^*$ . . . . .  | 52 |
| 2.20 | Some examples of polarizations: a) linear, b) Circular right handed, c) Circular left handed. . . . .  | 57 |
| 2.21 | Basic extensions of a classical continuum. From the left to the right, <i>Rotation</i> then <i>Rotation+Stretch</i> are added to the kinematics. For higher-order continua these stretches are independent DOF, for higher-grade continua they are controlled by higher-order gradients of the displacement field. . . . . | 59 |
| 3.1  | Example of hexagonal elementary cell . . . . .   | 74 |
| 3.2  | Hexagonal tiling . . . . .   | 75 |
| 3.3  | Hexachiral elementary cell . . . . .   | 75 |
| 3.4  | Hexachiral unit cell parameters . . . . .  | 76 |
| 3.5  | Hexachiral tiling . . . . .  | 76 |
| 3.6  | Configurations corresponding to different values of $\alpha$ for $\gamma = 0.2$ . . . . .  | 77 |
| 3.7  | Tetragonal elementary cell . . . . .   | 78 |
| 3.8  | Tetragonal tiling . . . . .  | 78 |
| 3.9  | Tetrachiral tiling . . . . .   | 79 |
| 3.10 | Configurations corresponding to different values of $\alpha$ for $\gamma = 0.3$ . . . . .  | 79 |
| 3.11 | Trichiral elementary cell . . . . .  | 80 |
| 3.12 | Trichiral unit cell parameters . . . . .   | 80 |
| 3.13 | Trichiral tiling . . . . .   | 81 |
| 3.14 | Rotational invariance of the trichiral tiling : a) the proposed tiling, b) the commonly used tiling . . . . .  | 81 |
| 3.15 | Trichiral elementary cell . . . . .  | 82 |
| 3.16 | Trigonal unit cell parameters . . . . .  | 82 |
| 3.17 | Trigonal tiling . . . . .  | 83 |
| 3.18 | Left-hand figure : Hexachiral $Z_6$ lattice and its unit cell. Right-hand figure : First Brillouin zone (gray area), IBZ (brown area) and its contour (red triangle) . . . . .   | 86 |
| 3.19 | Iso-frequency contours of the slowness surfaces . . . . .  | 86 |
| 3.20 | Iso-frequency contours of the first two slowness surfaces over IBZ . . . . .   | 87 |
| 3.21 | Dispersion curves for $Z_6$ honeycomb lattice . . . . .  | 87 |
| 3.22 | Phase velocities of the Hexachiral PAM . . . . .   | 89 |
| 3.23 | Group velocities of the Hexachiral PAM . . . . .   | 89 |
| 3.24 | Left-hand figure : Hexagonal $D_6$ lattice and its unit cell. Right-hand figure : First Brillouin zone (gray area), IBZ (brown area) and its contour (red triangle) . . . . .  | 90 |

|      |   |     |
|------|---|-----|
| 3.25 | Iso-frequency countours of the slowness surfaces . . . . .  | 90  |
| 3.26 | Iso-frequency countours of the first two slowness surfaces over IBZ . . . . .   | 91  |
| 3.27 | Dispersion curves for $D_6$ honeycomb lattice . . . . .   | 91  |
| 3.28 | Phase and group velocities of the hexagonal PAM . . . . .   | 92  |
| 3.29 | Left-hand figure : Tetrachiral $Z_4$ lattice and its unit cell. Right-hand figure : First Brillouin zone (gray area), IBZ (brown area) and its contour (red triangle) . . . . . | 93  |
| 3.30 | Iso-frequency countours of the first two slowness surfaces over IBZ . . . . .   | 93  |
| 3.31 | Dispersion curves for $Z_4$ honeycomb lattice . . . . .   | 94  |
| 3.32 | Phase and group velocities of the tetrachiral PAM . . . . .   | 95  |
| 3.33 | Left-hand figure : Tetragonal $D_4$ lattice and its unit cell. Right-hand figure : First Brillouin zone (gray area), IBZ (brown area) and its contour (red triangle) . . . . .  | 96  |
| 3.34 | Iso-frequency countours of the first two slowness surfaces over IBZ . . . . .   | 96  |
| 3.35 | Dispersion curves for $D_4$ honeycomb lattice . . . . .   | 97  |
| 3.36 | Phase and group velocities of the tetragonal PAM . . . . .  | 98  |
| 3.37 | Left-hand figure : Trichiral $Z_3$ lattice and its unit cell. Right-hand figure : First Brillouin zone (gray area), IBZ (brown area) and its contour (red triangle) . . . . .   | 99  |
| 3.38 | Iso-frequency countours of the first two slowness surfaces over IBZ . . . . .   | 99  |
| 3.39 | Dispersion curves for $Z_3$ honeycomb lattice . . . . .   | 100 |
| 3.40 | Phase and group velocities of the tetragonal PAM . . . . .  | 101 |
| 3.41 | Left-hand figure : Trichiral $D_3$ lattice and its unit cell. Right-hand figure : First Brillouin zone (gray area), IBZ (brown area) and its contour (red triangle) . . . . .   | 102 |
| 3.42 | Iso-frequency countours of the first two slowness surfaces over IBZ . . . . .   | 102 |
| 3.43 | Dispersion curves for $D_3$ honeycomb lattice . . . . .   | 103 |
| 3.44 | Phase and group velocities of the tetragonal PAM . . . . .  | 104 |
| 3.45 | Unit cell of square composite . . . . .   | 105 |
| 3.46 | Dispersion curves of the first six modes . . . . .  | 105 |
| 3.47 | Iso-frequency countours of the first two slowness surfaces over IBZ . . . . .   | 106 |
| 3.48 | Phase and group velocities of the medium . . . . .  | 106 |
| 3.49 | The different configurations of the inclusion's orientation . . . . .   | 107 |
| 3.51 | Evolution of the band gap with respect to inclusion's orientation . . . . .   | 108 |
| 4.1  | Schematic of elastodynamic homogenisation method . . . . .  | 122 |
| 4.2  | Studied PAMs geometries . . . . .   | 124 |
| 4.3  | Polar plots of phase velocities for different symmetry classes . . . . .  | 126 |
| 4.4  | Evolution of effective elastic moduli with respect to the volume fraction $\rho/\rho_s$ . . . . .   | 127 |
| 4.5  | <b>a)</b> Periodic microstructure; <b>b)</b> Representative Elementary Volume (REV) as a unit periodic cell . . . . .   | 130 |
| 5.1  | Schematics of an infinite heterogeneous periodic media and its unit cell . . . . .  | 138 |
| 5.2  | Two well distinct scales are considered: the macro-scale, described by $\mathbf{x}$ , and the micro-scale, described by $\mathbf{y}$ . . . . .                                  | 138 |
| 6.2  | Cell-functions $\chi^{1(11)}, \chi^{1(22)}$ and $\chi^{1(12)}$ produced by each macroscopic strain loading . . . . .  | 164 |
| 6.3  | $D_4$ unit-cell with a square inclusion . . . . .   | 166 |

---

|     |  |     |
|-----|--|-----|
| 6.4 | Mesh convergence : Evolution of the homogenized components of the elasticity tensor $\mathbf{C}^H$ with respect to the number of elements . . . . .                          | 166 |
| 6.5 | Mesh convergence : Evolution of the homogenized components of the homogenized micro-inertia tensor $\mathbf{J}^H$ with respect to the number of elements . . . . .           | 167 |
| 6.6 | Mesh convergence : Evolution of the homogenized components of the homogenized second order elasticity tensor $\mathbf{A}^H$ with respect to the number of elements . . . . . | 167 |
| 6.7 | Mesh convergence : Evolution of the homogenized components with respect to the number of elements . . . . .  | 167 |
| 6.8 | Evolution of the homogenized components with respect to the volume fraction of heterogeneities . . . . .   | 168 |
| 6.9 | Evolution of the homogenized components with respect to the unit cell size . . . . .   | 169 |

# List of Tables

|      |   |     |
|------|---|-----|
| 2.1  | Composition of all possible isometries in 2D . . . . .  | 25  |
| 2.2  | Geometrical characteristics of Bravais lattice in 2D space [Armstrong, 1997]<br>. . . . .   | 29  |
| 2.3  | Classification of the Bravais lattice and their point groups . . . . .  | 30  |
| 2.4  | Symbols used for lattice diagrams . . . . .   | 31  |
| 2.5  | Summary of the 17 2D wallpaper groups, their properties and notations   | 32  |
| 2.6  | 2D symmetry groups . . . . .  | 40  |
| 2.7  | The matrix normal forms of the elasticity tensor for each symmetry<br>class . . . . .   | 47  |
| 2.8  | Covariant conditions for symmetry classes . . . . .   | 47  |
| 2.9  | Invariant and Covariant conditions for symmetry classes . . . . .   | 48  |
| 2.10 | Lattice vectors in the direct and reciprocal spaces . . . . .   | 51  |
| 2.11 | High symmetry points of the Hexagonal IBZ corresponding to fig-<br>ure 2.19 . . . . .   | 52  |
| 2.12 | Strain and stress measures of micromorphic elasticity [Forest, 2006,<br>Eringen, 2001]. . . . .   | 60  |
| 2.13 | Type of enrichment and intermediate higher-order models are obtained  | 61  |
| 2.14 | Strain and stress measures of Strain-gradient elasticity [Forest, 2006].  | 64  |
| 2.15 | Comparison of key characteristics between the Cosserat model and the<br>Strain-gradient model . . . . .                                     | 67  |
| 3.1  | Geometric properties of the studied lattices . . . . .  | 85  |
| 3.2  | Material properties of the constitutive material . . . . .  | 85  |
| 3.3  | First, second, third and fourth wave modes at high symmetry point $\Gamma$ ,<br>$K$ and $M$ of the IBZ (total displacement in mm) . . . . . | 88  |
| 3.4  | First, second, third and fourth wave modes at high symmetry point $\Gamma$ ,<br>$K$ and $M$ of the IBZ (total displacement in m) . . . . .  | 92  |
| 3.5  | First, second, third and fourth wave modes at high symmetry point $\Gamma$ ,<br>$X$ and $M$ of the IBZ (total displacement in m) . . . . .  | 94  |
| 3.6  | First, second, third and fourth wave modes at high symmetry point $\Gamma$ ,<br>$X$ and $M$ of the IBZ (total displacement in m) . . . . .  | 97  |
| 3.7  | First, second, third and fourth wave modes at high symmetry point $\Gamma$ ,<br>$X$ and $M$ of the IBZ (total displacement in m) . . . . .  | 100 |
| 3.8  | First, second, third and fourth wave modes at high symmetry point $\Gamma$ ,<br>$K$ and $M$ of the IBZ (total displacement in m) . . . . .  | 103 |
| 3.9  | Material properties . . . . .   | 105 |
| 4.1  | Symmetry classes . . . . .  | 123 |
| 4.2  | Comparison of the features of the different approaches . . . . .  | 128 |

|     |   |     |
|-----|---|-----|
| 6.1 | The material properties . . . . .                             | 163 |
| 6.2 | Kelvin notation used for 2D strain tensors . . . . .          | 164 |
| 6.3 | Kelvin notation used for 2D strain-gradient tensors . . . . . | 164 |
| 6.4 | . . . . .   | 170 |

# Notation

## Groups:

- $O(2)$  : the orthogonal group of  $\mathbb{R}^2$  ;
- $SO(2)$ : The subgroup of  $O(2)$  of elements with determinant 1, called the special orthogonal group;
- $\mathfrak{so}(2)$ : Lie algebra that consists of real skew-symmetric matrices which is the tangent space to  $SO(2)$ ;
- $Z_k(k \geq 2)$  : the cyclic group with  $k$  elements generated by the rotation of angle  $2\pi/k$ . Geometrically,  $Z_k$  is the symmetry group of  $k$ -sided chiral polygons;
- $D_k^n(k \geq 2)$  : the dihedral group with  $2k$  elements generated by the rotation of angle  $2\pi/k$  and by the reflection in the normal axis to  $\mathbf{n}$ . Geometrically,  $D_k^n$  is the symmetry group of  $k$ -sided regular polygons.

## Tensors and matrices:

- $a$  : Scalar;
- $\{\mathbf{a}\}$  : Vector;
- $[\mathbf{A}]$  : Matrix;

## Tensor spaces:

- $\mathbb{T}^n$  : Space of  $n$ -th order tensors on  $\mathbb{R}^d$ ;
- $T_{i_1 \dots i_n}$  : Components of  $\mathbf{T} \in \mathbb{T}^n$  with respect a given basis  $\mathcal{B}$ ;
- $S^2(\mathbb{R}^d)$  the space of symmetric second-order tensor  $\mathbb{R}^d$ ;
- $\mathbb{K}^n$ : the space of  $n$ -th order harmonic tensors on  $\mathbb{R}^2$ , (i.e. totally symmetric and traceless tensors), with

$$\dim(\mathbb{K}^n) = \begin{cases} 2 & \text{if } n \geq 1, \\ 1 & \text{if } n \in \{-1, 0\}. \end{cases} \quad (0.0.1)$$

Among them:

- $\mathbb{K}^0$  is the space of scalars (isotropic coefficients);
  - $\mathbb{K}^2$  is the space of deviators;
  - $\mathbb{K}^4$  is the space of 4<sup>th</sup> order deviators.
- $\mathbb{E}la$  : the space of elasticity tensors.

## Tensor products and operators:

- $\otimes$  : The classical tensor product;
- $\otimes^s$  : The symmetrized tensor product;
- $\otimes^n$  : The  $n$ -th power of the classical tensor product;
- $\underline{\otimes}$  indicates the twisted tensor product defined by :  $(\mathbf{A} \underline{\otimes} \mathbf{B})_{ijkl} = \frac{1}{2}(A_{il}B_{jk} + A_{ik}B_{jl})$ ;
- $(\mathbf{A} \cdot \mathbf{B})_{i_1 \dots i_n} = A_{i_1 \dots i_p j} B_{j i_{p+1} \dots i_n}$  : Simple contraction;
- $(\mathbf{A} : \mathbf{B})_{i_1 \dots i_n} = A_{i_1 \dots i_p j k} B_{j k i_{p+1} \dots i_n}$  : Double contraction;
- $(\mathbf{A} :: \mathbf{B})_{i_1 \dots i_n} = A_{i_1 \dots i_p j k l m} B_{j k l m i_{p+1} \dots i_n}$  : Quadruple contraction;
- $(\mathbf{A} \hat{\cdot} (\mathbf{n} \otimes \mathbf{n}))_{jk} = (\mathbf{n} \cdot \mathbf{A} \cdot \mathbf{n})_{jk} = A_{ijkl} n_i n_l$  : The twisted double contraction of a fourth-order tensor and a first-order tensor.
- $\nabla$  : Nabla operator;
- $\nabla \cdot \mathbf{A}$  : Divergence of  $\mathbf{A}$ ;
- $\mathbf{A} \otimes \nabla$  : Gradient of  $\mathbf{A}$ ;

## Special tensors:

- $\mathbf{I}$  : Second-order identity tensor,  $(\mathbf{I})_{ij} = \delta_{ij}$ ;
- $\mathbf{1}$  : Fourth-order identity tensor of  $S^2(\mathbb{R}^2)$ ,  $(\mathbf{1})_{ijkl} = (\mathbf{I} \underline{\otimes} \mathbf{I})_{ijkl} = \frac{1}{2}(\delta_{ik}\delta_{jl} + \delta_{il}\delta_{jk})$  ;
- $\mathbf{P}^0 = \frac{1}{2}\mathbf{I} \otimes \mathbf{I}$  the spherical fourth-order projector;
- $\mathbf{P}^2 = \mathbf{1} - \mathbf{P}^0$  the deviatoric fourth-order projector.
- $\epsilon$  : 2D *Levi-Civita* pseudo-tensor :

$$(\epsilon)_{ij} = \begin{cases} 1 & \text{if } ij = 12, \\ -1 & \text{if } ij = 21, \\ 0 & \text{if } i = j. \end{cases}$$

## Constitutive parameters:

- $E$  : Young's modulus ;
- $\nu$  : Poisson's ratio ;
- $\mathbf{C}$  : Elasticity tensor ;
- $\mathbf{\Gamma}$  : Christoffel tensor (actoustic tensor) ;

**Part I :**

**Modelling of Periodic  
Architected Materials**



# General introduction

## Context

The field of architected materials has significantly developed over the past 15 years, and several industrial applications have emerged, particularly in the automotive and aerospace sectors, where the weight reductions achieved through these materials have resulted in significant performance improvements [AB03]. Applications have also emerged in civil engineering, where additive manufacturing techniques for concrete structures have expanded construction methodologies previously employed in metallic structures, enabling new architectural feats that were previously unattainable [GDR+16]. The biomedical field has also adopted the concept of architected materials to create similar to bones, thus facilitating the development and the design of lighter prosthetics and implants. Besides weight reduction, the use of cellular architectures aims to endow these materials with additional functions such as wave guiding, thermal or acoustic insulation, and energy absorption. Most of the architected materials considered in the applications mentioned above share a common feature - a periodic architecture. It is well-known that in such a case, the geometry of the elementary cell (characterized by its point group) as well as the manner in which it paves space (characterized by its space group) play an essential role in determining the material's effective properties. This approach, based on symmetries, is classical in condensed matter physics and has led to the design of numerous innovative materials [New05]. In mechanics and materials engineering, design approaches do not exploit this method. The design of an architecture is currently either purely heuristic, i.e., based on mechanical intuition complemented by a trial-and-error process, or via shape optimization approaches that do not take into account aspects related to the symmetries of medium.

This research is a part of the MAX-OASIS (Matériaux Architecturés eXtremes, Ones, Anisotropie, Instabilités) project funded by ANR (AAP2019), aiming to develop a systematic design approach based on the use of group theory. This approach thus allows the optimization of the local arrangement of matter for addressing issues such as wave guidance, control of the structure stability, or the design of elastically isotropic materials with a tetragonal mesostructure imposed by manufacturing constraints for instance. The latter situation is an example of an exotic material, i.e., whose mechanical response to a given solicitation is more symmetric than that the medium itself (local architecture). Integrating these various aspects during the design process opens up possibilities for additional multifunctional applications: Creating different types of anisotropy based on the regime (whether static or dynamic), controlling the band-gaps through instabilities, etc.

The proposed applications of this project include, on one hand, the control of wave propagation in architected environments (Axis 1), and on the other hand, tuning the multifunctional properties through controlled instabilities (Axis 2). The design of the elementary cell is an important factor in each of these applications. The process of identifying this design based on the targeted effective properties via an inverse architecture problem forms the core of Objective 3 in the current project.

This project is structured around three study axes, complemented by a transversal axis related to the development of appropriate testing methods:

1. **Elastodynamics of architected media:** Dynamics add to the optimization problem of stiffness distribution, the challenge of inertia. Depending on the targeted application, different networks may or may not be congruent.
2. **Controlled instabilities**, achieved by a sequence of controlled post-bifurcation configurations. For this, an optimization of the crystallographic symmetries of architected materials is necessary. The applications here concern the adjustment of the multifunctional properties of materials through a change in the mesostructure due to instabilities controlled by mechanical loading.
3. The definition of an **Inverse problem of architecture** that can determine, for a given set of effective material invariants, associated mesostructures. This axis aims to “*dehomogenize*” the results obtained in Axes 1 and 2 in order to obtain a real architecture, but also to explore and classify the mesostructures associated with *exotic* elastic anisotropies (standard 2D and 3D).
4. Development of appropriate **experimental methods** for architected materials for the identification and validation of equivalent homogeneous media. Experimental homogenization implies specific control of boundary conditions, moreover, instabilities will generate significant displacements at the borders requiring the development of suitable experimental means.

In this axis, we will focus on 2D plane geometries, and consider linear elasticity. Understanding elastodynamic phenomena within architected materials is a topic with high industrial potential, where the targeted applications can be divided into two categories: design and control. In the design approach, the emphasis is on designing a mesostructure that allows control of wave propagation in a given medium. In the control and characterization part, addressed in this thesis, we take the inverse approach of the previous part. Given an cellular, what can the analysis of wave propagation tell us about this medium and, importantly, its evolution? Applications include the control of architected materials, with significant application in biomechanics due to the architectural nature of bones: monitoring the integration of bone implants, and assessing the state of trabecular bone in people suffering from osteoporosis, for instance.

While the application domains are very different, the scientific problem is the same: understanding how an elastic wave of wavelength  $\lambda$  interacts with a mesostructure, of characteristic size  $l$ , when the scale separation is weak ( $6 < l/\lambda < 10$ ). The approach consists of replacing the architected medium with an equivalent homogeneous medium. This allows us to retain, within the considered range of parameters and frequencies, only the necessary information for the problem. The advantages of

continuous modeling are numerous [R18] : On one hand, the continuous description allows the problem to be solved without explicitly describing the geometry of the mesostructure, which reduces meshing problems and the computational cost. On the other hand, a continuous model offers the possibility of an analytical calculation (in most cases) of field variables of interest or propagation constants expressed in terms of material properties and/or geometric characteristics, which can be useful in the context of topological optimization or characterization, for example.

In any case, broadening the application of architected materials necessitates the ability to execute and perform fast simulations, which is incompatible with simulating a complex internal architecture. An efficient solution to this lies in homogenization, replacing the complex heterogeneous material with an equivalent homogeneous one having, under certain assumptions, an equivalent behavior. While this approach is now well understood for materials with strong scale separation, its extension to the case of weak scale separation remains an open question. In such a case, the substitution medium may fail to be a classical Cauchy continuum, and generalized continua may have to be considered. The insufficiency of homogenization using the Cauchy continuum is well understood in both static and dynamic situations. Therefore, the nature of the overall continuum to be considered is the first question to be answered. There are essentially two options to extend classical continuum mechanics : higher-order continua, where the degrees of freedom are extended, such as Cosserat elasticity and micromorphic elasticity; and higher-grade continua, where displacement field is the only degree of freedom, but higher-order gradients of the displacement field are added to the energy density, such as Mindlin's first and second strain-gradient elasticity.

The choice of which generalized continuum to consider is an open question, and approaches can be mathematical, numerical, or experimental. Once the type of continuum has been chosen, the next issue lies in determining the associated constitutive parameters or the material properties of the homogeneous material that will mimic the behavior of the actual medium within specific range of parameters. This process, while established for the classical elasticity (Cauchy type medium), is still an open question when extended to a generalised continuum. Approaches can be mathematical, such as asymptotic methods, numerical based on simulations, or experimental, relying on real-world data.

In order to maintain, in a continuous manner, the influence of mesostructure effects, the substitute medium must be a generalized continuous medium [ADR15,S15,NHA16]. Indeed, as the frequency increases, the mesostructure begins to play a role in dynamic equilibrium and effects emerge at the macroscopic scale. The relationship between frequency and wave number becomes nonlinear, and the medium is said to be dispersive (Fig. 2). In this regime, the periodicities given by standard models are insufficient [FNP+18,RPA18]. The consequence of this is that propagation constants such as phase speed and energy speed depend on frequency. In this case, the direction of wave propagation and that of energy are not necessarily aligned. This phenomenon will be used to deflect acoustic energy without affecting the wave vector.

## Objectives and organisation of the manuscript

The work presented here aims to characterize the elastodynamic behaviour of periodic architected materials, through two approaches: Characterization and identification of effective properties through wave propagation; and the computation of effective properties using the asymptotic homogenization method. The starting point is to look at how the local architecture, i.e. the geometry of the elementary cell of a given periodic architected material, influences the elastodynamic behaviour of the overall medium. Once the elastodynamic signature is established, through Bloch analysis, we can then propose a method of identifying apparent properties from the information extracted by wave propagation. In contrast to this “*phenomenological*” identification method, we propose another approach, much more mathematical, aiming to calculate the effective properties of the medium.

This manuscript is organized into six chapters.

**Chapter 1** is a general introduction and a brief state of the art on architected materials, providing a definition of this new class of materials, with an idea of how to manufacture them and how to model them.

**Chapter 2** groups a set of theoretical elements, essential for modelling and investigating the elastodynamic behaviour of architected materials. This chapter covers several physical and mathematical concepts, revolving around group theory, linear elasticity, wave propagation in periodic media, but also a brief review of generalized continuous media.

**Chapter 3**, divided into two parts, provides examples of periodic architected materials with a geometric parameterization approach based on symmetry criteria, in part 1; As for part 2, it groups together the results of numerical simulations of wave propagation, allowing exploration of the elastodynamic behaviour. A qualitative analysis of these behaviours is proposed in this chapter.

**Chapter 4**, presents a method for identifying the apparent properties of periodic architected materials, in the low-frequency/long-wavelength regime, based on the invariants of the Christoffel tensor.

**Chapter 5**, presents the asymptotic homogenisation method in elastodynamics. The contribution and novelty of this chapter lie in the establishment of some reciprocity relations, and the mathematical construction of a Strain-gradient type model derived from the asymptotic development method. This chapter was written in collaboration with Marc BONNET (POEMS, Ensta Paris).

**Chapter 6**, presents some numerical results related to the validation of the FEM code for the construction of the tensors of the strain-gradient model.

Ultimately, some conclusions and openings for future developments are drawn in the two concluding and perspective chapters.

# Chapter 1

## Architected material : a brief state of art

### Contents

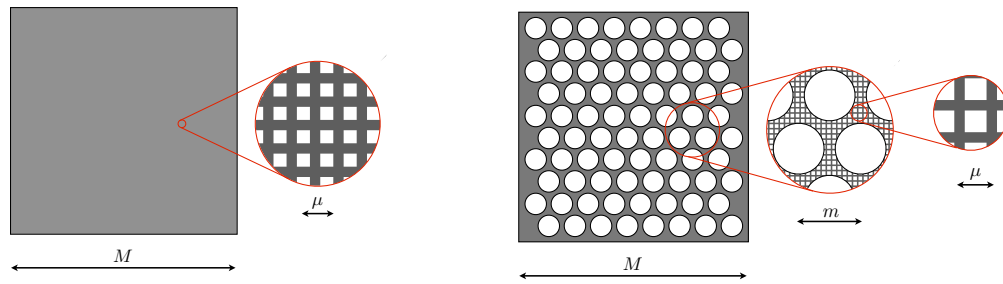
---

|     |   |    |
|-----|---|----|
| 1.1 | INTRODUCTION . . . . .  | 6  |
| 1.2 | DEFINITION OF ARCHITECTURED MATERIALS . . . . .                               | 8  |
| 1.3 | SPATIAL ORGANIZATION OF THE MATTER . . . . .                                  | 10 |
| 1.4 | OVERVIEW OF DESIGN AND MANUFACTURING TECHNIQUES . . . . .                     | 12 |
| 1.5 | MECHANICAL PROPERTIES OF ARCHITECTURED MATERIALS . . . . .                    | 17 |
| 1.6 | MODELLING AND CHARACTERIZATION OF ARCHITECTURED MATERIALS BEHAVIOUR . . . . . | 19 |
| 1.7 | SYNTHESIS . . . . .   | 20 |

---

## 1.1 Introduction

Architected materials are heterogeneous media with a well-chosen microstructure, typically displaying periodicity, situated at an intermediate scale between the macroscopic and constituent material heterogeneities. This microstructure plays a crucial role in governing the material's overall behavior, granting access to properties that conventional materials cannot achieve. As a result, these materials are classified as metamaterials [Barthelat, 2015, Kadic et al., 2019]. To be termed "*architected*", a material must exhibit at least three scales of matter organization: the classical micro and macroscopic scales, along with one or several intermediate scales known as mesoscopic. Furthermore, if its intermediate scales possess a characteristic size similar to the macroscopic scale but significantly larger than the microscopic scale, it may be called "*macro-architected*," indicating a weak scale separation between the macroscopic and mesoscopic levels (see section 1.1) [Bouaziz et al., 2008, Poncelet et al., 2018, Dirrenberger, 2018]



(a) Architected material with 2 well-separated scales: macroscopic scale  $M$  and microscopic scale  $\mu$  (constitutive material) with  $\mu \ll M$ .

(b) An architected material with weak scale separation presenting 3 scales: macroscopic scale  $M$ , mesoscopic (inner structure) scale  $m$  and microscopic scale (constitutive material)  $\mu$ .

Figure 1.1: The different scales of materials

The growing interest in architected materials has arisen due to the increasing demand and the need for materials with improved properties, leading researchers to explore new regions in Ashby diagrams that were previously inaccessible [Fleck et al., 2010]. Ashby and Bréchet [Ashby and Bréchet, 2003b] use charts where materials are positioned in space based on their properties, with figure 1.2 being an example of such a chart. In this figure, the distribution of existing materials in the density - Young's modulus space reveals a correlation between these two properties and leaves certain areas of the chart empty. Specifically, the region representing materials with high stiffness (high Young's modulus) and low density is of particular interest.

The concept of "Materials by design" has recently gained prominence in material development [Ashby and Bréchet, 2003b, Reis et al., 2015, Yeo et al., 2018]. This approach involves precisely the control of matter's organization at mesoscopic or even microscopic scales during both the material design phase and its subsequent fabrication, with the primary objective of achieving specific mechanical properties. Through this novel approach, the creation of materials capable of meeting increasingly stringent performance requirements becomes feasible. Consequently, architected materials



## 1.2 Definition of architected materials

One common aspect among the definitions in the literature is that architected materials possess an internal structure at the mesoscopic scale, called local architecture. However, some definitions are inadequate due to their reductive nature, imposing constraints on the characteristic size of mesoscopic structures, for instance [Barthelat, 2015]. Additionally, certain authors also define architected materials based on their fabrication methods, such as additive manufacturing [Tamburrino et al., 2018], while there are other methods, such as perforation and folding, used to create such structures [Wadley et al., 2003].

Taking Ashby's definition as an example. [Ashby, 2013] provides a definition for "Architected or hybrid materials," which are combinations of two or more materials (or a material and void) assembled in a manner to exhibit properties not found in any of the individual constituent materials alone. The concept of hybrid materials aligns with that of composites, and [Ashby, 2013] illustrates this with examples in Figure xx : Particulate, fibre composites, sandwich structures, foams, lattice structures, segmented structures, zero expansion materials, and more.

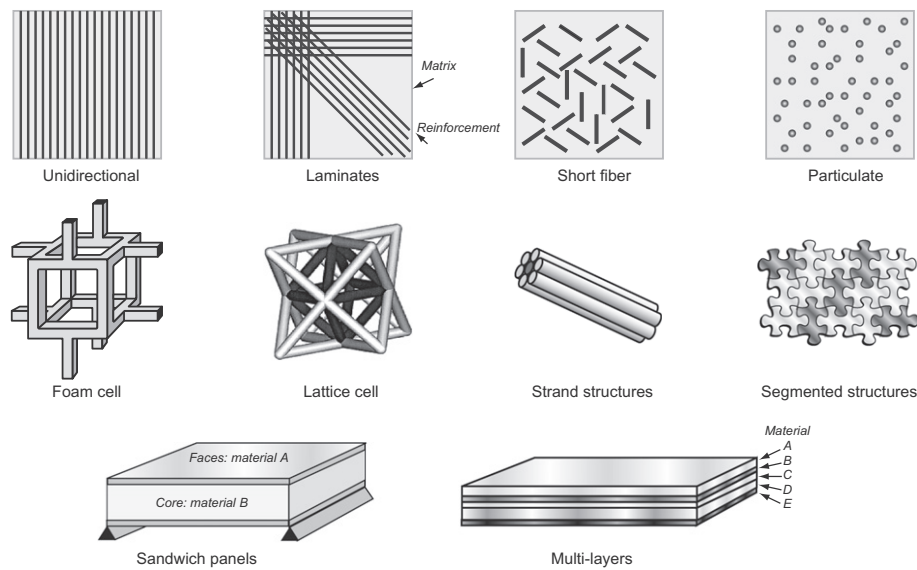


Figure 1.3: Examples of architected materials with differing configurations and connectivities. [Ashby, 2013]

According to [Ashby and Bréchet, 2003a], the configuration and shape of different constituent phases in a hybrid material play a decisive role in its properties. This configuration is defined as a new parameter in material design, described as the “*phase A + phase B + shape + scale*” process, indicating that composite material design involves the following steps [Faure, 2017]:

- Selecting the constituent materials;
- Determining their configuration, i.e., local spatial organization of the matter ;
- Choosing the scale of the configuration.

Figure xx illustrates the orders of magnitude at which microstructure, configuration, and structure interact.

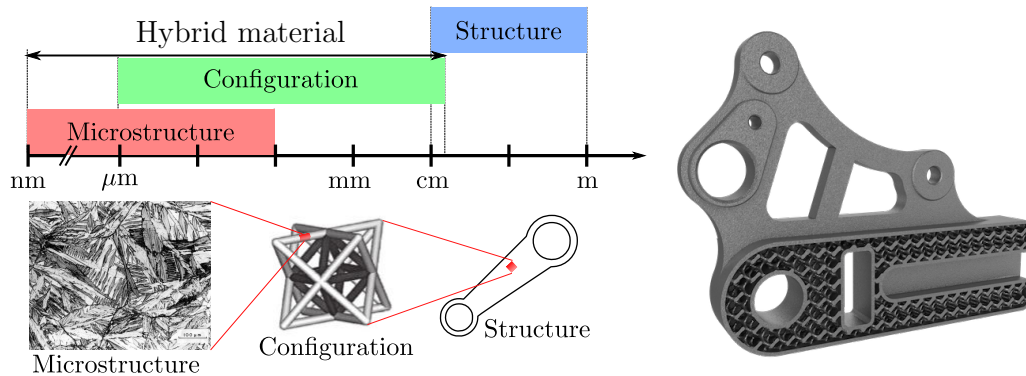


Figure 1.4: Examples of architected materials with differing configurations and connectivities. [Faure, 2017]

Our definition of architected materials won't differ significantly from Ashby's.

**Definition : Architected materials [Auffray, 2017]**

*A material will be said to be architected if:*

1. *It possess an inner geometry, that is, a local architecture or shape;*
2. *It presents of one to several scales of organization of the matter between the micro and the macrostructure;*
3. *The intermediate scales of organization are commensurable with those of the micro and/or macrostructure.*

This aligns with the definition provided by Bouaziz et al., Poncelet et al., and Dirrenberger respectively in [Bouaziz et al., 2008, Poncelet et al., 2018, Dirrenberger, 2018], which state that a material is termed architected if it consists of matter systematically organized and structured in a controlled manner at various scales to achieve specific properties and performances.

### Architected materials vs Metamaterials

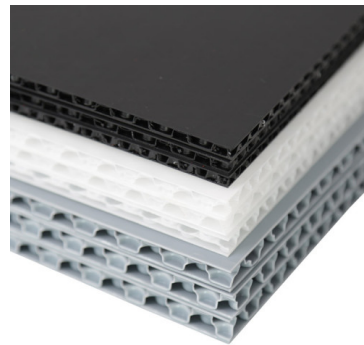
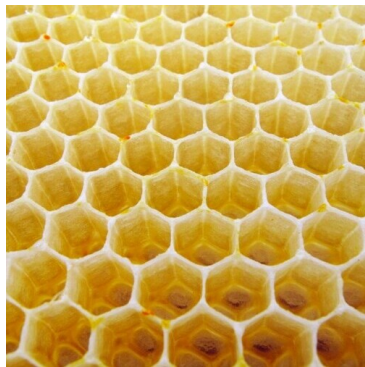
The terms “*metamaterials*” and “*architected materials*” are often used interchangeably, yet they harbor subtle distinctions. Metamaterials predominantly refer to materials with structures that have been intricately engineered to give rise to unique, multi-physical characteristics encompassing optical, magnetic, and even more exotic properties, such as cloaking [Liu et al., 2008, Landy et al., 2008, Cummer et al., 2016]. These materials draw considerable attention due to the extraordinary phenomena stemming from their distinctive architecture. Their focus initially revolved around dynamic attributes but has since extended to investigate static behaviors [Nassar et al., 2022, Xu et al., 2020, Nassar et al., 2020]. Conversely, architected materials adopt a more geometric point of view. They refer to materials with structures deliberately designed on various scales, often with a focus on mechanical or thermal properties [Bouaziz et al., 2008, Poncelet et al., 2018].

## 1.3 Spatial organization of the matter

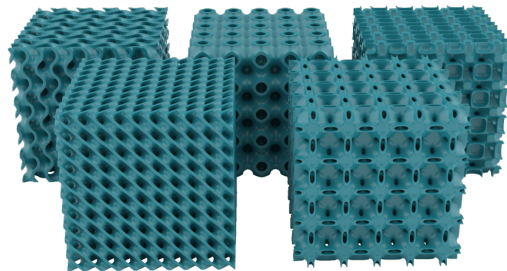
Architected materials can be classified in various ways, one of which is through their spatial organization. In this context, architected materials can be grouped into three primary categories: periodic, quasi-periodic, and aperiodic structures.

### Periodic Structures

Periodic structures are a type of spatial organization where a single unit cell is translated in specific ways to fill space. The inherent organization of these structures integrates the point group of the 'primitive cell' with the Bravais lattice. The combined operations result in the space group of the structure.



(a) Natural honeycomb. Source: <http://www.nature.com> (b) Sandwich panel. Source: <http://www.polyreflex.com>

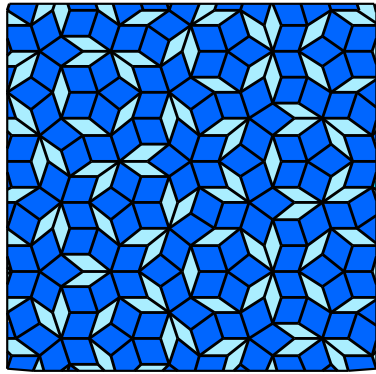


(c) Lattice structures obtained by additive manufacturing. Source: <https://gen3d.com>

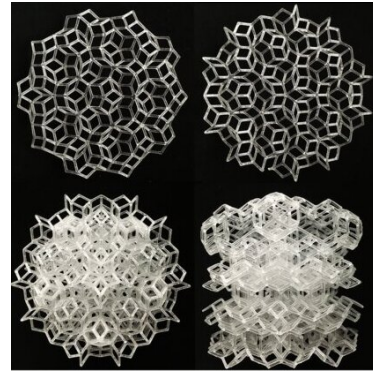
Figure 1.5: Examples of periodic architected materials

### Quasi-periodic Structures

Quasi-periodic structures, as the name suggests, are not strictly periodic but display some form of order. While they do not exhibit the strict repetition found in periodic structures, they still maintain a distinct long-range order. This means that although the pattern does not repeat exactly, it follows a discernible rule or set of rules, making the structure predictable over large scales.



(a) Example of Penrose tiling

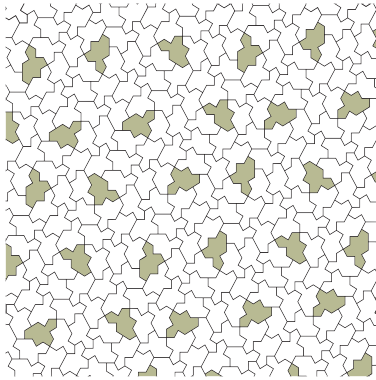


(b) Icosahedral quasi-periodic structures fabricated using off-the-shelf stereolithography 3D printer

Figure 1.6: Examples quasi-periodic structures

### Aperiodic Structures

Contrasting periodic and quasi-periodic structures, aperiodic structures lack any consistent, repeating patterns or symmetry that can be seen in regular or periodic structures. They can be broadly categorized into two main types: ordered and random. Ordered aperiodic structures, despite lacking a regular pattern, still maintain a form of order that spans across their entire structure. On the other hand, random aperiodic structures exhibit no noticeable order or pattern, regardless of the scale at which they are observed.



(a) An ordered aperiodic organisation: "hat" aperiodic monotile

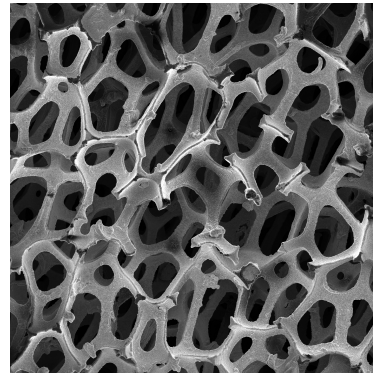
(b) An random aperiodic organisation: open-cell nickel foam. Source <https://www.zeiss.com/>

Figure 1.7: Examples quasi-periodic structures

## 1.4 Overview of design and manufacturing techniques

Designing and manufacturing architected materials involve complex processes and techniques due to the need to manage the inner geometry at various scales. Numerous techniques have been developed to meet these requirements. This section offers a brief overview of these methods; Manufacturing architected materials can pose a challenge, particularly when dealing with complex architectures. Two key categories of methods exist: additive and non-additive manufacturing. It is worth noting that, these methods aren't exclusive to architected materials but can be applied to conventional materials as well [Uribe-Lam et al., 2021, Alomar and Concli, 2020, Wadley et al., 2003, Wadley, 2006, Molitch-Hou, 2018].

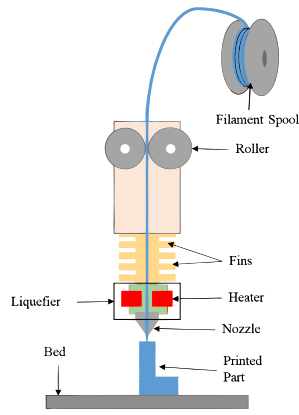
### Additive Manufacturing

Additive manufacturing, commonly known as 3D printing, marks a transformative development in the fabrication of architected materials. Through meticulous control of both micro and macro structural scales, this method allows for the synthesis of materials with precisely tailored mechanical characteristics.

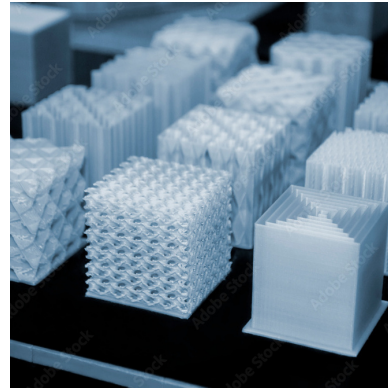
One of the remarkable achievements of additive manufacturing lies in its capability to produce architected materials exhibiting unconventional properties. This includes the creation of materials with negative Poisson's ratios, which contract laterally when stretched, and materials with shape memory effects, capable of returning to their pre-defined shapes under specific conditions. Numerous additive manufacturing methods exist. The choice of method is based on the nature of the constituent materials, the scale, the size of the environment, and especially the properties one aims to achieve. Among the methods used, let's mention a few:

- **Filament-based raw material technique** such as Fused Deposition Modelling (FDM), where a heated thermoplastic filament is deposited layer by layer to construct a 3D object. Bonding between layers depends on the used material (thermal properties, Viscosity, surface contacting ...);
- **Liquid-based raw material technique** such as Stereolithography (SLA), which involves the use of a UV light source to selectively cure a photosensitive resin. In this technique, a laser is utilized to solidify the resin following a line pattern, with the process repeating layer by layer.
- **Powder-based raw material method** including Selective Laser Sintering (SLS) and Direct Metal Laser Sintering (DMLS), wherein small particles of materials such as plastic, metal, ceramic, or glass are fused using a high-intensity laser to form the desired 3D shape.

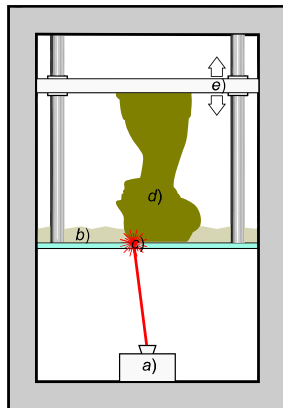
As mentioned earlier, these techniques, grounded in the principle of sequential material addition, provide specific advantages and are employed depending on the requirements of precision, material compatibility, and mechanical properties in the architected materials design.



(a) Fused Deposition Modelling process



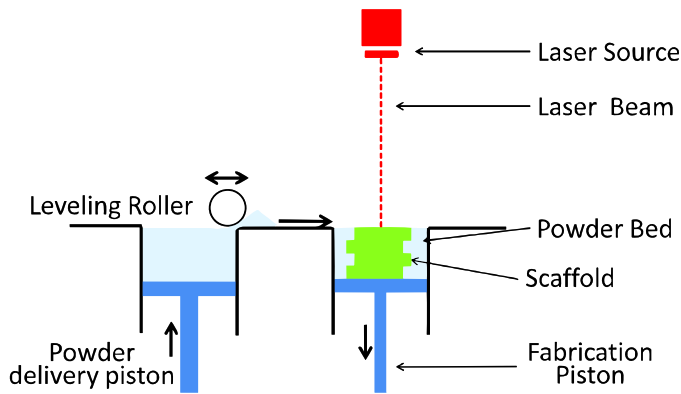
(b) Lattice structure obtained by FDM process



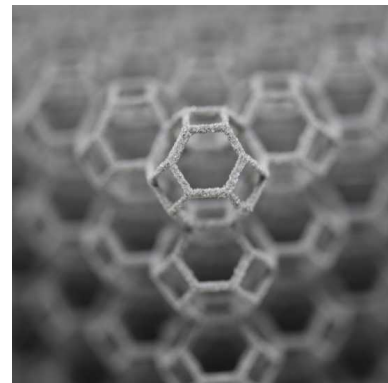
(c) Stereolithography process



(d) 3D printed structure obtained by SLA process



(e) Selective Laser Sintering process



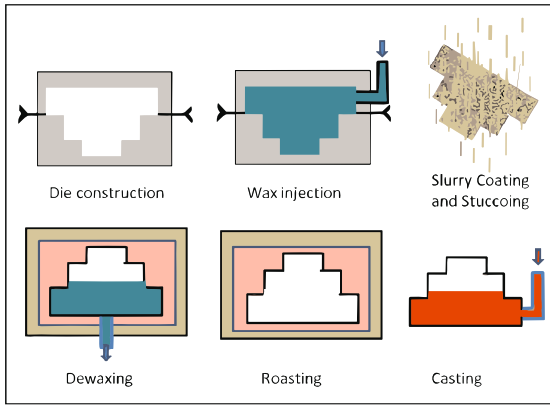
(f) Examples of several additive manufacturing processes and the structures that can be achieved using them.

Figure 1.8: Examples additive manufacturing methods

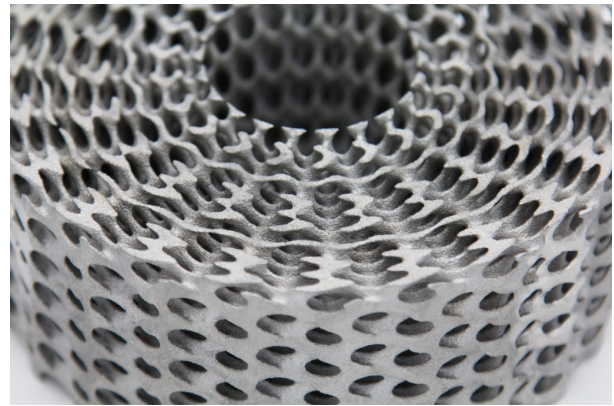
## Non-additive manufacturing

Non-additive, also known as traditional manufacturing, refers to a range of techniques in which material is either deformed or reshaped to create desired structures. These techniques remain essential in the fabrication of architected materials, We will mention few ones:

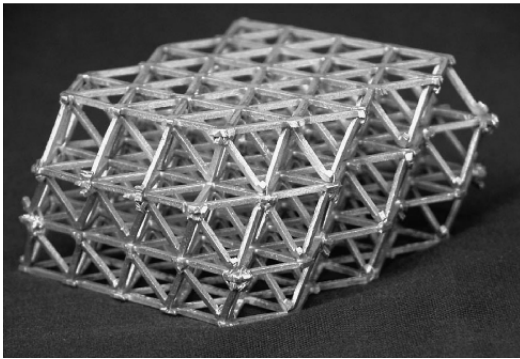
- **Investment Casting** Also known as lost-wax casting, this process is utilized for the creation of detailed metal parts with complex geometries. It often involves making truss patterns with attached face sheets using wax through injection molding, though additive manufacturing methods can also be employed. This technique has proven effective in the fabrication of intricate architected materials, including metal lattice structures;
- **Metal Wire Approaches** These methods involve manipulating metal wires into various shapes to create architected materials. Such approaches enable the production of 2D/3D structures through techniques like welding, braiding, or weaving, and are commonly employed to fabricate materials such as wire-woven bulk Kagome lattices. The properties of the resulting architected materials depend significantly on the mechanical characteristics of the wire material and the geometry of the wire arrangement. This dependency allows for the design of metallic architected materials with high strength-to-weight ratios and adjustable mechanical properties [Fleck and Deshpande, 2004, Gibson and Ashby, 1997];
- **Deformation Forming** Deformation forming involves the application of force to a material to induce a change in its shape. Techniques frequently employed include sheet forming, tube hydroforming, and stretch forming. Despite certain limitations in design scope, deformation forming is a cost-effective strategy for fabricating large-scale architected materials [Goyos-Ball et al., 2017, Hewage et al., 2016];
- **Other technique** Chemical methods, particularly used for foam fabrication, involve adding bubbles (usually inert gases) to create irregular or periodic meso/micro-structures. Such techniques can be applied to a variety of materials like metals, ceramics, polymers, glasses, and composites [Gibson and Ashby, 1997, Uribe-Lam et al., 2021]. Procedures vary, from high-pressure gas introduction in polymer foams to using hydrogen-containing metal powder for metallic foams. Besides chemical methods, other techniques, such as bonding processes, are also used for foam fabrication.



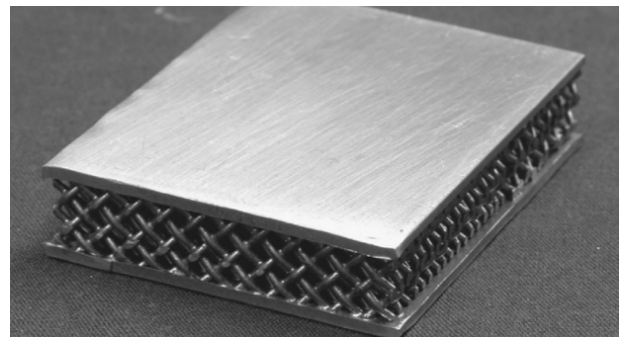
(a) Casting investment process



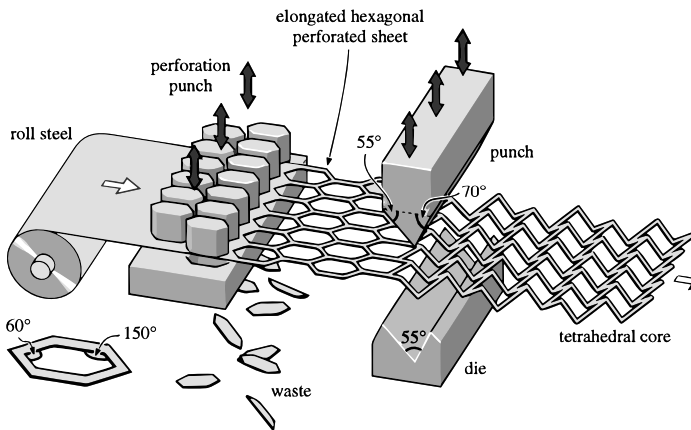
(b) Lattice structure obtained Casting investment process



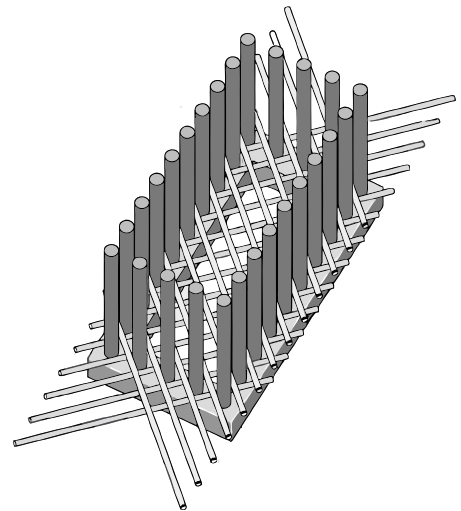
(c) Examples of several additive manufacturing processes and the structures that can be achieved using them.



(d) 3D printed structure obtained by SLA



(e) Selective Laser Sintering process



(f) Stereolithography process

Figure 1.9: Examples non-additive manufacturing methods

## Topology Optimization

Topological optimization, first proposed by Bendsøe and Kikuchi [Bendsøe and Kikuchi, 1988], is a strategic approach to design where material layout is specifically structured to optimize performance while adhering to predetermined design specifications. This technique is instrumental in realizing optimal material use, reducing unnecessary weight and design time. In the past, topological optimization was primarily used for mono-scale structures, largely due to the complexity associated with manufacturing multi-scale materials [Bendsoe, 1988, Zhou and Rozvany, 1991]. However, the advent of advanced additive manufacturing technologies has renewed interest in the optimal design of multi-scale structures. These technologies enable the fabrication of complex optimized geometries that were previously unachievable with traditional manufacturing methods. It's noteworthy that the same modeling techniques used in mono-scale structure optimization can also serve multi-scale designs through finer meshing of the design domain. Despite the computational expense associated with this approach, it is still a viable and powerful tool for complex designs.

To alleviate the computational challenges of multi-scale modeling, the implementation of the homogenization technique has been suggested. This method allows for computational efficiency by creating a link between microscopic geometries and their macro-scale effective properties [Bendsøe and Kikuchi, 1988]. Therefore, it presents a potential pathway for architected materials design and optimization that maximizes lifecycle efficiency, reduces environmental impact, and accommodates the selection of recyclable materials. Topological optimization, in essence, offers a comprehensive strategy that harmonizes material use, design intricacy, manufacturing needs, and performance objectives to deliver efficient, innovative, and sustainable designs.

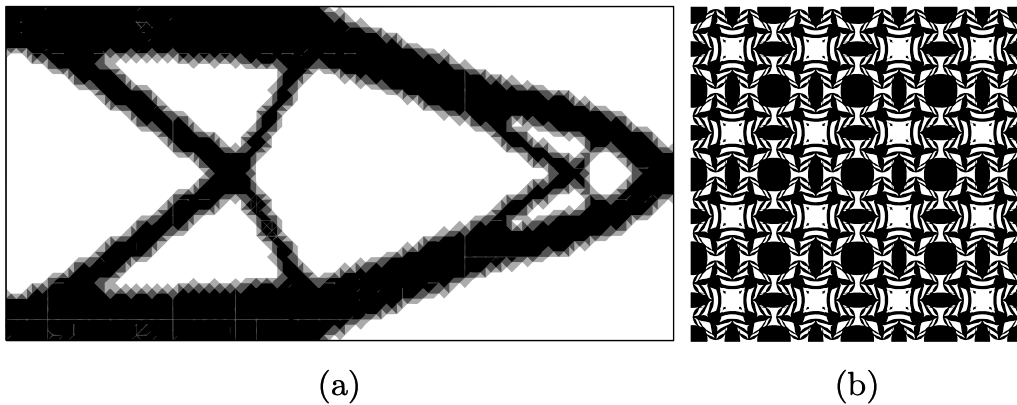


Figure 1.10: Two different optimisation modellings (a) Mono-scale modelling [Amstutz and André, 2006] and (b) Multi-scale modelling [Amstutz et al., 2010]

In view of the rapid development of topology optimisation of multi-scale structure over the last three decades, variety of optimisation methods have been proposed, among which the density-based method [Zhou and Rozvany, 1991], the level set method [Allaire et al., 2002, Wang et al., 2003] and the topological derivative [Sokolowski and Zochowski, 1999] are the most representatives.

## 1.5 Mechanical properties of architected materials

Architected materials are garnering substantial research interest due to their diverse intrinsic properties and unique behaviours. Their characteristics are particularly distinctive in both static and dynamic regimes, with a significant focus on both periodic and aperiodic lattice structures. When it comes to static behaviours, they provide a balance between density and mechanical properties, notably in terms of strength and stiffness which are investigated [Wicks and Hutchinson, 2001, Budiansky, 1999, Wadley et al., 2003, Bouaziz et al., 2008, Deshpande et al., 2001a, Deshpande et al., 2001b, Wallach and Gibson, 2001, Wicks and Hutchinson, 2001]. Further exploration into architected materials static behaviour has led to the development of auxetic materials, characterised by a negative Poisson's ratio, exhibiting lateral expansion under tension [Prall and Lakes, 1997, Dirrenberger et al., 2011, Li et al., 2017, Meena and Singamneni, 2019]

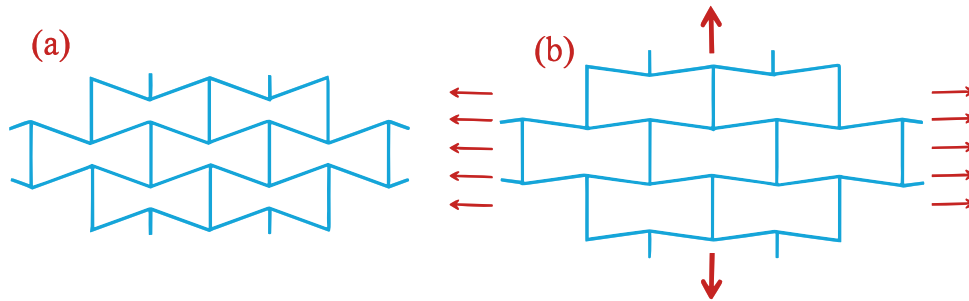
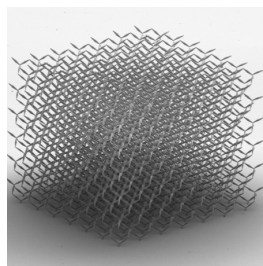


Figure 1.11: Example of auxetic behaviour : (a) unloaded configuration, (b) loaded configuration

Pentamode metamaterials are also worth noting, as they behave like fluids behavior despite being in a solid state. These materials are characterized by a disappearing shear modulus and a non-zero bulk modulus, facilitating shear deformation but complicating uniform compression [Milton and Cherkaev, 1995, Kadic et al., 2013]. Within the scope of topological optimization, the elasticity tensor of these materials can be custom-designed. This process employs homogenization and topological optimization to design a homogeneous medium with a tuned elasticity tensor. The corresponding optimized microstructure can then be identified through a subsequent dehomogenization process [Amstutz et al., 2010].



(a) Example of pentamode structure [Kadic et al., 2012]



(b) Example of exotic material unit cell obtained by optimizing the elasticity tensor

Figure 1.12

In elastodynamics, architected materials exhibit non-classical behaviors including non-linearities, dispersion, anisotropic wave propagation, presence of band gaps, and can be purposed as waveguides [Rosi and Auffray, 2016, Glacet et al., 2019, McGee et al., 2019, Spadoni et al., 2009] or even in the creation of an "invisibility cloak" [Bückmann et al., 2015]

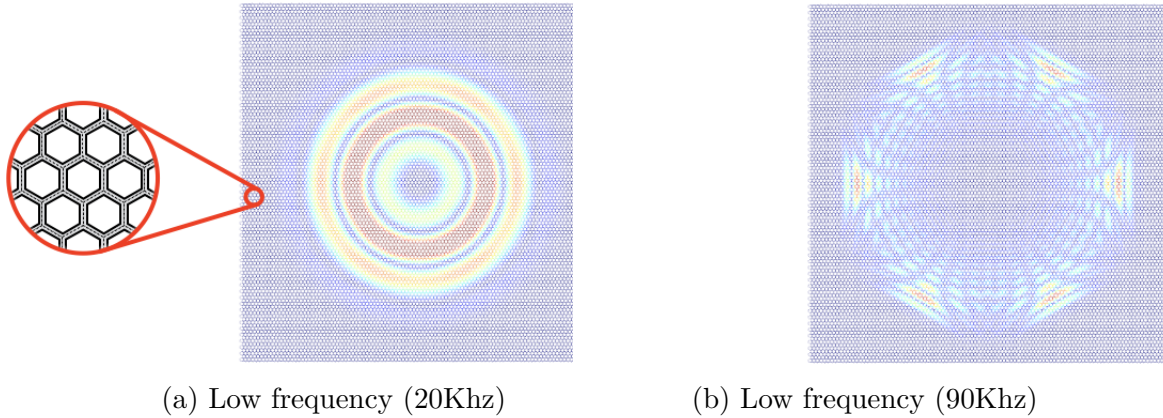


Figure 1.13: Time transient Finite Elements simulation of energy propagation in a hexagonal lattice at a given instant for shear pulses of different central frequency [Rosi and Auffray, 2016]

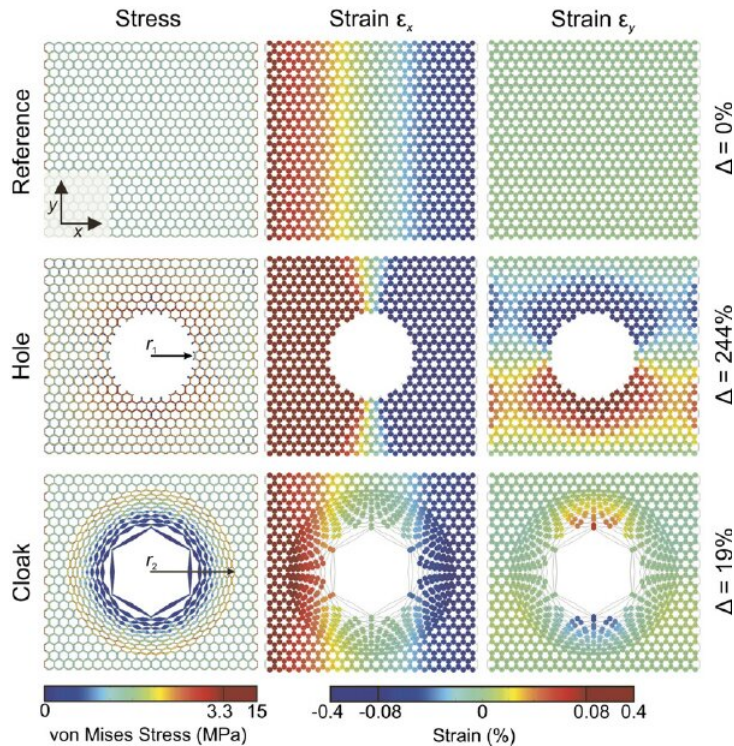


Figure 1.14: Example of concept of an invisibility cloak [Bückmann et al., 2015]

The Non-linear phenomena such as buckling are also leveraged to manifest behaviours similar to auxetic materials [Bertoldi et al., 2010, Shim et al., 2013, Babae et al., 2013]. They facilitate dynamic adjustment of band gaps' position and width [Rudykh and Boyce, 2014, Wang et al., 2014, Shan et al., 2014], which can be used to change the dynamic response of the structure. Regarding energy absorption properties, architected materials exhibits excellent performance due to reversible or irreversible non-linearities

[Schaedler et al., 2014, Czech et al., 2015]. They serve as effective shock absorbers and elastomer replacements. Bistable architected materials can also function as reusable energy-absorbing devices or actuators [Shan et al., 2015, Rafsanjani and Pasini, 2016].

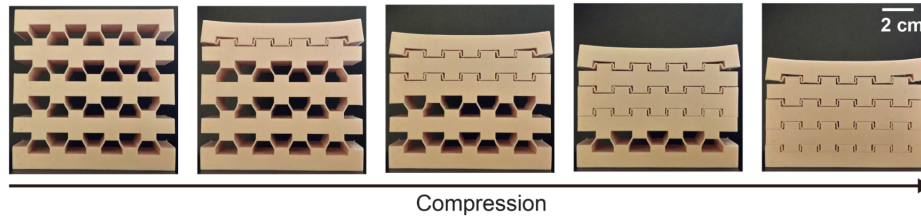


Figure 1.15: Example of a multistable lattice for trapping elastic strain energy [Shan et al., 2015]

## 1.6 Modelling and characterization of architected materials behaviour

A detailed understanding of the elastodynamic behaviour of architected materials (AMs) represents an important key in order for determining their potential applications. Various methods have been deployed to capture their behaviour in static and dynamic regime, with each approach offering unique insights. Below is concise overview of some key methods used in this context.

- **Experimental Testing:** Experimental methods serve as an essential cornerstone for characterizing the behaviour of architected materials. These techniques involve subjecting the material under investigation to static or dynamic loading with prescribed boundary conditions and subsequently measuring its response. For instance, dynamic mechanical analysis (DMA) is a standard method that examines the viscoelastic properties, providing important informations about modulus, damping, and other dynamic mechanical properties across a range of temperatures and frequencies [Menzel, 2002]. These methods are often combined with advanced imaging techniques, such as digital image correlation (DIC), to measure strain distributions across the material, thereby offering a detailed understanding of material behaviour under realistic loading conditions [Sutton et al., 2009].
- **Full Field Numerical Simulations:** Numerical simulations, such as those utilizing the Finite Element Method (FEM), where the internal architecture is thoroughly described, and small elements are used to mesh the structure, provides access to the whole behaviour of the material, local and global. As no simplifications are made concerning the constitutive material, classical behaviour laws can be used at the local scale, which allows to simulate a variety of loading scenarios and gain insight into the response of the medium, deformation behaviour, and potential points of failure. This approach is particularly useful when investigating structures with complex designs that may be difficult or impossible to evaluate experimentally.

- **Wave Propagation Analysis:** Analysis of wave propagation within architected materials provides valuable information regarding their dynamic response. Techniques such as Floquet-Bloch analysis, particularly when the medium is periodic, allows to construct the elastodynamic signature of the medium and can predict the presence of bandgaps and determine their frequency ranges, i.e. range of frequencies in which wave propagation is forbidden or highly attenuated. This understanding is crucial in applications that require vibration isolation, sound absorption or wave propagation control. Another example is Lamb wave analysis, used to investigate guided wave propagation in thin plates, a feature commonly found in layered architected materials. This technique can reveal information about the material’s internal structure, identifying defects or material properties variations [Rose, 2004].
- **Homogenization Methods:** Homogenization methods are used to derive effective properties of a heterogeneous material by considering its microstructure. This process bridges the scale gap between the microscopic geometries and macro-scale effective properties, simplifying the complexity of architected materials geometry. Homogenization has been used extensively in the context of periodic media where the response of the individual unit cells is replaced by an averaged response over the whole structure [Sanchez-Palencia, 1980]. It is a powerful approach allowing for efficient computational simulations while still capturing essential behaviour traits of the medium.
- **Non-linear Analysis:** Non-linear analysis tools are required when AMs display complex dynamic behaviours such as buckling or large deformations under specific loading conditions. Non-linear finite element analysis is one such tool that integrates experimental testing with advanced computational simulations, capturing and predicting these complex behaviours. It has been particularly valuable in the study of auxetic materials, which exhibit unconventional mechanical properties such as negative Poisson’s ratios [Lakes, 1987].

## 1.7 Synthesis

The fascination for architected materials has noticeably increased in recent years, mainly due to the simplification of their production through innovative manufacturing methods, and their appealing mechanical properties. This chapter offered a brief yet comprehensive introduction to them. It detailed the definition of an architected material and provided the current understanding on how to model and decipher their mechanical characteristics.

In the next chapter, we will present and provide a set of theoretical elements, essential for modelling and investigating the elastodynamic behaviour of architected materials. This chapter covers several physical and mathematical concepts, revolving around group theory, linear elasticity, wave propagation in periodic media, but also a brief review of generalized continuous media.

# Chapter 2

## Mathematical modelling of periodic architected materials

### Contents

---

|       |   |           |
|-------|---|-----------|
| 2.1   | FROM GEOMETRY TO MATHEMATICS . . . . .  | <b>22</b> |
| 2.1.1 | SYMMETRY IN THE PLANE . . . . .   | 22        |
| 2.1.2 | LATTICES . . . . .  | 25        |
| 2.1.3 | POINT GROUPS . . . . .  | 29        |
| 2.1.4 | SPACE GROUP . . . . .   | 31        |
| 2.2   | THE SPACE OF BIDIMENSIONAL CLASSIC ELASTICITY TENSORS . . . . .                 | <b>36</b> |
| 2.2.1 | CONSTITUTIVE EQUATIONS . . . . .  | 36        |
| 2.2.2 | MATERIAL AND PHYSICAL SYMMETRIES . . . . .                                      | 37        |
| 2.2.3 | REPRESENTATION OF THE ELASTICITY TENSOR SPACE . . . . .                         | 41        |
| 2.2.4 | SYMMETRY CLASSES AND INVARIANTS OF $\mathbb{E}La$ . . . . .                     | 45        |
| 2.3   | ELASTODYNAMICS OF ARCHITECTED MATERIALS . . . . .                               | <b>50</b> |
| 2.3.1 | PERIODIC MEDIA : SOME ELEMENTS OF THEORY . . . . .                              | 50        |
| 2.3.2 | FLOQUET-BLOCH ANALYSIS . . . . .  | 53        |
| 2.4   | EFFECTIVE GENERALIZED CONTINUUM : FROM ELASTOSTATIC TO ELASTODYNAMICS . . . . . | <b>58</b> |
| 2.4.1 | INTRODUCTION TO GENERALIZED CONTINUUM . . . . .                                 | 58        |
| 2.4.2 | MICROMORPHIC ELASTICITY . . . . .   | 59        |
| 2.4.3 | COSSERAT ELASTICITY IN 2D . . . . .   | 61        |
| 2.4.4 | STRAIN-GRADIENT ELASTICITY IN 2D . . . . .                                      | 64        |
| 2.5   | SYNTHESIS . . . . .   | <b>69</b> |

---

In order to simplify the understanding, we will define here the terminology used throughout the manuscript. We consider an affine Euclidean space  $\mathcal{E}$  of dimension  $d$  with an underlying vector space  $E$ . The two are identified through the selection of a reference point, denoted as  $O$ . Let  $\mathcal{B} = \{\mathbf{e}_i\}_{i=1\dots d}$  be an orthonormal basis of the vector space  $E$ , the couple  $(O, \mathcal{B})$  formed by the point  $O \in \mathcal{E}$  and the basis  $\mathcal{B}$  is called a reference frame. Therefore, any point  $P \in \mathcal{E}$  can be represented in the basis  $\mathcal{B}$  by its position vector  $\mathbf{x}$  as follows :

$$\underline{OP} = \mathbf{x} = \sum_{i=1}^d x_i \mathbf{e}_i \quad (2.0.1)$$

where  $\{x_i\}_{i=1\dots d}$  are the local coordinates of the point  $P$  with respect to  $\mathcal{B}$ . The vector space  $\mathbb{E}$  is equipped with an inner product denoted  $\langle \cdot, \cdot \rangle$

$$\langle \mathbf{u}, \mathbf{v} \rangle = \sum_{i=1}^d \sum_{j=1}^d u_i v_j g_{ij} \quad (2.0.2)$$

in which  $g_{ij} = \langle \mathbf{e}_i, \mathbf{e}_j \rangle$  is the metric tensor of the basis  $\mathcal{B}$ . In the following, we will consider  $g_{ij} = \delta_{ij}$ . It is worth noting, that the Einstein's convention will be systematically used throughout the present manuscript. In this chapter, we will provide a concise exploration of architected materials within the framework of 2D elasticity. The chapter is structured into four sections, each devoted to the in-depth exploration of fundamental aspects within periodic architected materials. In the first section, we lay the mathematical foundation by examining symmetry operations, lattices, and point/space groups. The second section focuses on key elements such as the constitutive equations in linear elasticity, material and physical symmetries, and tensors decomposition. Moving forward, the third section delves into the study of wave propagation in periodic heterogeneous media through the Floquet-Bloch analysis. Finally, the fourth section explores the concept of an equivalent homogeneous continuum and investigates various homogenization techniques.

## 2.1 From geometry to mathematics

### 2.1.1 Symmetry in the plane

An isometry is a geometrical transformation that can transform an object into either an identical object or its image with respect to a point, line, or plane. It preserves the distance between any two points [Armstrong, 1997]. There are three types of isometries of the plane:

- translations;
- rotations;
- simple reflections.

The combination (in the sense of composition or product) of two or several of these elementary isometries obviously gives rise to a new isometry [Malgrange et al., 2014]. We shall distinguish two classes of isometry: a direct isometry, which preserves angles and orientation, and an indirect one, which reverses the orientation. Let us give a brief definition of these transformations [Hestenes and Holt, 2007].

#### Translation

For a given vector  $\mathbf{a} \in \mathbb{R}^2$ , the linear mapping  $\mathbf{T}$  defined by

$$\begin{cases} \mathbf{T} : & \mathbb{R}^2 \longrightarrow \mathbb{R}^2 \\ \mathbf{T}_{\mathbf{a}}(\mathbf{x}) & = \mathbf{x} + \mathbf{a}, \quad \forall \mathbf{x} \in \mathbb{R}^2, \end{cases} \quad (2.1.1)$$

is a translation by the vector  $\mathbf{a}$ . There are no invariant points under a translation. Since the translation is a proper transformation, the product of  $p$  translation is also a direct isometry equal to the translation  $p\mathbf{a}$ .

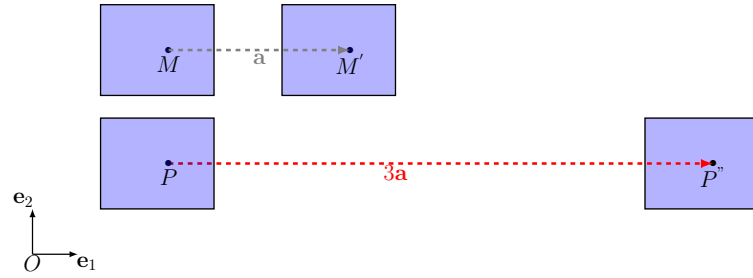


Figure 2.1: Translation of the point  $M$  and  $P$  respectively by vectors  $\mathbf{a}$  and  $3\mathbf{a}$

## Rotation

A 2D rotation is a geometrical transformation of a plane in which each point of the plane is turned by a given angle around a fixed point, the center of rotation. Let denote by  $\mathbf{R}(\theta)$ , the rotation by angle  $\theta$  around the origin  $O$  in Cartesian coordinates. For a given vector  $\mathbf{x} \in \mathbb{R}^2$ , we have

$$\mathbf{R}(\theta) \cdot \mathbf{x} = \mathbf{y} \iff \begin{pmatrix} \cos(\theta) & -\sin(\theta) \\ \sin(\theta) & \cos(\theta) \end{pmatrix}_{\mathcal{B}} \begin{pmatrix} x_1 \\ x_2 \end{pmatrix}_{\mathcal{B}} = \begin{pmatrix} y_1 \\ y_2 \end{pmatrix}_{\mathcal{B}}$$

Rotation by angle  $\theta$  around an arbitrary point  $M \in \mathbb{R}^2$  can be defined as the composition of rotation about  $O$  and translation by  $\mathbf{u} = \underline{OM}$ , such as

$$\mathbf{R}_M(\theta) = \mathbf{T}_{\mathbf{u}} \circ \mathbf{R}(\theta) \circ \mathbf{T}_{-\mathbf{u}}$$

more precisely, we have

$$\mathbf{R}_M(\theta) \cdot \mathbf{x} = \mathbf{R}(\theta) \cdot (\mathbf{x} - \mathbf{u}) + \mathbf{u}.$$

When a planar object can be rotated around a fixed point  $P$  and superimposed upon itself  $k$  times, we say that it has a  $k$ -fold rotational symmetry around  $P$ . This symmetry can be described by  $k$  symmetry elements, which are the rotations by angles of  $2\pi/k, 4\pi/k, \dots, 2k\pi/k, \dots$  where  $k$  is the order of the rotational symmetry. It is also worth noting that the composition of two rotations by angles  $\theta$  and  $\phi$  about a given point is itself a rotation by an angle of  $\theta + \phi$ . This means that the set of rotations with  $k$ -fold symmetry forms a group under composition, which has some interesting mathematical properties.

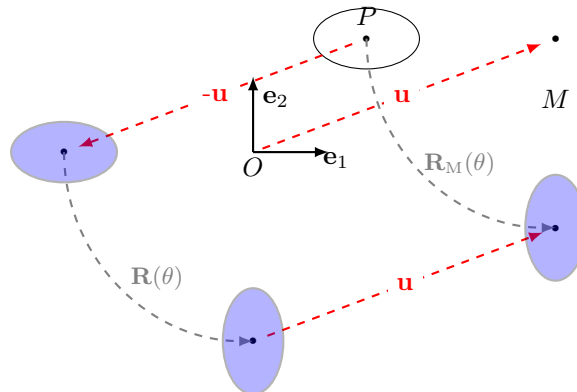


Figure 2.2: Rotation around a given  $M$

## Reflection

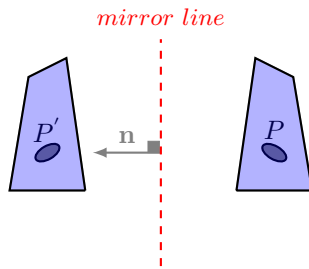
A reflection is a transformation that flips all points across a line called mirror. Let  $\mathbf{n}$  be the normal unit vector to a mirror line going through the origin, then the reflection  $\pi(\mathbf{n})$  of vector  $\mathbf{x}$  across the line of normal  $\mathbf{n}$  is defined by

$$\pi(\mathbf{n}) \cdot \mathbf{x} = 2(\mathbf{n} \cdot \mathbf{x})\mathbf{x} - \mathbf{n}, \quad \text{with} \quad \pi(\mathbf{n}) = \mathbf{I} - 2\mathbf{n} \otimes \mathbf{n}.$$

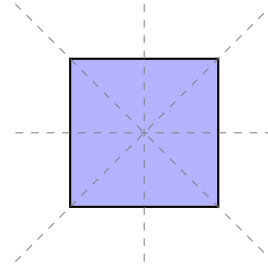
By parameterizing the vector  $\mathbf{n}$  with an angle theta such as  $\mathbf{n} = (\cos(\theta), \sin(\theta))$ , one can write

$$\pi(\mathbf{n}) \cdot \mathbf{x} = \mathbf{y} \iff \begin{pmatrix} -\cos(2\theta) & -\sin(2\theta) \\ -\sin(2\theta) & \cos(2\theta) \end{pmatrix}_B \begin{pmatrix} x_1 \\ x_2 \end{pmatrix}_B = \begin{pmatrix} y_1 \\ y_2 \end{pmatrix}_B$$

In which  $\theta$  designates the angle between  $\mathbf{n}$  and the horizontal axis  $\mathbf{e}_1$ . The points along the mirror line are all invariant (points that map onto themselves). If there are  $n$ -lines passing through the center of an object that leave it unchanged when reflected across them, we say that the object has  $n$ -mirror lines. In other words, an object has  $n$ -lines of symmetry if  $n$ -lines of reflection divide it into  $n$  identical parts. It is important to note that an object possessing  $n$ -mirror lines implies that it can be rotated by specific angles around a fixed point while maintaining its original appearance, i.e. a rotation invariance. These angles of rotation, which preserve the object's shape, are typically multiples of  $2\pi/n$ .



(a) Reflection across a line of normal  $\mathbf{n}_{\pi/2}$



(b) Object with 4-mirror lines

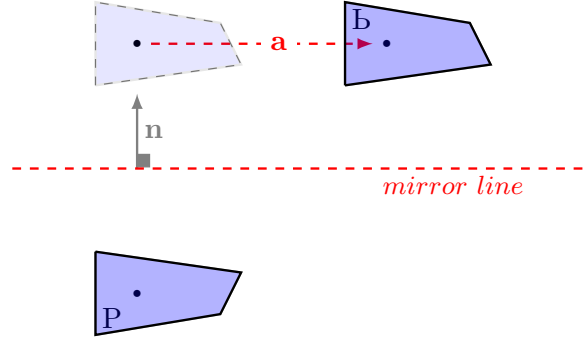
## Glide reflection

A glide reflection is a transformation that reflects an object across a mirror then slides it along that line. It can be defined as the composition of a reflection and a translation along a line parallel to the reflection's line. Let  $\pi(\mathbf{n})$  be a reflection across the line of normal  $\mathbf{n}$  and  $\mathbf{a}$  a translation vector perpendicular to  $\mathbf{n}$ . Then, for a given vector  $\mathbf{x} \in \mathbb{R}^2$ , the glide reflection can be defined as <sup>1</sup>

$$\mathcal{G}_{\mathbf{n},\mathbf{a}} := \{\pi(\mathbf{n}) | \mathbf{a}\} = \mathbf{T}_{\mathbf{a}} \circ \pi(\mathbf{n})$$

More formally, a glide reflection of a point  $\mathbf{x}$  is obtained by first reflecting it across the mirror line, and then translating it by the vector  $\mathbf{a}$  along the direction of the mirror, such as

$$\mathcal{G}_{\mathbf{n},\mathbf{a}}(\mathbf{x}) = \pi(\mathbf{n}) \cdot \mathbf{x} + \mathbf{a}.$$


 Figure 2.4: Glide reflection across the horizontal axis  $\mathbf{e}_1$  and displacement  $\mathbf{a}$ 

| Composition                                 | Identity                                    | $\mathbf{T}_{\mathbf{u}}$                    | $\pi(\mathbf{n}_\theta)$                        | $\mathbf{R}(\alpha)$  | $\mathcal{G}_{\mathbf{n}_\theta, \mathbf{t}}$                        |
|---|---|--|---|---|--|
| Identity                                    | Identity                                    | $\mathbf{T}_{\mathbf{u}}$                    | $\pi(\mathbf{n}_\theta)$                        | $\mathbf{R}(\alpha)$  | $\mathcal{G}_{\mathbf{n}_\theta, \mathbf{t}}$                        |
| $\mathbf{T}_{\mathbf{v}}$                   | $\mathbf{T}_{\mathbf{v}}$                   | $\mathbf{T}_{\mathbf{u}+\mathbf{v}}$         | $\mathcal{G}_{\mathbf{n}_\theta, \mathbf{v}}$   | $\mathbf{R}_M(\alpha)$  | $\mathcal{G}_{\mathbf{n}_\theta, \mathbf{t}'}$                       |
| $\pi(\mathbf{n}_\phi)$                      | $\pi(\mathbf{n}_\phi)$                      | $\mathcal{G}_{\mathbf{n}_\phi, \mathbf{u}}$  | $\mathbf{R}(2\phi - 2\theta)$                   | $\pi(\mathbf{n}_\phi + \mathbf{n}_{\theta/2})$                      | $\mathbf{R}_N(2\phi - 2\theta)$                                      |
| $\mathbf{R}(\beta)$                         | $\mathbf{R}(\beta)$                         | $\mathbf{R}_{M'}(\beta)$                     | $\pi(\mathbf{n}_\theta - \mathbf{n}_{\beta/2})$ | $\mathbf{R}(\beta + \alpha)$  | $\mathcal{G}_{\mathbf{n}_\theta - \mathbf{n}_{\beta/2}, \mathbf{t}}$ |
| $\mathcal{G}_{\mathbf{n}_\psi, \mathbf{w}}$ | $\mathcal{G}_{\mathbf{n}_\psi, \mathbf{w}}$ | $\mathcal{G}_{\mathbf{n}_\psi, \mathbf{w}'}$ | $\mathbf{R}_{N'}(2\psi - 2\phi)$                | $\mathcal{G}_{\mathbf{n}_\psi + \mathbf{n}_{\alpha/2}, \mathbf{w}}$ | $\mathbf{R}_P(2\psi - 2\theta)$                                      |

Table 2.1: Composition of all possible isometries in 2D

where:

- $M$  is the center of the rotation such as  $\mathbf{x}_M = \frac{1}{2} \left( \mathbf{I} - \frac{1}{\tan(\alpha/2)} \mathbf{R}(\alpha) \right) \cdot \mathbf{v}$ . Note that the angle of rotation  $\alpha$  must not be equal to 0 or  $\pi$ ;
- $\mathbf{t}'$  is the glide reflection translation vector defined by  $\mathbf{t}' = \mathbf{R}(\theta) \cdot \mathbf{v} + \mathbf{t}$ ;
- The construction of  $\mathbf{w}'$  is similar to that of  $\mathbf{t}'$ ;
- The coordinates of the rotation centers  $N$ ,  $M'$ ,  $N'$  and  $P$  are obtained in the same way as for the point  $M$ .

In-plane chirality is a property of an object which means that it cannot be superimposed on its mirror image, even when subjected to rotations or translations. More formally, an object is chiral if it lacks of mirror line. However, some isometries can affect an object's chirality. Rotations and translations do not have any effect on an object's chirality, but reflections and glide reflections can change it.

## 2.1.2 Lattices

Now that the basic geometrical transformations have been introduced, let us explore how these transformations can be used to describe the geometrical symmetry properties of a periodic architected material. In order to describe the structure of these materials, it is essential to introduce some concepts such as lattices, elementary cell, point group and space group.

<sup>1</sup>The group of Glide-reflection is an affine group constructed as the semidirect product of  $\mathbb{R}^2$  and  $O(2)$ . Interested readers can refer to [Rosi et al., 2020] for the construction of such transformation corresponding to the adopted convention of notation.

## Direct space

A medium  $\Omega$  is said to be periodic when its geometry exhibits a translational invariance with respect to a family of linearly independent translations. The medium is constructed by a simple translation of a single pattern, called elementary cell, that fills the whole plane. Due to its periodicity, a periodic architected material can be assimilated to a crystal and associated with a fairly simple structure, *the Bravais lattice* [Malgrange et al., 2014, Armstrong, 1997, Armstrong, 1997, McWeeny, 2002]. The set of the mentioned translations is called the *Lattice*, defined by

$$\mathcal{R} = \{\mathbf{r} \in \mathcal{E} \mid \mathbf{r} = m_1 \mathbf{e}_1 + m_2 \mathbf{e}_2, m_i \in \mathbb{Z}\} \quad (2.1.2)$$

in which  $\mathbf{e}_j$  denotes the basis vectors of the lattice, and represents the direct space. For a periodic architected material, each point is equivalent to an infinite number of others with an identical environment due to the translational symmetry. Hence, physical properties defined over the medium are invariant under the set  $\mathcal{R}$ . For instance, the elasticity tensor  $\mathbf{C}$  and the scalar mass  $\rho$  of a periodic medium verify the following condition

$$\begin{cases} \mathbf{C}(\mathbf{x} + \mathbf{r}) = \mathbf{C}(\mathbf{x}) \\ \rho(\mathbf{x} + \mathbf{r}) = \rho(\mathbf{x}) \end{cases} \quad \forall \mathbf{x} \in \Omega, \forall \mathbf{r} \in \mathcal{R} \quad (2.1.3)$$

The set  $\mathcal{R}$  is a group acting on  $\Omega \subset \mathcal{E}$ . For a given material point  $\mathbf{x} \in \Omega$ , we define the orbit of  $\mathbf{x}$  for the action of  $\mathcal{R}$

$$\text{Orb}(\mathbf{x}) = \{\mathbf{x}' \in \Omega, \mathbf{x}' = \mathbf{x} + \mathbf{r} \mid \mathbf{r} \in \mathcal{R}\} \quad (2.1.4)$$

In other words, the orbit  $\text{Orb}(\mathbf{x})$  consists of all material points in  $\Omega$  that are equivalent to a given point  $\mathbf{x}$  under the action of the group  $\mathcal{R}$ . Since  $\mathcal{R}$  represents a set of translations that preserve the medium's properties, the physical properties defined over the medium are also invariant under the action of  $\mathcal{R}$ . This invariance gives rise to what is referred to as the “*point lattice*”<sup>2</sup> [Senechal, 1996]. The figure figure 2.5 shows that  $\mathbf{x}$  and  $\mathbf{x}'$  are equivalent points within the medium. These equivalent points in the orbit share the same physical properties due to the invariance of those properties under the action of  $\mathcal{R}$ .

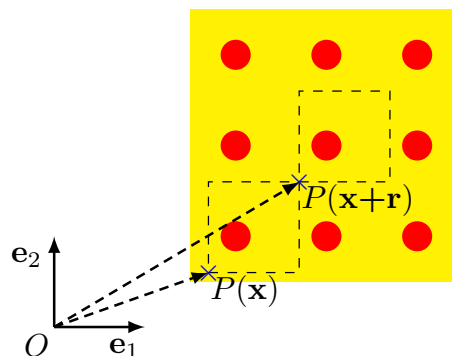


Figure 2.5: The equivalence of material points  $\mathbf{x}$  and  $\mathbf{x}'$  under the action of  $\mathcal{R}$

<sup>2</sup>The point lattice is the orbit of the lattice, encompassing all points reachable through linear combinations of the generating vectors. It specifically refers to the arrangement of points formed by the  $\mathbb{Z}$ -module, i.e. the collection of points the lattice can generate

A periodic medium is constructed from a point lattice and a pattern, as illustrated on figure 2.6. The point lattice is defined by the set of points obtained by considering all the points that are equivalent to a given point<sup>3</sup>, which are called nodes. The content of the point lattice is called the pattern, or more conventionally the unit cell, which contains the basic information of the medium. It is important to note that the pattern is not univocally defined, it can be reduced to a single primitive cell, as it can contains several. Therefore, the symmetry of the lattice cannot be directly associated with the symmetry of a pattern since the pattern does not have a univocal mathematical meaning.

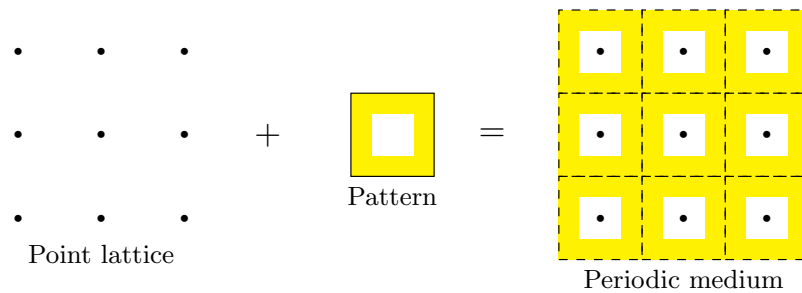


Figure 2.6: Example of bidimensional periodic medium

### Unit/elementary/primitive cell

In the literature, three related concepts are found regarding the pattern that tiles the space: the unit cell, elementary cell, and primitive cell.

- A unit cell of the direct-space is the smallest pattern (parallelogram or rectangle) that can be repeated over and over by unit translations to fill the space of the medium without gaps or overlaps. It contains one or more lattice points and reproduces the lattice arrangement when stacked. The elementary cell is the smallest repeating unit that captures essential lattice features. It may or may not be equivalent to the unit cell and is chosen based on the lattice's symmetry.
- The elementary cell may or may not be equivalent to the unit cell, depending on the lattice's symmetry. In some cases, they have the same shape and size, while in other cases, the elementary cell is a smaller subset with a different shape or size. The elementary cell represents the minimum symmetry required to describe the point lattice.

<sup>3</sup>The set of all the points obtained by the action of  $\mathcal{R}$  on the origin point

Without loss of generality, only the elementary cell (denoted as  $\mathcal{T}_0$ ) will be considered. The elementary cell  $\mathcal{T}_0$  is a fundamental domain for the action of  $\mathcal{R}$  on  $\Omega$ . It contains exactly one point per  $\mathcal{R}$ -orbit, and the properties of the medium can be entirely characterized by the values taken in the cell  $\mathcal{T}_0$ .

$$\mathcal{T}_0 = \{ \mathbf{x}_0 \in \mathcal{E} \mid \mathbf{x}_0 = \sum_{j=1}^2 [0, 1[ \mathbf{e}_j \} \subset \Omega \quad (2.1.5)$$

Figure figure 2.7 illustrates a 2D example of a elementary cell, with a chosen couple of vectors basis  $\{\mathbf{e}_j\}_{j \in [1,2]}$ . Note that the choice of the unit cell is not unique, several choices are possible.

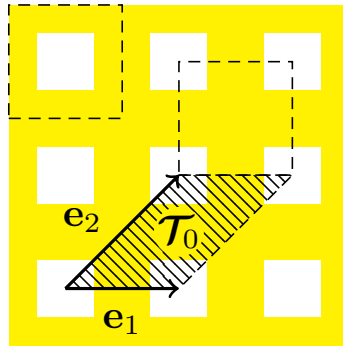


Figure 2.7: Definition of an elementary cell

### Bravais lattice

In 2D space, there are 5 types of Bravais lattices grouped in 4 crystal systems, according to the shape of the basic parallelogram formed by the elementary translation vectors  $\mathbf{a}$  and  $\mathbf{b}$ : *monoclinic*, *orthorhombic*, *hexagonal* and *tetragonal* (see figure 2.8). These lattices are entirely characterised by  $\theta$ , the angle between the vectors  $\mathbf{a}$  and  $\mathbf{b}$ , and their respective norms as reported in table 2.10. The study of Bravais lattices in 3D space is more complex and an exhibits rich informations (14 lattices in 3D), the interest reader can refer to [Malgrange et al., 2014, Armstrong, 1997].

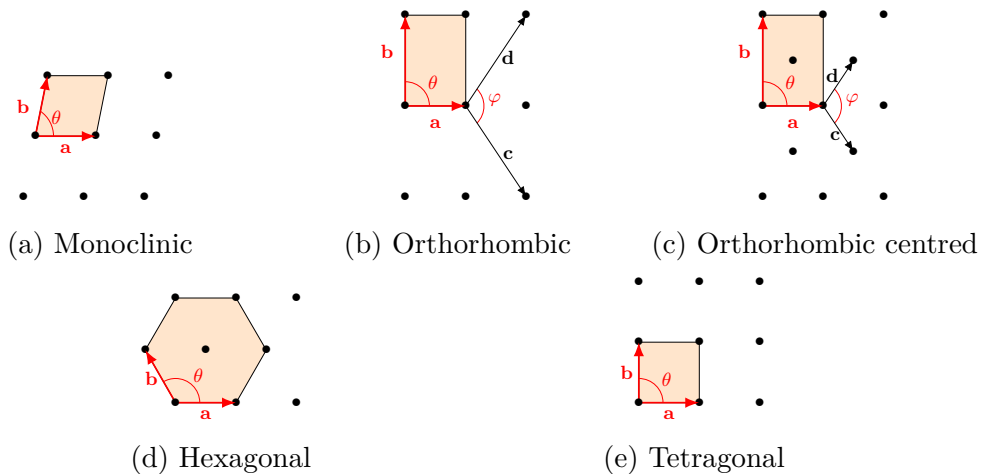


Figure 2.8: Bravais lattices in 2D space and their unit cell shapes (coloured area)

| Crystal system | Lattice system      | Edge length conditions  | Axial angle                                |
|----------------|---------------------|---|--|
| Monoclinic     | Oblic               | $\ \mathbf{a}\  < \ \mathbf{b}\  < \ \mathbf{a-b}\  < \ \mathbf{a+b}\ $ | $\theta \neq 90^\circ$                     |
| Orthorhombic   | Rectangular         | $\ \mathbf{a}\  < \ \mathbf{b}\  < \ \mathbf{a-b}\  = \ \mathbf{a+b}\ $ | $\theta = 90^\circ, \varphi \neq 90^\circ$ |
|                | Centred rectangular | $\ \mathbf{a}\  < \ \mathbf{d}\  = \ \mathbf{a-d}\  < \ \mathbf{a+d}\ $ | $\theta = 90^\circ, \varphi \neq 90^\circ$ |
| Tetragonal     | Square              | $\ \mathbf{a}\  = \ \mathbf{b}\  < \ \mathbf{a-b}\  = \ \mathbf{a+b}\ $ | $\theta = 90^\circ$                        |
| Hexagonal      | Hexagonal           | $\ \mathbf{a}\  = \ \mathbf{b}\  = \ \mathbf{a-b}\  < \ \mathbf{a+b}\ $ | $\theta = 120^\circ$                       |

Table 2.2: Geometrical characteristics of Bravais lattice in 2D space [Armstrong, 1997]

Now that the 5 possible Bravais lattices in 2D have been introduced, one can wonder how symmetry operations act on it. As said before, isometries can be generated by combinations of translations, rotations or glide reflections, let us list the so-called point and space groups, the different subgroups describing the properties of lattices that exhibits certain symmetries.

### 2.1.3 Point groups

The set of isometries that leave the lattice identical with respect to a fixed point (modulo a translation) constitutes the point group of the lattice. However, the lattice generally has other symmetries but subjected to a constraint called *Crystallographic restriction*.

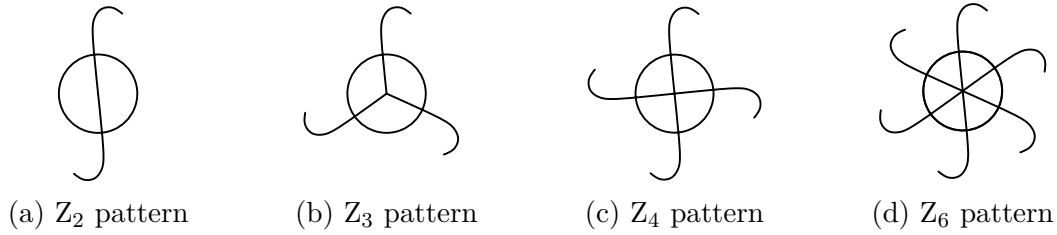
**Theorem 1.1: Crystallographic restriction principle** [Armstrong, 1997]

*“The rotational symmetries of a crystal are usually limited to 2-fold, 3-fold, 4-fold, and 6-fold” .*

In other words, only rotation of order 1, 2, 3, 4 and 6 are allowed. There are 2 common conventions used to describe lattice point groups: the first is the *Hermann-Mauguin notation*, known as the international notation and used by the crystallography community [Hermann, 1934]. The second is the *Schoenflies notation*, more commonly used in spectroscopy, and this is the one we will adopt throughout this manuscript. Let us introduce the point groups for the Schoenflies system [Schoenflies, 1891].

**Definition : Cyclic group  $Z_k$**

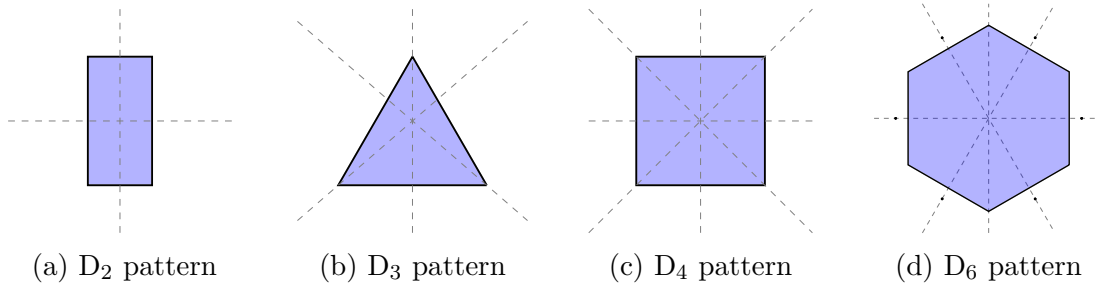
The cyclic group with  $k$  elements is a subgroup of the dihedral group  $D_k$  that contains only rotation generated by  $\mathbf{R}(\theta_k)$ , with  $\theta_k = \{2\pi n/k\}_{n \in \llbracket 1, k-1 \rrbracket}$ .

Figure 2.9: Examples of  $k$ -sided chiral polygons;**Definition : Dihedral group  $D_k$** 

The dihedral group with  $2k$  elements is a group that contains rotations generated by  $\{\mathbf{R}(\theta_k)\}$  and reflections across lines generated by  $\boldsymbol{\pi}(\mathbf{n}_{\theta_k})$ , such as

$$\mathbf{R}(\theta_k)^k = \boldsymbol{\pi}(\mathbf{n}_{\theta_k})^2 = \mathbf{I}, \quad \boldsymbol{\pi}(\mathbf{n}_{\theta_k}) \cdot \mathbf{R}(\theta_k) = \mathbf{R}(\theta_k)^{-1} \cdot \boldsymbol{\pi}(\mathbf{n}_{\theta_k})$$

whith  $\theta_k = \{2\pi n/k\}_{n \in [1, k-1]}$ . Geometrically, it represents the symmetry group of  $k$ -side regular polygons.

Figure 2.10: Examples of  $k$ -sided regular polygons;

For practical simplicity throughout, the subgroups  $Z_1$  and  $D_1$  will be denoted as  $\mathbb{1}$  and  $Z_2^\pi$ , respectively.

**Classification of point groups**

Accordingly, one can make a first classification of the point groups of each lattice system. These point groups are summarized in section 2.1.3

| Lattice system | Point group | Rotational-symmetry | Reflection symmetry |
|----------------|-------------|---------------------|---------------------|
| Oblic          | $C_2$       | 2-fold axis         | $\emptyset$         |
| Orthorhombic   | $D_2$       | 2-old axis          | 2 mirror lines      |
| Square         | $D_4$       | 4-fold axis         | 4 mirror lines      |
| Hexagonal      | $D_6$       | 6-old axis          | 6 mirror lines      |

Table 2.3: Classification of the Bravais lattice and their point groups

After this brief introduction of the different Bravais lattices point groups, one would now introduce the concept of space group, known as *Wallpaper groups* in 2D, which can arise as symmetry groups of periodic architected materials.

### 2.1.4 Space group

The set of isometries that leave a periodic architected (lattice + pattern) invariant constitutes the space group of the medium. In addition to the point group symmetry operations, the space group contains additional symmetry elements, such as translation, glide reflection, etc. Unlike the point group, the space group has no fixed point under the application of all symmetry operations. Before tackling the classification of all possible wallpaper groups, we shall introduce the *Hermann-Mauguin notation* for which, each wallpaper group name is made up of four symbols [Sasse, 2020]: letters and digits. An example of full wallpaper name is  $p31m$ . The first letter refers to nature of the lattice unit cell;  $p$  for primitive and  $c$  for centred. This is followed by a digit,  $n$ , which indicates the highest order of rotational symmetry about a perpendicular axis to the plane of the tiling: 1-fold (identity transformation), 2-fold, 3-fold, 4-fold or 6-fold. The next two symbols, when present, are either an  $m, g$ , or  $1$ , indicates additional symmetries: at the place of third symbol, it designates respectively a reflection line, glide reflection line, or identity, through a given axis while a  $1$  means that there is no additional symmetry; at the place of fourth symbol,  $m$  and  $g$  represents respectively, a reflection line and glide reflection at an angle  $\phi = 2\pi/n$  to the main axis. If the last two symbols are omitted, then the medium has no mirror and glide reflection lines. For instance, the group name  $p3m1$  represents a group with a primitive cell, 3-fold rotation and reflection line with respect to the horizontal axis. There are two types of space groups: symmorphic and non-symmorphic. Symmorphic groups are only generated by the symmetry elements of its point group, which leave invariant a given fixed point of the lattice. In the other hand, non-symmorphic groups possess additional symmetry operations such as glide reflections, which does not preserve the lattice points [Armstrong, 1997]. Now let us list all the possible space groups for 2D periodic media.

#### Classification of Wallpaper groups

In 2D, there are a total of 17 space groups that can be defined and characterized by a unique lattice diagram, point groups and a set of generators. To facilitate the comprehension of the lattice diagrams, the symmetry operations such as centers of rotations, positions of mirror lines and glide reflection lines, are represented using the well-established symbols listed in section 2.1.4.

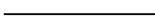
| Symbol  | Meaning                       |
|---|-------------------------------|
|  | 2-fold rotation center (180°) |
|  | 3-fold rotation center (120°) |
|  | 4-fold rotation center (90°)  |
|  | 6-fold rotation center (60°)  |
|  | reflection line               |
|  | glide reflection line         |
|  | unit cell edge                |

Table 2.4: Symbols used for lattice diagrams

To illustrate in some details the concepts introduced in this section, one can now start the classification of the 17 possible wallpaper groups. This classification, presented

in table 2.5, is based on the Hermann-Mauguin notation, which gives a unique name to each group [Grünbaum and Shephard, 1987, Zheng and Bohler, 1994].

| Space group | Lattice system | Point group  | Type           | Generators   |
|-------------|----------------|--------------|----------------|--|
| $p1$        | monoclinic     | $\mathbf{1}$ | symmorphic     | $\{\mathbf{I}, \mathbf{a}, \mathbf{b}\}$   |
| $p2$        | monoclinic     | $Z_2$        | symmorphic     | $\{\mathbf{R}(\pi)\}$  |
| $pm$        | orthorhombic   | $Z_2\pi$     | symmorphic     | $\{\mathcal{G}_{\mathbf{e}_1, \mathbf{0}}, \mathbf{a}, \mathbf{b}\}$                                   |
| $pg$        | orthorhombic   | $Z_2\pi$     | non-symmorphic | $\{\mathcal{G}_{\mathbf{e}_1, \mathbf{b}/2}, \mathbf{a}, \mathbf{b}\}$                                 |
| $p2mm$      | orthorhombic   | $D_2$        | symmorphic     | $\{\mathbf{R}(\pi), \pi(\mathbf{e}_2), \mathbf{a}, \mathbf{b}\}$                                       |
| $p2mg$      | orthorhombic   | $D_2$        | non-symmorphic | $\{\mathbf{R}(\pi), \mathcal{G}_{\mathbf{e}_1, \mathbf{b}/2}, \mathbf{a}, \mathbf{b}\}$                |
| $p2gg$      | orthorhombic   | $D_2$        | non-symmorphic | $\{\mathbf{R}(\pi), \mathcal{G}_{\mathbf{e}_1, (\mathbf{a}+\mathbf{b})/2}, \mathbf{a}, \mathbf{b}\}$   |
| $cm$        | orthorhombic   | $D_1$        | symmorphic     | $\{\pi(\mathbf{e}_1), \mathbf{a}, \mathbf{b}\}$  |
| $c2mm$      | orthorhombic   | $D_2$        | symmorphic     | $\{\mathbf{R}(\pi), \pi(\mathbf{e}_1 + \mathbf{e}_2)\}$  |
| $p4$        | square         | $Z_4$        | symmorphic     | $\{\mathbf{R}(\pi/2), \mathbf{a}, \mathbf{b}\}$  |
| $p4m$       | square         | $D_4$        | symmorphic     | $\{\mathbf{R}(\pi/2), \pi(\mathbf{e}_2), \mathbf{a}, \mathbf{b}\}$                                     |
| $p4g$       | square         | $D_4$        | non-symmorphic | $\{\mathbf{R}(\pi/2), \mathcal{G}_{\mathbf{e}_2, (\mathbf{a}+\mathbf{b})/2}, \mathbf{a}, \mathbf{b}\}$ |
| $p3$        | hexagonal      | $Z_3$        | symmorphic     | $\{\mathbf{R}(2\pi/3), \mathbf{a}, \mathbf{b}\}$   |
| $p3m1$      | hexagonal      | $D_3$        | symmorphic     | $\{\mathbf{R}(2\pi/3), \mathbf{R}(2\pi/3) \circ \pi(\mathbf{e}_2), \mathbf{a}, \mathbf{b}\}$           |
| $p31m$      | hexagonal      | $D_3$        | symmorphic     | $\{\mathbf{R}(2\pi/3), \mathbf{R}(2\pi/3) \circ \pi(\mathbf{e}_1), \mathbf{a}, \mathbf{b}\}$           |
| $p6$        | hexagonal      | $Z_6$        | symmorphic     | $\{\mathbf{R}(\pi/3), \mathbf{a}, \mathbf{b}\}$  |
| $p6mm$      | hexagonal      | $D_6$        | symmorphic     | $\{\mathbf{R}(\pi/3), \mathbf{R}(\pi/3) \circ \pi(\mathbf{e}_2), \mathbf{a}, \mathbf{b}\}$             |

Table 2.5: Summary of the 17 2D wallpaper groups, their properties and notations

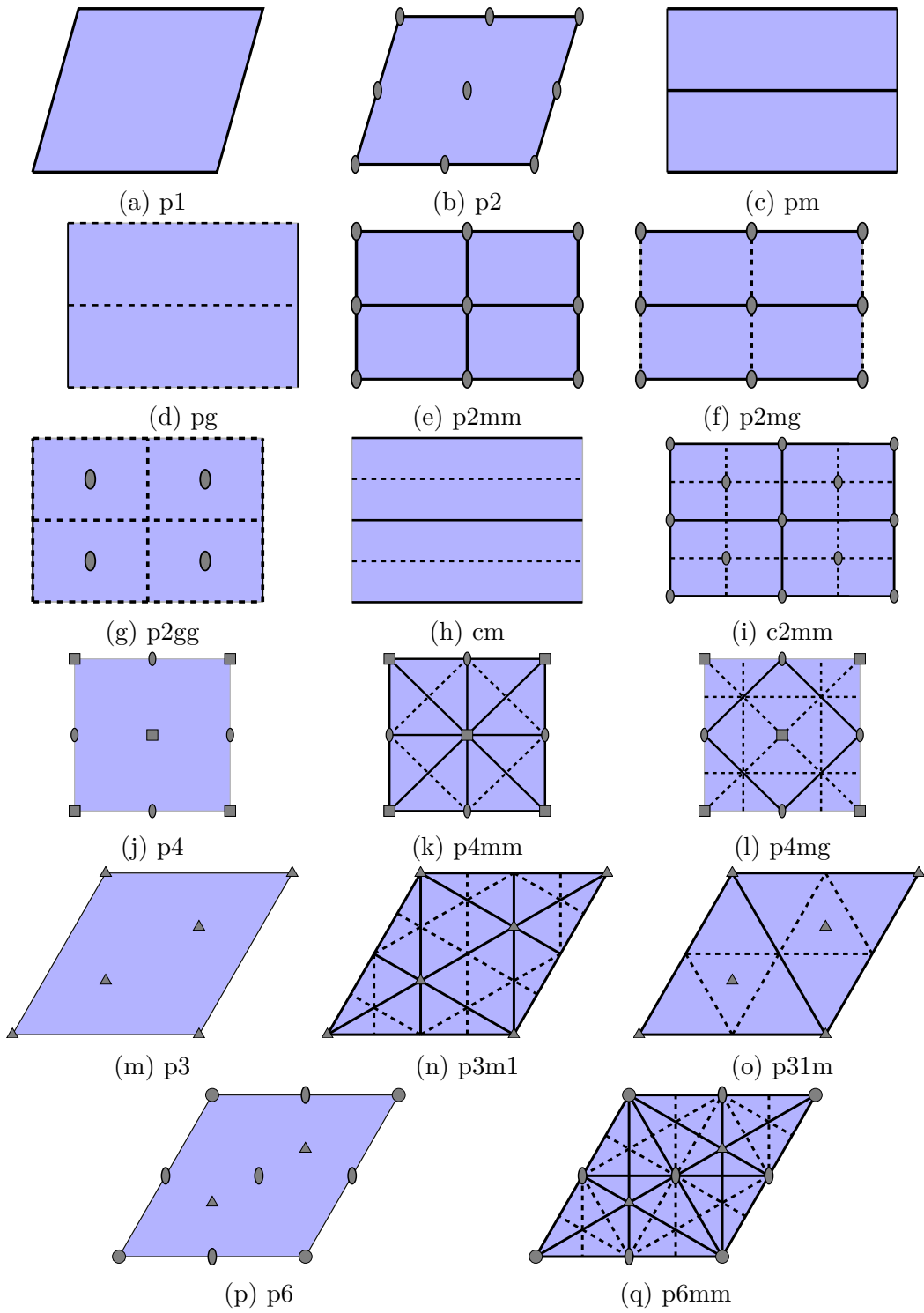


Figure 2.11: Lattice diagrams of the 17 wallpaper groups

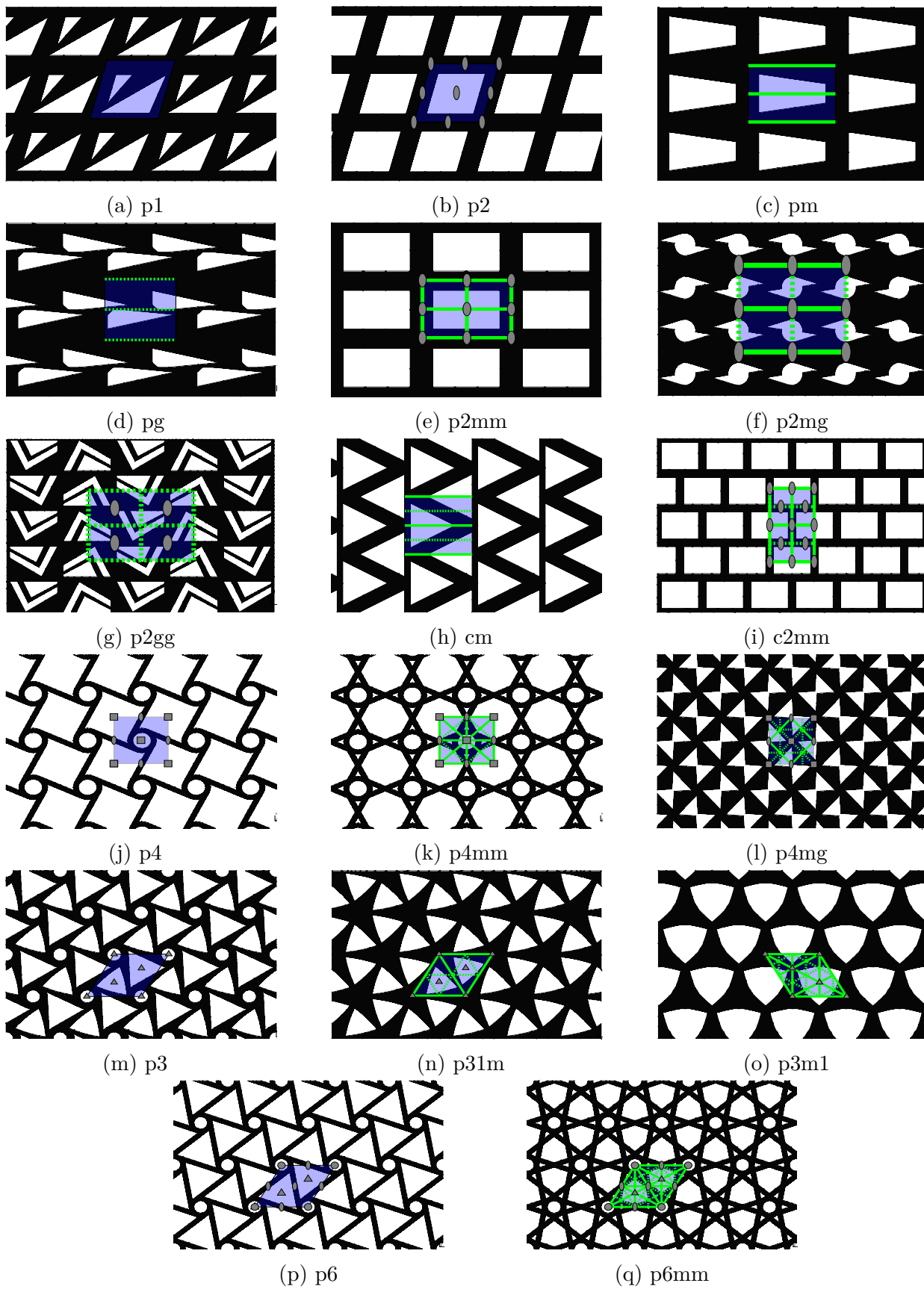


Figure 2.12: Examples of periodic architected materials of the 17 wallpaper groups

## Chirality and non-centrosymmetry

Point and space groups have been introduced in terms of the nature of their generators, before closing this section it is interesting to look at their geometric content. To that aim we will consider geometric figures that are left fixed by each kind of group and look at their symmetry properties. Consider the following figure

$$\begin{array}{ccc}
 \begin{array}{c} \text{Chiral Figure} \\ \downarrow \pi(\mathbf{n}) \end{array} & \xrightarrow{\mathbf{R}(\pi)} & \begin{array}{c} \text{Mirror Image} \\ \downarrow \pi(\mathbf{n}) \end{array} \\
 \begin{array}{c} \text{Star Figure} \\ \downarrow \pi(\mathbf{n}) \end{array} & \xrightarrow{\mathbf{R}(\pi)} & \begin{array}{c} \text{Hexagon} \\ \downarrow \pi(\mathbf{n}) \end{array}
 \end{array} \quad (2.1.6)$$

It appears that the  $Z_3$  and  $Z_6$ -invariant figures do not possess mirror invariance and can therefore turn left or right. As such, they will be called *chiral*. It can be observed that  $Z_6$  and  $D_6$ -invariant figures are centrosymmetric, meaning that they are invariant under the transformation  $-\mathbf{I}$  which correspond, in  $\mathbb{R}^2$  to  $\mathbf{R}(\theta)$ , this property is clearly not satisfied by the  $Z_3$  and  $D_3$ -invariant figures. Hence from this example introduce the notions of *chirality* and *centrosymmetry*. These concepts are very important for the intended physical applications. For a more formal definition:

### Definition

A subgroup of  $O(2)$  will be said to be:

- *centrosymmetric* (denoted by  $\mathcal{I}$ ) if it contains the inversion  $\mathbf{R}(\pi)$ , and *non-centrosymmetric* ( $\overline{\mathcal{I}}$ ) otherwise;
- *chiral* (noted  $\mathcal{C}$ ) if it only contains rotations, and *achiral* (noted  $\overline{\mathcal{C}}$ ) otherwise (i.e. if it contains reflections).

$O(2)$ -closed subgroups can be divided into four subsets according to the nature of their generators. The different situations are reported in the following table:

|                          |               |                          |
|--------------------------|---------------|--------------------------|
|                          | $\mathcal{I}$ | $\overline{\mathcal{I}}$ |
| $\overline{\mathcal{C}}$ | $D_{2k}$      | $D_{2k+1}$               |
| $\mathcal{C}$            | $Z_{2k}$      | $Z_{2k+1}$               |

After introducing periodic architected materials from a mathematical point of view, it is important to understand how their geometry can affect their physical properties and mechanical behaviour. In the following subsection, the concept of physical and material symmetries in linear elasticity will be introduced, which will provide further insight into the mathematical description of physical properties.

## 2.2 The space of bidimensionnal classic elasticity tensors

### 2.2.1 Constitutive equations

In the theory of linear elasticity for anisotropic homogeneous body, the strain and the stress state are described by the infinitesimal strain tensor  $\boldsymbol{\varepsilon} \in \mathcal{S}^2(\mathbb{R}^2)$  and by the Cauchy stress tensor  $\boldsymbol{\sigma} \in \mathcal{S}^2(\mathbb{R}^2)$ . These two quantities are second-order symmetric tensors, i.e. there are elements of  $\mathcal{S}^2(\mathbb{R}^2)$ . Since we are in the context of infinitesimal strain theory, the strain tensor can be expressed in terms of the displacements field, such as

$$\boldsymbol{\varepsilon} := \frac{1}{2} (\mathbf{u} \otimes \boldsymbol{\nabla} + \boldsymbol{\nabla} \otimes \mathbf{u}), \quad (2.2.1)$$

in which  $\mathbf{u} \otimes \boldsymbol{\nabla}$  is the displacement gradient. The Cauchy stress tensor obeys the following local momentum balance equation

$$\boldsymbol{\nabla} \cdot \boldsymbol{\sigma} + \mathbf{f} = \rho \frac{\partial^2 \mathbf{u}}{\partial t^2}, \quad (2.2.2)$$

and  $\mathbf{f}$  is the body force density (force by unit of volume) and  $\rho$  is mass density of material. These tensors  $(\boldsymbol{\sigma}, \boldsymbol{\varepsilon})$  are both symmetric and characterize the local strain and stress state of the matter. The constitutive law in linear elasticity, also called generalized Hooke's law, is a local relation between the components of the stress and strain tensors

$$\boldsymbol{\sigma} := \mathbf{C} : \boldsymbol{\varepsilon} \quad (2.2.3)$$

The linear map from the set of infinitesimal strain tensors into the space of stress tensors is defined as fourth order tensor, called the elasticity tensor  $\mathbf{C}$ , which characterizes the linear behaviour of the matter under mechanical stress.  $\mathbf{C}$  has a priori 16 components in 2D space (81 in 3D), it can be represented by  $4 \times 4$  generic matrix which elements are the elastic constants. Since  $\sigma_{ij}$  and  $\varepsilon_{kl}$  are symmetric with respect to index permutations  $ij$  and  $kl$ , the elasticity tensor has the following minor symmetries

$$\begin{cases} \sigma_{ij} = \sigma_{ji} \\ \varepsilon_{kl} = \varepsilon_{lk} \end{cases} \implies \begin{cases} C_{ijkl} = C_{jikl} \\ C_{ijkl} = C_{ijlk} \end{cases} \quad (2.2.4)$$

This reduces the number of independant elastic constants from 16 to 9 in the 2D case and from 81 to 36 in 3D problems, hence the  $4 \times 4$  matrix becomes a  $3 \times 3$  matrix. The potential energy associated to the linear elastic behavior behaviour of the material can be expressed as a quadratic function of the strain :

$$W(\boldsymbol{\varepsilon}) = \frac{1}{2} C_{ijkl} \varepsilon_{ij} \varepsilon_{kl}. \quad (2.2.5)$$

Due to the equivalence of its second partial derivatives

$$\frac{\partial^2 W(\boldsymbol{\varepsilon})}{\partial \varepsilon_{ij} \partial \varepsilon_{kl}} = \frac{\partial^2 W(\boldsymbol{\varepsilon})}{\partial \varepsilon_{kl} \partial \varepsilon_{ij}}, \quad (2.2.6)$$

the elasticity tensor has therefore the following symmetry, called the major symmetry

$$C_{ijkl} = C_{klij}. \quad (2.2.7)$$

Hence, the  $3 \times 3$  matrix becomes symmetric and contains only 6 independent components of  $\mathbf{C}$ . It worth noting that the index symmetries of the elasticity tensor are independent of those imposed by the material. The elasticity tensor space is the vector space defined by

$$\mathbb{E}la = \{C_{ijkl} \in \otimes^4(\mathbb{R}^2) \mid C_{\underline{(ij)} \underline{(kl)}}\}, \quad \dim \mathbb{E}la = 6, \quad (2.2.8)$$

in which the notation  $(..)$  indicates invariance under permutations of the indices in parentheses (the minor index symmetries) and  $\underline{\dots}$  indicates symmetry with respect to permutations of the underlined blocks (the major one). In the next subsection, in order to talk about the symmetry, and therefore the anisotropy of a material, the transformation that acts on the space of its elasticity tensor will be introduced.

### 2.2.2 Material and physical symmetries

To choose a group of transformations is to choose a point of view to say whether two objects are equivalent or not. Let denote by  $\mathcal{M}$  a microstructure attached to a given material point  $P$  as shown in figure 2.13. The microstructure which describes the local organization of the matter can possess certain symmetries with respect to orthogonal transformations  $\mathbf{Q} \in O(2)$ , where  $O(2)$  is the group of linear isometries of  $\mathbb{R}^2$  that contains both proper transformations (rotations with  $\det \mathbf{Q} = 1$ ) and improper transformations (mirror symmetries, inversion, . . . with  $\det \mathbf{Q} = -1$ ). This can be experimentally shown when the measure of a material property with respect to a given set of orientations, within a chosen reference frame, consistently leads to the same result.

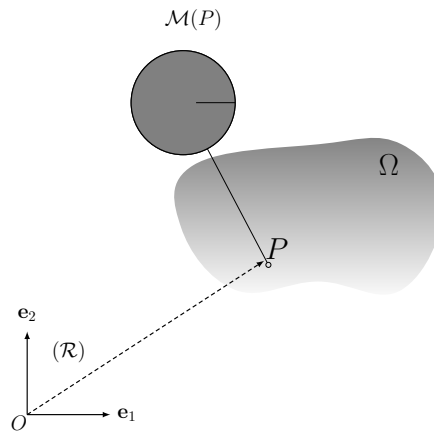


Figure 2.13: A microstructure  $\mathcal{M}(P)$  attached to a given material point  $P$

The set of all linear isometries with respect to a fix point that preserves  $\mathcal{M}$  forms a point group  $G_{\mathcal{M}(P)}$ , called the *material symmetry* group [Auffray and Ropars, 2016], such that

$$G_{\mathcal{M}(P)} := \{\mathbf{Q} \in O(2), \quad \mathbf{Q} \star \mathcal{M}(P) = \mathcal{M}(P)\}. \quad (2.2.9)$$

An important point to avoid any misunderstanding is the following. In most part of this manuscript, the *active interpretation* of a transformation will be considered. This means that, with respect to a fixed reference, the transformation of an object gives rise to a new object which is usually different from the original object. This interpretation has to be distinguished from the *passive interpretation* in which the object

is unchanged but the basis used for its description is transformed. The difference between of point of view is illustrated figure 2.14

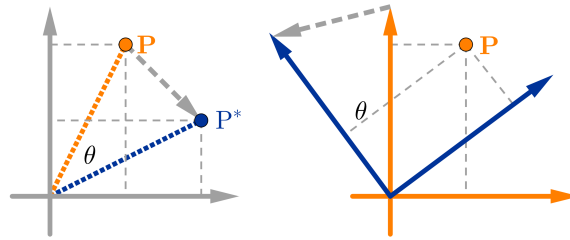


Figure 2.14: Active transformation on the left figure: a new vector is obtained; Passive transformation on the right figure, in which only the basis is changed.

Since the material element  $\mathcal{M}(P)$  is transformed under the action of  $O(2)$ , the physical properties described over it are also transformed [Auffray and Ropars, 2016, Forte and Vianello, 2014, Auffray et al., 2017]. In the context of our study, the behaviour of the matter is described by the fourth-order elasticity tensor  $\mathbf{C}$  attached to each material point  $P$  of the physical body<sup>4</sup>. The action of  $O(2)$  on an element of  $\mathbb{E}la$  is defined by

$$(\mathbf{Q} \star \mathbf{C})_{ijkl} = Q_{ip}Q_{jq}Q_{kr}Q_{ls}C_{pqrs},$$

within our hypotheses, the symmetry group of  $\mathbf{C}$  is defined by:

$$G_{\mathbf{C}} := \{\mathbf{Q} \in O(2), \mathbf{Q} \star \mathbf{C} = \mathbf{C}\}, \quad (2.2.10)$$

in which the  $\star$  product stands for the standard tensorial action.  $G_{\mathbf{C}(P)}$  represents the *symmetry group* of the elasticity  $\mathbf{C}$ , which describes the *physical symmetry*. The interdependence of material and physical symmetries should be acknowledged, as they are not independent of each other. This connection is established through the Curie-Neumann principle [Zheng and Boehler, 1994], which asserts that:

### Theorem 2.1: Curie-Neumann's principle

*“For a material element and for any of its physical properties, every material symmetry transformation of the material element is a physical symmetry transformation of the physical property”.*

In other words, the material symmetry group is included in the physical symmetry group<sup>5</sup>. Mathematically,

$$G_{\mathcal{M}} \subseteq G_{\mathbf{C}},$$

this means that, that a physical property can be more symmetrical than the microstructure is. The Hermann theorem [Hermann, 1934] gives some indications on that point, which can be stated as follows:

<sup>4</sup>For the sake of simplicity, the tensor will be denoted simply as  $\mathbf{C}$ . In case of a change of point, the notation will indicate the relevant point.

<sup>5</sup>Accordingly, every symmetry transformations of  $\mathcal{M}$  is a symmetry transformation of  $\mathbf{C}$ .

**Theorem 2.2: Hermann's theorem**

*“ Consider  $\mathcal{M}$  be a microstructure left invariant by a rotation of order  $n$  and  $\mathbf{T}$  a  $m$ -th order tensor describing its effective properties. If  $n > m$  then  $\mathbf{T}$  is at least  $SO(2)$ -invariant (hemitropic). ”*

Accordingly, materials with hexagonal symmetries in their microstructure will be elastically isotropic. As mentioned before, when a material is subjected to a given linear isometry, its nature does not change. However, the corresponding elasticity tensor will be transformed. As a consequence, different elasticity tensors can be associated to the same elastic material. For instance, if we rotate a sample of material in a fixed reference frame, although the material nature is still unchanged, we will obtain two different<sup>6</sup> elasticity tensors  $\mathbf{C}_1$  and  $\mathbf{C}_2$ , associated to the same elastic material, we say that both belong to the same orbit [Abud and Sartori, 1983]. The orbit  $\mathcal{O}_{\mathbf{C}}$  of  $\mathbf{C}_1$  in  $\mathbb{E}la$  is defined as the set of all elasticity tensors  $\mathbf{C}^*$  resulting from  $O(2)$  operations which represent the same material:

$$\mathcal{O}_{\mathbf{C}} := \{\mathbf{C}^* \in \mathbb{E}la \mid \mathbf{Q} \in O(2) \text{ , } \mathbf{C}^* = \mathbf{Q} \star \mathbf{C}\} \quad (2.2.11)$$

Depending on  $\mathbf{C}$ , for certain transformations, the resulting tensor may be identical to the original one. The set of such transformations constitutes its symmetry group, the definition of which was introduced in equation (2.2.10) [Auffray et al., 2014].

When an object is represented in the same basis but in two different orientations, it may possess different symmetry groups (although conjugate). Therefore, relying solely on the symmetry group is inadequate for accurately characterizing the intrinsic symmetries of an object. From a physical point of view, it is interesting to introduce another notion describing and characterizing properly the symmetry of a physical object independently of its orientation. To make this more concrete, let  $\mathbf{C}_1$  et  $\mathbf{C}_2$  be two different elasticity tensors and let  $G_{\mathbf{C}_1}$  and  $G_{\mathbf{C}_2}$  denote their respective symmetry groups, we say that their respective symmetry groups are  $O(2)$ -conjugate if

$$\exists \mathbf{Q} \in O(2) \text{ , } G_{\mathbf{C}_2} = \mathbf{Q} G_{\mathbf{C}_1} \mathbf{Q}^T.$$

In this case, we can write

$$\mathbf{C}_1 \approx \mathbf{C}_2.$$

The latter relation is called equivalence relation, which means that the tensors are equivalents. A conjugacy class is the set of groups which can be obtained from a given group element by conjugation. It has been demonstrated in [Armstrong, 1997] that a conjugacy class is a an equivalence class. Hence, the collection of all tensors which are related to it is the equivalence class of  $\mathbf{C}_1$ . We shall define the symmetry class of a tensor  $\mathbf{C}$  as the set of  $O(2)$ -subgroups conjugate to  $G_{\mathbf{C}}$ :

$$[G_{\mathbf{C}}] := \{G = \mathbf{Q} G_{\mathbf{C}} \mathbf{Q}^T \subset O(2) \text{ , } \mathbf{Q} \in O(2)\}. \quad (2.2.12)$$

As mentioned in [Auffray, 2017], the symmetry class of  $\mathbf{C}$  corresponds to its symmetry group modulo its orientation in  $O(2)$ . Moreover, it is known that there is only a finite number of different symmetry classes and that each symmetry class is conjugate to

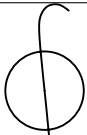
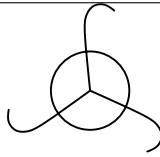
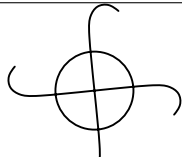
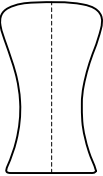
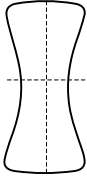
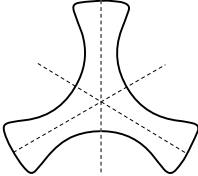
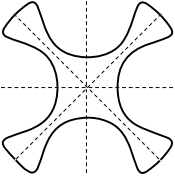
<sup>6</sup>Different in terms of components, since both tensors are taken in the same frame

a closed subgroup of  $O(2)$ . These subgroups can be regrouped in the following set [Armstrong, 1997] :

$$\{\mathbb{1}, Z_2^{\pi(\mathbf{n})}, Z_k, D_k, O(2), SO(2)\}_{k \in \mathbb{N}, k \geq 2}$$

wherein:

- $\mathbb{1}$  : the identity group;
- $Z_k$  : the cyclic group with  $k$  elements generated by the rotation  $\mathbf{R}(2\pi/k)$ . Geometrically,  $Z_k$  is the symmetry group of  $k$ -side chiral polygons;
- $Z_2^\pi$  : the group with 2 element generated by  $\pi(\mathbf{n})$ ;
- $D_k$  : the dihedral group with  $2k$  elements generated by  $\mathbf{R}(2\pi/k)$  and  $\pi(\mathbf{n})$ . Geometrically,  $D_n$  is the symmetry group of  $k$ -side regular polygons;
- $SO(2)$  : the group of rotation generated by  $\mathbf{R}(\theta)$  where  $\theta \in [0, 2\pi[$ ;
- $O(2)$  : the orthogonal group generated by  $\mathbf{R}(\theta)$  and  $\pi(\mathbf{e}_1)$ .

| Rotation order | 1   | 2   | 3  | 4   |
|----------------|---|---|--|---|
| Cyclic         |   |   |   |   |
| Dihedral       |  |  |  |  |

In  $\mathbb{R}^2$ , there exist four equivalence classes of the elasticity tensor with respect to  $O(2)$ . These classes correspond to the following symmetry types: *biclinic*, *orthotropic*, *tetragonal* and *isotropic materials*. The section 2.2.2 summarizes the different symmetry classes, their corresponding symmetry group, and the dimension of the elasticity tensor for each class."

| Symmetry class           | Biclinic | Orthotropic | Tetragonal | Isotropic |
|--------------------------|----------|-------------|------------|-----------|
| $[G_C]$                  | $[Z_2]$  | $[D_2]$     | $[D_4]$    | $[O(2)]$  |
| $\#_{indep}(\mathbf{C})$ | 6        | 4           | 3          | 2         |

Table 2.6: 2D symmetry groups

Let  $\Sigma_{[G]}$  denotes the set that regroup each type of tensor,  $\Sigma_{[G]}$  is called stratum and contains tensors which symmetry group is conjugate to  $O(2)$ . The space 2D elasticity tensor  $\mathbb{E}la$  can be divided into 4 strata [He and Zheng, 1996, Vianello, 1997, Forte and Vianello, 2014] :

$$\mathbb{E}la = \Sigma_{[Z_2]} \cup \Sigma_{[D_2]} \cup \Sigma_{[D_4]} \cup \Sigma_{[O(2)]}$$

Since the elasticity tensor is a fourth-order tensor and the basis  $\mathcal{B}$  has a different dimension, a direct representation of the tensor within  $\mathcal{B}$  is not feasible. Therefore, it is necessary to introduce a linear application that transform a fourth-order symmetric tensor to a second-order one. This can be achieved by using a  $3 \times 3$  symmetric matrix within an appropriately chosen basis. In the next section, harmonic decomposition of the elasticity tensor will be proposed, starting with an introduction to Kelvin basis and harmonic spaces. Then, the Clebsch-Gordan formula will be used in order to decompose the elasticity tensor over the harmonic sub-spaces. Finally, we will provide a overview of the relationship between the different symmetry classes and the invariants of  $\mathbb{E}la$ .

### 2.2.3 Representation of the elasticity tensor space

#### Kelvin basis

The general expression of Hooke's law requires the use of four-index objects, which is heavy to handle. That is why some simplified notations have been proposed. Such a simplification is interesting for both theoretical and numerical reasons. In particular, they allow for a matrix representation of equation (2.2.3), the aim of this formalism is to transfer the algebra of 4th-order tensor to that of a  $3 \times 3$  symmetric matrix. This means that we aim to construct a  $\mathbf{T}_{(ij)} \simeq \mathbb{R}^3$  basis in order to rewrite Hooke's law as a matrix product:

$$\{\boldsymbol{\sigma}\} = [\mathbf{C}]\{\boldsymbol{\varepsilon}\} \quad (2.2.13)$$

which means

$$\begin{pmatrix} \sigma_1 \\ \sigma_2 \\ \sigma_3 \end{pmatrix} = \begin{pmatrix} C_{11} & C_{12} & C_{13} \\ C_{12} & C_{22} & C_{23} \\ C_{13} & C_{23} & C_{33} \end{pmatrix} \begin{pmatrix} \varepsilon_1 \\ \varepsilon_2 \\ \varepsilon_3 \end{pmatrix} \quad (2.2.14)$$

The most used convention to represent an element of  $\mathbf{T}_{(ij)}$  as a vector of  $\mathbb{R}^3$  is the “*Voigt notation*” [Voigt, 1910], which takes into account the symmetries  $\mathbf{T}_{(ij)}$  to reduce each pair of indices into one index according to the following two-to-one subscript correspondances :

$$\begin{array}{c|ccc} \alpha & 1 & 2 & 3 \\ \hline ij & 11 & 22 & 12 \end{array}$$

In what follows, we will use the *Kelvin notation* [François, 1995], which is symmetric and preserves the tensorial structure of the product. The idea is to construct an orthonormal basis  $\mathcal{K} = (\tilde{\mathbf{e}}_1, \tilde{\mathbf{e}}_2, \tilde{\mathbf{e}}_3)$  of  $\mathbf{T}_{(ij)}$  from the canonical basis of  $\mathbb{R}^3$ . This construction is as follows

$$\begin{cases} \tilde{\mathbf{e}}_\alpha = \mathbf{e}_i \otimes \mathbf{e}_i, \\ \tilde{\mathbf{e}}_\alpha = \frac{\sqrt{2}}{2} (\mathbf{e}_i \otimes \mathbf{e}_j + \mathbf{e}_j \otimes \mathbf{e}_i), \text{ if } i \neq j \end{cases} \quad (2.2.15)$$

Since being orthonormal, the basis  $\mathcal{K}$  coincides with its dual basis  $\mathcal{K}^*$  and both  $\boldsymbol{\varepsilon}$  and  $\boldsymbol{\sigma}$  can be represented with the same convention as vectors in  $\mathbb{R}^3$ , such that

$$\begin{pmatrix} \varepsilon_{11} & \varepsilon_{12} \\ \varepsilon_{12} & \varepsilon_{22} \end{pmatrix}_{\mathcal{B}} \implies \begin{pmatrix} \varepsilon_1 = \varepsilon_{11} \\ \varepsilon_2 = \varepsilon_{22} \\ \varepsilon_3 = \sqrt{2}\varepsilon_{12} \end{pmatrix}_{\mathcal{K}} \quad \text{and} \quad \begin{pmatrix} \sigma_{11} & \sigma_{12} \\ \sigma_{12} & \sigma_{22} \end{pmatrix}_{\mathcal{B}} \implies \begin{pmatrix} \sigma_1 = \sigma_{11} \\ \sigma_2 = \sigma_{22} \\ \sigma_3 = \sqrt{2}\sigma_{12} \end{pmatrix}_{\mathcal{K}^*} .$$

Similarly, the Hooke's law can be written with convention as a matrix in  $\mathbb{R}^3$  as follows :

$$\begin{pmatrix} \sigma_{11} \\ \sigma_{22} \\ \sqrt{2}\sigma_{12} \end{pmatrix}_{\mathcal{K}} = \begin{pmatrix} C_{1111} & C_{1122} & \sqrt{2}C_{1112} \\ C_{1122} & C_{2222} & \sqrt{2}C_{1222} \\ \sqrt{2}C_{1112} & \sqrt{2}C_{1222} & 2C_{1212} \end{pmatrix}_{\mathcal{K}} \begin{pmatrix} \varepsilon_{11} \\ \varepsilon_{22} \\ \sqrt{2}\varepsilon_{12} \end{pmatrix}_{\mathcal{K}} \quad (2.2.16)$$

Since the constitutive law involves second-order tensors and a fourth order tensor, respectively, the way they transform under the action of a linear isometry is often not trivial to describe : some components are transformed (turned at different speeds), while others remain invariant. One way of understanding the involved mechanisms when these tensors are subjected to an orthogonal transformation is to investigate their harmonic structures. To reach this point, the first step is to decompose the space  $\mathbb{E}la$  into a collection of  $O(2)$ -irreducible spaces , i.e. a direct sum of elementary spaces where each subspace is  $O(2)$ -invariant. This decomposition is known as the harmonic decomposition, which provides a way to extract useful information about the material's properties [Forte and Vianello, 2014, Auffray et al., 2017, Desmorat and Auffray, 2019]. Before providing its explicit decomposition for the elasticity tensor space, let us take an example of the space of second order symmetric tensors  $S^2(\mathbb{R}^2)$  to illustrate the main idea behind this decomposition.

For a given element  $\mathbf{T} \in S^2(\mathbb{R}^2)$  ,  $\mathbf{T}$  can be decomposed into deviatoric and a spherical part :

$$\mathbf{T} = \mathbf{T}^d + \mathbf{T}^s = \mathbf{T}^d + \alpha \mathbf{I} = \Phi(\mathbf{T}^d, \alpha) \quad (2.2.17)$$

where  $\mathbf{T}^d \in \mathbb{K}^2$  and  $\alpha \in \mathbb{K}^0$  are, respectively, the deviatoric part and spherical part of  $\mathbf{T}$  such as :

$$\alpha := \frac{1}{2} \mathbf{T} : \mathbf{I}, \quad \text{and} \quad \mathbf{T}^d := \mathbf{T} - \alpha \mathbf{I}$$

The decomposition equation (2.2.17) implies that  $S^2(\mathbb{R}^2)$  and the direct sum  $\mathbb{K}^2 \oplus \mathbb{K}^0$  are isomorphic, we can write

$$S^2(\mathbb{R}^2) \simeq \mathbb{K}^2 \oplus \mathbb{K}^0$$

The decomposition above is irreducible since each its elements of the harmonic subspaces can not be decomposed into smaller tensors, note that each subspace is  $O(2)$ -invariant .

### Irreducible representation of the elasticity tensor space

The aim of this subsection is to establish the harmonic structure of elasticity tensor space using the Clebsch-Gordan formula. More details and mathematical proofs concerning these notions can be found in [Auffray et al., 2021]. We recall that the elasticity tensor space is defined by

$$\mathbb{E}la = \{C_{ijkl} \in \otimes^4(\mathbb{R}^2) \mid C_{\underline{(ij)} \underline{(kl)}}\}$$

Which can be defined also as  $\mathbb{E}la = S^2(S^2(\mathbb{R}^2))$ . We can decompose  $\mathbb{E}la$  into irreducible elements, namely harmonic spaces. We shall write :

$$\mathbb{E}la \simeq \bigoplus_k \alpha_k \mathbb{K}^k, \quad (2.2.18)$$

In which the integer  $\alpha_k$  corresponds to the multiplicity of the harmonic space  $\mathbb{K}^k$ . The expression equation (2.2.18) is called *isotypic decomposition* of  $\mathbb{E}la$  [Auffray et al., 2017]. In order to determine the structure of the latter decomposition, let us introduce the Clebsch-gordan formula.

### Clebsch-Gordan formula and harmonic decomposition

After introducing the concept of the Kelvin basis and harmonic spaces, the Clebsch-Gordan formula will be introduced in the what follows to further elaborate on the harmonic decomposition of the elasticity tensor. This formula allows to decompose the elasticity tensor over harmonic sub-spaces, and provides the explicit expression of each sub-space element.

#### Lemma 2.1: Isotypic decomposition

For every integer  $m > 0$  and  $n > 0$ , we have the following isotypic decompositions, in which  $\times$  indicates meaningless products:

|                   |   |                   |                   |
|-------------------|---|-------------------|-------------------|
| $\otimes$         | $\mathbb{K}^n$  | $\mathbb{K}^0$    | $\mathbb{K}^{-1}$ |
| $\mathbb{K}^m$    | $\begin{cases} \mathbb{K}^{2n} \oplus \mathbb{K}^0 \oplus \mathbb{K}^{-1} & , n = m; \\ \mathbb{K}^{n+m} \oplus \mathbb{K}^{ n-m } & , n \neq m; \end{cases}$ | $\mathbb{K}^m$    | $\mathbb{K}^m$    |
| $\mathbb{K}^0$    | $\mathbb{K}^n$  | $\mathbb{K}^0$    | $\mathbb{K}^{-1}$ |
| $\mathbb{K}^{-1}$ | $\mathbb{K}^n$  | $\mathbb{K}^{-1}$ | $\mathbb{K}^0$    |

|                   |                                       |                |                   |
|-------------------|---------------------------------------|----------------|-------------------|
| $S^2$             | $\mathbb{K}^n$                        | $\mathbb{K}^0$ | $\mathbb{K}^{-1}$ |
| $\mathbb{K}^m$    | $\mathbb{K}^{2n} \oplus \mathbb{K}^0$ | $\times$       | $\times$          |
| $\mathbb{K}^0$    | $\times$                              | $\mathbb{K}^0$ | $\times$          |
| $\mathbb{K}^{-1}$ | $\times$                              | $\times$       | $\mathbb{K}^0$    |

Using the previous result, we can establish the harmonic structure of the elasticity tensor space  $\mathbb{E}la = \mathbf{C}_{\underline{(ij)} \underline{(kl)}}$ . As mentioned before, this space can be viewed as  $S^2(S^2(\mathbb{R}^2))$ , we can write :

$$\begin{aligned} \mathbb{E}la &\simeq S^2(S^2(\mathbb{R}^2)) \simeq S^2(\mathbb{K}^2 \oplus \mathbb{K}^0) \simeq S^2(\mathbb{K}^2) \oplus S^2(\mathbb{K}^0) \oplus (\mathbb{K}^2 \oplus \mathbb{K}^0) \\ &\simeq \mathbb{K}^4 \oplus \mathbb{K}^0 \oplus \mathbb{K}^0 \oplus \mathbb{K}^2 \simeq \mathbb{K}^4 \oplus \mathbb{K}^2 \oplus 2\mathbb{K}^0 \end{aligned} \quad (2.2.19)$$

### Theorem 2.3: Harmonic decomposition of $\mathbf{C}$

Due to the harmonic structure of  $\mathbb{E}la$ , it results that any elasticity tensor can be explicitly decomposed as

$$\mathbf{C} = \mathbf{H} + \frac{1}{2}(\mathbf{h} \otimes \mathbf{I} + \mathbf{I} \otimes \mathbf{h}) + \frac{\alpha_2}{2}\mathbf{P}^2 + 2\alpha_0\mathbf{P}^0 \quad (2.2.20)$$

in which  $\mathbf{H} \in \mathbb{K}^4$ ,  $\mathbf{h} \in \mathbb{K}^2$ ,  $\alpha_2, \alpha_0 \in \mathbb{R}$  and  $\mathbf{P}^0, \mathbf{P}^2$  are the standard spherical and deviatoric projectors. This parametrisation is known as the Clebsch-Gordan harmonic decomposition [Auffray et al., 2021].

The decomposition 2.2.20 is orthogonal and we have

$$\mathbf{C} :: \mathbf{C} = 4\alpha_0^2 + \frac{\alpha_2^2}{2} + 4\mathbf{h} : \mathbf{h} + \mathbf{H} :: \mathbf{H}$$

The compact notation  $\mathbf{C} = \varphi(\mathbf{H}, \mathbf{h}, \alpha_2, \alpha_0)$  will condense the previous expression, which means that the elasticity tensor can be decomposed in a fourth-order harmonic tensor  $\mathbf{H}$ , a second-order harmonic tensor  $\mathbf{h}$  and two scalar  $\alpha^2$  and  $\alpha^0$ . Those elements can be explicitly defined from  $\mathbf{C}$  as follows:

| $\mathbb{K}^0$  | $\mathbb{K}^2$  | $\mathbb{K}^4$   |
|---|---|--|
| $\alpha_0 = \mathbf{P}^0 :: \mathbf{C}$                                 | $\mathbf{h} = \mathbf{P}^2 : \mathbf{C} : \mathbf{I}$ | $\mathbf{H} = \mathbf{P}^2 : \mathbf{C} : \mathbf{P}^2 - \frac{\alpha_2}{2}\mathbf{P}^2$ |
| $\alpha_2 = (\mathbf{P}^2 : \mathbf{C} : \mathbf{P}^2) :: \mathbf{P}^2$ |   |  |

Using equation (2.2.20), the matrix representation of  $\mathbf{C}$  within the Kelvin basis  $\mathcal{K}^7$  gives

$$[\mathbf{C}] = \begin{pmatrix} 2h_1 + H_1 + \alpha_0 + \frac{\alpha_2}{4} & -H_1 + \alpha_0 - \frac{\alpha_2}{4} & \sqrt{2}(h_2 + H_2) \\ -H_1 + \alpha_0 - \frac{\alpha_2}{4} & -2h_1 + H_1 + \alpha_0 + \frac{\alpha_2}{4} & \sqrt{2}(h_2 - H_2) \\ \sqrt{2}(h_2 + H_2) & \sqrt{2}(h_2 - H_2) & \frac{1}{2}(-4H_1 + \alpha_2) \end{pmatrix}_{\mathcal{K}} \quad (2.2.21)$$

The harmonic decomposition is of high interest for the future discussions since it allows us to characterise the symmetry class of an object rather than its specific symmetry about a given orientation, by computing the elements of the harmonic decomposition. From a geometric point of view, since the harmonic decomposition is  $O(2)$ -invariant, it is more interesting to see how a given transformation acts on harmonic decomposition elements rather than on the full tensor. For instance, for a rotation  $\mathbf{R}$  by an angle  $\theta$ , and for each  $\mathbf{C} \in \mathbb{E}la$ , we have

$$\mathbf{R}(\theta) \star \mathbf{C} = \varphi(\mathbf{R}(\theta) \star \mathbf{H}, \mathbf{R}(\theta) \star \mathbf{h}, \alpha_2, \alpha_0) = \varphi(\mathbf{H}^*, \mathbf{h}^*, \alpha_2, \alpha_0) = \mathbf{C}^*,$$

where

$$\{\mathbf{h}^*\} = \begin{pmatrix} h_1 \cos(2\theta) - h_2 \sin(2\theta) \\ -h_1 \sin(2\theta) + h_2 \cos(2\theta) \\ \sqrt{2}(h_1 \sin(2\theta) + h_2 \cos(2\theta)) \end{pmatrix}_{\mathcal{K}},$$

and

<sup>7</sup>More details about the Kelvin representation can be found in [Desmorat and Auffray, 2019]

$$[\mathbf{H}^*] = \begin{pmatrix} H_1 \cos(4\theta) - H_2 \sin(4\theta) & H_1 \cos(4\theta) + H_2 \sin(4\theta) & \sqrt{2}(H_2 \cos(4\theta) + H_1 \sin(4\theta)) \\ H_1 \cos(4\theta) + H_2 \sin(4\theta) & H_1 \cos(4\theta) - H_2 \sin(4\theta) & \sqrt{2}(H_2 \cos(4\theta) - H_1 \sin(4\theta)) \\ \sqrt{2}(H_2 \cos(4\theta) + H_1 \sin(4\theta)) & \sqrt{2}(H_2 \cos(4\theta) - H_1 \sin(4\theta)) & 2(H_1 \cos(4\theta) + H_2 \sin(4\theta)) \end{pmatrix}_{\mathcal{K}},$$

are the transformed elements expressed in the Kelvin basis  $\mathcal{K}$ .

## 2.2.4 Symmetry classes and invariants of $\mathbb{E}la$

To study more in-depth the symmetry properties and the action of  $O(2)$  on an element of  $\mathbb{E}la$ , from a geometrical point of view, let us look at the links between this harmonic parametrisation and the symmetry classes through the set  $\{\mathbf{h}, \mathbf{H}\}$ , called the anisotropic harmonic bouquet  $\mathcal{HB}$ . section 2.2.4 gives the graphical presentation of the harmonic bouquet, within  $\mathcal{K}^2 = (\mathbf{K}_1^2, \mathbf{K}_2^2)$  and  $\mathcal{K}^4 = (\mathbf{K}_1^4, \mathbf{K}_2^4)$ , respectively orthonormal canonical bases of  $\mathbb{K}^2$  and  $\mathbb{K}^4$  of which the construction is detailed in [Forte and Vianello, 2014]

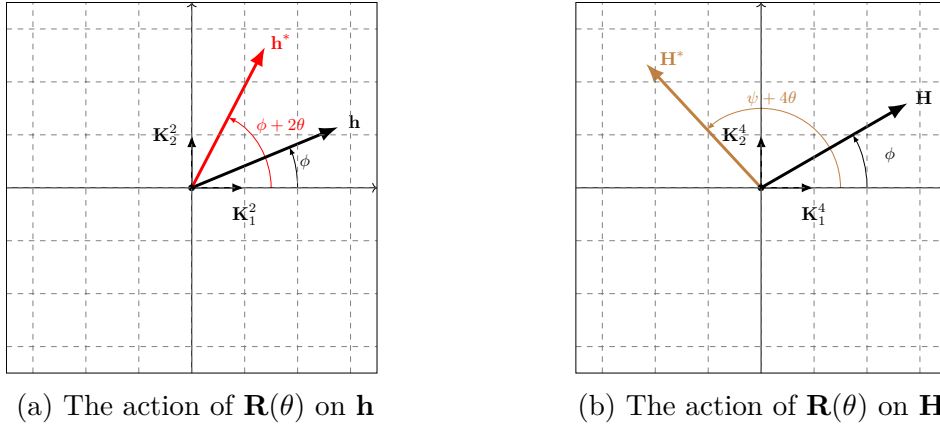


Figure 2.15: Graphical presentation of the harmonic bouquet, within the bases  $\mathcal{K}^2$  and  $\mathcal{K}^4$

Wherein  $\phi$  designates, the angle between  $\mathbf{h}$  and the horizontal axis  $\mathbf{K}_1^2$ , and  $\psi$  the angle between  $\mathbf{H}$  and  $\mathbf{K}_1^4$ . For a generic elasticity tensor [Mou et al., 2023],  $\mathcal{HB}$  is said non degenerated when

- neither  $\mathbf{h}$  nor  $\mathbf{H}$  is null;
- they are no *aligned*, meaning that  $(\mathbf{h} * \mathbf{h}) \times \mathbf{H} \neq 0$ ;

in which  $*$  and  $\times$  denote, respectively, the harmonic and the generalised cross product, their definitions are provided in [Mou et al., 2023]. This last condition motivates the introduction of the concept of *Homogeneous Harmonic Bouquet*  $\mathcal{HHB} = \{\mathbf{h} * \mathbf{h}, \mathbf{H}\}$ , in which all elements belong to the same harmonic space and therefore transform in the same way. This notion will allow us to introduce the *harmonic normal form* of an elasticity tensor. To this end, let denote by  $\tilde{\mathcal{K}}^4 = (\tilde{\mathbf{K}}_1^4, \tilde{\mathbf{K}}_2^4)$  the orthonormal basis of  $\mathbb{K}^4$  constructed from the canonical basis  $\mathcal{B}$  of  $\mathbb{R}^2$  [Desmorat et al., 2020]. Since elasticity tensors sharing the same orbit have conjugate  $\mathcal{HHB}$ , the following result is natural

$$\forall \mathbf{C} \in \mathbb{E}la, \exists \mathbf{Q} \in O(2) \text{ s.t. } (\mathbf{Q} * \mathbf{H})_2 = 0, (\mathbf{Q} * \mathbf{H})_1 > 0$$

with  $(\mathbf{H})_i = \mathbf{H} :: \tilde{\mathbf{K}}_i^4$ . A generic tensor  $\mathbf{C}$  is in its harmonic normal form, if  $(\mathbf{H})_2 = 0$ , and  $(\mathbf{H})_1 > 0$ . Geometrically, this corresponds to the configuration depicted on figure 2.16.

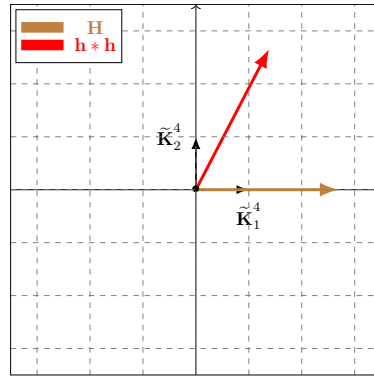


Figure 2.16: Harmonic normal form of a generic elasticity tensor

When a tensor exhibits a spatial invariance with respect to some transformations, its harmonic bouquet is said to be degenerated<sup>8</sup>. Hence, the different transitions from a symmetry class to another can be expressed in terms of covariant conditions, as follows:

$$\Sigma_{[Z_2]} \xrightarrow{(\mathbf{h} * \mathbf{h}) \times \mathbf{H} = 0} \Sigma_{[D_2]} \xrightarrow{\mathbf{h} : \mathbf{h} = 0} \Sigma_{[D_4]} \xrightarrow{\mathbf{H} :: \mathbf{H} = 0} \Sigma_{[O(2)]}$$

Geometrically, the harmonic normal forms of elasticity tensors in the three remaining classes are presented in section 2.2.4.

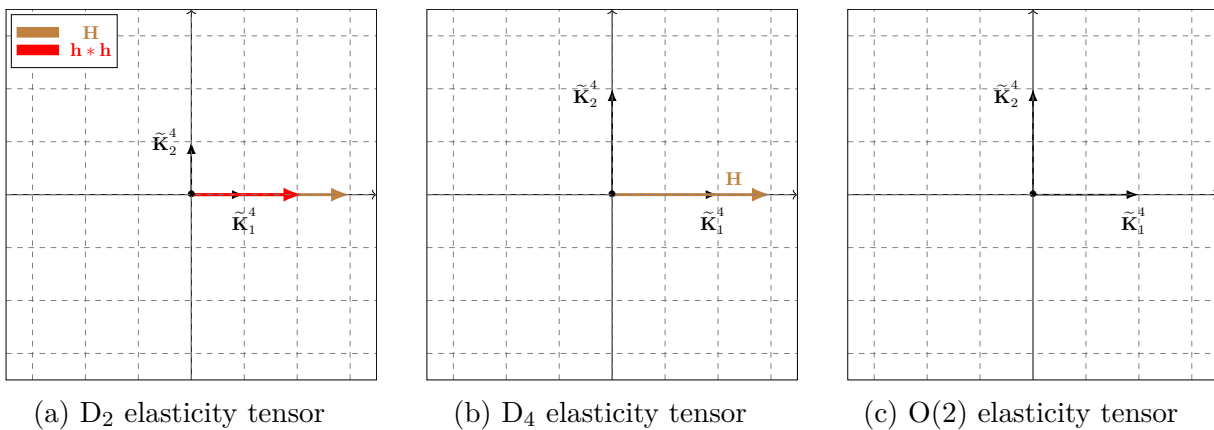


Figure 2.17: Harmonic normal form of non generic elasticity tensors

<sup>8</sup>In other words, the conditions of genericity are no longer fulfilled.

The corresponding matrix representation of  $\mathbf{C}$  for each symmetry class is given in table 2.7.

| Symmetry class        | Dimension | Matrix   |
|-----------------------|-----------|--|
| $[Z_2]$ , biclinic    | 5         | $\begin{pmatrix} 2h_1 + H_1 + \alpha_0 + \frac{\alpha_2}{4} & \alpha^0 - H_1 - \frac{\alpha_2}{4} & \sqrt{2}(h_2 + H_2) \\ * & H_1 - 2h_1 + \alpha_0 + \frac{\alpha_2}{4} & \sqrt{2}(h_2 - H_2) \\ * & * & \frac{\alpha_2}{2} - 2H_1 \end{pmatrix}_\kappa$ |
| $[D_2]$ , orthotropic | 4         | $\begin{pmatrix} 2h_1 + H_1 + \alpha_0 + \frac{\alpha_2}{4} & \alpha_0 - H_1 - \frac{\alpha_2}{4} & 0 \\ * & H_1 - 2h_1 + \alpha_0 + \frac{\alpha_2}{4} & 0 \\ * & * & \frac{\alpha_2}{2} - 2H_1 \end{pmatrix}_\kappa$                                     |
| $[D_4]$ , tetragonal  | 3         | $\begin{pmatrix} H_1 + \alpha_0 + \frac{\alpha_2}{4} & \alpha_0 - H_1 - \frac{\alpha_2}{4} & 0 \\ * & H_1 + \alpha_0 + \frac{\alpha_2}{4} & 0 \\ * & * & \frac{\alpha_2}{2} - 2H_1 \end{pmatrix}_\kappa$   |
| $[O(2)]$ , isotropic  | 2         | $\begin{pmatrix} \alpha_0 + \frac{\alpha_2}{4} & \alpha_0 - \frac{\alpha_2}{4} & 0 \\ * & \alpha_0 + \frac{\alpha_2}{4} & 0 \\ * & * & \frac{\alpha_2}{2} \end{pmatrix}_\kappa$  |

Table 2.7: The matrix normal forms of the elasticity tensor for each symmetry class

| Tensor representations                                       | Symmetry class               | Covariant conditions  | Dimension |
|--|------------------------------|---|-----------|
| $\mathbf{C} = f(\alpha_0, \alpha_2, \mathbf{h}, \mathbf{H})$ | $[Z_2]$ , biclinic           | -   | 5         |
| $\mathbf{C} = f(\alpha_0, \alpha_2, \mathbf{h}, \mathbf{H})$ | $[D_2]$ , orthotropic        | $(\mathbf{h} * \mathbf{h}) \times \mathbf{H} = \mathbf{0}$ and $\mathbf{h} \neq \mathbf{0}$ | 4         |
| $\mathbf{C} = f(\alpha_0, \alpha_2, \mathbf{h}, \mathbf{0})$ | $[D_2]$ , $R_0$ -orthotropic | $\mathbf{H} = \mathbf{0}$ and $\mathbf{h} \neq \mathbf{0}$                                  | 4         |
| $\mathbf{C} = f(\alpha_0, \alpha_2, \mathbf{0}, \mathbf{H})$ | $[D_4]$ , tetragonal         | $\mathbf{h} = \mathbf{0}$   | 3         |
| $\mathbf{C} = f(\alpha_0, \alpha_2, \mathbf{0}, \mathbf{0})$ | $[O(2)]$ , isotropic         | $\mathbf{h} = \mathbf{H} = \mathbf{0}$  | 2         |

Table 2.8: Covariant conditions for symmetry classes

### Invariants of the elasticity tensor

Another geometrical interpretation to understand the action of  $O(2)$  on  $\mathbb{E}la$  can be made by considering some polynomial functions that are formulated using tensor components. To see that, we need to introduced the invariants of the elasticity tensor. Consider the following quantities:

$$i_1 = \alpha_0, \quad j_1 = \alpha_2, \quad i_2 = \mathbf{h} : \mathbf{h}, \quad j_2 = \mathbf{H} :: \mathbf{H}, \quad i_3 = \mathbf{h} : \mathbf{H} : \mathbf{h}. \quad (2.2.22)$$

Using index notation, we have more explicitly

$$i_1 = \alpha_0, \quad j_1 = \alpha_2, \quad i_2 = 2(h_1^2 + h_2^2), \quad j_2 = 8(H_1^2 + H_2^2), \quad i_3 = 4H_1(h_1^2 - h_2^2) + 8H_2h_1h_2 \quad (2.2.23)$$

These elements are polynomial functions of  $\mathbf{C}$  that are  $O(2)$ -invariant [Vianello, 1997, Mou et al., 2023]. In the notation, the subscript indicates the degree of the polynomial in the elasticity tensor. As demonstrated in [Vianello, 1997] they constitute a basis for the invariants of elasticity tensors. They satisfy the following inequalities

$$i_2 \geq 0, \quad j_2 \geq 0, \quad i_2^2 j_2 - 2i_3^2 \geq 0. \quad (2.2.24)$$

that can be added to ensure the positive-definiteness of the elasticity tensor [Desmorat and Auffray, 2019]. One can parameterise the elements of  $\mathcal{HB}$  in terms of two invariants such as

$$\mathbf{H} = \sqrt{j_2} (\cos(\psi)\mathbf{K}_1^4 + \sin(\psi)\mathbf{K}_2^4), \quad \mathbf{h} = \sqrt{i_2} (\cos(\phi)\mathbf{K}_1^2 + \sin(\phi)\mathbf{K}_2^2), \quad (2.2.25)$$

and

$$\mathbf{H}^* = \sqrt{j_2} (\cos(\psi + 4\theta)\mathbf{K}_1^4 + \sin(\psi + 4\theta)\mathbf{K}_2^4), \quad \mathbf{h}^* = \sqrt{i_2} (\cos(\phi + 2\theta)\mathbf{K}_1^2 + \sin(\phi + 2\theta)\mathbf{K}_2^2). \quad (2.2.26)$$

Since a rotation  $\mathbf{R}(\theta)$  acts on  $\mathbf{h}$  and  $\mathbf{H}$  respectively, as a rotation of angles  $2\theta$  and  $4\theta$ , the angle  $\Phi = 2\phi - \psi$  remains invariant under the action of  $SO(2)$  [Vianello, 1997]. Indeed, we have

$$((\mathbf{h} * \mathbf{h}) \times \mathbf{H}) \cdot ((\mathbf{h} * \mathbf{h}) \times \mathbf{H}) = i_2^2 j_2 \sin(\Phi)^2. \quad (2.2.27)$$

Using the parameterisation below, it can be easily proved that, for (at least) orthotropic materials, the following polynomial relation is satisfied

$$i_2^2 j_2 \sin(\Phi)^2 = i_2^2 j_2 - 2i_3^2 = 0, \quad \text{and} \quad i_2 \geq 0, \quad j_2 \geq 0 \quad (2.2.28)$$

One can write this conditions in terms of  $\mathbf{h}$  and  $\mathbf{H}$  components, it yields

$$i_2^2 j_2 - 2i_3^2 = 32 \left( 2H_1 h_1 h_2 - H_2 (h_1^2 - h_2^2) \right)^2 = 0. \quad (2.2.29)$$

The links between harmonic decomposition, symmetry classes and invariants are reported in the table below

| Tensor representations                                       | Symmetry class        | Polynomial conditions       | Dimension |
|--|-----------------------|-----------------------------|-----------|
| $\mathbf{C} = f(\alpha_0, \alpha_2, \mathbf{h}, \mathbf{H})$ | $[Z_2]$ , biclinic    | $i_2^2 j_2 - 2i_3^2 \geq 0$ | 5         |
| $\mathbf{C} = f(\alpha_0, \alpha_2, \mathbf{h}, \mathbf{H})$ | $[D_2]$ , orthotropic | $i_2^2 j_2 - 2i_3^2 = 0$    | 4         |
| $\mathbf{C} = f(\alpha_0, \alpha_2, 0, \mathbf{H})$          | $[D_4]$ , tetragonal  | $i_2 = 0$                   | 3         |
| $\mathbf{C} = f(\alpha_0, \alpha_2, 0, 0)$                   | $[O(2)]$ , isotropic  | $i_2 + j_2 = 0$             | 2         |

Table 2.9: Invariant and Covariant conditions for symmetry classes

In figure 2.18b are summed-up the different transitions from a symmetry class to another expressed in terms of polynomial relations between invariants, where  $\Sigma_{[D_2]}^e$  designates  $R_0$ -orthotropic materials or *exotic* materials [Vannucci, 2002, Mou et al., 2023], satisfying the following polynomial condition

$$\mathbf{C} \in \Sigma_{[D_2]}^e \iff j_2 = 0 \quad \text{and} \quad i_2 \neq 0.$$

The different transitions from a symmetry class to another expressed in terms of polynomial relations between invariants are summed-up in figure 2.18b.

In the case of 2D elasticity, the geometry of the elastic material space can be visualised. figure 2.18a depicts the elastic material space with respect to  $(i_2, j_2, i_3)$ . The surface, which corresponds to the polynomial equation:  $i_2 j_2 - 2i_3^2 = 0$  contains all the at-least-orthotropic materials. Finally, we get that, independently of the values of the isotropic invariants  $i_1$  and  $j_1$ :

- Point O corresponds to isotropic materials (stratum  $\Sigma_{[O(2)]}$ );
- Open ray  $]OA)$  corresponds to tetragonal materials (stratum  $\Sigma_{[D_4]}$ );
- Surface without  $\{O\} \cup ]OA) \cup ]OB)$  corresponds to ordinary orthotropic materials (stratum  $\Sigma_{[D_2]}$ );
- Biclinic materials (stratum  $\Sigma_{[Z_2]}$ ) are strictly inside the volume defined by the surface.

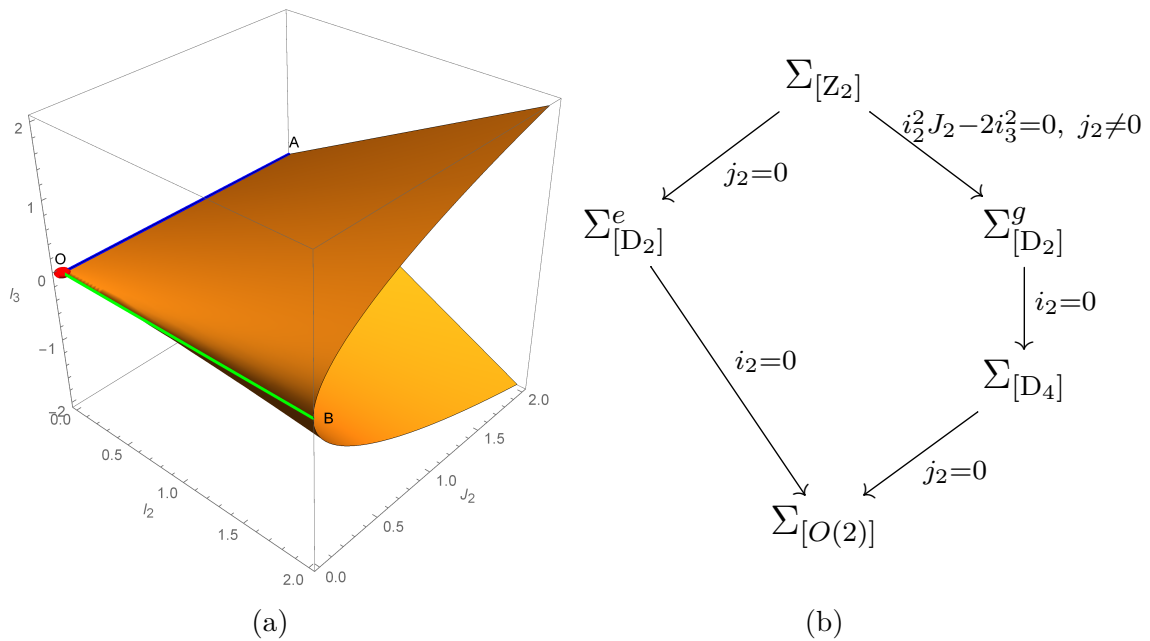


Figure 2.18: (a): Semi-algebraic variety of elastic materials with respect to  $(i_2, j_2, i_3)$ , (b): Transitions between symmetry classes

After introducing some fundamental mathematical concepts on the geometrical aspect of periodic architected materials and how the constitutive law takes into account their symmetries, one can now explore the behaviour of these materials by studying wave propagation. The study of elastic wave propagation within periodic media provides a foundation and allows a deeper understanding of how waves interact with and are affected by the properties of the material they are propagating through. This is an essential step towards developing a comprehensive understanding of periodic architected material properties.

## 2.3 Elastodynamics of architected materials

In this section, we will introduce some basic elements about wave propagation within periodic media. First, the concepts of direct and reciprocal spaces are introduced through the unit cell and the Brillouin zone, which are indispensable notions to understand the physical contents and the dynamic behavior of periodic media and in particular, architected materials. Then, the Floquet-Bloch [Gazalet et al., 2013, Nassar, 2015] theorem will be used in order to set up an analysis of wave propagation within periodic media by solving the elastodynamic equations. Finally, the last part of this section will be devoted to some numerical examples by computing the dispersion curves, the choice made on the studied geometries and the adopted assumptions.

### 2.3.1 Periodic media : some elements of theory

#### Reciprocal space

Let  $\mathcal{E}^*$  denote the dual space of the direct space  $\mathcal{E}$ . This dual space corresponds to the wave vector space, which is also known as the phase space. To further comprehend this notion, we introduce the reciprocal lattice  $\mathcal{R}^*$  as the dual set of  $\mathcal{R}$ .

$$\mathcal{R}^* = \{\boldsymbol{\xi} \in \mathcal{E}^* \mid \boldsymbol{\xi} = \xi_1 \mathbf{b}_1^* + \xi_2 \mathbf{b}_2^*, \xi_i \in \mathbb{Z}\}, \quad (2.3.1)$$

in which  $\mathcal{B}^* = \{\mathbf{b}_j^*\}_{j=1..2}$ <sup>9</sup> is a basis of the reciprocal space  $\mathcal{R}^*$ , i.e.

$$\mathbf{b}_j^* \cdot \mathbf{e}_i = 2\pi \delta_{ij}. \quad (2.3.2)$$

Consider the wave vector  $\boldsymbol{\xi} \in \mathcal{R}^*$  of a given plane wave, there exist  $\mathbf{x}_0 \in \mathcal{T}_0$  and  $\mathbf{r} \in \mathcal{R}$  such that

$$e^{-i\boldsymbol{\xi} \cdot \mathbf{x}} = e^{-i\boldsymbol{\xi} \cdot (\mathbf{x}_0 + \mathbf{r})}, \quad \forall \mathbf{x} \in \Omega \quad (2.3.3)$$

the wave is said to be  $\mathcal{R}$ -periodic if and only if

$$\boldsymbol{\xi} \cdot \mathbf{r} \in 2\pi\mathbb{Z}. \quad (2.3.4)$$

From equation (2.3.4), it yields

$$e^{-i\boldsymbol{\xi} \cdot \mathbf{x}} = e^{-i\boldsymbol{\xi} \cdot (\mathbf{x}_0 + \mathbf{r})} = e^{-i\boldsymbol{\xi} \cdot \mathbf{x}_0} \quad (2.3.5)$$

Thus,  $\mathcal{R}^*$  is the support of the complex-valued  $\mathcal{R}$ -periodic functions. Table 2.10 resumes the expression of primitive vectors in the direct and reciprocal space for each lattice system.

---

<sup>9</sup>The followed methodology in the construction of reciprocal's basis vectors can be found in the reference [Armstrong, 1997] (respect. [Malgrange et al., 2014] for the 3D).

| System       | Lattice             | $\mathbf{e}_1$                                    | $\mathbf{e}_2$                                   | $\mathbf{b}_1^*$  | $\mathbf{b}_2^*$                                    |
|--------------|---------------------|---|--|---|---|
| Monoclinic   | Oblic               | $(b_1, 0)$  | $b_2 (\cos\theta, \sin\theta)$                   | $\left(\frac{2\pi}{b_1}, \frac{-2\pi}{b_1 \tan\theta}\right)$ | $\left(0, \frac{2\pi}{b_2 \sin\theta}\right)$       |
| Orthorhombic | Rectangular         | $(b_1, 0)$  | $(0, b_2)$                                       | $\left(\frac{2\pi}{b_1}, 0\right)$                            | $\left(0, \frac{2\pi}{b_2}\right)$                  |
|              | Centred rectangular | $(b_1, 0)$  | $\left(\frac{b_1}{2}, \frac{b_2}{2}\right)$      | $\left(\frac{2\pi}{b_1}, \frac{-2\pi}{b_2}\right)$            | $\left(0, \frac{4\pi}{b_2}\right)$                  |
| Tetragonal   | Square              | $(b, 0)$  | $(0, b)$   | $\left(\frac{2\pi}{b}, 0\right)$                              | $\left(0, \frac{2\pi}{b}\right)$                    |
| Hexagonal    | Hexagonal           | $b \left(\frac{\sqrt{3}}{2}, \frac{-1}{2}\right)$ | $b \left(\frac{\sqrt{3}}{2}, \frac{1}{2}\right)$ | $\frac{2\pi}{b} \left(\frac{1}{\sqrt{3}}, -1\right)$          | $\frac{2\pi}{b} \left(\frac{1}{\sqrt{3}}, 1\right)$ |

Table 2.10: Lattice vectors in the direct and reciprocal spaces

### First Brillouin zone

While an infinite number of elementary cells can exist for any point lattice, only one cell, referred to as the *Wigner-Seitz cell*<sup>10</sup>, contains exactly one node of the point lattice [Malgrange et al., 2014, Ashcroft and Mermin, 2022]. The Wigner-Seitz cell serves as a fundamental domain for  $\mathcal{R}$  and carries all the informations about the periodic medium, particularly its symmetry properties. Geometrically, the Wigner-Seitz cell is defined as the set of points that are closer to a given point than to any other point in the point lattice.

We define the *First Brillouin Zone* (FBZ)  $\mathcal{T}^*$  as the primitive cell in the reciprocal space, its construction is analogous to the Wigner-Seitz's construction in direct space [Brillouin, 1930]. It represents the set of all points in reciprocal space that are closer to the origin  $\mathbf{k} = \mathbf{0}$  than any other points,

$$\mathcal{T}^* = \{\mathbf{k} \in \mathcal{R}^* \mid \forall \boldsymbol{\xi} \in \mathcal{R}^* - \{\mathbf{0}\}, \quad \|\mathbf{k}\| \leq \|\mathbf{k} - \boldsymbol{\xi}\| \} \subset \mathcal{E}^* \quad (2.3.6)$$

From equation (2.3.1) et equation (2.3.6), we have

$$\forall \mathbf{k} \in \mathcal{E}^*, \exists (\mathbf{k}_0, \boldsymbol{\xi}) \in (\mathcal{T}^*, \mathcal{R}^*), \quad \mathbf{k} = \mathbf{k}_0 + \boldsymbol{\xi}. \quad (2.3.7)$$

Figures figure 2.19a and figure 2.19b show a representation of a hexagonal lattice in the direct space and in the reciprocal space. The cell  $\mathcal{T}_0$  corresponds to the Wigner-Seitz cell whose primitive vectors are given by

$$\mathbf{b}_1 = b \left(\frac{\sqrt{3}}{2}, \frac{-1}{2}\right), \quad \mathbf{b}_2 = b \left(\frac{\sqrt{3}}{2}, \frac{1}{2}\right)$$

The cell  $\mathcal{T}^*$  corresponds to the FBZ, its primitive reciprocal vectors are

<sup>10</sup>The *Wigner-Seitz cell* is a specific type of *Voronoi cell* associated with a point lattice, representing a fundamental domain around a node of the point lattice

$$\mathbf{b}_1^* = \frac{2\pi}{b} \left( \frac{1}{\sqrt{3}}, -1 \right), \quad \mathbf{b}_2^* = \frac{2\pi}{b} \left( \frac{1}{\sqrt{3}}, 1 \right).$$

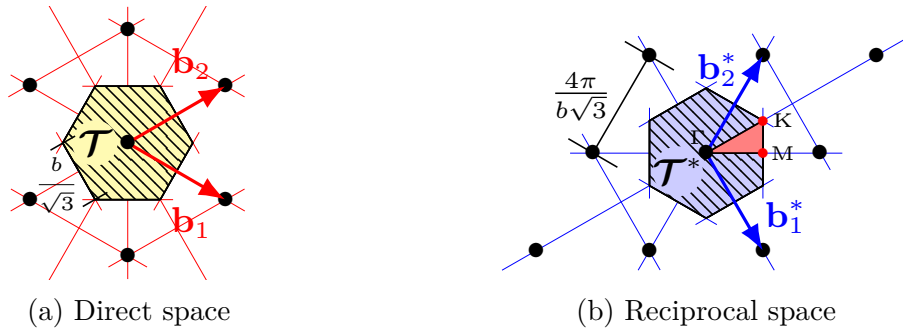


Figure 2.19: A 2D example of hexagonal unit cell. Left-hand figure : the Wigner-Seitz unit cell  $\mathcal{T}_0$  in  $\mathcal{R}$ . Right-hand figure : FBZ  $\mathcal{T}^*$  associated with  $\mathcal{T}_0$  in the reciprocal space  $\mathcal{R}^*$ .

The FBZ concept is of major importance, it contains all the information necessary to characterize the reciprocal lattice of a periodic medium. This can be shown through the Bloch wave analysis which will be the subject of the next section, where the solutions can be completely characterized by their behaviour in this zone [Brillouin, 1953]. It is interesting to note that when the lattice has additional symmetries, for example orientation-invariance, the FBZ can be reduced to a region bounded by the points of high symmetries, called the *Irreducible Brillouin Zone* (IBZ). The red region in figure figure 2.19b represents the IBZ for a two dimensional hexagonal lattice. It corresponds to the triangle formed by the points  $\Gamma$ ,  $M$  and  $K$ . Restricting the study to the IBZ is of great interest, it means to consider only the solutions whose wave vectors found in this zone by following the path  $\Gamma \rightarrow M \rightarrow K \rightarrow \Gamma$ .

| Point    | Coordinates  | Definition                           |
|----------|--|--------------------------------------|
| $\Gamma$ | $(0, 0)$   | Center of the FBZ                    |
| $M$      | $\left( \frac{2\pi}{b\sqrt{3}}, 0 \right)$               | Edge's midpoint of the hexagonal FBZ |
| $K$      | $\left( \frac{2\pi}{b\sqrt{3}}, \frac{2\pi}{3b} \right)$ | Corners of the hexagonal FBZ         |

Table 2.11: High symmetry points of the Hexagonal IBZ corresponding to figure 2.19

## 2.3.2 Floquet-Bloch analysis

### Elasodynamic equations

Let consider a periodic heterogeneous medium denoted by  $\Omega$ , and let  $\mathcal{T}^*$  be its elementary unit cell.  $\Omega$  consists of at least two linear elastic phases (or at least one elastic phase and void). At a material point  $P \in \Omega$  identified by its position vector  $\mathbf{x}$ , we have the following equations:

- The motion equation

$$\nabla \cdot \boldsymbol{\sigma}(\mathbf{x}) + \mathbf{f}(\mathbf{x}) = \dot{\mathbf{p}}(\mathbf{x}), \quad \forall \mathbf{x} \in \Omega; \quad (2.3.8)$$

- The strain field<sup>11</sup>

$$\boldsymbol{\varepsilon} := \frac{1}{2} [\mathbf{u}(\mathbf{x}) \otimes \nabla + \nabla \otimes \mathbf{u}(\mathbf{x})] \equiv \mathbf{u}(\mathbf{x}) \otimes^s \nabla, \quad \forall \mathbf{x} \in \Omega; \quad (2.3.9)$$

- The velocity field  $\mathbf{v}$  :

$$\mathbf{v} := \frac{\partial \mathbf{u}(\mathbf{x})}{\partial t} \equiv \dot{\mathbf{u}}(\mathbf{x}), \quad \forall \mathbf{x} \in \Omega; \quad (2.3.10)$$

- Constitutive law (Hooke's law) :

$$\boldsymbol{\sigma}(\mathbf{x}) = \mathbf{C}(\mathbf{x}) : \boldsymbol{\varepsilon}(\mathbf{x}), \quad \forall \mathbf{x} \in \Omega; \quad (2.3.11)$$

- The momentum field  $\mathbf{p}$ :

$$\mathbf{p} := \rho(\mathbf{x})\dot{\mathbf{v}}(\mathbf{x}), \quad \forall \mathbf{x} \in \Omega. \quad (2.3.12)$$

By combining those equations, equation (2.3.8) can be rewritten as

$$\nabla \cdot [\mathbf{C}(\mathbf{x}) : (\mathbf{u}(\mathbf{x}) \otimes \nabla)] + \mathbf{f}(\mathbf{x}) = \rho(\mathbf{x})\ddot{\mathbf{u}}(\mathbf{x}). \quad (2.3.13)$$

It should be noted that solving the previous problem using Fourier transform is not straightforward due to the heterogeneous nature of the medium. To analyze the elastodynamic response of the medium, the Floquet-Bloch analysis is introduced [Floquet, 1883]. This method involves studying the propagation of free waves within the medium by computing dispersion curves. The Fourier transform is adapted to the operators of equation (2.3.13), whose coefficients are periodic, to enable this approach. Since the medium is only invariant under the action of  $\mathcal{R}$ , plane waves are no longer solutions to equation (2.3.13).

### Bloch waves

Consider the free-wave propagation problem<sup>12</sup>, the corresponding motion equation is given by

$$\nabla \cdot [\mathbf{C}(\mathbf{x}) : (\mathbf{u}(\mathbf{x}) \otimes \nabla)] = \rho(\mathbf{x})\ddot{\mathbf{u}}(\mathbf{x}). \quad (2.3.14)$$

<sup>11</sup>Defined as the second-order infinitesimal strain tensor

<sup>12</sup>In a free-wave problem, the term corresponding to the volume force density in equation (2.3.13) vanishes

The application of the Floquet-Bloch theorem allows us to express the elementary solutions of equation (2.3.14) in  $\Omega$  in the form of Bloch waves [Nassar, 2015]:

$$\mathbf{u}_{\mathbf{k}}(\mathbf{x}, t) = \text{Re} [\hat{\mathbf{u}}_{\mathbf{k}}(\mathbf{x}, t)] = \text{Re} [\tilde{\mathbf{u}}_{\mathbf{k}}(\mathbf{x})e^{i(\omega t - \mathbf{k} \cdot \mathbf{x})}], \quad \tilde{\mathbf{u}}_{\mathbf{k}}(\mathbf{x}) \in \mathbb{C}^2 \quad (2.3.15)$$

### Theorem 3.1: Floquet-Bloch theorem [Gazalet et al., 2013]

Consider an elastic medium with a periodic structure, characterized by a periodic elasticity tensor  $\mathbf{C}$  and mass density  $\rho$  satisfying

$$\begin{cases} \mathbf{C}(\mathbf{x} + \mathbf{r}) &= \mathbf{C}(\mathbf{x}) \\ \rho(\mathbf{x} + \mathbf{r}) &= \rho(\mathbf{x}) \end{cases} \quad \forall \mathbf{x} \in \Omega, \forall \mathbf{r} \in \mathcal{R}.$$

If  $\hat{\mathbf{u}}(\mathbf{x})$  is a solution to the wave equation 2.3.14, then there exist Bloch functions  $\tilde{\mathbf{u}}_{\mathbf{k}}(\mathbf{x})$  and a set of complex numbers  $c_k^a$ , such that

$$\hat{\mathbf{u}}(\mathbf{x}) = \sum_k c_k \hat{\mathbf{u}}_{\mathbf{k}}(\mathbf{x}) = \sum_k c_k \tilde{\mathbf{u}}_{\mathbf{k}}(\mathbf{x})e^{i(\mathbf{k} \cdot \mathbf{x} - \omega t)},$$

Wherein,  $\mathbf{k}$  a wavevector that lies in the FBZ, and  $\tilde{\mathbf{u}}_{\mathbf{k}}(\mathbf{x})$  are the periodic functions that satisfy:

$$\tilde{\mathbf{u}}_{\mathbf{k}}(\mathbf{x} + \mathbf{r}) = \tilde{\mathbf{u}}_{\mathbf{k}}(\mathbf{x})e^{i\mathbf{k} \cdot \mathbf{r}}, \quad \forall \mathbf{r} \in \mathcal{R}^*$$

<sup>a</sup>Here, the complex numbers  $c_k$  represent the coefficients of the superposition

A Bloch wave can be viewed as a plane wave modulated by a  $\mathcal{R}$ -periodic polarization field  $\tilde{\mathbf{u}}_{\mathbf{k}}$ , i.e. a field which exhibits the periodicity of the lattice

$$\tilde{\mathbf{u}}_{\mathbf{k}}(\mathbf{x} + \mathbf{r}) = \tilde{\mathbf{u}}_{\mathbf{k}}(\mathbf{x}), \quad \forall (\mathbf{x}, \mathbf{r}) \in \Omega \times \mathcal{R}.$$

Bloch waves are a generalization of plane waves for periodic heterogeneous media. Indeed, as the lattice parameters approach zero, i.e., when the medium becomes homogeneous, Bloch waves can be identified as plane waves with a constant polarization field.

### Discrete translational invariance

Let  $\mathbf{T}_{\mathbf{a}}$  be the spatial translation operator, such as

$$\mathbf{T}_{\mathbf{a}}(\hat{\mathbf{u}}_{\mathbf{k}}(\mathbf{x})) = \hat{\mathbf{u}}_{\mathbf{k}}(\mathbf{x} + \mathbf{a})$$

If  $\mathbf{a} \in \mathcal{R}$ ,  $\exists \mathbf{k} \in \mathcal{R}^*$  such that<sup>13</sup>

$$\mathbf{T}_{\mathbf{a}}(\hat{\mathbf{u}}_{\mathbf{k}}(\mathbf{x})) = e^{-i\mathbf{k} \cdot \mathbf{a}} \hat{\mathbf{u}}_{\mathbf{k}}(\mathbf{x}) \quad (2.3.16)$$

which is usually written in the following form

<sup>13</sup>This result derives from using *Born-Von-Karman* conditions, the methodology followed by Bloch rigorously detailed in [Gazalet et al., 2013]

$$\hat{\mathbf{u}}_{\mathbf{k}}(\mathbf{x} + \mathbf{a}) = e^{-i\mathbf{k}\cdot\mathbf{a}}\hat{\mathbf{u}}_{\mathbf{k}}(\mathbf{x}) \quad (2.3.17)$$

which is another formulation of the phase relationship. This relation allows to express the boundary conditions in the Bloch analysis. It is convenient to write equation (2.3.16) in the following form

$$\mathbf{T}_{\mathbf{a}}(\hat{\mathbf{u}}_{\mathbf{k}}(\mathbf{x})) = \lambda_{\mathbf{a}}\hat{\mathbf{u}}_{\mathbf{k}}(\mathbf{x}) \quad (2.3.18)$$

The latter relationship shows that equation (2.3.16) exhibits an eigenvalue problem for the translation operator  $\mathbf{T}_{\mathbf{a}}$ , where  $\lambda_{\mathbf{a}} = e^{-i\mathbf{k}\cdot\mathbf{a}}$  represents the eigenvalue associated with the translation by the vector  $\mathbf{a}$ . It is worth noting that equation (2.3.17) can be viewed as a generalization of the standard periodic boundary conditions. Specifically, as  $\mathbf{k} \rightarrow \mathbf{0}^+$  and the wavelength  $2\pi/\|\mathbf{k}\|$  tends to infinity, the Bloch boundary conditions reduce to the standard periodic boundary conditions.

Now, let us verify that Bloch waves satisfy the property equation (2.3.17). Using the following change of variables  $\mathbf{x} \rightarrow \mathbf{x} + \mathbf{a}$ , it yields

$$\begin{aligned} \hat{\mathbf{u}}_{\mathbf{k}}(\mathbf{x}) &= \tilde{\mathbf{u}}_{\mathbf{k}}(\mathbf{x} + \mathbf{a})e^{i(\omega t - \mathbf{k}\cdot(\mathbf{x} + \mathbf{a}))} \\ &= \tilde{\mathbf{u}}_{\mathbf{k}}(\mathbf{x})e^{i(\omega t - \mathbf{k}\cdot\mathbf{x})}e^{-i\mathbf{k}\cdot\mathbf{a}} \\ &= \hat{\mathbf{u}}_{\mathbf{k}}(\mathbf{x})e^{-i\mathbf{k}\cdot\mathbf{a}} \end{aligned} \quad (2.3.19)$$

Which highlights the fact that a discrete translation of a vector  $\mathbf{a} \in \mathcal{R}$  in direct space will not affect the wavefront during propagation, but, it creates a phase-shift  $e^{-i\mathbf{k}\cdot\mathbf{a}}$

### Floquet-Bloch transform and elastodynamic equations

Taking into account the differentiation and the multiplication operators of the Floquet-Bloch transform [Nassar, 2015], kinematical, constitutive and motion equations can be rewritten in terms of Floquet-Bloch components

$$\tilde{\boldsymbol{\varepsilon}} = \tilde{\mathbf{u}} \otimes^s (\nabla - i\mathbf{k}), \quad \tilde{\mathbf{v}} = -i\omega \tilde{\mathbf{u}}, \quad \tilde{\boldsymbol{\sigma}} = \mathbf{C} : \tilde{\boldsymbol{\varepsilon}}, \quad \tilde{\mathbf{p}} = \rho \tilde{\mathbf{v}}. \quad (2.3.20)$$

The equation of motion 2.3.13 formulated for the ansatz equation (2.3.15), takes the form

$$(\nabla - i\mathbf{k}) \cdot \{\mathbf{C}(\mathbf{x}) : [\tilde{\mathbf{u}}_{\mathbf{k}}(\mathbf{x}) \otimes^s (\nabla - i\mathbf{k})]\} = -\omega^2 \rho(\mathbf{x}) \tilde{\mathbf{u}}_{\mathbf{k}}(\mathbf{x}), \quad (2.3.21)$$

the periodicity of the medium implies

$$\hat{\mathbf{u}}_{\mathbf{k}}(\mathbf{x}, t) = \hat{\mathbf{u}}_{\mathbf{k}}(\mathbf{x}_0 + \mathbf{r}, t) = \tilde{\mathbf{u}}_{\mathbf{k}}(\mathbf{x}_0 + \mathbf{r})e^{i(\mathbf{k}\cdot(\mathbf{x}_0 + \mathbf{r}) - \omega t)} = \hat{\mathbf{u}}_{\mathbf{k}}(\mathbf{x}_0, t)e^{i\mathbf{k}\cdot\mathbf{r}}. \quad (2.3.22)$$

Here,  $\mathbf{x} \in \Omega$ ,  $\mathbf{x}_0 \in \mathcal{T}$ , and  $\mathbf{r} \in \mathcal{R}$ . The latter relation expresses the phase shift between the solutions at two different points within the periodic medium. Consequently, the solution of a partial differential equation with periodic coefficients is not necessarily periodic itself. In other words, the periodicity of  $\mathbf{C}$  and  $\rho$  does not imply the periodicity of  $\mathbf{u}$ . By analogy, one can emphasize that the polarization field  $\tilde{\mathbf{u}}_{\mathbf{k}}$  is  $\mathcal{R}^*$ -periodic<sup>14</sup>, given by

$$\tilde{\mathbf{u}}_{\mathbf{k}+\boldsymbol{\xi}}(\mathbf{x}_0) = \tilde{\mathbf{u}}_{\mathbf{k}}(\mathbf{x}_0), \quad \forall (\mathbf{k}, \boldsymbol{\xi}) \in \mathcal{R}^* \quad (2.3.23)$$

<sup>14</sup>The proof was established in [Nassar, 2015]

The  $\mathcal{R}^*$ -periodicity of the solution is of great practical interest. As mentioned earlier, it is not necessary to explore the entire set  $\mathbf{k} \in \mathcal{R}^*$ ; the study can be limited to the wave vectors within the FBZ.

### Dispersion curves

A free wave, represented by the expression equation (2.3.15), is a non-null solution of the motion equation. equation (2.3.21) can thus be interpreted as a family of eigenvalue problems parameterized by  $\mathbf{k}$ , where  $\tilde{\mathbf{u}}_{(\mathbf{k},\omega)}(\mathbf{x})$  is an eigenmode, and  $\{\omega_i^2(\mathbf{k})\}_{1 \leq i \leq N}$ <sup>15</sup> represents the eigenvalues. The concept here is analogous to the study of eigenstates in a crystal where wave propagation is governed by the Schrödinger equation [Gazalet et al., 2013]. The motion equation can be rewritten as:

$$\left[ (\nabla - i\mathbf{k}) \cdot \mathbf{C}(\mathbf{x}) \cdot (\nabla - i\mathbf{k}) - \omega^2 \rho(\mathbf{x}) \mathbf{I} \right] \cdot \tilde{\mathbf{u}}_{\mathbf{k}}(\mathbf{x}) = \mathbf{Z}_{\mathbf{k}}(\omega) \cdot \tilde{\mathbf{u}}_{\mathbf{k}}(\mathbf{x}) = \mathbf{0}, \quad (2.3.24)$$

where  $\mathbf{Z}_{\mathbf{k}}$  can be defined as an impedance. The existence condition of free waves is known as the dispersion relation. Thus, for a set of wave vectors  $\mathbf{k} \in \mathcal{R}^*$ , equation (2.3.21) admits a set of eigenfrequencies  $\{\omega_n(\mathbf{k})\}_{n \geq 1}$  and corresponding eigenmodes  $\{\tilde{\mathbf{u}}_{n,\mathbf{k}}\}_{n \geq 1}$  if the following condition is satisfied:

$$\det \mathbf{Z}_{\mathbf{k}}(\omega) = \det \left[ (\nabla - i\mathbf{k}) \cdot \mathbf{C}(\mathbf{x}) \cdot (\nabla - i\mathbf{k}) - \omega^2 \rho(\mathbf{x}) \mathbf{I} \right] = 0. \quad (2.3.25)$$

To specify the solution class of the problem, we introduce the following Sobolev space:

$$\left[ \mathbf{H}^{1,\#}(\mathbf{k}, \Omega) \right]^2 = \{ \tilde{\mathbf{u}}_{\mathbf{k}} \in \left[ \mathbf{H}^1(\Omega) \right]^2, \tilde{\mathbf{u}}_{\mathbf{k}} \text{ is } \mathcal{R} \text{ - periodic} \}. \quad (2.3.26)$$

The graphical representation of the set of all couples  $(\mathbf{k}, \omega)$  satisfying the dispersion relation equation (2.3.25), defines the dispersion curve. The eigenmodes  $\tilde{\mathbf{u}}_{\mathbf{k}}(\mathbf{x}) \in \left[ \mathbf{H}^{1,\#}(\mathbf{k}, \Omega) \right]^2$  are vectors of infinite dimension. In the case of numerical modelling such as the finite element method, this field is approximated by a vector of finite dimension determined by the discretization of the problem. The collection of dispersion curves constitutes the dispersion diagram, and hence, the dispersion diagram has a finite number of branches, unlike the continuous problem, which has an infinite number of branches.

### Polarization of waves

To complement our understanding of wave propagation, the following paragraph delves into the specific properties and characteristics of polarization states in a 3D framework. The field  $\tilde{\mathbf{u}}_{\mathbf{k}}$  describes the motion of the material during wave propagation, so it is important to determine and examine the polarization state of Bloch waves. For convenience, we will denote the polarization field as  $\tilde{\mathbf{u}}$  and decompose it into its real and imaginary parts:

$$\tilde{\mathbf{u}} = \tilde{\mathbf{u}}^{\mathbb{R}} + i\tilde{\mathbf{u}}^{\mathbb{C}}.$$

Let  $\mathbf{n} = \mathbf{k}/\|\mathbf{k}\|$  be the unit vector defining the direction of propagation, when the vectors  $\tilde{\mathbf{u}}^{\mathbb{R}}$  and  $\tilde{\mathbf{u}}^{\mathbb{C}}$  are not collinear, they define the plane of oscillation of the wave;

---

<sup>15</sup>With  $N = +\infty$  in a continuous medium

otherwise, it corresponds to the line of oscillation [Toupin, 1962]. If the line of oscillation is collinear with the direction of propagation, i.e.,  $\langle \tilde{\mathbf{u}}, \mathbf{n} \rangle = \alpha$ , where  $\alpha \in \mathbb{C}$ , then the wave is longitudinally polarized. If the plane of oscillation is perpendicular to the direction of propagation, the wave is transversely polarized. The wave is linearly polarized when  $\tilde{\mathbf{u}}^{\mathbb{R}}$  and  $\tilde{\mathbf{u}}^{\mathbb{C}}$  are collinear, which can also be determined by the necessary and sufficient condition  $\tilde{\mathbf{u}} \wedge \tilde{\mathbf{u}}^* = 0$ , where  $\tilde{\mathbf{u}}^*$  is the conjugate of  $\tilde{\mathbf{u}}$ . Circular polarization occurs when  $\tilde{\mathbf{u}}^{\mathbb{R}}$  and  $\tilde{\mathbf{u}}^{\mathbb{C}}$  are perpendicular and have the same magnitude, i.e.,  $\langle \tilde{\mathbf{u}}, \tilde{\mathbf{u}} \rangle = 0$ . Finally, if  $\langle \tilde{\mathbf{u}}, \tilde{\mathbf{u}} \rangle \neq 0$  and  $\tilde{\mathbf{u}} \wedge \tilde{\mathbf{u}}^* = 0$ , the wave is said to have elliptical polarization.

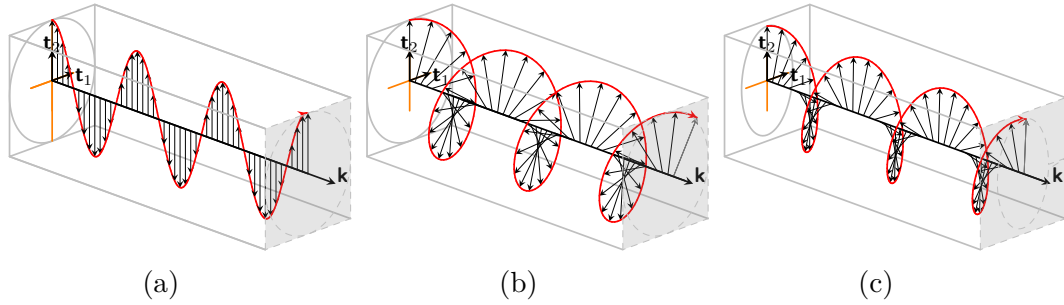


Figure 2.20: Some examples of polarizations: a) linear, b) Circular right handed, c) Circular left handed.

Having explored the intricacies of wave propagation in periodic heterogeneous media, we now shift our focus towards the homogenization of such media. While the study of wave behaviour in periodic structures provides valuable insights, the analysis becomes increasingly complex when dealing with practical applications. To overcome these challenges, the concept of elastodynamic effective generalized continuum arises, offering a powerful framework for characterizing and modeling the macroscopic behaviour of periodic heterogeneous materials. In the next section, we will explore the concept of generalized continua, specifically focusing on their application in the static case. We will see how generalized continua provide a framework for extending classical elasticity to describe complex materials and structures that exhibit unconventional behavior. We will delve into the different models and their corresponding constitutive laws that can potentially capture the overall behaviour of periodic architected materials.

## 2.4 Effective generalized continuum : from elastostatic to elastodynamics

### 2.4.1 Introduction to generalized continuum

Due to the complexity of their inner geometry and the presence of several intermediate scales of matter's organisation, studying the mechanical behaviour of architected materials can be very challenging, especially for numerical simulations. In order to understand all the mechanisms involved and to capture the emerging effects at the macro-scale, two approaches can be envisaged:

1. performing a full-field computation of the architected material, wherein the inner geometry is explicitly meshed;
2. considering an equivalent homogeneous medium.

The first approach is not favored since it can be prohibitively expensive and does not allow, at least with difficulty, to filter the different contributions and to analyse the overall properties in a rigorous manner. The second approach consists in substituting the original heterogeneous continuum with a homogeneous one having, under certain assumptions, an equivalent behaviour. Such equivalent continuum will be denoted *Equivalent Homogeneous Medium* (EHM), in which the level of the equivalence to consider will depend mainly on the domain of application (i.e. statics or dynamics) and on the range of parameters considered. Moreover, this approach provides very interesting results such as for design optimization or properties optimization while allowing a considerable reduction of the numerical cost. In the context of linear elasticity, classical homogenization have always considered as an efficient strategy and got many successes to describe the effective behaviour of heterogeneous media with strong scale separation [Bornert et al., 2001, Yvonnet, 2019]. Nevertheless, when the scale separation is weak, this approach being based on a *Cauchy-type* EHM may fail to describe correctly the effective behaviour, since classical elasticity is not rich enough to capture some specific mesostructural effects emerging at the macroscale [Allaire and Yamada, 2018, Poncelet et al., 2018, Rosi and Auffray, 2016, Rosi and Auffray, 2019, Rosi et al., 2020]. Therefore, the overall continuum model needs to be enriched, which gives rise to a *Generalised Continuum*. A generalised continuum can be seen as an extension of the classical continuum mechanics, where the nature of enrichments depend mainly on the physical phenomena to describe. There are several ways to enrich classical continuum mechanics, one can classify generalised continuum into two main families [Toupin, 1962, Mindlin, 1964, Mindlin, 1965, Eringen, 1968, Mindlin and Eshel, 1968]:

- High-order continua, obtained by the introduction of additional Degrees Of Freedom (DOF) that are independent of those of Cauchy continua. One the example of this family of models is the *Cosserat continuum* [Cosserat and Cosserat, 1909] in which, in addition to the classical three translational DOF, the local rotation of the microstructure is considered as a new DOF. This model is a special case of the *micromorphic elasticity* [Green and Rivlin, 1964, Mindlin, 1964, Germain, 1973], where other modes of microstructure deformation are taken into account (kinematics are more rich). These models are necessary to model optical branches and are particularly useful in the study of band-gaps.
- High-grade continua in which, the displacement field remains the only degree of

freedom, but the energy density is modified to include higher-order gradients of the displacement field. Examples of this type of model include Mindlin's first strain-gradient elasticity (SGE) [Mindlin, 1964, Mindlin and Eshel, 1968] and second strain-gradient elasticity [Mindlin, 1965]. In these models, the effects of small-scale variations in the displacement field are captured by introducing additional terms in the energy density that depend on higher-order gradients of the displacement field. These models can be used to describe the behaviour of materials with microstructural effect that are not captured by classical elasticity, such as dispersion, directivity and high order anisotropy.

Figure 2.21 illustrates the situation where four different types of generalized continua are taken into consideration. Among them, two types involve extended degrees of freedom, which are Cosserat<sup>16</sup> and Micromorphic, while the other two, Koiter<sup>17</sup> and Strain-Gradient, comprise higher gradients of the displacement field. By imposing a kinematic constraint  $\gamma$ , the Koiter model is derived from the Cosserat model, which is similar to how the Euler-Bernoulli beam model is obtained from the Timoshenko beam model. The same principle applies to the Strain-Gradient model, which is obtained from the Micromorphic model.

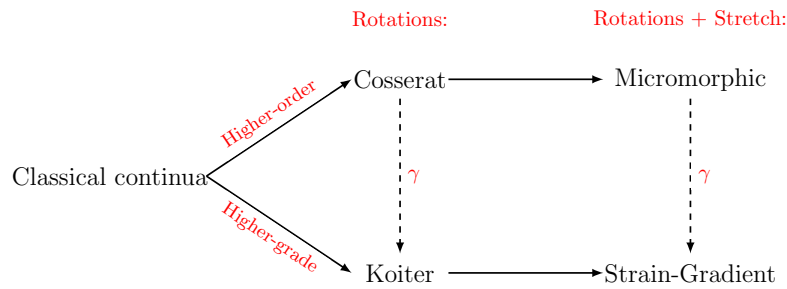


Figure 2.21: Basic extensions of a classical continuum. From the left to the right, *Rotation* then *Rotation+Stretch* are added to the kinematics. For higher-order continua these stretches are independent DOF, for higher-grade continua they are controlled by higher-order gradients of the displacement field.

The selection of a suitable generalized continuum remains potentially an open question, and involves two main considerations. First, what is the least possible kinematic extension required to capture the predominant mechanism of deformation that affects the overall behaviour, given scale separation ratio? Second, should this extended kinematic be treated as a separate degree of freedom, as in the micromorphic approach, or should it follow the macroscopic transformation, as in the strain-gradient approach?

## 2.4.2 Micromorphic elasticity

The micromorphic approach, in addition to the displacement field, extends the degrees of freedom by incorporating a non-symmetric second-order tensor  $\mathbf{X}$  that characterizes the micro-deformation of the material. In this model, we have the following DOF and their associated Primary State Variables (PSV) :

<sup>16</sup>The Cosserat continuum is sometimes also called a micropolar continuum (*cf.* Eringen) or a couple-stress continuum (*cf.* Toupin and Mindlin).

<sup>17</sup>The Koiter continuum is sometimes also called a constrained couple-stress continuum.

$$\text{DOF} := \{\mathbf{u}, \mathbf{X}\} \in \mathbb{R}^2 \times \otimes^2 \mathbb{R}^2, \quad \text{PSV} = \{\mathbf{u}, \mathbf{u} \otimes \nabla, \mathbf{X}, \mathbf{X} \otimes \nabla\}.$$

The following strain and stress measures are used:

| Primary state tensors - Strain measures   |                              | Dual state tensors - Stress measures                 |                        |
|---|------------------------------|--|------------------------|
| $\boldsymbol{\varepsilon} \in \mathbb{S}^2(\mathbb{R}^2)$                         | classical strain tensor      | $\boldsymbol{\sigma} \in \mathbb{S}^2(\mathbb{R}^2)$ | Cauchy stress tensor   |
| $\mathbf{e} \in \otimes^2 \mathbb{R}^2 := \mathbf{u} \otimes \nabla - \mathbf{X}$ | relative strain              | $\mathbf{s} \in \otimes^2 \mathbb{R}^2$              | relative stress tensor |
| $\boldsymbol{\kappa} \in \otimes^3 \mathbb{R}^2 := \mathbf{X} \otimes \nabla$     | micro-strain gradient tensor | $\boldsymbol{\tau} \in \otimes^3 \mathbb{R}^2$       | hyperstress tensor     |

Table 2.12: Strain and stress measures of micromorphic elasticity [Forest, 2006, Eringen, 2001].

Assuming a linear mapping between the primary and dual state tensors, we obtain the following linear constitutive law :

$$\begin{cases} \boldsymbol{\sigma} &= \mathbf{C} : \boldsymbol{\varepsilon} + \mathbf{B} : \mathbf{e} + \mathbf{M} \cdot \cdot \boldsymbol{\kappa} \\ \mathbf{s} &= \mathbf{B}^T : \boldsymbol{\varepsilon} + \mathbf{D} : \mathbf{e} + \mathbf{E} \cdot \cdot \boldsymbol{\kappa} \\ \boldsymbol{\tau} &= \mathbf{M}^T : \boldsymbol{\varepsilon} + \mathbf{E}^T : \mathbf{e} + \mathbf{A} \cdot \cdot \boldsymbol{\kappa} \end{cases} \quad (2.4.1)$$

in which the following tensors are involved:

- 3 fourth-order tensors :  $\mathbf{C} \in \mathbb{S}^2(\mathbb{S}^2(\mathbb{R}^2))$ ,  $\mathbf{B} \in \mathbb{S}^2(\mathbb{R}^2) \times \otimes^2 \mathbb{R}^2$  and  $\mathbf{D} \in \mathbb{S}^2(\otimes^2 \mathbb{R}^2)$ ;
- 2 fifth-order tensors :  $\mathbf{M} \in \mathbb{S}^2(\mathbb{R}^2) \times \otimes^3 \mathbb{R}^2$  and  $\mathbf{E} \in \otimes^5 \mathbb{R}^2$ ;
- 1 sixth-order tensor :  $\mathbf{A} \in \mathbb{S}^2(\otimes^3 \mathbb{R}^2)$ .

The kinematic enrichment of a micromorphic continuum is generally composed of three independent elements, denoted by  $\mathbf{X}^D$ ,  $\mathbf{X}^A$ , and  $\mathbf{X}^S$ , which together constitute the micro-deformation tensor  $\mathbf{X}$  in the space  $\otimes^2 \mathbb{R}^2$ , such as

$$\mathbf{X} := \mathbf{X}^D + \mathbf{X}^A + \mathbf{X}^S.$$

More formally, we have the following expression:

$$\mathbf{X} = \mathbf{X}^D + \theta \boldsymbol{\varepsilon} + \frac{1}{2} \alpha \mathbf{I},$$

wherin :

- $\mathbf{X}^D \in \mathbb{H}^{(2,2)}$  a deviatoric tensor;
- $\mathbf{X}^A \in \mathbb{H}^{(2,-1)}$  the Cosserat rotation or micro-rotation tensor;
- $\mathbf{X}^S \in \mathbb{H}^{(2,0)}$  the micro-dilatation tensor;
- $\theta \in \mathbb{K}^{-1}$  the micro-rotation pseudo scalar;
- $\alpha \in \mathbb{K}^0$  the micro-dilatation scalar;

with  $\mathbb{H}^{(n,k)}$  is a subspace of  $\mathbb{T}^n$  isomorphic to  $\mathbb{K}^k$ , it is the embedding space for the elements belonging to  $\mathbb{K}^k$ . Depending on the partial enrichment, intermediate higher-order models are obtained [Forest and Sievert, 2006] as reported in table 2.13.

| Case                          | DOF                              |      |
|-------------------------------|----------------------------------|------|
| Model                         | $\mathbf{X}$                     | $\#$ |
| Cauchy                        | $\emptyset$                      | 2    |
| Microdilatation <sup>18</sup> | $\alpha$                         | 3    |
| Cosserat                      | $\theta$                         | 3    |
| Microstretch                  | $(\theta, \alpha)$               | 4    |
| Incompressible Microstrain    | $\mathbf{X}^D$                   | 4    |
| Microstrain                   | $(\mathbf{X}^D, \alpha)$         | 5    |
| Incompressible Micromorphic   | $(\mathbf{X}^D, \theta)$         | 5    |
| Micromorphic                  | $(\mathbf{X}^D, \theta, \alpha)$ | 6    |

Table 2.13: Type of enrichment and intermediate higher-order models are obtained

For a more comprehensive understanding of the enrichment in the 3D framework, interested readers can refer to [Forest, 2006, Auffray, 2017, Somera, 2022], where the constitutive laws are provided for each model. In what follows, we will focus on the Cosserat model and strain-gradient model, as they are the most commonly used and have been extensively studied in the literature.

### 2.4.3 Cosserat elasticity in 2D <sup>19</sup>

A Cosserat continuum [Cosserat and Cosserat, 1909], also known as a micropolar continuum<sup>20</sup> [Nowacki, 1972], is a material system in which the constituents are modeled as infinitesimal rigid bodies instead of point masses. This means that the material points have both translational and rotational degrees of freedom.

#### DOF and strain measures

The theory is characterized by the presence of a micro-rotation field in addition to the displacement field such as

$$\text{DOF} := \{\mathbf{u}, \mathbf{R}(\theta)\} \in \mathbb{R}^2 \times \text{SO}(2),$$

in which  $\theta$  is the angle associated with the micro-rotation field  $\mathbf{R}(\theta)$ . Under the hypothesis where the translations and microrotations are point-wisely infinitesimally small, the infinitesimal rotation can be expressed as

$$\mathbf{R} \simeq \mathbf{I} + \mathbf{w},$$

with  $\mathbf{w} \in \mathfrak{so}(2)$ . In the classical formulation of Cosserat elasticity, the second-order skew symmetric tensor is usually substituted with the pseudo-scalar  $\theta$ :

$$\mathbf{w} = -\theta \boldsymbol{\epsilon} \quad , \quad \theta = -\frac{1}{2} \boldsymbol{\epsilon} : \mathbf{w}.$$

<sup>19</sup> This section has been extracted from a previously published article [Auffray et al., 2023] with the consent and agreement of the other authors, and has been meticulously adapted to suit the context of this manuscript.

<sup>20</sup> Also called a micropolar or couple-stress continuum [Eremeyev et al., 2013]

The Cosserat elasticity is a first-gradient theory, as such the linearized degrees of freedom (DOF) and the set of the associated PSV are

$$\text{DOF} := \{\mathbf{u}, \mathbf{w}\} \in \mathbb{R}^d \times \mathfrak{so}(2), \quad \text{PSV} = \{\mathbf{u}, \mathbf{u} \otimes \nabla, \theta, \theta \otimes \nabla\}.$$

There are two different sets of strain measures available in the literature [ref]. The first set is known as the *Classical formulation*, which was introduced, for instance, in [Forest, 2005, Eringen, 2012], and is defined by the following measures:

$$\mathbf{e} = \mathbf{u} \otimes \nabla - \theta \boldsymbol{\epsilon}, \quad \boldsymbol{\kappa} = \theta \otimes \nabla, \quad (\mathbf{e}, \boldsymbol{\kappa}) \in \otimes^2 \mathbb{R}^2 \times \mathbb{R}^2$$

The second is the *Micromorphic formulation* which involves the classical strain and spin tensors  $\boldsymbol{\epsilon}$  and  $\boldsymbol{\omega}$ , respectively. The strain measures used in this formulation are:

$$\boldsymbol{\epsilon}, \quad \boldsymbol{\eta} = \boldsymbol{\omega} - \theta \boldsymbol{\epsilon}, \quad \boldsymbol{\kappa} = \theta \otimes \nabla, \quad (\boldsymbol{\epsilon}, \boldsymbol{\eta}, \boldsymbol{\kappa}) \in \mathbb{S}^3(\mathbb{R}^2) \times \mathfrak{so}(2) \times \mathbb{R}^2.$$

This last partition follows the one classically used in the micromorphic approach of the elasticity [Mindlin, 1964], from which Cosserat is a special case. This choice emphasizes that the kinematic constraint  $\boldsymbol{\eta} = \mathbf{0}$ <sup>21</sup> results in the Cosserat model becoming the Koiter one, also known as constrained couple-stress, which is a special case of a strain-gradient continuum. In the following discussion, only the first formulation will be taken into consideration.

### Constitutive law

By duality we define the stress tensors:  $\mathbf{s}$  the asymmetric stress tensor, and  $\mathbf{m}$  the couple-stress tensor. Consequently,  $(\mathbf{s}, \mathbf{m}) \in \otimes^2 \mathbb{R}^2 \times \mathbb{R}^2$ , and the linear constitutive law between the primary and dual state tensors is expressed as:

$$\begin{cases} \mathbf{s} &= \mathbf{A} : \mathbf{e} + \mathcal{M} \cdot \boldsymbol{\kappa} \\ \mathbf{m} &= \mathcal{M}^T : \mathbf{e} + \mathbf{d} \cdot \boldsymbol{\kappa} \end{cases} \quad (2.4.2)$$

in which the involved constitutive tensors belong to the following vector spaces

$$\begin{aligned} \mathbf{A} &\in \text{Cos} := \{\mathbf{T} \in \mathbb{S}^2(\otimes^2 \mathbb{R}^2) \mid \mathbf{T}_{ijkl}\} \\ \mathcal{M} &\in \text{Cou} := \{\mathcal{T} \in \otimes^3 \mathbb{R}^2 \mid \mathcal{T}_{ijk}\} \\ \mathbf{d} &\in \text{Rot} := \{\mathbf{T} \in \mathbb{S}^2(\mathbb{R}^2) \mid \mathbf{T}_{(ij)}\} \end{aligned}$$

From their definitions, and using the isotypic decomposition, the harmonic structure of the constitutive tensors can be obtained. These results are provided in the following table

| Constitutive tensor space | Harmonic structure  |
|---------------------------|---|
| Cos                       | $\mathbb{K}^4 \oplus 2\mathbb{K}^2 \oplus 3\mathbb{K}^0 \oplus \mathbb{K}^{-1}$ |
| Cou                       | $\mathbb{K}^3 \oplus 3\mathbb{K}^1$   |
| Rot                       | $\mathbb{K}^2 \oplus \mathbb{K}^0$  |

From these tensor spaces, one can define the complete vector space of Cosserat elasticity

$$\mathcal{C}\text{os} = \text{Cos} \oplus \text{Cou} \oplus \text{Rot} \quad (2.4.3)$$

<sup>21</sup>The Euler-Bernoulli beam and the Kirchhoff-Love plate are examples of models obtained by imposing kinematic constraints on the Timoshenko beam model and, in 2D, the Reissner-Mindlin plate model.

## Classification

Knowing the harmonic structure of the constitutive tensors, and using the clips operators defined in [Auffray et al., 2017], the symmetry classes of each constitutive tensor space can be obtained

### Theorem 4.1: Symmetry classes of 2D Cosserat elasticity [Auffray et al., 2023]

As for  $\mathbb{E}la$ , the spaces  $\mathcal{C}os$ ,  $\mathcal{C}ou$  and  $\mathcal{R}ot$  are respectively partitioned into 6, 4 and 2 symmetry classes:

$$\begin{aligned}\mathfrak{J}(\mathcal{C}os) &= \{[Z_2], [D_2], [Z_4], [D_4], [SO(2)], [O(2)]\}. \\ \mathfrak{J}(\mathcal{C}ou) &= \{[\mathbf{1}], [Z_2^\pi], [D_3], [O(2)]\}. \\ \mathfrak{J}(\mathcal{R}ot) &= \{[D_2], [O(2)]\}.\end{aligned}\tag{2.4.4}$$

Hence, the space  $\mathcal{C}os$  is partitioned into 10 symmetry classes

$$\mathfrak{J}(\mathcal{C}os) = \{[\mathbf{1}], [Z_2^\pi], [Z_2], [D_2], [Z_3], [D_3], [Z_4], [D_4], [SO(2)], [O(2)]\}$$

The global form of the constitutive law can be detailed for each symmetry class, the constitutive laws have the following synthetic form<sup>22</sup>

$$\begin{aligned}\mathcal{L}_{\mathbf{1}} &= \begin{pmatrix} \mathbf{A}_{Z_2} & \mathbf{K}_x \\ \mathbf{K}_x^\top & \mathbf{H}_x \end{pmatrix} ; & \mathcal{L}_{Z_2^\pi} &= \begin{pmatrix} \mathbf{A}_{D_2} & \mathbf{K}_{Z_2^\pi} \\ \mathbf{K}_{Z_2^\pi}^\top & \mathbf{H}_{D_2} \end{pmatrix} \\ \mathcal{L}_{Z_2} &= \begin{pmatrix} \mathbf{A}_{Z_2} & \mathbf{0} \\ \mathbf{0} & \mathbf{H}_{D_2} \end{pmatrix} ; & \mathcal{L}_{D_2} &= \begin{pmatrix} \mathbf{A}_{D_2} & \mathbf{0} \\ \mathbf{0}^\top & \mathbf{H}_{D_2} \end{pmatrix} \\ \mathcal{L}_{Z_3} &= \begin{pmatrix} \mathbf{A}_{SO(2)} & \mathbf{K}_{D_3} \\ \mathbf{K}_{D_3}^\top & \mathbf{H}_{O(2)} \end{pmatrix} ; & \mathcal{L}_{D_3} &= \begin{pmatrix} \mathbf{A}_{O(2)} & \mathbf{K}_{D_3} \\ \mathbf{K}_{D_3}^\top & \mathbf{H}_{O(2)} \end{pmatrix} \\ \mathcal{L}_{Z_4} &= \begin{pmatrix} \mathbf{A}_{D_4} & \mathbf{0} \\ \mathbf{0} & \mathbf{H}_{O(2)} \end{pmatrix} ; & \mathcal{L}_{D_4} &= \begin{pmatrix} \mathbf{A}_{D_4} & \mathbf{0} \\ \mathbf{0}^\top & \mathbf{H}_{O(2)} \end{pmatrix} \\ \mathcal{L}_{SO(2)} &= \begin{pmatrix} \mathbf{A}_{SO(2)} & \mathbf{0} \\ \mathbf{0} & \mathbf{H}_{O(2)} \end{pmatrix} ; & \mathcal{L}_{O(2)} &= \begin{pmatrix} \mathbf{A}_{O(2)} & \mathbf{0} \\ \mathbf{0} & \mathbf{H}_{O(2)} \end{pmatrix}\end{aligned}\tag{2.4.5}$$

Using trace formula [Auffray et al., 2017], the following table, which gives the number of independent constitutive coefficients for each symmetry class, can be constructed:

| $[G_C]$                   | $[\mathbf{1}]$ | $[Z_2^\pi]$ | $[Z_2]$   | $[D_2]$  | $[Z_3]$ | $[D_3]$ | $[Z_4]$  | $[D_4]$  | $[SO(2)]$ | $[O(2)]$ |
|---------------------------|----------------|-------------|-----------|----------|---------|---------|----------|----------|-----------|----------|
| $\#_{indep}(\mathbf{d})$  | (2)            | (2)         | <b>2</b>  | (2)      | (1)     | (1)     | (1)      | (1)      | (1)       | <b>1</b> |
| $\#_{indep}(\mathcal{M})$ | <b>8</b>       | <b>4</b>    | (0)       | (0)      | (1)     | (0)     | (0)      | (0)      | (0)       | <b>0</b> |
| $\#_{indep}(\mathbf{A})$  | (10)           | (10)        | <b>10</b> | <b>6</b> | (4)     | (3)     | <b>6</b> | <b>4</b> | <b>4</b>  | <b>3</b> |
| $\#_{indep}(\mathcal{C})$ | 20             | 16          | 12        | 8        | 6       | 5       | 7        | 5        | 5         | 4        |

In the table above, when the symmetry class of a constitutive tensor coincides with that of  $\mathcal{C}$ , the dimension is noted in bold. On the contrary, when the symmetry classes differ, the dimension is indicated in parenthesis. For instance, the class  $[\mathbf{1}]$  is a symmetry class for  $\mathcal{C}$  but not for  $\mathbf{A}$ , whose symmetry class is  $[Z_2^\pi]$ , as such the number of parameters is indicated in parenthesis.

<sup>22</sup>For practical applications, the matrix forms of the different constitutive tensors are detailed, symmetry class by symmetry class, in [Auffray et al., 2023].

### 2.4.4 Strain-gradient elasticity in 2D

The strain-gradient continuum is a class of continua that considers the second displacement gradient as a strain measure in the energy formulation, having an energetic price. Unlike micromorphic elasticity, it is a high-grade continuum representation that does not introduce any additional degrees of freedom. The incorporation of higher-order terms in energy density enables a more precise characterization of the deformation and stress fields in these materials. As a result, the strain-gradient continuum can provide a better understanding of the mechanical behavior behaviour of materials with small length scales and/or high gradients in strain. In what follows, we will provide a brief description Mindlin strain-gradient elasticity (SGE) theory.

#### DOF and strain measures

The strain-gradient theory of linear elasticity, first introduced in [Mindlin, 1964] and later developed in [Mindlin and Eshel, 1968], considers only the displacement field  $\mathbf{u}$  as the degree of freedom. As previously mentioned, the strain-gradient model is derived from the micromorphic model by imposing a kinematic constraint that sets the relative strain field to zero, such as

$$\mathbf{e} = \mathbf{u} \otimes \nabla - \mathbf{X} = \mathbf{0} \implies \mathbf{X} = \mathbf{u} \otimes \nabla,$$

The microstrain becomes the displacement gradient and the previous strain and stress measures become <sup>23</sup>

| Primary state tensors - Strain measures   |                                 | Dual state tensors - Stress measures                                   |                      |
|---|---------------------------------|--|----------------------|
| $\boldsymbol{\varepsilon} \in \mathbb{S}^2(\mathbb{R}^2)$   | classical strain tensor         | $\boldsymbol{\sigma} \in \mathbb{S}^2(\mathbb{R}^2)$                   | Cauchy stress tensor |
| $\boldsymbol{\kappa} \in \mathbb{S}^2(\mathbb{R}^2) \times \mathbb{R}^2 := \mathbf{u} \otimes^2 \nabla$ | second gradient of $\mathbf{u}$ | $\boldsymbol{\tau} \in \mathbb{S}^2(\mathbb{R}^2) \times \mathbb{R}^2$ | hyperstress tensor   |

Table 2.14: Strain and stress measures of Strain-gradient elasticity [Forest, 2006].

Infinitesimal strain-gradient elasticity can be formulated in three equivalent ways, as described in [Mindlin, 1964, Mindlin and Eshel, 1968]. These formulations are as follows:

- *Type I formulation:* The strain measure is the second gradient of the displacement field, given by  $\boldsymbol{\kappa} = \mathbf{u} \otimes^2 \nabla$ ;
- *Type II formulation:* The strain measure is the gradient of the strain field, given by  $\boldsymbol{\eta} = \boldsymbol{\varepsilon} \otimes \nabla$ ;
- *Type III formulation:* The strain measure is divided into two tensors of order three: a tensor field of completely symmetric, and the gradient of rotation given by  $\boldsymbol{\omega} = \boldsymbol{\varepsilon} : (\mathbf{u} \otimes \nabla)$ .

In the following, we will focus on the constitutive law expressed in terms of *type II formulation*.

<sup>23</sup>As said earlier, the same construction leads to the Euler-Bernoulli beam model from the Timoshenko beam model.

## Constitutive law

Assuming a linear mapping between the primary and dual state tensors, we obtain the following linear constitutive law :

$$\begin{cases} \boldsymbol{\sigma} &= \mathbf{C} : \boldsymbol{\varepsilon} + \mathbf{M} :: \boldsymbol{\eta} \\ \boldsymbol{\tau} &= \mathbf{M}^T : \mathbf{e} + \mathbf{A} :: \boldsymbol{\eta} \end{cases} \quad (2.4.6)$$

in which the involved constitutive tensors belong to the following vector spaces :

$$\begin{aligned} \mathbf{C} &\in \mathbb{E}la_4 := \{\mathbf{T} \in S^2(S^2(\mathbb{R}^2)) | \mathbf{T}_{(ij)(kl)}\}, \\ \mathbf{M} &\in \mathbb{E}la_5 := \{\mathbf{T} \in S^2(S^2(\mathbb{R}^2)) \otimes \mathbb{R}^2 | \mathbf{T}_{(ij)(kl)m}\}, \\ \mathbf{A} &\in \mathbb{E}la_6 := \{\mathbf{T} \in S^2(S^2(\mathbb{R}^2) \otimes \mathbb{R}^2) | \mathbf{T}_{(ij)k (lm)n}\}. \end{aligned}$$

From their definitions, and using the isotypic decomposition, the harmonic structure of the constitutive tensors can be obtained [Auffray et al., 2021]. These results are provided in the following table

| Constitutive tensor space | Harmonic structure   |
|---------------------------|--|
| $\mathbb{E}la_4$          | $\mathbb{K}^4 \oplus \mathbb{K}^2 \oplus 2\mathbb{K}^0$  |
| $\mathbb{E}la_5$          | $\mathbb{K}^5 \oplus 3\mathbb{K}^3 \oplus 5\mathbb{K}^1$   |
| $\mathbb{E}la_6$          | $\mathbb{K}^6 \oplus 2\mathbb{K}^4 \oplus 5\mathbb{K}^2 \oplus 4\mathbb{K}^0 \oplus \mathbb{K}^{-1}$ |

From these space tensors, one can define the complete vector space of Strain-gradient elasticity law:

$$\mathcal{SGE} = \mathbb{E}la_4 \oplus \mathbb{E}la_5 \oplus \mathbb{E}la_6 \quad (2.4.7)$$

## Classification

### Theorem 4.2: Symmetry classes of 2D Strain-gradient elasticity

As for Cosserat elasticity, the spaces  $\mathbb{E}la_4$ ,  $\mathbb{E}la_5$  and  $\mathbb{E}la_6$  are respectively partitioned into 4, 7 and 8 symmetry classes [Auffray et al., 2015]

$$\begin{aligned} \mathfrak{J}(\mathbb{E}la_4) &= \{[Z_2], [D_2], [D_4], [O(2)]\} \\ \mathfrak{J}(\mathbb{E}la_5) &= \{[\mathbf{1}], [Z_2^\pi], [Z_3], [D_3], [Z_5], [D_5], [O(2)]\}. \\ \mathfrak{J}(\mathbb{E}la_6) &= \{[Z_2], [D_2], [Z_4], [D_4], [Z_6], [D_6], [SO(2)], [O(2)]\}. \end{aligned} \quad (2.4.8)$$

Hence, the space  $\mathcal{SGE}$  is partitioned into 14 symmetry classes

$$\mathfrak{J}(\mathcal{SGE}) = \left\{ \begin{array}{l} [\mathbf{1}], [Z_2], [Z_2^\pi], [D_2], [Z_3], [D_3], [Z_4], [D_4], \\ [Z_5], [D_5], [Z_6], [D_6], [SO(2)], [O(2)] \end{array} \right\} \quad (2.4.9)$$

The results presented in the above theorem can also be achieved by utilizing the clips operators and the harmonic structure of the constitutive tensors, as established and demonstrated later in [Auffray et al., 2021]. The global form of the constitutive law can be detailed for each symmetry class, the constitutive laws have the following synthetic form footnoteFor practical applications, the matrix forms of the different constitutive tensors are detailed, symmetry class by symmetry class, in [Auffray et al., 2015].

$$\begin{aligned}
\mathcal{L}_{\mathbf{1}} &= \begin{pmatrix} \mathbf{C}_{Z_2} & \mathbf{M}_{\mathbf{1}} \\ \mathbf{M}_{\mathbf{1}}^T & \mathbf{A}_{Z_2} \end{pmatrix} ; & \mathcal{L}_{Z_2^\pi} &= \begin{pmatrix} \mathbf{C}_{Z_2} & \mathbf{M}_{Z_2^\pi} \\ \mathbf{M}_{Z_2^\pi}^T & \mathbf{A}_{Z_2} \end{pmatrix} \\
\mathcal{L}_{Z_2} &= \begin{pmatrix} \mathbf{C}_{Z_2} & \mathbf{0} \\ \mathbf{0} & \mathbf{A}_{D_2} \end{pmatrix} ; & \mathcal{L}_{D_2} &= \begin{pmatrix} \mathbf{C}_{D_2} & \mathbf{0} \\ \mathbf{0} & \mathbf{A}_{D_2} \end{pmatrix} \\
\mathcal{L}_{Z_3} &= \begin{pmatrix} \mathbf{C}_{O(2)} & \mathbf{M}_{Z_3} \\ \mathbf{M}_{Z_3}^T & \mathbf{A}_{Z_6} \end{pmatrix} ; & \mathcal{L}_{D_3} &= \begin{pmatrix} \mathbf{C}_{O(2)} & \mathbf{M}_{D_3} \\ \mathbf{M}_{D_3}^T & \mathbf{A}_{D_6} \end{pmatrix} \\
\mathcal{L}_{Z_4} &= \begin{pmatrix} \mathbf{C}_{Z_4} & \mathbf{0} \\ \mathbf{0} & \mathbf{A}_{Z_4} \end{pmatrix} ; & \mathcal{L}_{D_4} &= \begin{pmatrix} \mathbf{C}_{D_4} & \mathbf{0} \\ \mathbf{0}^T & \mathbf{A}_{D_4} \end{pmatrix} \\
\mathcal{L}_{Z_5} &= \begin{pmatrix} \mathbf{C}_{O(2)} & \mathbf{M}_{Z_5} \\ \mathbf{M}_{Z_5}^T & \mathbf{A}_{SO(2)} \end{pmatrix} ; & \mathcal{L}_{D_5} &= \begin{pmatrix} \mathbf{C}_{O(2)} & \mathbf{M}_{D_5} \\ \mathbf{M}_{D_5}^T & \mathbf{A}_{O(2)} \end{pmatrix} \\
\mathcal{L}_{Z_6} &= \begin{pmatrix} \mathbf{C}_{O(2)} & \mathbf{0} \\ \mathbf{0} & \mathbf{A}_{Z_6} \end{pmatrix} ; & \mathcal{L}_{D_6} &= \begin{pmatrix} \mathbf{C}_{O(2)} & \mathbf{0} \\ \mathbf{0} & \mathbf{A}_{D_6} \end{pmatrix} \\
\mathcal{L}_{SO(2)} &= \begin{pmatrix} \mathbf{C}_{O(2)} & \mathbf{0} \\ \mathbf{0} & \mathbf{A}_{O(2)} \end{pmatrix} ; & \mathcal{L}_{O(2)} &= \begin{pmatrix} \mathbf{C}_{O(2)} & \mathbf{0} \\ \mathbf{0} & \mathbf{A}_{SO(2)} \end{pmatrix}
\end{aligned} \tag{2.4.10}$$

In what follows, we will delve into a concise comparative analysis between the Cosserat model and Strain-gradient model, two notable extensions of classical elasticity.

#### 2.4.4.1 Cosserat elasticity vs Strain-gradient elasticity

While both models introduced in this section aim to capture non-standard effects beyond traditional assumptions, they approach the overall behaviour of the medium from distinct perspectives. The Cosserat model incorporates internal degrees of freedom, accounting for microrotations and capturing intricate microstructural effects, particularly torsional deformations. It is widely used for static modeling of the effective properties of cellular, porous, and architected materials under weak scale separation [Lakes and Benedict, 1982, Spadoni and Ruzzene, 2012, Liu et al., 2012, Addessi et al., 2013, Bacigalupo and Gambarotta, 2014a, Giorgio et al., 2022, Lemkalli et al., 2023]. In the other hand, strain-gradient elasticity focuses on the energetic contribution of higher gradients of the displacement field and their influence on the overall behaviour, addressing size effects and heterogeneity induced by the mesostructure. Modeling the overall static behaviour of periodic architected materials using The Strain-Gradient model is relatively more recent [Trinh et al., 2012, Bacigalupo and Gambarotta, 2014a, Réthoré et al., 2015, Placidi et al., 2017, Khakalo et al., 2018, Abdoul-Anziz and Seppecher, 2018, Yvonnet et al., 2020, Durand et al., 2022].

The problem addressed here is to consider the constitutive material of the architected medium as Cauchy-type continuum, but what generalized continuum to choose as an equivalent homogeneous medium? The choice of the minimal kinematic extension for modeling the effective properties periodic architected materials can be approached through local kinematics or anisotropic behavior. Local kinematics can be directly observed through numerical or experiments, while anisotropic behavior can be indirectly observed through the kinematics induced by the mesostructure. Once the appropriate kinematic extension is identified, it is essential to determine whether it represents an independent DOF or not. This distinction becomes particularly evident in elastodynamics, where rotational modes of vibration occur in the optical branches or a strong dispersion in the acoustic branches, for instance. The Cosserat model

and the Strain-Gradient model offer distinct approaches to static modeling of 2D periodic architected materials. These models differ in their theoretical foundations and modeling methodologies. The choice between the Cosserat and Strain-Gradient models relies on various factors, including the specific characteristics and behavior of the architected material under analysis. Examples of such factors may include the need to capture microstructural effects such or size-dependent phenomena in different scenarios. Both models are able to describe chirality and non-centrosymmetry which is absent from Cauchy elasticity, but this description involves fewer coefficients using the Cosserat model rather than the full Strain-gradient model. Another option would be to consider the constrained couple stress model which is a sub-model of the strain gradient elasticity corresponding to a constrained Cosserat model. This model is expected to be the least expensive to take into account the sensitivity to chirality and non centro-symmetry. Another noteworthy observation is that the Cosserat model provides a good approximation of the acoustic and optical branches in both LW-LF and SW-LF regimes. However, due to its maximal anisotropy class being tetragonal, this model cannot capture hexagonal and hexachiral anisotropy which can be correctly described by a SGE model. On the other hand, the latter is unable to describe optical branches, and hence not suitable for modeling rotational vibration modes as it does not incorporate the corresponding kinematics. By examining the formulations, constitutive laws, different couplings, and their classification of each model, valuable insights and crucial information can be provided regarding their similarities, differences, and their accuracy. A concise comparison is presented in section 2.4.4.1, facilitates a better understanding of their strengths and limitations, and assists in selecting the appropriate equivalent homogeneous medium based on the phenomena of interest.

| Model                 | Cosserat             | Strain-gradient  |
|-----------------------|----------------------|------------------|
| # of DOF              | Additional DOF       | Kept the same    |
| Nature of coupling    | Translation-rotation | Strain-gradient  |
| # Symmetry classes    | 10                   | 14               |
| Maximal anisotropy    | Tetragonal $D_4$     | Hexagonal $D_6$  |
| Maximal coupling      | Trigonal $D_3$       | Pentagonal $D_5$ |
| # material parameters | Reduced              | Huge amount      |
| Non centrosymmetry    | Sensitive            | Sensitive        |
| Chirality             | Sensitive            | Sensitive        |

Table 2.15: Comparison of key characteristics between the Cosserat model and the Strain-gradient model

However, the practical challenge lies in determining the coefficients of the selected constitutive law, using information about the microstructure and constitutive materials, i.e. find an equivalent homogeneous medium that will have the same macroscopic behaviour as the actual material within a specific range of parameters. While the determination of coefficients for the constitutive law in classical elasticity is a well-established procedure [ref homogenization], its extension to the generalized continuum is still an open question. In general, there are three approaches that can be used to tackle this problem: mathematical, numerical, and experimental. As this work focuses on the numerical and mathematical modelling of periodic media, it seems that this type of problem has already been studied through asymptotic homogenization

in statics for the Cosserat-type medium in [Forest et al., 2001] as well as for high-order elasticity in [Gambin and Kröner, 1989, Boutin, 1996], while elastodynamics has been explored in [Boutin and Auriault, 1993]. Nevertheless, there is a notable lack of studies addressing the identification of the effective strain-gradient medium in elastodynamics, whether it is through phenomenological models or derived from asymptotic homogenization [Bacigalupo and Gambarotta, 2014b, Nassar, 2015].

#### 2.4.4.2 Towards elastodynamics : Remarks on the role of micro-inertia

Taking into account the inertial contribution in Cosserat continua allows for the modeling of materials with complex microstructures or micro-rotations, where the internal degrees of freedom contribute to the overall inertia of the system. These additional terms offers an accurate prediction of the elastodynamic behavior where the coupling between translations and rotations is taken into account. By taking into account the inertial contribution in the Cosserat model, it is naturally able to describe the coupling between microrotations and translations and offers an accurate prediction of the elastodynamic overall behavior of architected materials. In particular, the Cosserat model captures rotational modes of vibrations that occur in the optical branches, which cannot be captured by Classical or strain-gradient elasticity.

In Strain-gradient elasticity, the focus is primarily on capturing the influence of stiffness (strain gradients) on medium behavior, while micro-inertia effects are not explicitly considered in the formulation [Mindlin, 1965]. Instead, the emphasis is placed on incorporating higher-order gradients of displacement or deformation to account for size effects and material heterogeneity.

| Model                      | Cosserat               | Strain-gradient        |
|----------------------------|------------------------|------------------------|
| Micro-inertia contribution | Yes                    | No or often isotropic  |
| Dispersion                 | Less sensitive (?)     | Sensitive              |
| Acoustic branches          | Accurate approximation | Accurate approximation |
| Optical branches           | Accurate approximation | Cannot capture it      |
| LW-LF                      | Accurate approximation | Accurate approximation |
| SW-LF                      | Accurate approximation | Accurate approximation |
| LW-HF                      | Accurate approximation | Cannot capture it      |

The omission of micro-inertia in the Strain-gradient model is based on the assumption that its contribution is either negligible or often treated as isotropic. [Askes and Aifantis, 2011] highlights the influence of the micro-inertia on the elastodynamic behaviour in the 1D framework, while considering an isotropic contribution. It has shown that the phase velocities depend not only on the high-order stiffness terms but also on micro-inertia terms which provides a good approximation of the behaviour, especially in the SW-LF regime. Some investigations of a frequency dependent behaviour in hexagonal architected materials have been made and showed the emergence of anisotropic inertial effects, where Higher-order stiffnesses have been supplemented by higher-order inertia tensor in a strain-gradient model [Rosi and Auffray, 2019, Rosi et al., 2018].

The unanswered questions today concern the consideration of micro-inertia in the strain-gradient model. Should micro-inertia be taken into account in this model? And what is the contribution of these terms? In the case of a spatial distribution of

anisotropic mass (anisotropic inertial network), how can these effects be incorporated into the second-gradient model? If the asymptotic homogenization in elastodynamic allows us to construct higher-order elasticity and inertia tensors capable of accounting for microstructure and size effects, how can these tensors be adapted to complement the constitutive law of the strain-gradient model, taking into account all the involved symmetries?

## 2.5 Synthesis

In this chapter, a comprehensive set of theoretical elements to model the behavior of periodic architected materials from mathematical and physical perspectives have been presented. These elements encompass various aspects, including geometry and behavior, providing a complete toolbox for studying the elastodynamic response of these materials. A key topic introduced in section 2.2 is the wallpaper-group theory, which is of great interest in designing and parameterizing geometries. By leveraging this theory, it becomes possible to create materials with predetermined properties, such as anisotropic propagation or the presence of bandgaps. To analyze and verify these properties, we delve into mathematical concepts defined in section 2.2 and employ Floquet-Bloch analysis in section 2.2. Moreover, section 2.2 offers a brief overview of generalized continua, discussing the two most commonly used models in the literature for characterizing the behavior of architected materials within the framework of homogenization.

With the theoretical framework now well-defined, we can proceed to study specific families of architected materials with diverse geometric parameterizations that hold the potential to generate non-standard elastodynamic effects. Our focus will be on analyzing the behavior and investigating these effects in depth.

In the upcoming chapter, we will explore the elastodynamic behavior of reference architected materials by analyzing their signatures through Floquet-Bloch analysis. This phenomenological study aims to select the necessary enrichment from an identification and homogenization perspective. Additionally, we will investigate the influence of inertia on the dynamic behavior to settle the question of whether it needs to be considered or not, and whether it will be isotropic or anisotropic. By adopting this strategy, we can effectively address the numerous questions posed throughout this chapter while advancing our understanding of architected materials' elastodynamic behavior.



## **Part II :**

**Towards elastodynamic approaches  
for the design and characterization  
of the overall behavior of  
Architected Materials**



# Chapter 3

## From periodic lattices to overall homogeneous continuum

### Contents

---

|     |   |     |
|-----|---|-----|
| 3.1 | INTRODUCTION . . . . .                                      | 73  |
| 3.2 | EXPLICIT PARAMETERISATION OF A FAMILY OF LATTICES . . . . . | 74  |
| 3.3 | DETERMINATION OF THE ELASTODYNAMIC SIGNATURES . . . . .     | 83  |
|     | 3.3.1 FLOQUET-BLOCH COMPUTATIONAL SIGNATURE . . . . .       | 84  |
|     | 3.3.2 INVESTIGATION OF ANISOTROPIC INERTIA CONTRIBUTION     | 105 |
| 3.4 | DETERMINATION OF THE APPROPRIATE KINEMATICS EXTENSION       | 108 |
| 3.5 | SYNTHESIS . . . . .   | 110 |

---

### 3.1 Introduction

Architected materials have gained significant attention in recent years due to their unique properties and potential for various applications. Their properties are determined by their geometrical arrangement, which can be parameterized by certain characteristic parameters. The geometry of these materials can be designed to produce specific properties and non-standard behaviours that are not present in conventional materials. Among the different types of lattices in 2D, the tetragonal lattice is one of the simplest and most commonly studied. It is characterized by a periodic array of square cells, each of which contains a central core connected to four ligaments arranged at right angles. The tetrachiral lattice is a type of tetragonal lattice that contains additional ligaments connecting the corners of each square cell, resulting in a more complex microstructure. This lattice type can exhibit non-standard properties such as negative Poisson's ratio and auxeticity. Another commonly studied lattice type is the hexagonal lattice, which consists of a periodic array of hexagonal cells, each containing a central core connected to six ligaments arranged at 120-degree angles. This lattice type can exhibit properties such as negative thermal expansion and negative stiffness. The hexachiral lattice is a type of hexagonal lattice that contains additional ligaments connecting the corners of each hexagonal cell, resulting in a more complex microstructure. This lattice type can exhibit non-standard properties such as extreme auxeticity and negative compressibility and anisotropic dynamic behaviour. By manipulating the geometry of the microstructure, it is possible to create materials with

unprecedented properties, such as extreme stiffness or flexibility, negative Poisson's ratio, negative thermal expansion, and many others.

## 3.2 Explicit parameterisation of a family of lattices

In this section, we will examine the geometrical parameterization of these materials in greater detail, investigating various types of lattices and their distinctive characteristics. The choice of geometries will be based on the symmetries of the lattice and the elementary cell, i.e. from the point groups and space groups. Therefore, we will select patterns with specific symmetries that are likely to bring about non-standard effects.

### Hexagonal lattice $D_6$

Hexagonal honeycombs have been extensively studied for their mechanical properties and dynamic behavior. Gibson and Ashby [Ashby and Gibson, 1997] conducted in-depth investigations on the mechanical properties of cellular materials, with a particular focus on hexagonal honeycombs. Their work provided initial analytical expressions for the in-plane elastic moduli of these structures. Gonella and Ruzzene [Gonella and Ruzzene, 2008] explored wave propagation and dynamic behavior within these honeycombs. Additionally, Zou [Zou et al., 2009] investigated the dynamic response of hexagonal honeycombs under impact loading, studying their energy absorption capabilities. More recently, Rosi et al. [Rosi and Auffray, 2016, Rosi and Auffray, 2019] investigated anisotropic dispersive wave propagation within hexagonal lattices, proposing a continuous modeling approach based on generalized continua within the framework of homogenization. The hexagonal honeycomb lattices are characterized by a hexagonal unit cell, composed of six identical beams arranged in a hexagonal pattern. This lattice is invariant under a 6-fold rotational symmetry. Its geometry parameters include the length  $R$  and thickness  $t$  of the beams, which is related to the size of the unit cell  $a$  such as

$$L = \frac{a}{\sqrt{3}}, \quad t = L(1 - \sqrt{1 - \rho_s}),$$

wherein,  $\rho_s$  is the relative density (i.e., area fraction) of the hexagonal cell. The commonly used geometry is illustrated in 3.1

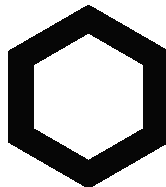


Figure 3.1: Example of hexagonal elementary cell

The hexagonal honeycomb lattice belongs to the hexagonal crystal system, characterized by a space group of  $p6mm$  and a point group  $D_6$ , which gives rise to six mirror lines in the lattice. This lattice can be generated by translating the unit cell (highlighted in yellow in figure 3.2) using the elementary vectors of the hexagonal Bravais

lattice. Notably, the choice of these vectors is not unique, leading to the consideration of at least two equivalent patterns, as depicted in figure 3.2.

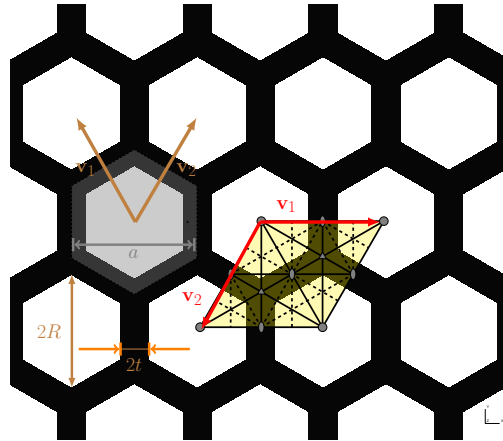


Figure 3.2: Hexagonal tiling

### Hexachiral lattice $Z_6$

The chirality effect in chiral honeycombs was initially reported by Wojciechowski in [Wojciechowski, 1989]. Chiral elasticity encompasses the coupling between local rotation, bending, and bulk deformation. [Prall and Lakes, 1997] conducted experimental and numerical studies on hexachiral lattices, confirming their in-plane negative Poisson's ratio. They demonstrated the occurrence of a negative Poisson's ratio within the range of  $-1 < \nu < 0$ . Alderson calculated the mechanical properties of various types of chiral lattices, where deformation mechanisms involve core rotation and ligament bending [Alderson et al., 2010, Liu et al., 2012]. Spadoni investigated wave propagation in periodic hexachiral lattices using Floquet-Bloch analysis to predict band-gap properties and their dependence on cell topology [Spadoni et al., 2009]. The commonly used geometry is illustrated in Figure 3.3

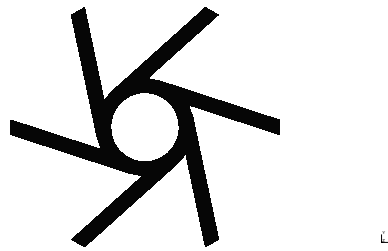


Figure 3.3: Hexachiral elementary cell

This unit cell can be described as circular nodes (cores or rings) of radius  $r$  connected tangentially to the ligaments of length  $L$ , having the same wall thickness  $t$  [Dirrenberger, 2012]. The distance between core centers is denoted  $R$  and the angle  $\beta$  is defined as the angle between the imaginary line connecting the centers of the cores and the ligaments. We define three dimensionless geometrical parameters :  $\beta$ ,  $\alpha$  and  $\gamma$ .

$$\sin(\beta) = \frac{2r}{R}, \quad \tan(\beta) = \frac{2r}{L}, \quad \cos(\beta) = \frac{L}{R}, \quad \theta = \frac{\pi}{6};$$

$$\alpha = \frac{L}{r}, \quad \gamma = \frac{t}{r},$$

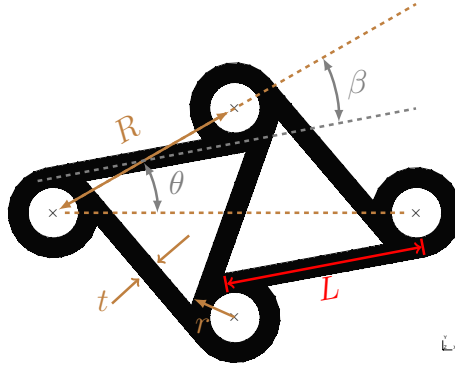


Figure 3.4: Hexachiral unit cell parameters

The unit cell possess six ligaments which makes the microstructure invariant by a rotation of order 6, which provides isotropic behaviour in classical elasticity [Dirrenberger, 2012]. The hexachiral lattice can be generated by transformation of a unit cell (yellow or blue area in figure 3.5) under a set of linear independent translations associated with the hexagonal Bravais lattice. The translations can be generated by the elementary vectors  $\mathbf{v}_1$  and  $\mathbf{v}_2$ . The choice of these vectors is not unique. Due to the lack of mirror lines and the centrosymmetric character of the pattern, the point group of this lattice is  $Z_6$ , and its corresponding wallpaper group is  $p6$ .

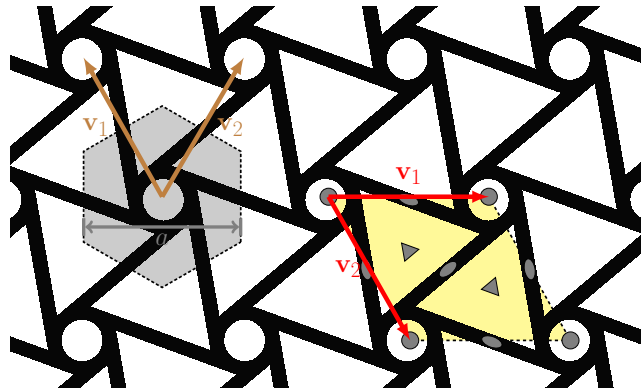


Figure 3.5: Hexachiral tiling

When the thickness of the ligaments is equal to that of the cores, it can be shown that the hexachiral cell depends only the two geometrical parameters  $\alpha$  and  $\gamma$ . The first parameter controls the slenderness of the ligaments, while the second parameter influences the material density. By denoting  $a$  the length of the unit cell, the parameters  $R$  is fixed, we have then the following relationships

$$R = a, \quad \beta = \arctan(2\alpha^{-1}), \quad r = \frac{R}{2}\sin(\beta), \quad L = R\cos(\beta), \quad t = \gamma r.$$

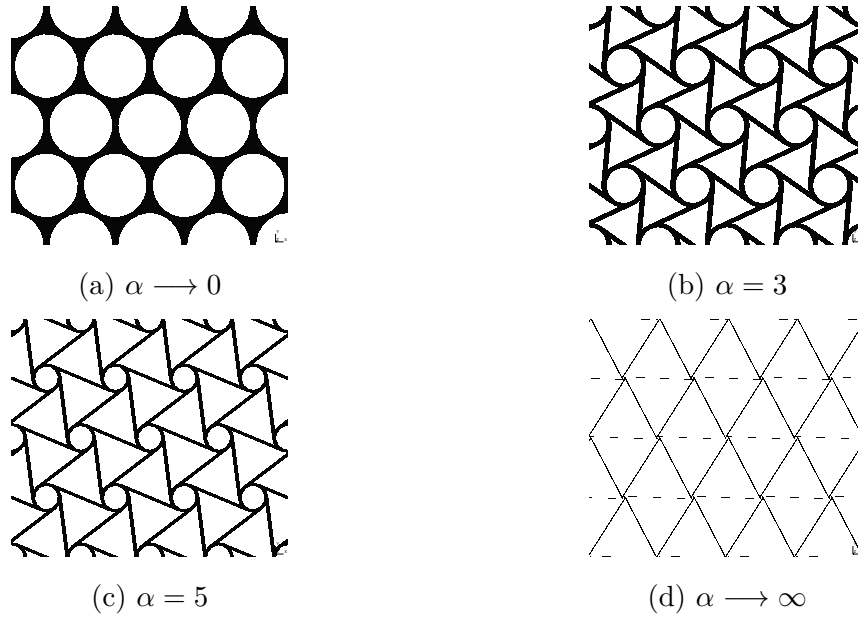


Figure 3.6: Configurations corresponding to different values of  $\alpha$  for  $\gamma = 0.2$ .

The ratio  $\alpha = r/L$  gives rise to significantly different configurations, as shown in Figure 3.6. It is expected that the behavior of the hexachiral architected material is highly dependent on this geometrical parameter.

### Tetragonal lattice $D_4$

Tetragonal lattices, also known as Square lattice, have been the subject of numerous studies. A.-J. Wang and D. L. McDowell [Wang and McDowell, 2004] explored the mechanical properties of square honeycombs, investigating their effective elastic stiffness and initial yield strength under in-plane compression, shear, and diagonal compression. Xiang Lee [Li et al., 2018] conducted a theoretical and experimental study on their mechanical response under off-axial compression. Their elastodynamic behavior, particularly in the field of phononics, has also been extensively studied. Zhao et al. [Zhao et al., 2021] studied wave propagation and bandgaps, shedding light on their dispersion characteristics and band structure. In a related study, Cheng et al. [Cheng et al., 2020] explored the impact of geometry and band gap properties through a topological design optimization approach, contributing to the optimization of lattice structures for specific applications. Moreover, the size effect within square honeycombs was investigated by Yang et al. [Yang and Müller, 2021], proposing an approach to estimate the elastic moduli of the structure using asymptotic expansions for the static case. Additionally, Rosi [Rosi et al., 2018] proposed an identification procedure for the elastodynamic effective properties of square honeycombs, based on a strain gradient-model and Floquet-Bloch analysis.

Tetragonal lattices are characterized by repeated square unit cells, where each cell consists of four identical beams arranged in a square pattern. This lattice is invariant under a 4-fold rotational symmetry. The geometrical description of the lattice involves two parameters: the size of the unit cell  $a$  and the thickness  $t$  of the beams (walls). The size of the unit cell, corresponds to the length of each side of the square cell. It defines the characteristic length scale of the lattice and determines the distance

between two nodes of the square lattice. The thickness controls the density of the unit cell and influences the mechanical properties of the lattice, such as its stiffness. The commonly used unit cell is shown in figure 3.7, for which thickness of the beams can be expressed in terms of the unit cell size and relative density as follows

$$t = \frac{a(1 - \sqrt{1 - \rho_s})}{2}.$$

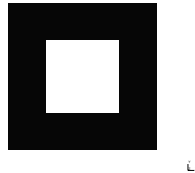


Figure 3.7: Tetragonal elementary cell

The tetragonal lattice belongs to the square crystal system, with a space group of  $p4mm$ . Its point group is  $D_4$ , which gives rise to four mirror lines in the lattice.

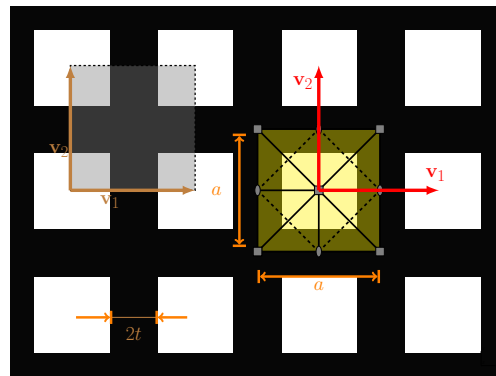


Figure 3.8: Tetragonal tiling

### Tetrachiral lattice $Z_4$

The tetrachiral lattice, also known as the square chiral lattice, is a model derived from the hexachiral lattice with the same geometric parameterization. Several studies have been conducted to investigate the static behavior of this structure. In [Grima et al., 2008, Mousanezhad et al., 2016], the mechanical properties are determined using analytical and numerical models. The coupling between normal and shear strains through an elastic modulus in static conditions was investigated in [Bacigalupo and Gambarotta, 2014a] and highlighted a remarkable variability of the Young's modulus and Poisson's ratio with the direction of the applied uniaxial stress. Similarly, a homogenization approach based on a micromorphic model was proposed in [Biswas et al., 2020] to predict these coupling mechanisms. The dynamic behavior has also been explored in [Lepidi and Bacigalupo, 2017], where the band structure was established through Floquet-Bloch analysis. The tetrachiral lattice is a type of square lattice that exhibits 4-fold chiral symmetry. Similar to the hexachiral geometry, it consists of a core with a radius of  $r$  connected tangentially to four ligaments of length

$L$ , which ensures that the lattice remains invariant under a rotation of order 4. The unit cell geometry can be described using the same parameters as the hexachiral unit cell:  $\alpha, \gamma, \theta = \pi/4$  and  $R = a$ . Figure 3.10 provides an illustration of a tetrachiral architected material, where the yellow area represents the unit cell.

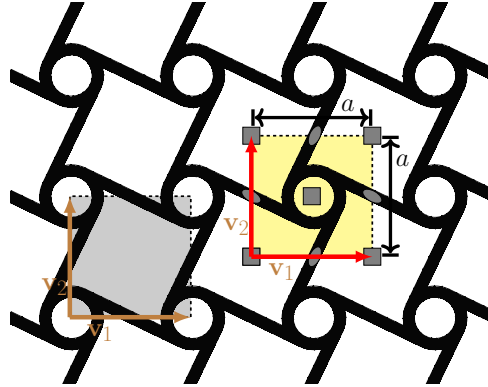


Figure 3.9: Tetrachiral tiling

The tetrachiral lattice belongs to the space group  $p4$ , which is the tetragonal space group exhibiting 4-fold rotational symmetry. Its point group is denoted as  $Z_4$ . The chiral characteristic of this geometry arises from the absence of mirror lines, leading to its unique asymmetric properties. Just like in the hexachiral lattice, the tetragonal lattice depends on the pre-defined geometrical parameters, which leads to multiple configurations with different behaviors impacting wave propagation velocities as well as band-gaps (see figure 3.10).

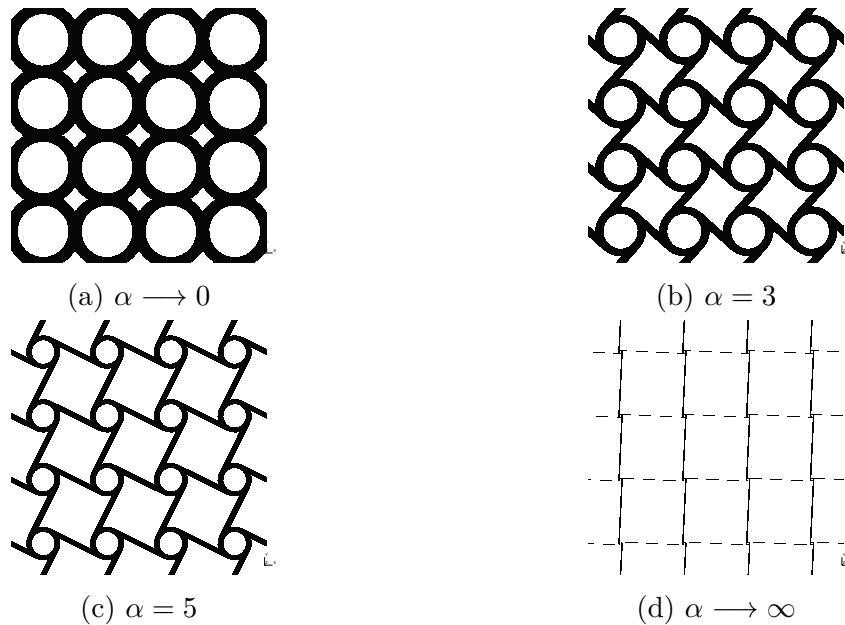


Figure 3.10: Configurations corresponding to different values of  $\alpha$  for  $\gamma = 0.3$ .

Before concluding this section, we will introduce two additional geometries of architected materials. In contrast to their counterparts, these geometries exhibit a lack of centrosymmetry and possess a 3-fold rotational symmetry, namely trichiral and trigonal type PAMs. Subsequently, we will define an example of each of these materials by providing a geometric parameterization for both.

### Trichiral lattice $Z_3$

The unit cell of trichiral lattice can be described as circular nodes of radius  $r$  and constant thickness  $t_c$ , connected tangentially to six ligaments of variable thickness  $t_l$  and length  $L_l$ . The distance between the core centers is denoted by  $R$ , which represents also the size of the unit cell, while the angle  $\beta$  defines the orientation between the imaginary line connecting the core centers and the ligaments. Remarkably, the unit cell exhibits a 3-fold rotational invariance, resulting in two successive ligaments with distinct shapes, which give rise to a pattern that combines non-centrosymmetry and chirality, as illustrated in figure 3.11

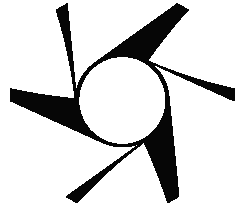


Figure 3.11: Trichiral elementary cell

In order to ensure a coherent and unified approach of the geometry modeling, we adopt the same set of dimensionless geometrical parameters utilized in the hexachiral and tetrachiral unit cells. This choice enables a consistent and standardized parametrization of the geometry as shown in figure 3.12

$$R = a, \quad \beta = \arctan(2\alpha^{-1}), \quad r = \frac{R}{2}\sin(\beta), \quad t_c = \gamma r, \quad L_l = \sqrt{a^2 - (2r + t_c)^2},$$

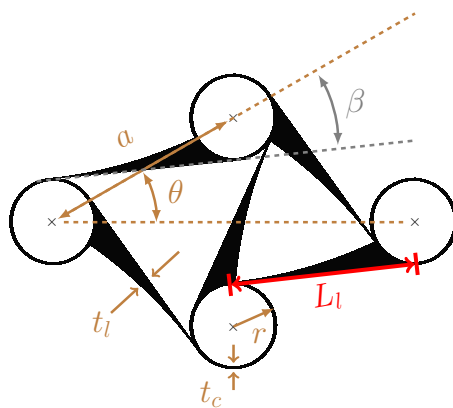


Figure 3.12: Trichiral unit cell parameters

The ligaments have been modeled with a quadratic profile having variable thickness  $t_l$ , depending on the size of the unit cell and the parameter  $\alpha$ , in order break the symmetry with respect to the fictive line tangent to the rod, such as

$$t_l(x) = \frac{a}{2} \sin(\beta) \left( 1 - \left( 1 - \frac{x}{L_l} \right)^2 \right), \quad x \in [0, L_l]$$

Then, to break the 6-fold rotational invariance, each ligament is followed by its mirror image with respect to the line that is orthogonal to it. It should be noted that this parameterization is not unique, and other profiles can be used as long as they break the 6-fold rotational invariance. The unit cell possesses two sets of three ligaments,

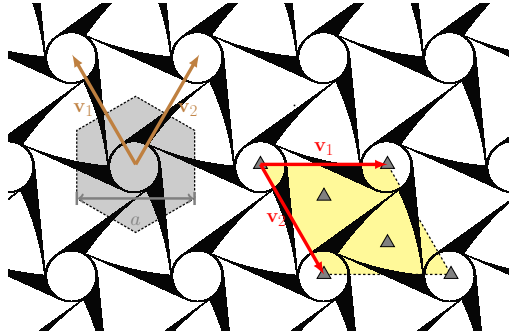


Figure 3.13: Trichiral tiling

which make the microstructure invariant under a rotation of order 3, with zero mirror lines.

The trichiral lattice is generated through the transformation of a unit cell (highlighted in the yellow area in figure 3.13) by employing a set of linear independent translations associated with the hexagonal Bravais lattice. Notably, the trichiral lattice exhibits a non-centrosymmetric pattern and lacks mirror lines, its point group is  $Z_3$ , while its corresponding wallpaper group is identified as  $p3$ . It is worth mentioning that numerous studies in the literature have utilized an inappropriate trichiral unit cell, the most used is shown in figure 3.14b [Mousanezhad et al., 2016, Shiyin et al., 2015]. In reality, as depicted in figures 3.14a and 3.14b, the commonly used unit cell indeed exhibits a 3-fold rotational invariance; however, the tiling itself is invariant under both 3-fold and 6-fold rotations. The proposed parameterization addresses this inconsistency by ensuring the compatibility between the space group of the unit cell and that of the tiling, which provide a more accurate representation of the trichiral lattice.

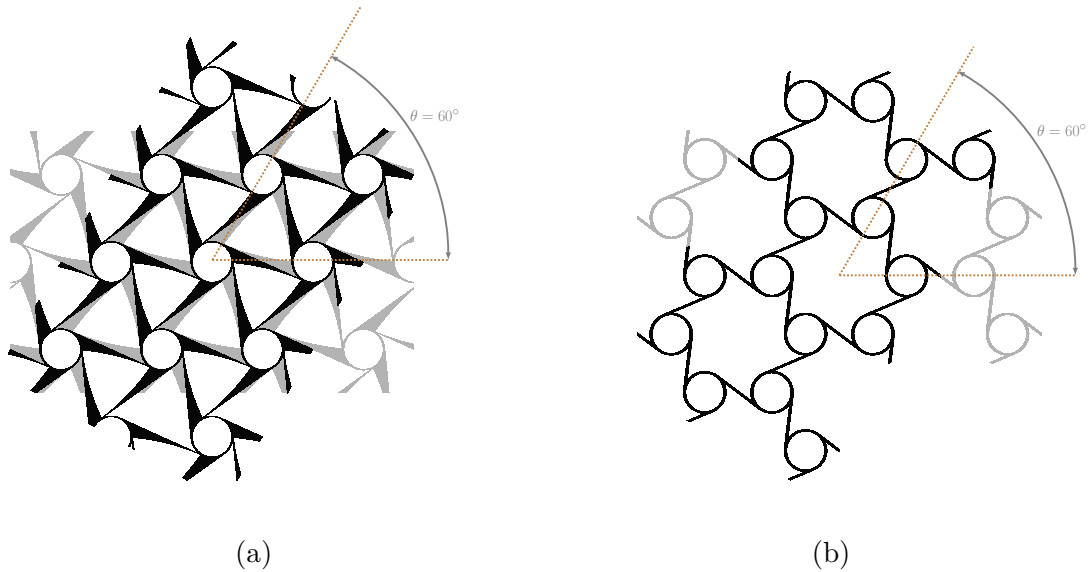


Figure 3.14: Rotational invariance of the trichiral tiling : a) the proposed tiling, b) the commonly used tiling

### Trigonal lattice $D_3$

The unit cell of the Trigonal lattice can be described in a similar manner to the trichiral one, utilizing the same geometrical parameters. However, its construction differs slightly. Here, we have chosen to use a base similar to that of the trichiral unit cell: circular nodes with a radius of  $r$  and constant thickness  $t_c$ . However, the ligaments, with a length of  $L_l$  and variable thickness  $t_l$ , are not connected tangentially but rather orthogonal to the cores. Despite this difference, the unit cell exhibits a 3-fold rotational invariance, resulting in two successive ligaments with distinct shapes but symmetric with respect to the mirror line passing through the core's center. This unique arrangement gives rise to a pattern that combines non-centrosymmetry and achirality, as illustrated in figure 3.15.

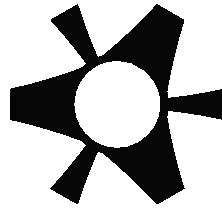


Figure 3.15: Trichiral elementary cell

figure 3.16 provides an overview of the geometric parameters of the trigonal cell.

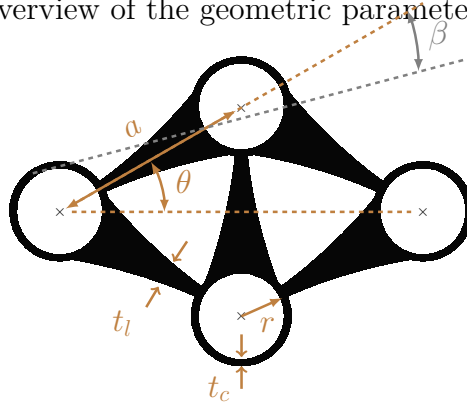


Figure 3.16: Trigonal unit cell parameters

The ligaments have been modeled with a symmetrized quadratic profile with respect to the fictive line connecting the centers of two adjacent cores, having variable thickness  $t_l$  such as

$$t_l(x) = -\frac{a}{2} \sin(\beta) \left(1 - \frac{x}{L_l}\right)^2, \quad x \in [0, L_l]$$

Then, to break the 6-fold rotational invariance, similar to the trigonal unit cell, each ligament is followed by its reflection with respect to its midpoint. It should be noted that this parameterization is not unique, and other profiles can be utilized as long as they disrupt the 6-fold rotational invariance and ensure the presence of mirror lines. The unit cell possesses two sets of three ligaments, which make the microstructure invariant under a rotation of order 3 and exhibit 3 mirror lines.

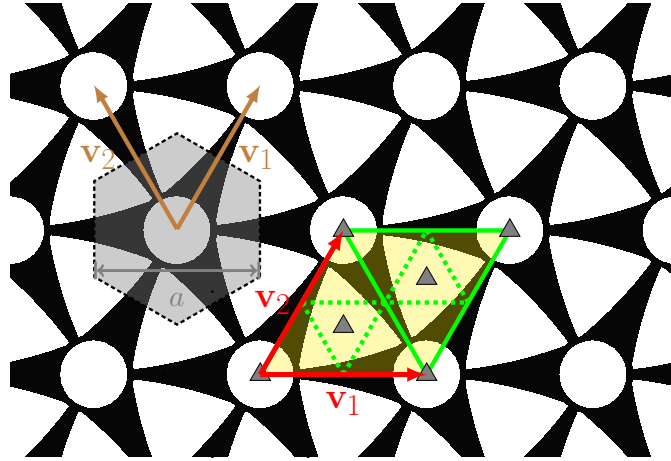


Figure 3.17: Trigonal tiling

Similar to the trichiral tiling, the trigonal tiling is also generated by transforming a unit cell, which is highlighted in the yellow area in figure 3.13, using a set of linear independent translations associated with the hexagonal Bravais lattice. In addition, the trigonal lattice possesses a non-centrosymmetric pattern and exhibits three mirror lines, i.e., its point group is  $D_3$ , while its corresponding wallpaper group is identified as  $p3m1$ .

Having established a diverse family of periodic architected materials, each characterized by distinct geometric constructions and affiliations with various wallpaper groups, our next step is to conduct a comprehensive exploration and analysis of their behavior through Floquet-Bloch analysis. In this study, we will closely examine their elastodynamic signatures, looking for any interesting effects that may emerge, notably investigating whether the underlying geometric symmetries manifest in the materials' behavior.

### 3.3 Determination of the elastodynamic signatures

The study of wave propagation in Periodic Architected Materials (PAM) has garnered significant interest due to their potential to exhibit exotic properties, such as band gaps, dispersive and anisotropic propagation, and the ability to change the direction of energy propagation, which arise from the design of the inner geometry. Moreover, PAMs offer opportunities to enhance non-destructive characterization properties, such as materials with specific acoustic signatures when damaged. The behavior of waves propagating in these materials is strongly influenced by frequency. Some PAMs exhibit isotropic behavior at low frequencies, transitioning to anisotropic behavior at high frequencies. To investigate these phenomena, dispersion curves of PAMs are commonly obtained through comprehensive computations based on Floquet-Bloch analysis performed on the unit cell. These dispersion curves play a crucial role in designing tailored meta-materials and waveguides as they establish a link between the geometric properties of the unit cell and the dynamic properties of the PAMs. To understand the diverse response of such materials, it is important to analyze the behavior of each geometry.

In order to determine a suitable substitution continuum for PAMs, several aspects need to be considered. The primary objective is to observe and analyze the phenomena that emerge during wave propagation in various regimes with the aim of identifying the most appropriate kinematical extension of the substitution continuum. For optimal design applications, it is crucial to establish a homogeneous overall description of the mechanical behavior exhibited by PAMs. This allows for the derivation of analytical expressions for quantities of interest, such as propagation constants, which can be used in optimization processes. However, the task of selecting the appropriate overall continuum is not straightforward. Several questions need to be addressed in this regard. Firstly, it is important to determine the domain encompassing wavelengths and frequencies within which the real material can be effectively substituted by an equivalent one. Additionally, the richness of information available within this domain needs to be evaluated to justify the use of a generalized continuum. Lastly, it is essential to identify the specific features related to wave propagation that must be preserved by the effective continuum. By answering these questions, the determination of a suitable substitution continuum for PAMs can be achieved. This section is devoted to the analysis of some common situations that have been chosen to illustrate the elastodynamic behaviour of PAMs. Finite Element simulations will be conducted on various geometries to provide insights into wave propagation characteristics. The dispersion diagram, obtained through Floquet-Bloch analysis, will be computed on the edges of the Irreducible Brillouin Zone (IBZ), capturing the essential propagation properties of the medium.

### 3.3.1 Floquet-Bloch computational signature

To study plane wave propagation, the software COMSOL Multiphysics 5.4 has been used to solve the eigenvalue problem and compute dispersion curves. The following case studies will be analyzed :

- 2D hexachiral ( $Z_6$ ) lattice;
- 2D hexagonal ( $D_6$ ) lattice;
- 2D tetrachiral ( $Z_4$ ) lattice;
- 2D tetragonal ( $D_4$ ) lattice;
- 2D trichiral ( $Z_3$ ) lattice;
- 2D trigonal ( $D_3$ ) lattice.

Throughout our study, we have made several key assumptions. Firstly, we consider the influence of the sample size to be negligible, assuming it to be infinitely large. Secondly, we assume that the internal architecture of the material is well-separated from the microscale, leading to the separation ratio assumption:

$$\frac{l_m}{L_i} \ll 1$$

where  $L_i$  represents the scale of the internal architecture (mesoscale), and  $l_m$  denotes the characteristic length scale associated with the constituent material of the architected material. For example, in the case of a metal,  $l_m$  could represent the average grain size, while for a polymer, it could indicate the average length of polymer chains. Additionally, we emphasize the importance of the ratio  $\eta = L_i/\lambda$ , which indicates the specific position of the architected material between a bulk material and a structure. This ratio is closely related to the condition of homogenizability, which states that the wavenumbers must be in the first Brillouin zone  $\mathcal{T}^*$ . In other words, the wavelength of the loading ( $\lambda = 2\pi/k$ ) must be at least twice as large as the size of the

unit cell. The geometric parameters of the unit cell, as well as the material constants, are listed in table 3.1. In this case study, the material is modelled as a Cauchy continuum in plane strain, using quadratic Lagrange triangular elements. The objective is to analyze the dynamic signature of periodic architected materials (PAMs). To achieve this, the dispersion diagram is computed using the Floquet-Bloch theorem, introduced in chapter 2. To do this, Floquet-Bloch periodic boundary conditions are enforced to accurately account for the free propagation of planar waves across adjacent cells. The dispersion diagram is computed following the edge of the IBZ that delimited by points of high symmetry. The wavevectors are chosen following the path connecting these high symmetry points along the edges of the IBZ, the latter depend on the space group type of each unit cell.

| Unit cell   | unit cell size $a$ | walls/ligaments thickness $t$ | $\alpha$ | $\gamma$ | volume fraction (%) |
|-------------|--------------------|-------------------------------|----------|----------|---------------------|
| Hexachiral  | 1 mm               | 0.04mm                        | 3        | 0.122    | 16.56               |
| Hexagonal   | 1 mm               | 0.05 mm                       | -        | -        | 16.6                |
| Tetrachiral | 1 mm               | 0.05mm                        | 3        | 0.135    | 16.57               |
| Tetragonal  | 1 mm               | 0.04 mm                       | -        | -        | 16.57               |
| Trichiral   | 1.93 mm            | variable                      | 3        | 0.038    | 16.80               |
| Trigonal    | 1.93 mm            | variable                      | 3        | 0.05     | 32.07               |

Table 3.1: Geometric properties of the studied lattices

|        |                              |                 |
|--------|------------------------------|-----------------|
| $E$    | 70 <i>GPa</i>                | Young's modulus |
| $\nu$  | 0.33                         | Poisson ratio   |
| $\rho$ | 2700 <i>kg/m<sup>3</sup></i> | mass density    |

Table 3.2: Material properties of the constitutive material

### Hexachiral lattice

Our exploration begins with an investigation into the elastodynamic behavior of hexachiral architected material, particularly focused on the first two modes corresponding to the acoustic branches. Figure 3.18 presents an illustration of the medium associated with the geometric parameters outlined in table 3.1.

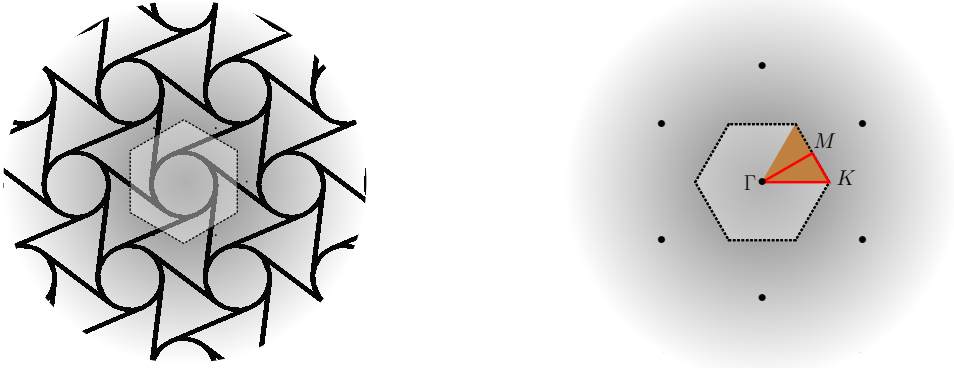


Figure 3.18: Left-hand figure : Hexachiral  $Z_6$  lattice and its unit cell. Right-hand figure : First Brillouin zone (gray area), IBZ (brown area) and its contour (red triangle)

The contours of dispersion surfaces for the first two modes are showcased in figure 3.19 for three frequencies, illustrating the iso-frequency contours and capturing the periodicity within the frequency-wavenumber spectrum accurately.

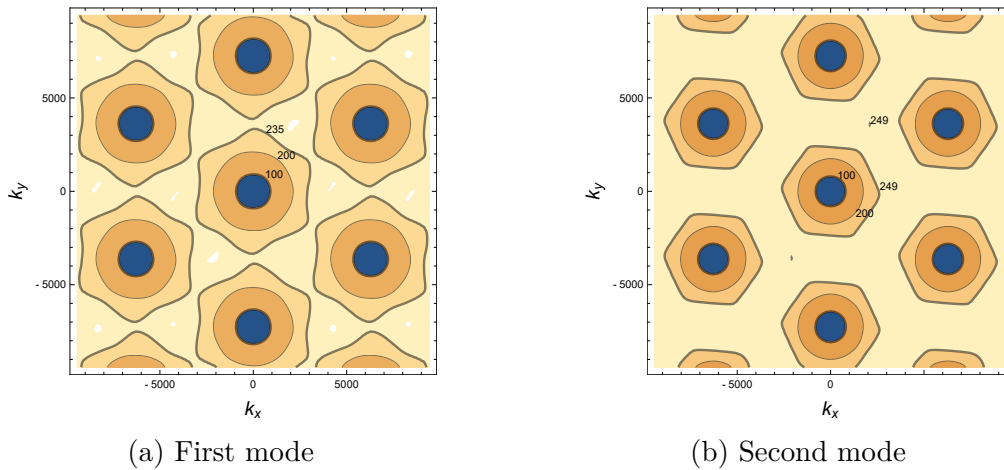


Figure 3.19: Iso-frequency countours of the slowness surfaces

An additional layer of insight is provided by the brown region in figure 3.18, representing the irreducible Brillouin zone. This zone, encompasses the essential characteristics of dispersion by leveraging the inherent symmetry within the first Brillouin zone. This inclusion enables a comprehensive and precise representation of the considered dispersion phenomena. Iso-frequency countours of the first two slowness surfaces showed in figure 3.20 clearly reveals the inherent hexagonal symmetry of the chiral lattice, which exhibit six lobes and become more pronounced at higher frequencies. Additionally, the circular iso-frequency contour curves showed in the figure, corresponding to lower frequencies and wave numbers, suggest an isotropic elasto-dynamic behavior of the chiral lattice. This observation further emphasizes the intriguing properties of

the chiral lattice, which exhibit distinct responses based on the frequency and wave number.

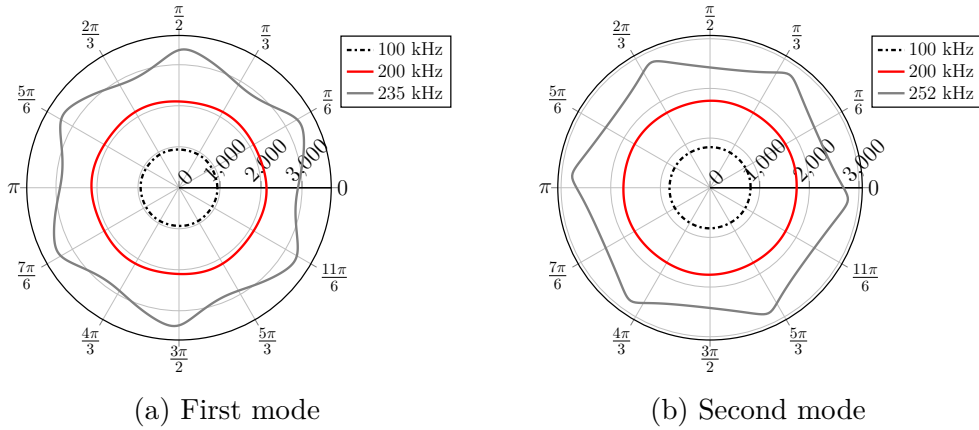


Figure 3.20: Iso-frequency contours of the first two slowness surfaces over IBZ

The elastodynamic signature of the medium is conveniently illustrated through dispersion diagrams, as shown in figure 3.21. These diagrams provide a visual representation of the relationship between wave frequency and the wave vector magnitude along the contours of the irreducible Brillouin zone. By analyzing these diagrams, one can discern the distinct behavior exhibited by each wave mode, enabling the detection of anisotropic behavior and the presence of band gaps.

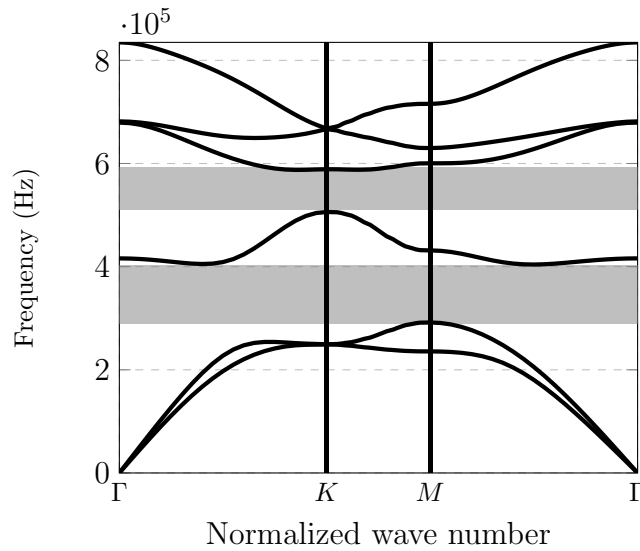


Figure 3.21: Dispersion curves for  $Z_6$  honeycomb lattice

The dispersion diagram, reveals distinct shapes in the behavior of wave modes and the presence of two band gaps. Notably, the dispersion curves of the first two modes exhibit "leveling-off" effect at low frequencies, gradually becoming flat as the frequency increases. Conversely, the third and fourth modes exhibit contrasting behavior. These modes undergo rapid changes at high frequencies, while their surfaces appear almost flat around the origin  $\Gamma$ , i.e. around  $\|\mathbf{k}\| = 0$ . Consequently, one can infer that the wave velocities of the third and fourth modes undergo notable variations within the first Brillouin zone. These observations highlight the intricate nature of wave propagation within the medium and emphasize the unique characteristics exhibited by

different wave modes.

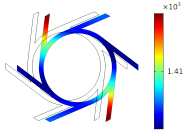
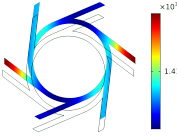
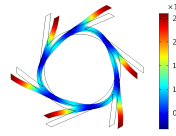
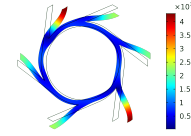
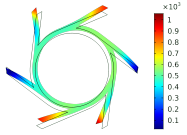
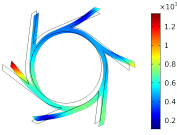
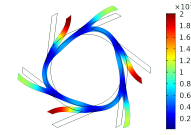
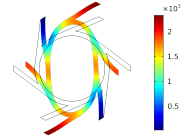
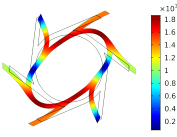
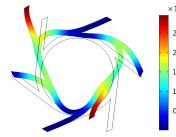
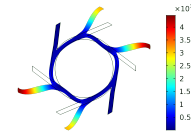
| Point    | Mode 1  | Mode 2  | Mode 3   | Mode 4  |
|----------|---|---|--|---|
| $\Gamma$ |  |  |  |  |
| $K$      |  |  |  |  |
| $M$      |  |  |  |  |

Table 3.3: First, second, third and fourth wave modes at high symmetry point  $\Gamma$ ,  $K$  and  $M$  of the IBZ (total displacement in mm)

The eigenmodes for each dispersion curve at the points  $\Gamma$ ,  $K$ , and  $M$  are presented in table 3.3. The table has three rows, corresponding to the three points of high symmetry, and four columns, representing the first four modes in ascending order. Let's focus on the four eigenmodes presented in the first column. At the point  $\Gamma$ , the unit cell exhibits rigid-body translation for the first two modes, while the third and fourth modes exhibit micro-rotation. Moving along the first branch, corresponding to transverse waves, the behavior becomes more complex as the wavenumber increases. The transverse nature of the eigenwaves is clearly evident from the cell deformation at point  $K$ . The second column of the table presents the second branch of the dispersion curve, which consists of a longitudinal wave. Similarly, for this mode, as the wavenumber increases, the mode exhibits a complex deformation.

In order to further advance the study, it is important to analyze the nature of velocities and their dependence on frequency and direction. Phase and group velocities provide valuable information about the behavior, particularly regarding the presence of anisotropy within a given frequency range. This suggests the existence of preferred directions for propagation and energy transmission, and consequently, indicates the dispersive nature of the medium. The energy flow associated with the propagation of wave packets within the PAM are provided by the group velocity, which define the direction of the energy flow and allows the identification of preferred or prohibited directions of propagation [spadoni]. We recall, for convenience, the expression of the phase velocity and define the group velocity as follows :

$$\mathbf{v}_\varphi = \frac{\omega}{\mathbf{k}}, \quad \mathbf{v}_g = \frac{\partial v_\varphi}{\partial \mathbf{n}} = \omega \otimes \nabla_{\mathbf{k}}.$$

The polar plot of the phase velocities are shown in figure 3.22. The phase velocity plots for the lowest frequency exhibit circular shapes, indicating an isotropic behavior, while at higher frequencies, The phase velocity plots for the lowest frequency exhibit circular shapes, indicating an isotropic behavior, while at higher frequencies, they

reveal the anisotropy of the lattice. Notably, as the frequency increases, the phase velocity decreases. This behavior aligns with the dispersion branches depicted in figure 3.21, where the slopes decrease as the wave vector approaches the edges of the first Brillouin zone.

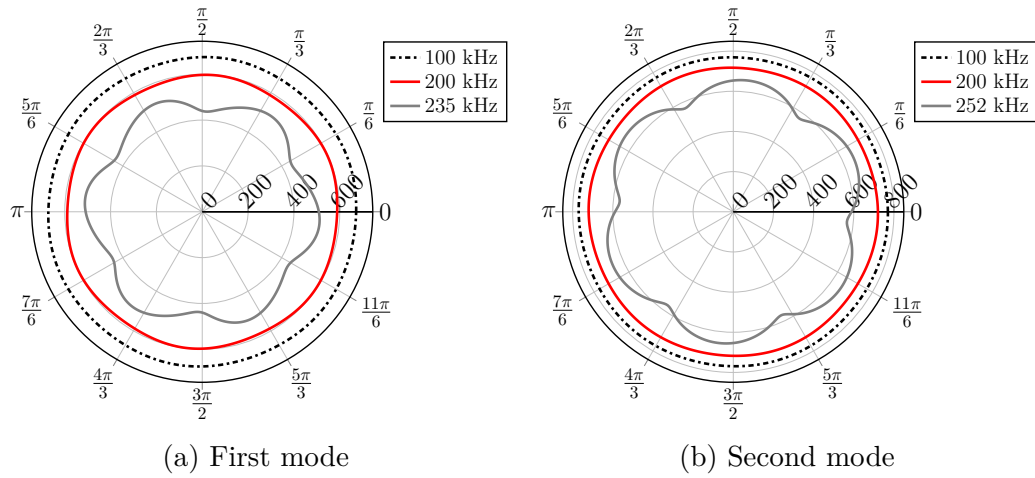


Figure 3.22: Phase velocities of the Hexachiral PAM

The polar plots of the group velocities are presented in section 3.3.1. As expected, for the first two modes at low frequencies, the group velocities closely resemble the corresponding phase velocities, indicating a non-dispersive and isotropic behavior that holds for long wavelengths. However, as the frequency increases, a breaking of symmetry occurs and the group velocities reveal a complex shapes, one can easily distinguish a hexagonal-like shape showcasing their pronounced dependence on frequency. This behavior can be attributed to the significant energy focusing that occurs in wave packets propagation along preferential directions. The chiral effect can also be observed, as each polar curve does not possess any mirror symmetries, while the rotational symmetries are preserved.

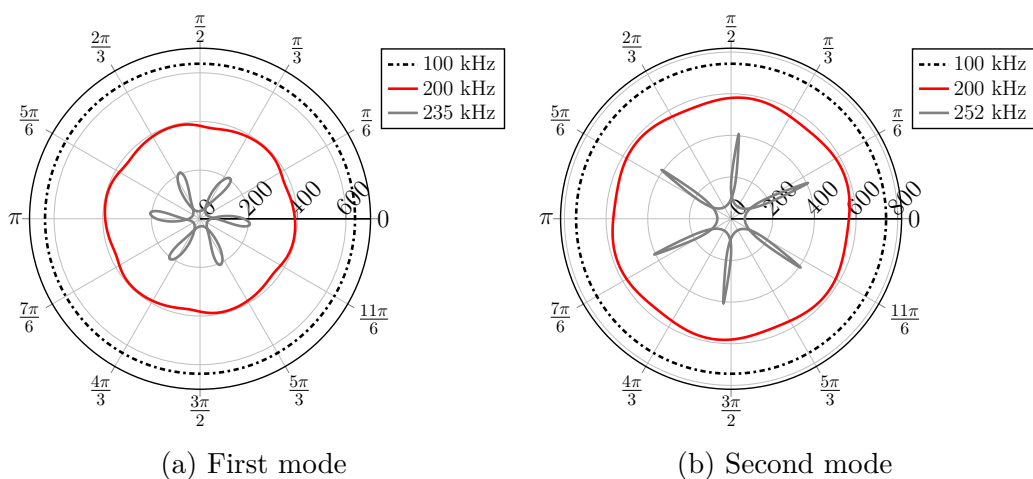


Figure 3.23: Group velocities of the Hexachiral PAM

### Hexagonal lattice

Let us now investigate the elastodynamic behavior of hexagonal architected materials. Figure 3.24 presents an illustration of the tiling associated with the geometric parameters outlined in table 3.1.

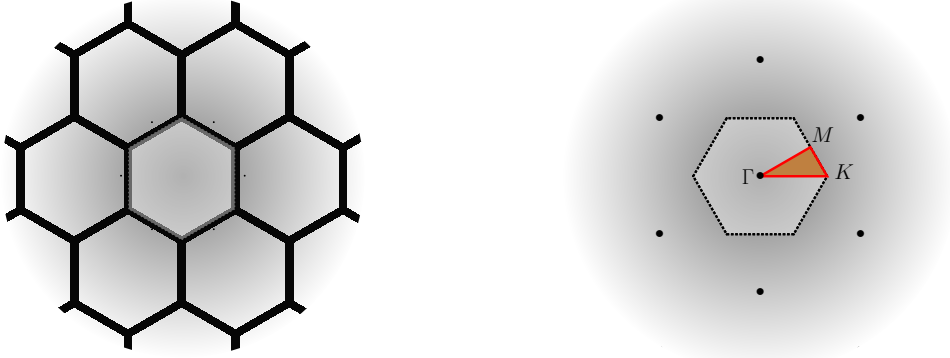


Figure 3.24: Left-hand figure : Hexagonal  $D_6$  lattice and its unit cell. Right-hand figure : First Brillouin zone (gray area), IBZ (brown area) and its contour (red triangle)

The contours of dispersion surfaces for the first two modes are showcased in figure 3.25 for three frequencies, illustrating the iso-frequency contours and capturing the periodicity within the frequency-wavenumber spectrum accurately.

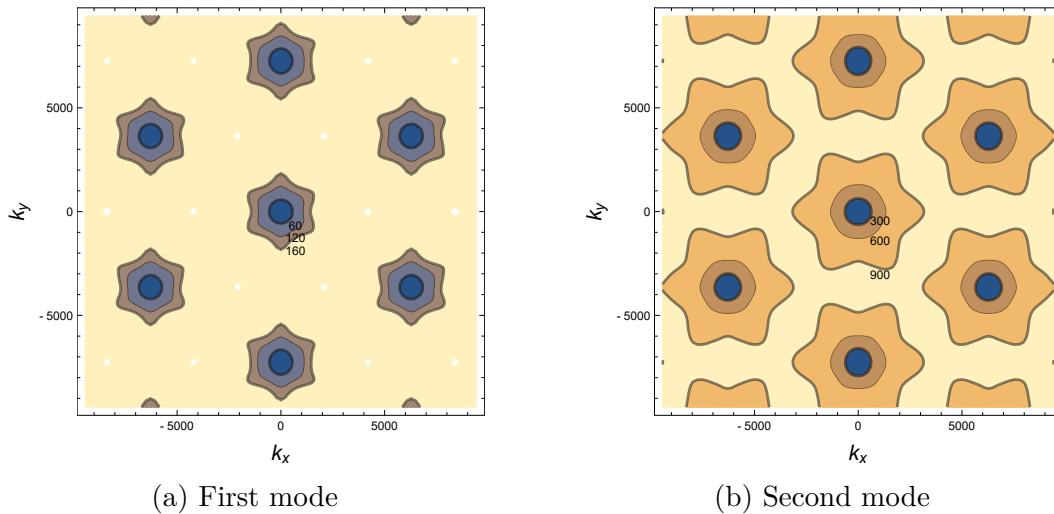


Figure 3.25: Iso-frequency countours of the slowness surfaces

the IBZ is represented by the brown area in figure 3.24. The Iso-frequency countours of the slowness surfaces illustrated in figure 3.26 clearly reveals the inherent hexagonal symmetry of the lattice. As in the hexachiral geometry, the contour curves of slowness surfaces exhibit six lobes, which become more pronounced at higher frequencies. Similarly, the iso-frequency contour exhibiting a circular shape, corresponding to lower frequencies and wave numbers, suggest an isotropic elasto-dynamic behavior.

The dispersion diagram figure 3.27 is computed along the IBZ, provide important information about anisotropic wave behavior the hexagoal PAM. This diagram exhibits notable distinctions in the behavior of the first two modes within the IBZ. Specifically, the acoustic branches appear noticeably distant from each other, which contrasts with

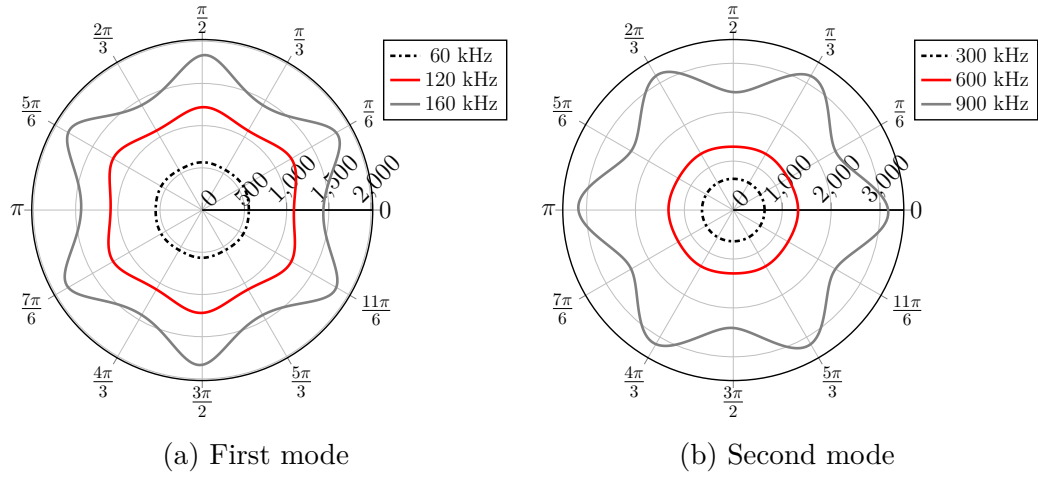


Figure 3.26: Iso-frequency contours of the first two slowness surfaces over IBZ

the hexachiral geometry where they are closer in proximity. This indicates a significant disparity in amplitude between their respective phase velocities. Additionally, it is observed that the second mode rapidly becomes anisotropic in the  $\Gamma K$  direction compared to the first mode, suggesting a greater impact on P-waves rather than S-waves. Although the anisotropy may not be highly pronounced, it certainly has significant effects on wave propagation, especially on S-waves. Furthermore, it is important to note that the selected frequency range (first six eigenmodes) shows a complete absence of a band-gap. This absence of a band-gap indicates a lack of coupling between the modes, which is commonly associated with the absence of chirality in the geometry.

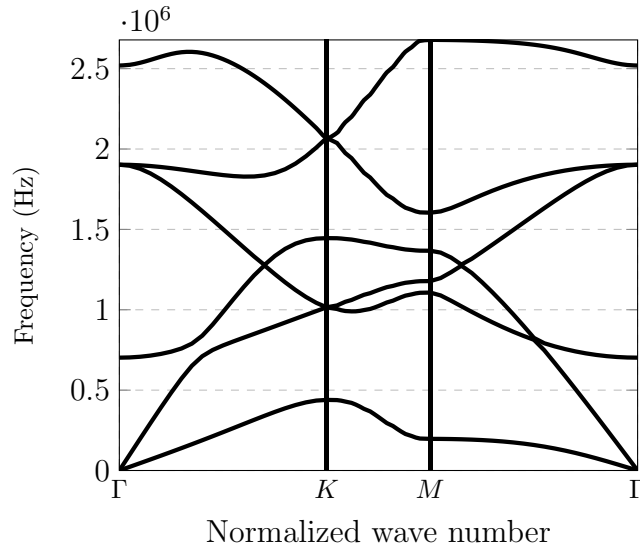


Figure 3.27: Dispersion curves for  $D_6$  honeycomb lattice

The eigenmodes for each dispersion curve at the points  $\Gamma$ ,  $K$ , and  $M$  are depicted in table 3.4. Similar to the hexachiral cell, we can make analogous observations. At  $\Gamma$ , the first two modes demonstrate rigid body motion, while the third and fourth modes display local rotational motion. As the wavenumber increases, we observe a more complex behavior, and the deformation becomes significantly more pronounced. The phase and group velocities can be analyzed similarly, as shown in figure 3.36. As expected, the behavior is strongly anisotropic and exhibits similar patterns. At

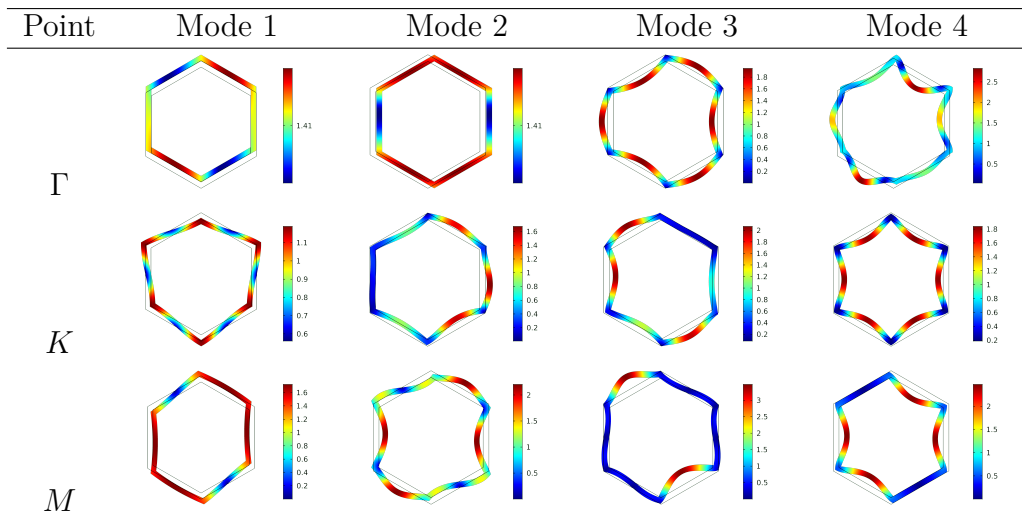


Table 3.4: First, second, third and fourth wave modes at high symmetry point  $\Gamma$ ,  $K$  and  $M$  of the IBZ (total displacement in m)

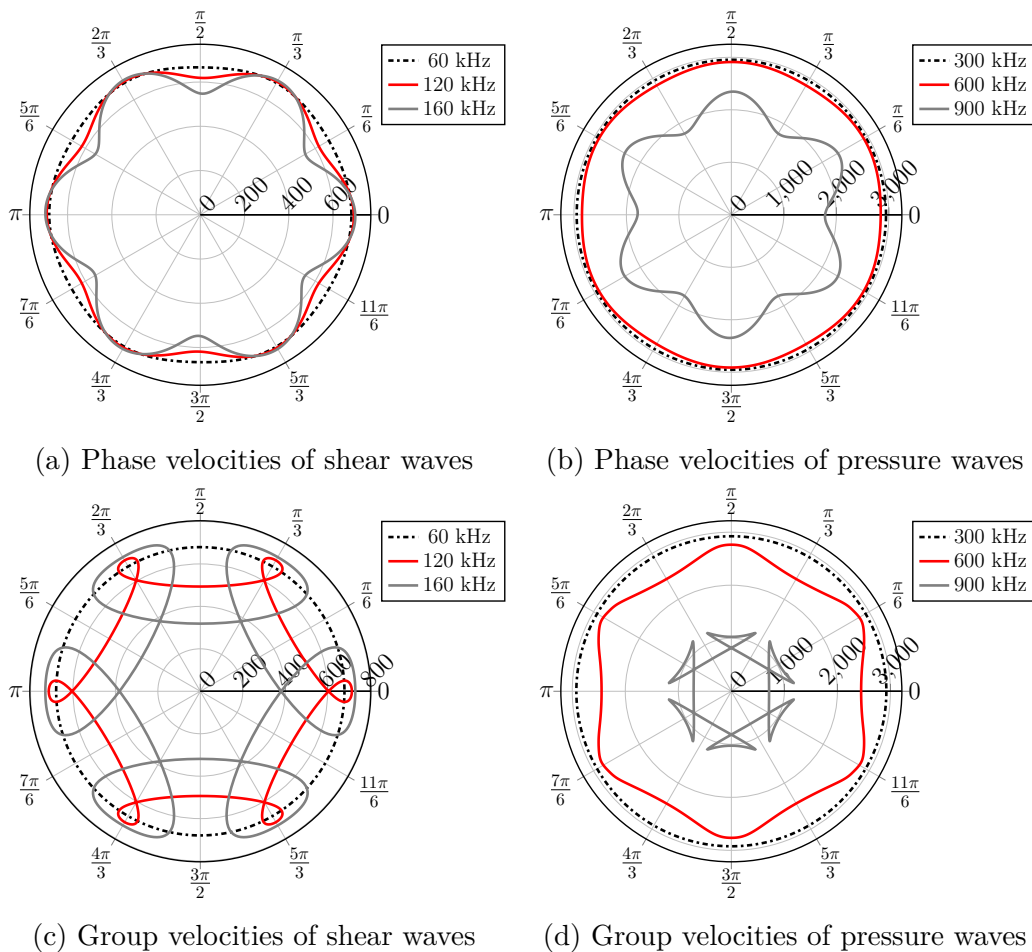


Figure 3.28: Phase and group velocities of the hexagonal PAM

the first chosen frequency, anisotropic features start to emerge, aligning with the shape of the tetrachiral unit cell, indicating a significant anisotropy at both low and high frequencies. The rotational symmetries are preserved throughout this frequency range; however, the velocity pattern does not exhibit any mirror lines, as anticipated.

### Tetrachiral lattice

Let us now investigate the elastodynamic behavior of tetrachiral architected materials. Figure 3.33 presents an illustration of the tiling associated with the geometric parameters outlined in table 3.1.

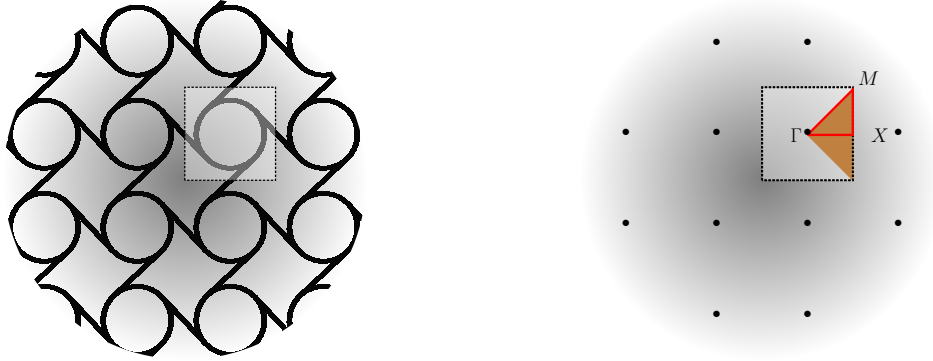


Figure 3.29: Left-hand figure : Tetrachiral  $Z_4$  lattice and its unit cell. Right-hand figure : First Brillouin zone (gray area), IBZ (brown area) and its contour (red triangle)

The Iso-frequency contours of the slowness surfaces shown in figure 3.30 clearly reveal the tetrachiral symmetry inherent in the lattice, as no mirror lines are observed in the contours. The contour curves of the slowness surfaces display four lobes, which are distinctly present both at low and high frequencies, signifying a strong anisotropic behavior.

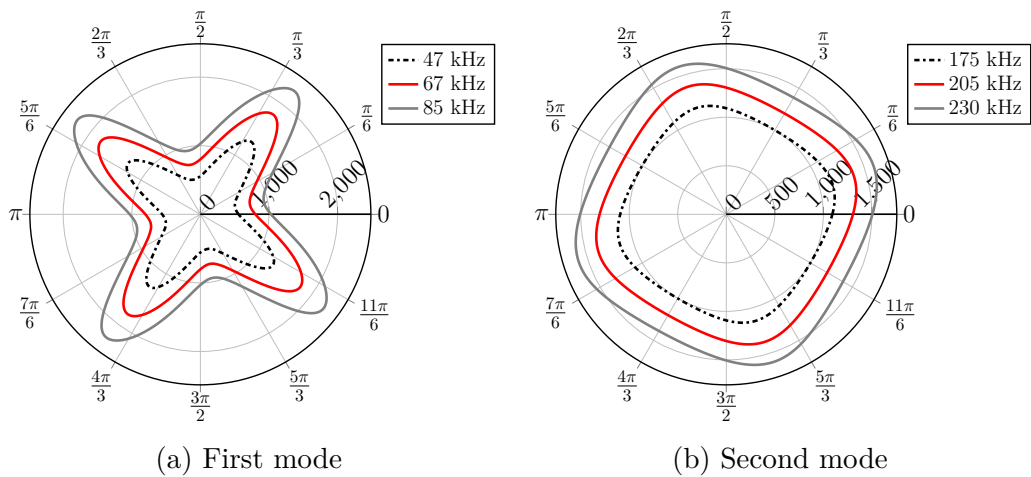


Figure 3.30: Iso-frequency contours of the first two slowness surfaces over IBZ

The dispersion diagram in figure 3.31, computed along the IBZ, reveals notable distinctions in the behavior of the first two modes within the IBZ, and the presence of two band-gaps. Similar to the hexachiral lattice, the acoustic branches are slightly close to each other due to the lattice's chiral character. Moreover, it is observed that both acoustic modes rapidly become anisotropic in the  $\Gamma X$  direction, indicating a strong anisotropy, as shown in the dispersion contours. Additionally, two band-gaps with a significant width are evident between the third and fourth modes, and between the fifth and sixth modes, which may indicate coupling between these modes. Their surfaces appear almost flat around the origin.

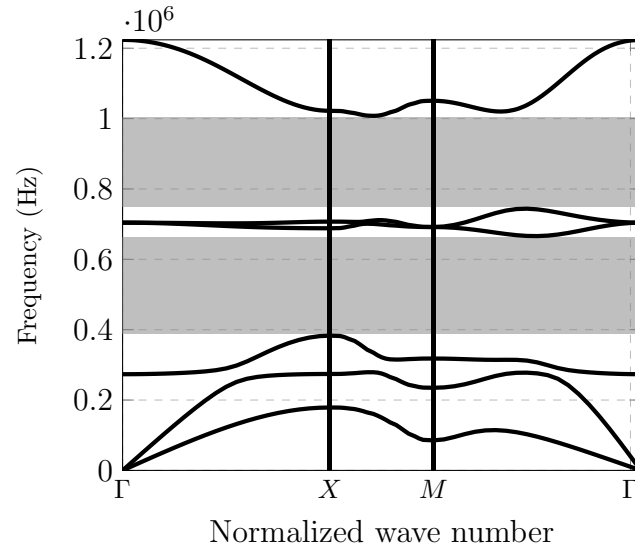


Figure 3.31: Dispersion curves for  $Z_4$  honeycomb lattice

The eigenmodes for each dispersion curve at the points  $\Gamma$ ,  $X$ , and  $M$  are illustrated in table 3.6. Similar to the previous cells, one can make similar observations. At  $\Gamma$ , the first two modes exhibit rigid body motion, while the third and fourth modes display local rotational motion. As the wavenumber increases, the behavior becomes increasingly complex, rapidly transitioning into anisotropy, and the deformation becomes significantly more pronounced. Particularly at  $X$ , we can observe a clear coupling between the transversal mode and the longitudinal mode. Less trivially, we observe a coupling between the longitudinal mode at point  $X$  and the first optical mode at  $\Gamma$ .

| Point    | Mode 1 | Mode 2 | Mode 3 | Mode 4 |
|----------|--------|--------|--------|--------|
| $\Gamma$ |        |        |        |        |
| $X$      |        |        |        |        |
| $M$      |        |        |        |        |

Table 3.5: First, second, third and fourth wave modes at high symmetry point  $\Gamma$ ,  $X$  and  $M$  of the IBZ (total displacement in m)

The phase and group velocities can be analyzed similarly, as shown in figure 3.36. As expected, the behavior is strongly anisotropic and exhibits similar patterns. At the first chosen frequency, anisotropic features start to emerge, aligning with the shape of the tetrachiral unit cell, indicating a significant anisotropy at both low and high frequencies. The rotational symmetries are preserved throughout this frequency range; however, the velocity pattern does not exhibit any mirror lines, as anticipated.

Additionally, one can observe that the apparent velocity patterns are tilted by an angle with respect to the reference frame. This angle is associated with the chiral parameter  $\beta$ , introduced in the first section devoted to the geometrical parameterization.

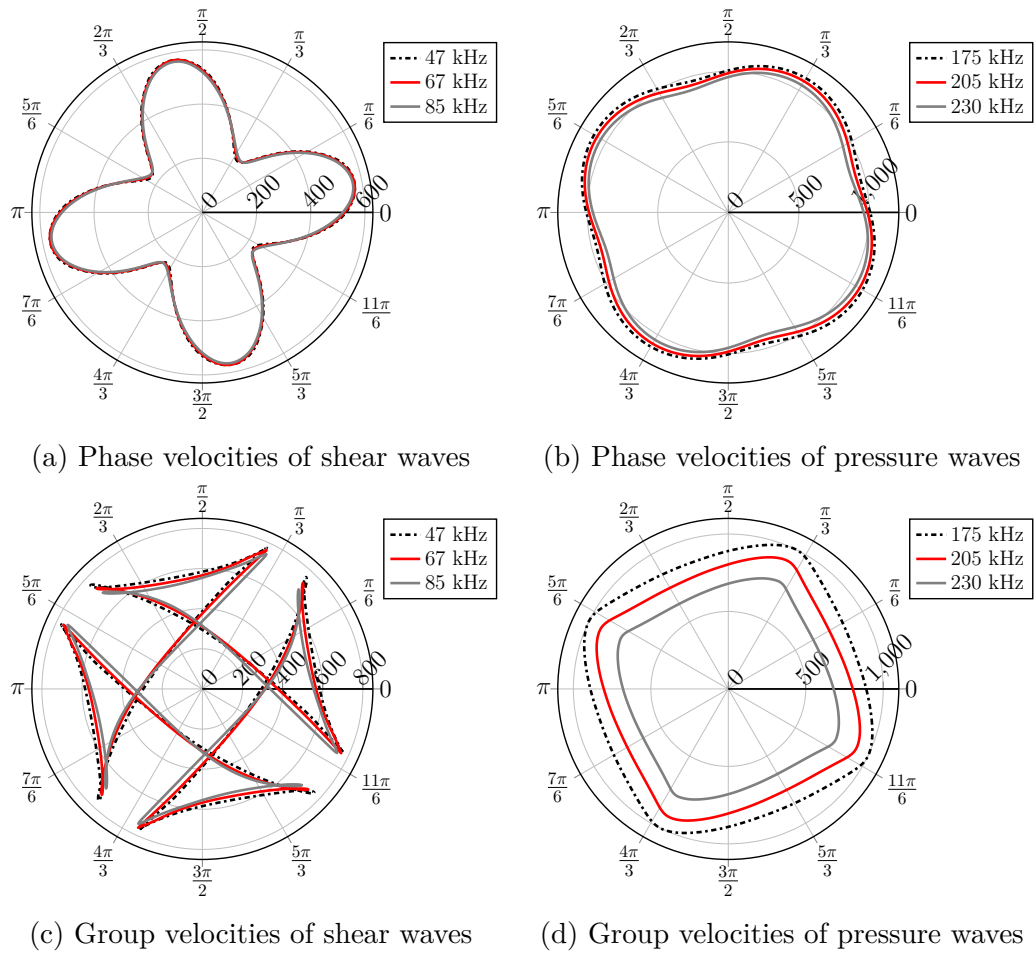


Figure 3.32: Phase and group velocities of the tetrachiral PAM

### Tetragonal lattice

Now, let's delve into the elastodynamic behavior of tetragonal architected materials, commonly referred to as the square lattice. ?? provides an illustration of the tiling corresponding to the geometric parameters outlined in table 3.1.

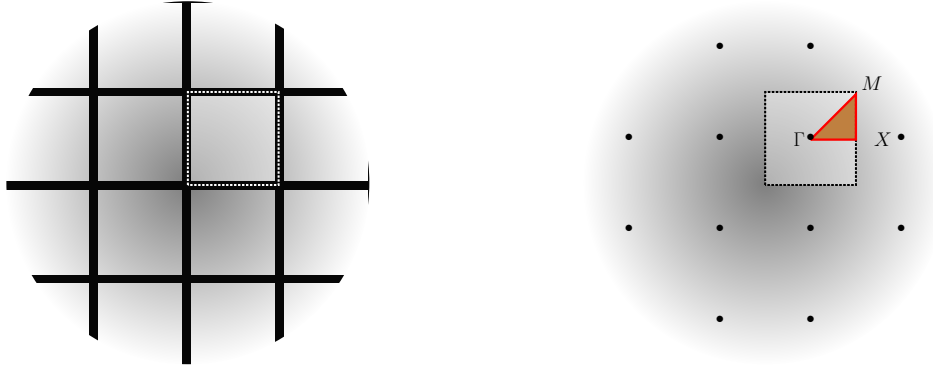


Figure 3.33: Left-hand figure : Tetragonal  $D_4$  lattice and its unit cell. Right-hand figure : First Brillouin zone (gray area), IBZ (brown area) and its contour (red triangle)

The Iso-frequency contours of the slowness surfaces depicted in figure 3.34 distinctly reveal the square symmetry inherent in the lattice, with four mirror lines observed in the contours. Similarly to the tetrachiral PAM, the contour curves of the slowness surfaces display four lobes, which are distinctly visible at both low and high frequencies, indicating a strong anisotropic behavior.

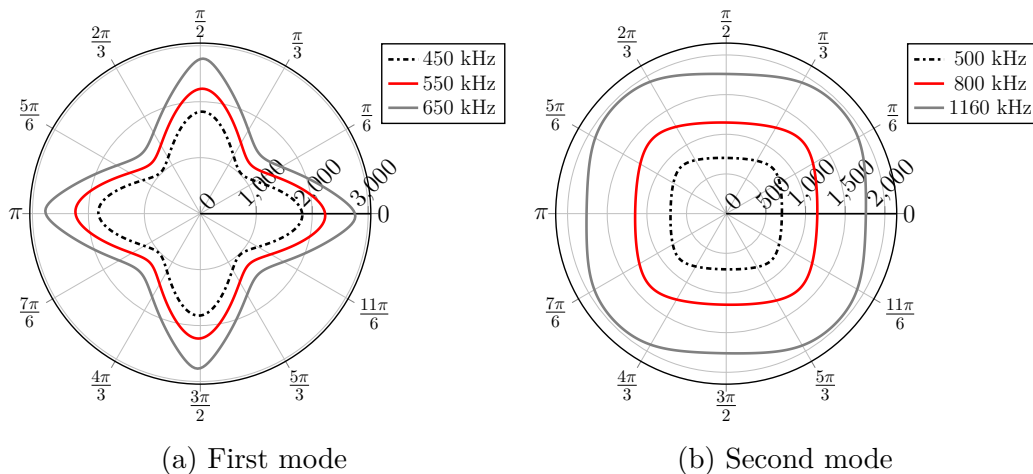


Figure 3.34: Iso-frequency countours of the first two slowness surfaces over IBZ

The dispersion diagram in figure 3.39, computed along the IBZ, reveals notable distinctions in the behavior of the first two modes within the IBZ. Similar to the hexagonal lattice, the acoustic branches appear noticeably distant from each other. Moreover, it is observed that both acoustic modes rapidly become anisotropic in the  $\Gamma X$  direction, indicating a strong anisotropy, as shown in the dispersion contours. Additionally, no band-gaps are observed, which may indicate the absence of coupling between the different modes.

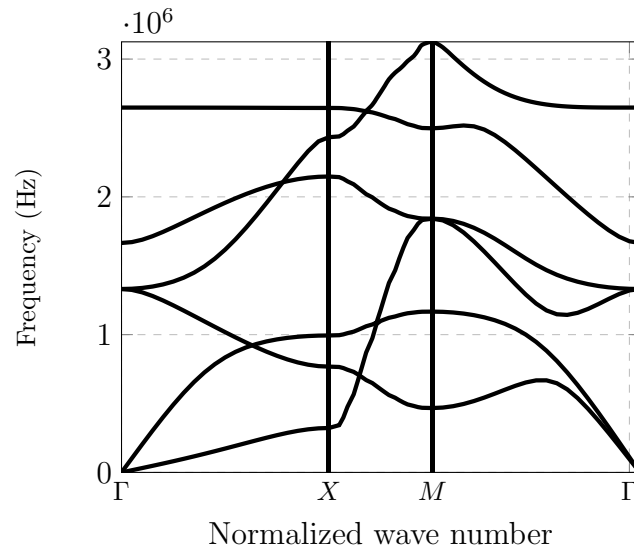


Figure 3.35: Dispersion curves for  $D_4$  honeycomb lattice

The eigenmodes for each dispersion curve at the points  $\Gamma$ ,  $X$ , and  $M$  are illustrated in ???. Similar to the previous cells, one can make similar observations. At  $\Gamma$ , the first two modes exhibit rigid body motion, while the third and fourth modes display local rotational motion. As the wavenumber increases, the behavior becomes increasingly complex, rapidly transitioning into anisotropy, and the deformation becomes significantly more pronounced. Particularly at  $X$ , we can observe a clear coupling between the rotational mode and the longitudinal mode.

| Point    | Mode 1 | Mode 2 | Mode 3 | Mode 4 |
|----------|--------|--------|--------|--------|
| $\Gamma$ |        |        |        |        |
| $X$      |        |        |        |        |
| $M$      |        |        |        |        |

Table 3.6: First, second, third and fourth wave modes at high symmetry point  $\Gamma$ ,  $X$  and  $M$  of the IBZ (total displacement in m)

The phase and group velocities can be analyzed similarly, as shown in ??. As expected, the behavior is strongly anisotropic and exhibits similar patterns. At the first chosen frequency, anisotropic features start to emerge, aligning with the shape of the tetragonal unit cell, indicating a significant anisotropy at both low and high frequencies. The rotational symmetries are preserved throughout this frequency range; Additionally, the velocity pattern exhibits four mirror lines, as anticipated.

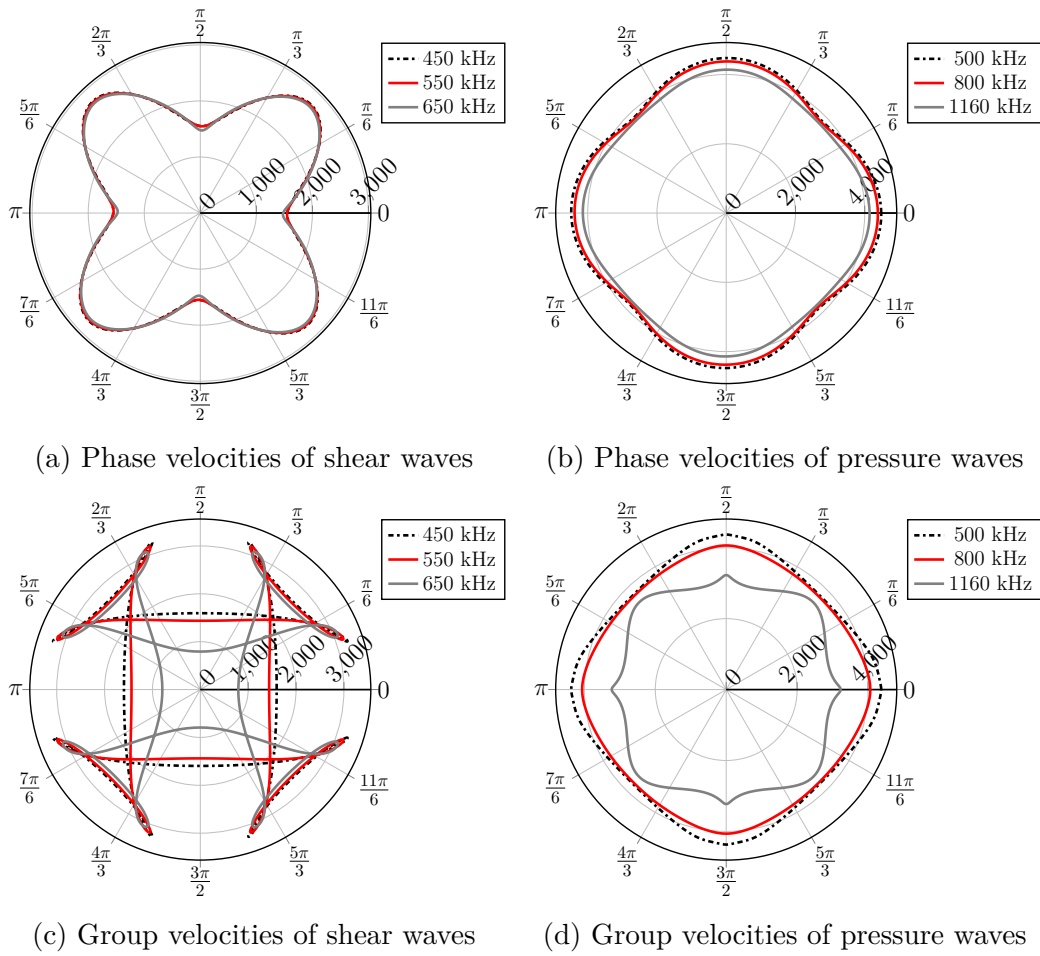


Figure 3.36: Phase and group velocities of the tetragonal PAM

### Trichiral lattice

Let's now explore the elastodynamic behaviour of trichiral PAM. Figure 3.37 illustrates the tiling associated with the geometric parameters described in table 3.1.

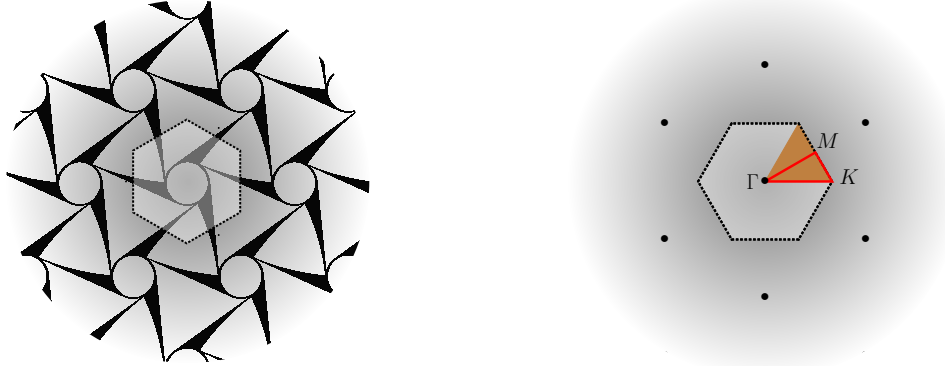


Figure 3.37: Left-hand figure : Trichiral  $Z_3$  lattice and its unit cell. Right-hand figure : First Brillouin zone (gray area), IBZ (brown area) and its contour (red triangle)

The slowness surfaces' iso-frequency contours shown in figure 3.38 clearly exhibit the trichiral symmetry inherent in the lattice. Similar to the hexachiral geometry, these contours feature six lobes, which become more prominent at higher frequencies. Additionally, the iso-frequency contour displaying a circular shape, associated with lower frequencies and wave numbers, indicates an isotropic elastodynamic behavior.

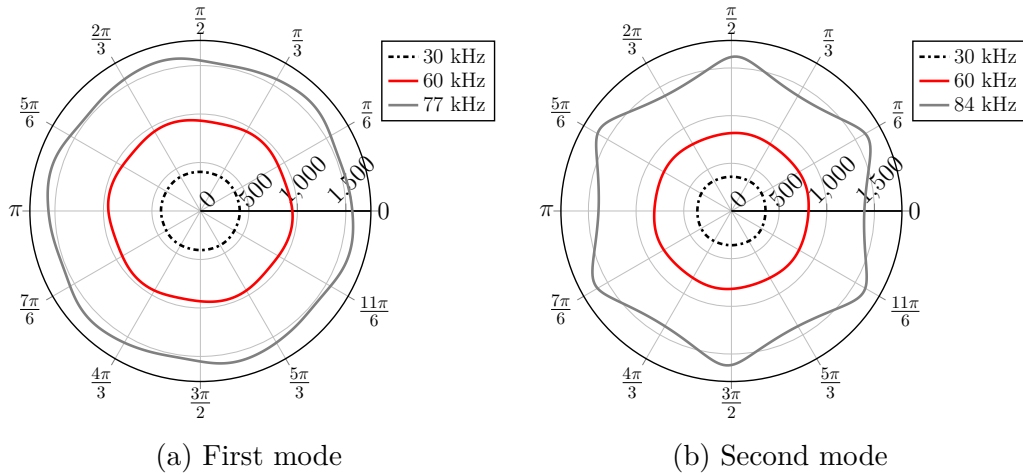
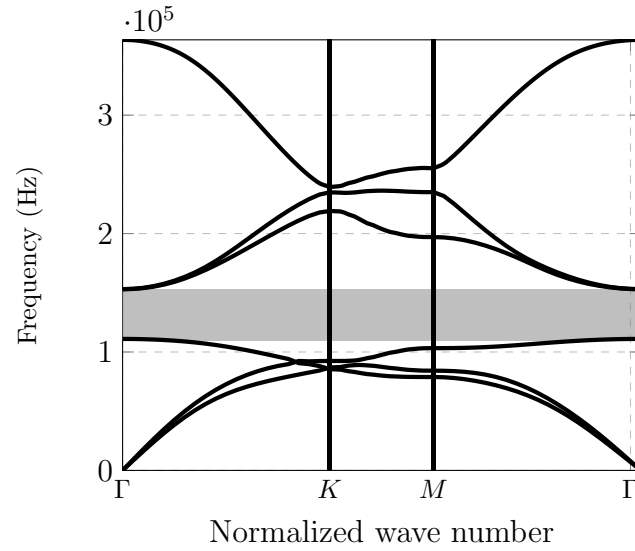


Figure 3.38: Iso-frequency countours of the first two slowness surfaces over IBZ

The dispersion diagram in ??, computed along the IBZ, reveals notable distinctions in the behavior of the first two modes within the IBZ, and the presence of one band-gap. Similar to the hexachiral lattice, the acoustic branches are slightly close to each other due to the lattice's chiral character. Moreover, it is observed that both acoustic modes rapidly become anisotropic in the  $\Gamma X$  direction, indicating a strong anisotropy, as shown in the dispersion contours. Additionally, a band-gap with a significant width is evident between the third and fourth modes, which may indicate coupling between these modes. Their surfaces appear almost flat around the origin.

The eigenmodes for each dispersion curve at the points  $\Gamma$ ,  $K$ , and  $M$  are illustrated in table 3.7. Similar to the previous cells, one can make similar observations. At  $\Gamma$ , the

Figure 3.39: Dispersion curves for  $Z_3$  honeycomb lattice

first two modes exhibit rigid body motion, while the third and fourth modes display local rotational motion. As the wavenumber increases, the behavior becomes increasingly complex, rapidly transitioning into anisotropy, and the deformation becomes significantly more pronounced. Particularly at  $K$ , we can observe a clear coupling between the rotational mode and the longitudinal mode. We can also observe many couplings between the third and fourth mode as expected from the dispersion diagram.

| Point    | Mode 1 | Mode 2 | Mode 3 | Mode 4 |
|----------|--------|--------|--------|--------|
| $\Gamma$ |        |        |        |        |
| $K$      |        |        |        |        |
| $M$      |        |        |        |        |

Table 3.7: First, second, third and fourth wave modes at high symmetry point  $\Gamma$ ,  $X$  and  $M$  of the IBZ (total displacement in m)

The phase and group velocities can be analyzed similarly, as shown in figure 3.40. As expected, the behavior is isotropic for the lowest frequency and become anisotropic for high frequencies, which reveals the anisotropy of the lattice. Notably, as the frequency increases, the phase velocity decreases. This behavior aligns with the dispersion branches where the slopes decrease as the wavenumber increases. The rotational symmetries are preserved throughout this frequency range; however, the velocities pattern does not exhibit any mirror lines, as anticipated. Furthermore, it is noticeable that the apparent velocity patterns exhibit a tilt at an angle relative to the

reference frame, due the chiral character of the geometry. Interestingly, the emerging pattern appears to resemble a six-fold pattern to some extent, rather than a three-fold pattern, which is less straightforward.

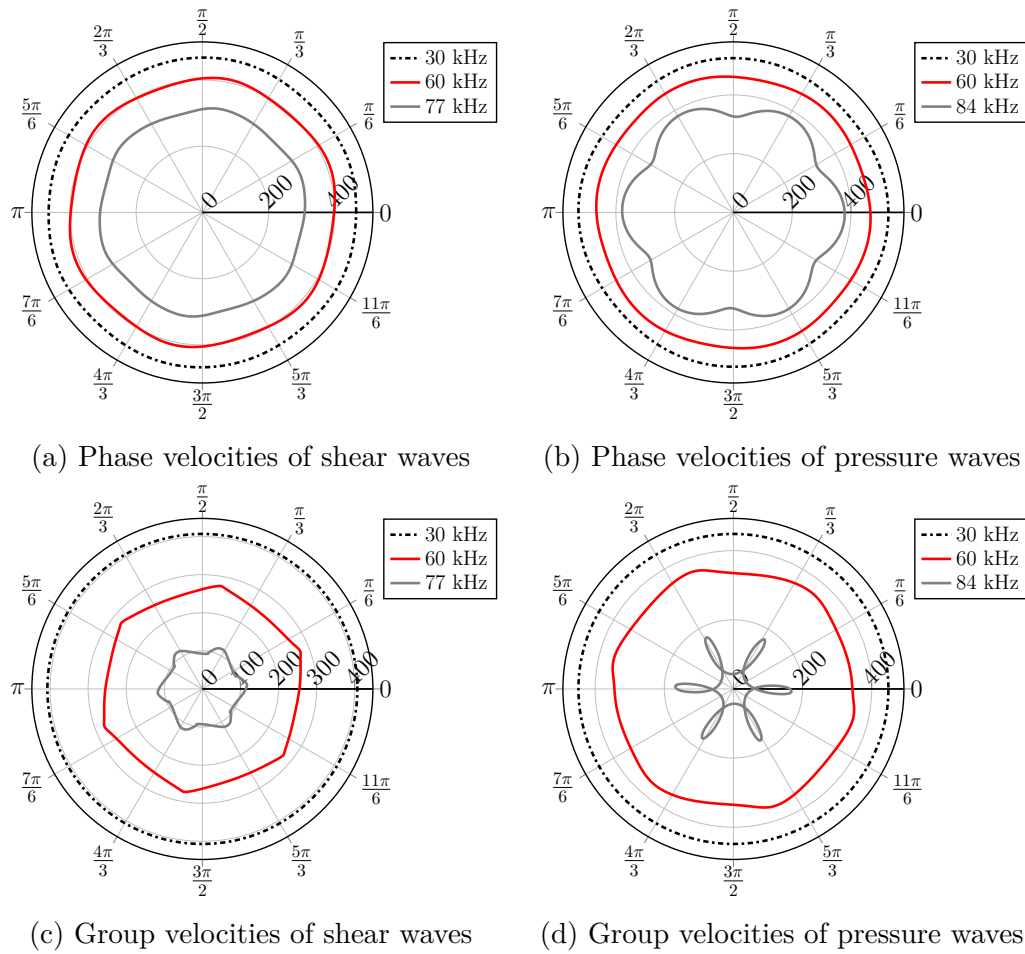


Figure 3.40: Phase and group velocities of the tetragonal PAM

### Trigonal lattice

Now, let's explore the elastodynamic behavior of trigonal PAM. Figure 3.41 provides an illustration of the tiling corresponding to the geometric parameters outlined in table 3.1.

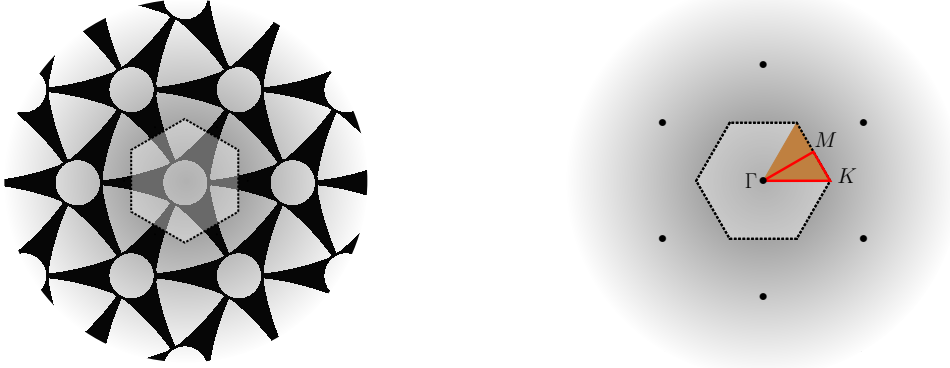


Figure 3.41: Left-hand figure : Trichiral  $D_3$  lattice and its unit cell. Right-hand figure : First Brillouin zone (gray area), IBZ (brown area) and its contour (red triangle)

The Iso-frequency contours of the slowness surfaces depicted in figure 3.42 distinctly reveal the trigonal symmetry inherent in the lattice, with six mirror lines observed in the contours. Similarly to the trichiral PAM, the contour curves of the slowness surfaces display six lobes, which are distinctly visible at both low and high frequencies, indicating a strong anisotropic behavior.

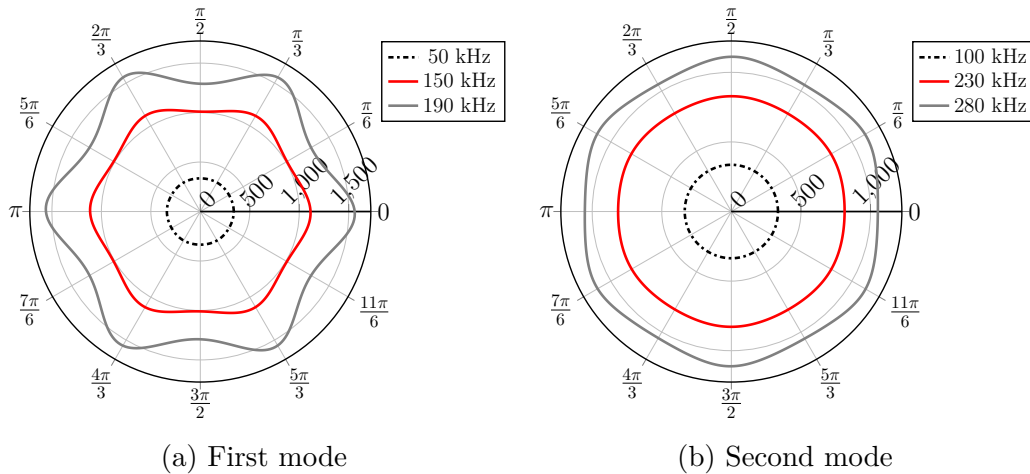


Figure 3.42: Iso-frequency countours of the first two slowness surfaces over IBZ

The dispersion diagram in figure 3.43, computed along the IBZ, reveals notable distinctions in the behavior of the first two modes within the IBZ, and the presence of one band-gap. Similar to the hexagonal lattice, the acoustic branches appear noticeably distant from each other, like in hexagonal lattice. Moreover, it is observed that both acoustic modes rapidly become anisotropic in the  $\Gamma K$  direction, indicating a strong anisotropy, as shown in the dispersion contours. Additionally, one band-gaps with a significant width is evident between the third and fourth modes, which may indicate coupling between these modes. A very interesting observation can be made regarding the symmetry of this cell. The proposed geometry here is both non-centrosymmetric

and achiral. However, the presence of band-gaps has typically been associated with the chiral nature of geometries. Yet, we observe the existence of one or more mode couplings in this case.

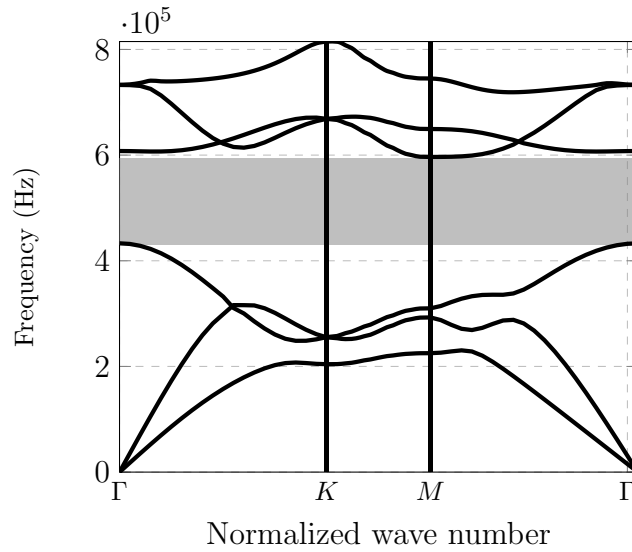


Figure 3.43: Dispersion curves for  $D_3$  honeycomb lattice

The eigenmodes for each dispersion curve at the points  $\Gamma$ ,  $K$ , and  $M$  are illustrated in table 3.8. Similar to the previous cells, one can make similar observations. At  $\Gamma$ , the first two modes exhibit rigid body motion, while the third and fourth modes display complex deformations. As the wavenumber increases, the behavior becomes increasingly complex, rapidly transitioning into anisotropy, and the deformation becomes significantly more pronounced.

| Point    | Mode 1 | Mode 2 | Mode 3 | Mode 4 |
|----------|--------|--------|--------|--------|
| $\Gamma$ |        |        |        |        |
| $K$      |        |        |        |        |
| $M$      |        |        |        |        |

Table 3.8: First, second, third and fourth wave modes at high symmetry point  $\Gamma$ ,  $K$  and  $M$  of the IBZ (total displacement in m)

The phase and group velocities can be analyzed similarly, as shown in figure 3.44. As expected, the behavior is isotropic for the lowest frequency and become anisotropic for high frequencies, which reveals the anisotropy of the lattice. The rotational symmetries are preserved throughout this frequency range and the velocities pattern exhibits six mirror lines, as anticipated. Interestingly, like in the trichiral lattice, the emerging

pattern appears to resemble a six-fold pattern to some extent, rather than a three-fold pattern, which is less straightforward.

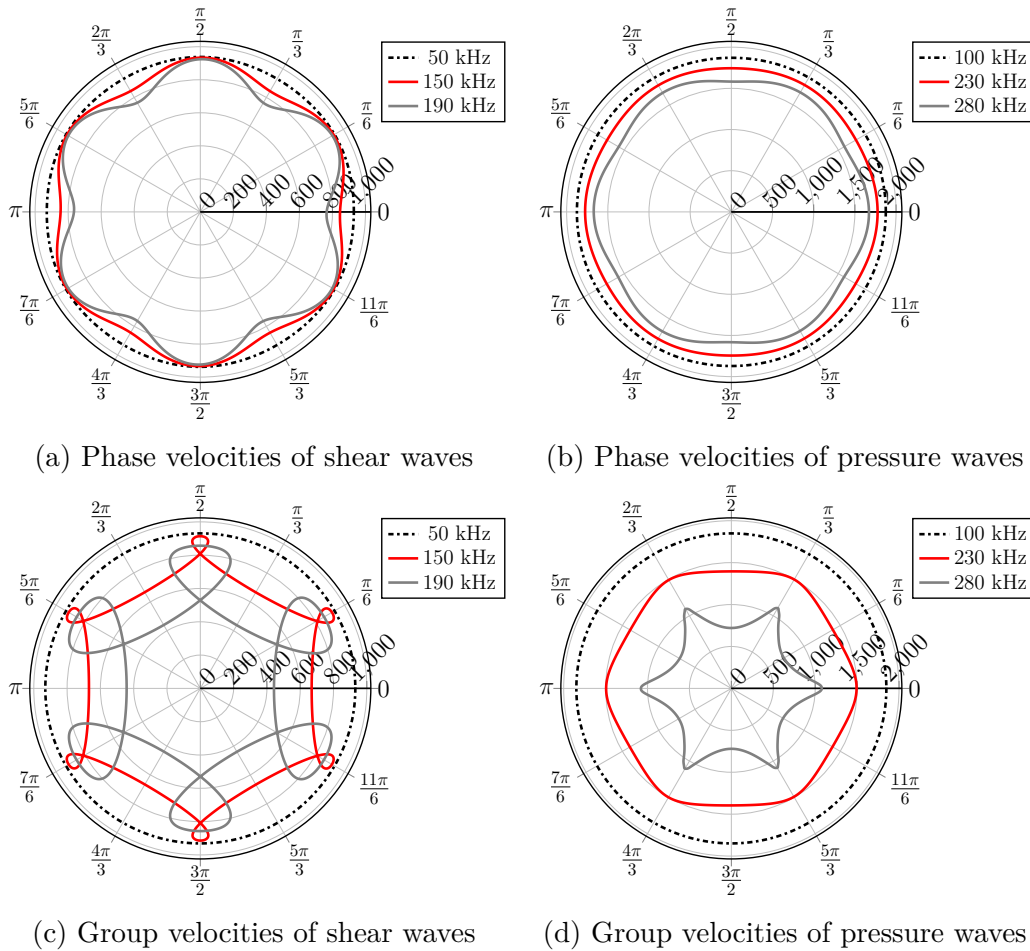


Figure 3.44: Phase and group velocities of the tetragonal PAM

The emergence of anisotropy in the high-frequency regime has often been considered as a contribution of stiffness. Indeed, as shown in [Rosi and Auffray, 2019], a second-gradient model can reproduce these effects that emerge in the SW-LF regime, where phase velocities can be seen as a sum of first-order and second-order contributions. The latter encodes the wave number dependence and, consequently, the frequency dependence. In [Askes and Aifantis, 2011], it was shown that this second-order contribution also depends on inertial terms and that it is important to incorporate these terms to have an accurate approximation of the medium's behavior. In the next section, we propose to investigate the effect of inertia on the response of the medium.

### 3.3.2 Investigation of anisotropic inertia contribution

The objective of this study is to investigate the influence of inertia on the behavior of a periodic heterogeneous medium and to quantify its contribution. To accomplish this, we will focus on a simplified scenario involving a periodic heterogeneous medium. Let  $\Omega$  denote the elementary cell of the medium, which is assumed to have a square pattern comprising two distinct linear phases,  $\Omega_1$  and  $\Omega_2$ , as illustrated in Figure 3.45. It is important to note that both phases possess the same stiffness but differ in their mass densities.

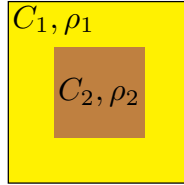


Figure 3.45: Unit cell of square composite

| $C_1 = C_2$ | $\rho_1 = \rho_2$ | $\rho_1 \neq \rho_2$     |
|-------------|-------------------|--------------------------|
| Reference   | Reference         | Anisotropic mass density |

In order to amplify effects, we consider a high inertial contrast between the matrix and the inclusion. The material parameters are reported in table 3.9.

| Phase     | E (Gpa) | $\nu$ | $\rho$ ( $kg.m^{-3}$ ) | density % |
|-----------|---------|-------|------------------------|-----------|
| Matrix    | 70      | 0.35  | 2700                   | 50        |
| Inclusion | 70      | 0.35  | 27000                  | 50        |

Table 3.9: Material properties

Figure 3.46 illustrates the dispersion diagram along the path  $\Gamma M$ . It clearly shows the emergence of anisotropy as the frequency increases. Interestingly, unlike the previous analysis with homogeneous stiffness, the P-waves are more significantly impacted compared to the S-waves.

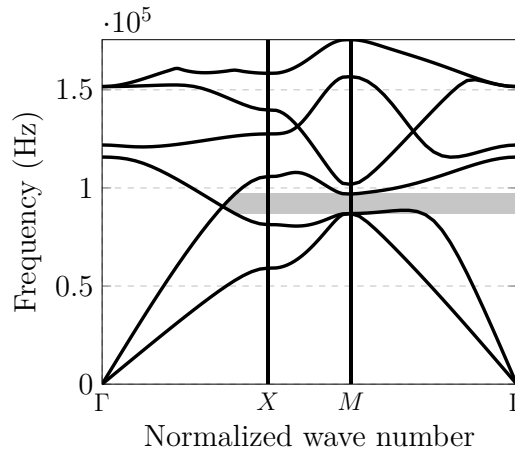


Figure 3.46: Dispersion curves of the first six modes

To further illustrate these effects, it is valuable to examine the iso-frequency contours of the slowness surfaces corresponding to the first two modes, for different values of wavelength. The idea here is to qualitatively assess from which wavelength the effects of inertial anisotropy appear. For this purpose, we will consider three different wavelengths, proportional to the size of the cell  $a$  :  $\lambda_1 = 50a, \lambda_1 = 6a, \lambda_1 = 4a$ .

The iso-frequency contours of the slowness surfaces shown in figure 3.47 indicate an isotropic behavior for  $\lambda_1$ . However, as the wavelength becomes comparable to the size of the cell, i.e., for short wavelengths (which is the case for  $\lambda_2$  and  $\lambda_3$ ), we notice that the shape of the contours is no longer circular but takes the form of square symmetry, indicating the emergence of anisotropic behavior.

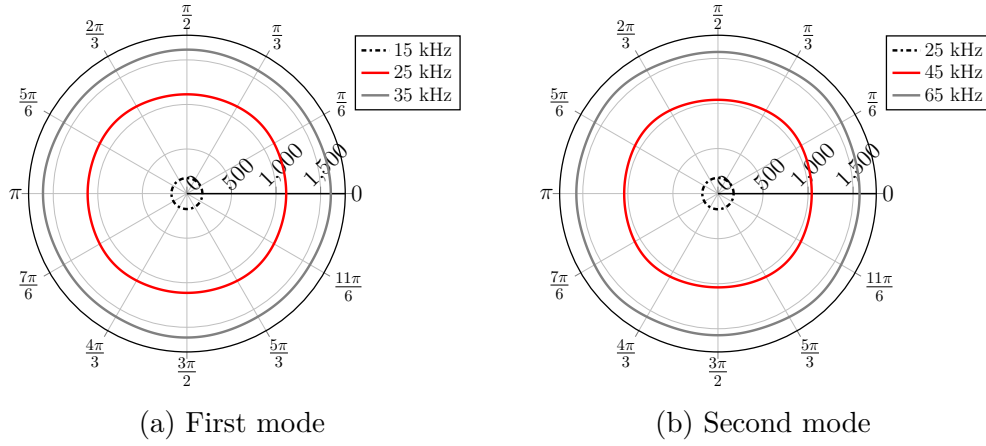


Figure 3.47: Iso-frequency countours of the first two slowness surfaces over IBZ

This observation can be further confirmed by computing the phase and group velocities associated with these two modes.

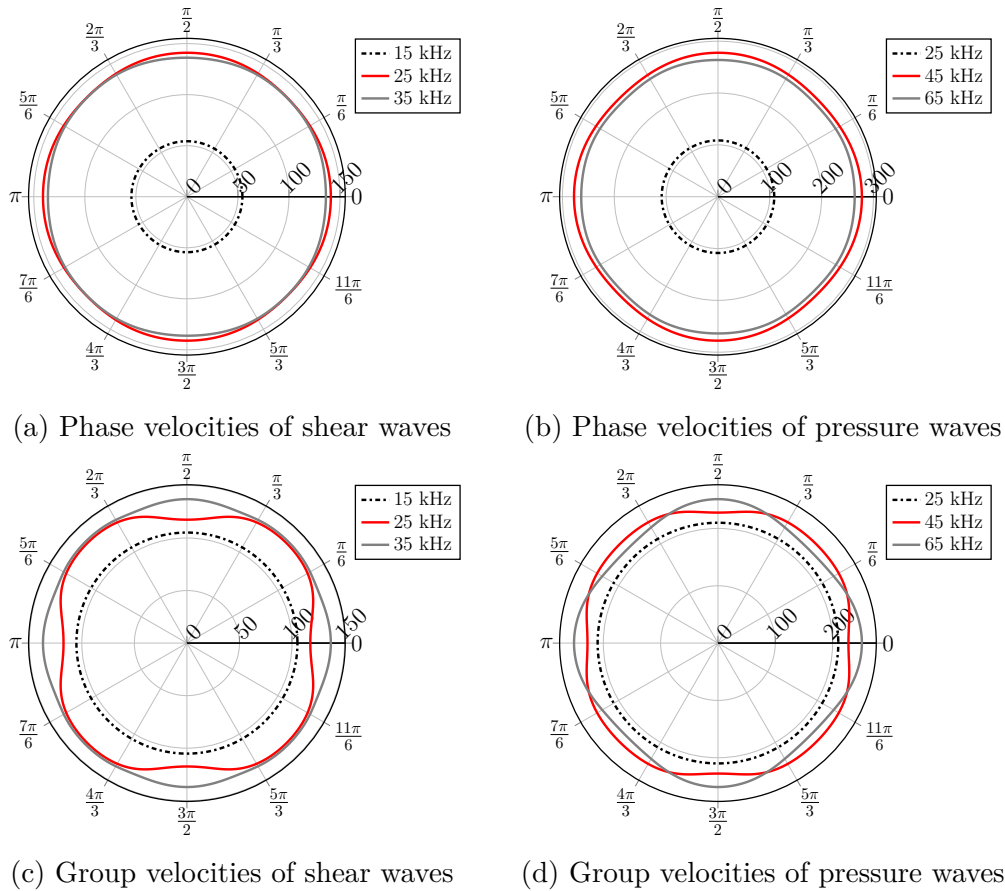


Figure 3.48: Phase and group velocities of the medium

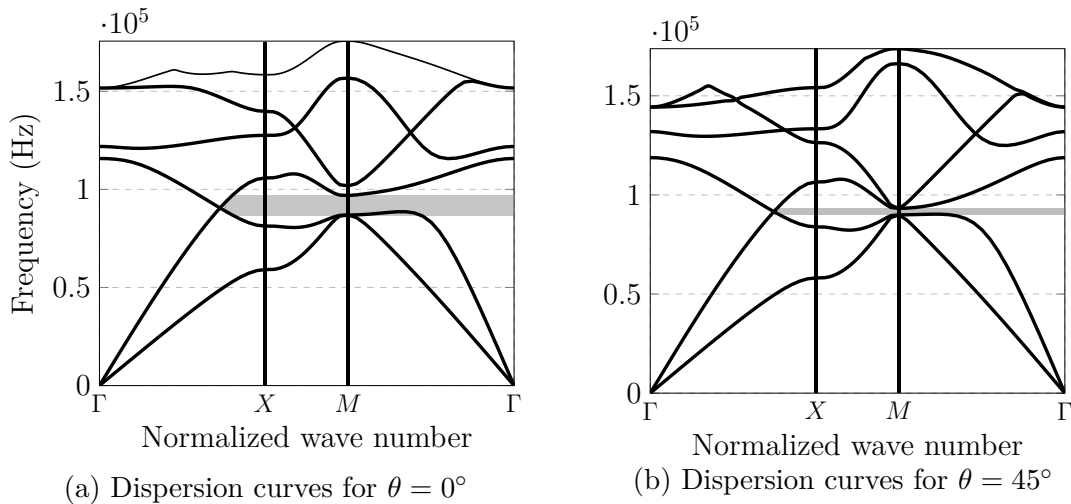
As illustrated in figure 3.48, we observe that at low frequencies, the propagation is isotropic, but it becomes anisotropic as the wave vector increases. The emerging anisotropy exhibits a tetragonal shape, which is consistent with the symmetry of the cell. Moreover, as anticipated from the dispersion diagram analysis, we find that P-waves are significantly more affected than S-waves. These observations qualitatively suggest that inertia plays a substantial role in the emergence of anisotropic effects, particularly when the wavenumber increases.

### Orientation effect

With that being said, one may question the impact of the inclusion's orientation. In the following analysis, we will explore a modified configuration of this medium, consisting of two phases. The first phase represents the fixed matrix, while the second phase represents the inclusion, which is capable of rotating within the cell. We will consider that both phases have different material properties. Two configurations should be considered: in the first one, the inclusion is not rotated with respect to the matrix, and this will serve as our reference configuration. In the second configuration, the inclusion will be rotated at an angle of  $\theta = 45^\circ$ .



Figure 3.49: The different configurations of the inclusion's orientation



The computed dispersion diagrams of the reference configuration shows the presence of a partial band-gap. We observe the same band-gap in the second configuration, but with a significantly smaller width. Indeed, rotating the inclusion with respect to the matrix in this case results in the emergence of intriguing effects, as shown in figure 3.51. The width of the band-gap can be controlled by the orientation of the cell, and thus, this effect is a direct consequence of a specific spatial distribution of the inertia network.

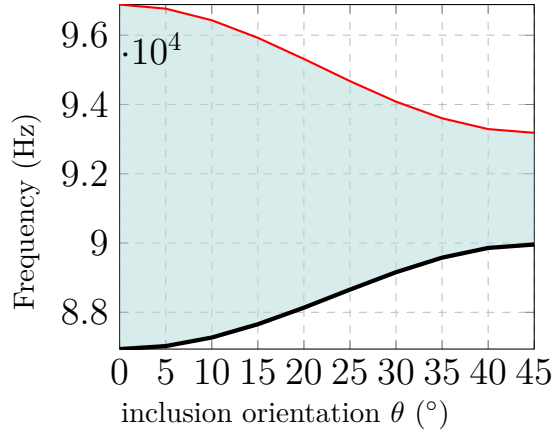


Figure 3.51: Evolution of the band gap with respect to inclusion's orientation

### 3.4 Determination of the appropriate kinematics extension

After studying the elastodynamic behavior of the different proposed PAMs, through the Floquet-Bloch analysis, we have established the elastodynamic signatures of each geometry, particularly focusing on the acoustic branches. It has been revealed that these materials exhibit different behaviors depending on the regime: isotropic behavior at low frequencies, anisotropic behavior at high frequencies, privileged directions of propagation, presence of band-gaps, and also mode couplings. The role of inertia has also been highlighted through numerical experiments. Now that we have all these elements, we need to address one of the questions posed at the end of Chapter 2, namely, which generalized model would better represent and predict the behavior of these media. Since we are only interested in the acoustic branches near the origin  $\Gamma$ , the optical modes will not be considered in determining an ideal candidate. Within this parameters window, i.e., LW-LF and SW-LF, we mainly observe dispersion, directivity, an absence of local rotation modes, but most importantly, higher-order anisotropy (4 and 6). Modeling the acoustic branches with a micromorphic-type model would be computationally expensive, which narrows down the choice to the Strain-gradient and Cosserat models. Since we do not require kinematic descriptors involving rotation, and the Cosserat medium, as mentioned in chapter 2, cannot account for higher-order anisotropy beyond 4 (due to Hermann's theorem), the ideal candidate would be the Strain-gradient model [Mindlin, 1964].

The constitutive law of the model was proposed in Chapter 2, and we will complement it with the inertia part, which appears essential to accurately describe the behavior. Let's define the Lagrangian density  $\mathcal{L}$  is defined as the difference between the kinetic and potential energy densities, respectively,  $\mathcal{K}$  and  $\mathcal{E}$ .

$$\mathcal{L} = \mathcal{K} - \mathcal{E}$$

In the case of Mindlin's Type II SGE theory, The kinetic and potential energies are are function of the displacement and its gradients up to the second-order :

$$\mathcal{E} := \frac{1}{2} (\boldsymbol{\sigma} : \boldsymbol{\varepsilon}) + \frac{1}{2} (\boldsymbol{\tau} \cdot \boldsymbol{\eta}), \quad \mathcal{K} := \frac{1}{2} (\mathbf{p} \cdot \dot{\mathbf{u}}) + \frac{1}{2} (\mathbf{q} : \dot{\mathbf{u}} \otimes \nabla),$$

wherein

- $\boldsymbol{\tau}$  : Hyper-stress tensor ( $3^{rd}$  order tensor);
- $\boldsymbol{\eta}$  : Gradient of the strain tensor;
- $\mathbf{p}$  : Momentum field ( $1^{st}$  order tensor);
- $\dot{\mathbf{u}}$  : Velocity field ( $1^{st}$  order tensor);
- $\mathbf{q}$  : Hyper-momentum tensor ( $2^{nd}$  order tensor);
- $\dot{\mathbf{u}} \otimes \boldsymbol{\nabla}$  : Gradient of the velocity field ( $2^{nd}$  order tensor).

are the primary and dual state tensors, already introduced in chapter 2 and recalled here for convenience. Taking into account this choice of variables, we define the total stress and the total momentum, respectively, as follows

$$\mathbf{s} = \boldsymbol{\sigma} - \boldsymbol{\nabla} \cdot \boldsymbol{\tau} \quad (3.4.1)$$

$$\boldsymbol{\pi} = \mathbf{p} - \boldsymbol{\nabla} \cdot \mathbf{q} \quad (3.4.2)$$

By application of the least action principle on the action functional [Mindlin, 1964], and neglecting body double force, the following bulk equations are obtained:

$$\boldsymbol{\nabla} \cdot \mathbf{s} = \dot{\boldsymbol{\pi}}, \quad (\sigma_{ij} - \tau_{ijk,k})_{,j} = \dot{p}_i - \dot{q}_{ij,j} \quad (3.4.3)$$

The constitutive law reads

$$\begin{aligned} p_i &= \rho \delta_{ip} v_p + K_{ipq} v_{p,q} \\ q_{ij} &= K_{pij} v_p + J_{ijpq} v_{p,q} \\ \sigma_{ij} &= C_{ijpq} \varepsilon_{pq} + M_{ijpqr} \eta_{pqr} \\ \tau_{ijk} &= M_{pqijk} \varepsilon_{pq} + A_{ijkpqr} \eta_{pqr} \end{aligned} \quad (3.4.4)$$

The constitutive law can be re-written in the following quadratic form

$$\begin{bmatrix} \mathbf{p} \\ \mathbf{q} \\ \boldsymbol{\sigma} \\ \boldsymbol{\tau} \end{bmatrix} = \begin{bmatrix} \rho \mathbf{I} & \mathbf{K} & \mathbf{0} & \mathbf{0} \\ \mathbf{K}^T & \mathbf{J} & \mathbf{0} & \mathbf{0} \\ \mathbf{0} & \mathbf{0} & \mathbf{C} & \mathbf{M} \\ \mathbf{0} & \mathbf{0} & \mathbf{M}^T & \mathbf{A} \end{bmatrix} \begin{bmatrix} \mathbf{v} \\ \mathbf{v} \otimes \boldsymbol{\nabla} \\ \boldsymbol{\varepsilon} \\ \boldsymbol{\eta} \end{bmatrix}$$

In which

- $\rho I_{(ij)}$  : Inertia tensor;
- $K_{ijk}$  : Coupling inertia tensor;
- $J_{(ij)(kl)}$  : Second order inertia tensor;
- $C_{(ij)(kl)}$  : Classical elasticity tensor;
- $M_{(ij)(kl)m}$  : Coupling elasticity tensor;
- $A_{(ij)k(lm)n}$  : Second order elasticity tensor.

The equation of motion reads,

$$C_{ijkl} u_{k,jl} + M_{ijklm}^{\#} u_{k,lmj} - A_{ijnklm} u_{k,lmnj} = \rho \ddot{u}_i + K_{ikl}^{\#} \ddot{u}_{k,l} - J_{ijkl} \ddot{u}_{k,lj} \quad (3.4.5)$$

where,

$$K_{ikl}^{\#} = (K_{ikl}^H - K_{kil}^H), \quad M_{ijklm}^{\#} = M_{ijklm}^H - M_{klmij}^H$$

As mentioned previously, classical elasticity is insensitive to chirality, whereas the sixth-order tensor exhibits sensitivity to chirality. Moreover, only odd-ranked tensors manifest sensitivity to the absence of centrosymmetry. The diverse effects captured by these tensors, i.e., their ability to describe certain phenomena, are summarized in the table below

|                              | # Symmetry classes | Dispersion | Non-centrosymmetry | Chirality |
|------------------------------|--------------------|------------|--------------------|-----------|
| $\rho \underline{I}_{(ij)}$  | 1                  | ✗          | ✗                  | ✗         |
| $\underline{C}_{(ij)(kl)}$   | 4                  | ✗          | ✗                  | ✗         |
| $\underline{J}_{(ij)(kl)}$   | 4                  | ✓          | ✗                  | ✗         |
| $\underline{A}_{(ij)k(lm)n}$ | 8                  | ✓          | ✗                  | ✓         |
| $\underline{M}_{(ij)(kl)m}$  | 4                  | ✓          | ✓                  | ✓         |
| $\underline{A}_{(ij)k(lm)n}$ | 8                  | ✓          | ✓                  | ✓         |

### 3.5 Synthesis

In this chapter, we have introduced a family of PAMs with different geometric symmetry properties, and we have explored their dynamic behavior through Floquet-Bloch analysis. The elastodynamic signature has revealed intriguing behaviors, including the presence of band-gaps, strong anisotropy, and privileged directions of propagation. We have also briefly investigated the role of inertia, particularly in a PAM with an anisotropic mass distribution, where the contribution of inertia in predicting dynamic behavior was highlighted.

In the context of homogenization, the choice of an EHM has led us to consider the Strain-gradient model as the optimal candidate under the assumptions of small deformations and propagation in the LW-LF and SW-LF regimes. Now that we have the elastodynamic signatures of the studied media and a generalized model that accurately approximates their behavior in the investigated regimes, the remaining question is: How do we identify the parameters of the constitutive law for this medium? As mentioned before, homogenization allows constructing an EHM when the scale separation is verified. In the next chapter, we will establish a phenomenological identification method that allows identifying the parameters of the constitutive law based on the information provided by the Floquet-Bloch analysis. This identification approach will be developed for the LW-LF regime and validated through comparison with elastostatic homogenization.

# Chapter 4

## Christoffel tensor based elastodynamic identification approach : LW-LF asymptotics

### Contents

---

|       |   |     |
|-------|---|-----|
| 4.1   | INTRODUCTION . . . . .  | 111 |
| 4.2   | THEORETICAL FRAMEWORK . . . . .   | 112 |
| 4.2.1 | HOMOGENEOUS EQUIVALENT MODEL IN LW-LF APPROX-<br>IMATION . . . . .          | 112 |
| 4.2.2 | CHRISTOFFEL TENSOR REVISITED . . . . .                                      | 114 |
| 4.3   | ELASTODYNAMIC IDENTIFICATION APPROACHES OF APPARENT<br>PROPERTIES . . . . . | 116 |
| 4.3.1 | POLARISATION-VELOCITY BASED APPROACH (PVBA) . . . . .                       | 117 |
| 4.3.2 | VELOCITY-BASED APPROACHES (VBA) . . . . .                                   | 118 |
| 4.4   | NUMERICAL VALIDATION . . . . .  | 122 |
| 4.4.1 | METHODOLOGY . . . . .   | 122 |
| 4.4.2 | RESULTS . . . . .   | 122 |
| 4.5   | SYNTHESIS . . . . .   | 127 |
| 4.6   | APPENDIX: ELASTOSTATIC HOMOGENIZATION . . . . .                             | 129 |
| 4.6.1 | INTRODUCTION . . . . .  | 129 |
| 4.6.2 | REPRESENTATIVE ELEMENTARY VOLUME . . . . .                                  | 129 |
| 4.6.3 | LOCALIZATION PROBLEM . . . . .  | 131 |
| 4.6.4 | AVERAGING FIELDS . . . . .  | 132 |

---

### 4.1 Introduction

By understanding the unique characteristics of periodic architected materials, one can develop a relevant strategy to study their effective behavior. One important question arises: How can we determine the effective properties based on the information obtained from Floquet-Bloch analysis? This question has already been addressed in the works of [Royer and Dieulesaint, 1999, François, 1995, Terroir, 2022], where an identification strategy based on wave velocities was proposed. However, the accuracy of this strategy remains a subject of inquiry as it relies on certain assumptions

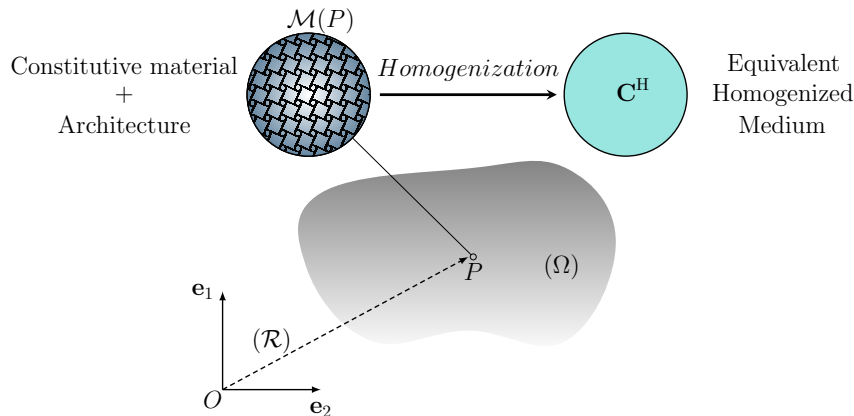
regarding the symmetry class of the medium and specific directions of propagation, thus some information concerning the effective might be lost. In addition, the algebraic structure of the Christoffel tensor, which plays a crucial role, has received limited attention in the literature. Exploring the algebraic features of this tensor can lead to the development of new identification strategies without assumptions on the symmetry class. It is essential to have a clear objective in mind and develop robust identification methods based on the invariants of the Christoffel tensor, which can be combined with experiments and techniques like topology optimization.

In this chapter, our focus will be on the signature of architected materials near the origin of the dispersion curve, specifically at long wavelengths. The objective is to revisit the identification method proposed in [Royer and Dieulesaint, 1999] by presenting different approaches based on available information such as velocities and polarizations. The first section aims to recall the general theoretical framework of wave propagation in the LW-LF regime. We will briefly introduce the Homogeneous Apparent Continuum (HAC) which, in the Long Wavelength-Low Frequency (LW-LF) regime, modeled as a classic Cauchy continuum. The second section will detail the parameterization of the Christoffel tensor using the harmonic decomposition of the classical elasticity tensor, introduced in chapter 2. This parameterization is crucial for the identification process described in section 3, where the invariants of the Christoffel tensor, will form the core of the identification process, offering a mathematical description of the anisotropy of the medium. Finally, in the last section, we will present numerical results obtained from the different identification approaches, including a comparison to elastostatic homogenization as it will be detailed in appendix.

## 4.2 Theoretical framework

### 4.2.1 Homogeneous equivalent model in LW-LF approximation

Let us consider a two dimensional domain  $\Omega$  occupied by a periodic heterogeneous medium whose elementary cell is denoted by  $\mathcal{T}$ . This cell consists of two phases made of Cauchy-type elastic material<sup>1</sup>.



It is well known that in the LW-LF regime a heterogeneous medium can be replaced

<sup>1</sup>In case of need, one of these phases can be degenerated to void in order to describe an hole.

by an equivalent homogeneous one [Boutin and Auriault, 1993, Nassar, 2015]. In this regime, the effective medium is generally considered of Cauchy type [Rosi et al., 2020]. In fact, when the wavelength is considerably longer than the size of the periodic unit cell, elastic waves travelling through the medium interact weakly with the internal architecture. Since the effective medium is homogeneous, the polarisation field  $\tilde{\mathbf{u}}$  is no longer space dependant. In other words, the Bloch waves have degenerated into plane waves. Thus, the solution of the motion equation 2.3.14 introduced in chapter 2 can be sought, in this specific regime, under the form

$$\mathbf{u}(\mathbf{x}, t) = \tilde{\mathbf{u}}e^{i(\omega t - \mathbf{k} \cdot \mathbf{x})}, \quad \mathbf{x} \in \Omega. \quad (4.2.1)$$

The main consequence is that, under LW-LF hypothesis the equation of motion 2.3.13 reduces to

$$\nabla \cdot \{ \mathbf{C}^{\text{hom}} : (\tilde{\mathbf{u}} \otimes^s \nabla) \} = -\omega^2 \rho^{\text{hom}} \tilde{\mathbf{u}}, \quad \mathbf{x} \in \Omega, \quad (4.2.2)$$

where in this equation  $\rho^{\text{hom}}$  denotes the effective density and  $\mathbf{C}^{\text{hom}}$  is the effective elasticity tensor. It is important to remark that  $\mathbf{C}^{\text{hom}}$  is the same as that obtained by classical elastostatic periodic homogenization as detailed later in Appendix [xx]. Within this regime, Equation 4.2.2 further simplifies into the classical Christoffel equation:

$$(\mathbf{n} \cdot \mathbf{C}^{\text{hom}} \cdot \mathbf{n}) \cdot \tilde{\mathbf{u}} = \rho^{\text{hom}} v_\phi^2 \tilde{\mathbf{u}}, \quad \tilde{\mathbf{u}} \in \mathbb{C}^2, \quad (4.2.3)$$

In which,  $\mathbf{n} = \mathbf{k} / \|\mathbf{k}\|$  is the unit vector giving the direction of propagation while  $v_\phi = \omega / \|\mathbf{k}\|$  is the phase velocity. In the present study, the wave vector is assumed to be real, which means that there is no attenuation during the propagation within the continuum. By setting

$$\forall \mathbf{n} \in \mathcal{S}^1, \quad \mathbf{\Gamma}(\mathbf{n}) = \mathbf{n} \cdot \mathbf{C}^{\text{hom}} \cdot \mathbf{n} \in \mathbb{S}^2(\mathbb{R}^2), \quad (4.2.4)$$

$\mathbf{\Gamma}$  can be seen a symmetric second-order tensor field over the unit 1-sphere  $\mathcal{S}^1$ . A point  $\mathbf{n} \in \mathcal{S}^1$  can be parameterised as

$$\mathbf{n}_\theta = \cos(\theta) \mathbf{e}_1 + \sin(\theta) \mathbf{e}_2 \quad (4.2.5)$$

and the notations  $\mathbf{\Gamma}(\mathbf{n})$  and  $\mathbf{\Gamma}(\theta)$  will be used indifferently. Further,  $\mathbf{\Gamma}$  will denote the tensor field, while  $\mathbf{\Gamma}(\theta)$  will designate the Christoffel tensor in the direction  $\theta$ . At the end, the Christoffel equation can be expressed as

$$\mathbf{\Gamma}(\theta) \cdot \tilde{\mathbf{u}} = \rho^{\text{hom}} v_\phi^2 \tilde{\mathbf{u}}. \quad (4.2.6)$$

This expression evidences the fact that the phase velocities  $\rho^{\text{hom}} v_\phi^2$  and the polarisation vectors  $\tilde{\mathbf{u}}$  are, respectively, the eigenvalues and the eigenvectors of  $\mathbf{\Gamma}(\theta)$ . The eigenvalues being the solutions of the equation

$$\det(\mathbf{\Gamma}(\theta) - \rho^{\text{hom}} v_\phi^2 \mathbf{I}) = 0. \quad (4.2.7)$$

which corresponds to the LW-LF version of the general dispersion equation (2.3.25). In the next sections, the solutions of equation (4.2.7) for different values of  $\theta$  will be used to determine  $\mathbf{C}^{\text{hom}}$ . To that aim let us first detail an adapted parameterisation of  $\mathbf{\Gamma}$ .

## 4.2.2 Christoffel tensor revisited

The aim of this subsection is to introduce a parameterisation of the Christoffel tensor field  $\mathbf{\Gamma}$  which is consistent with the symmetry properties of  $\mathbf{C}^{\text{hom}}$ . In order to tackle this problem, we will use some mathematical concepts concerning the symmetry classes of elasticity tensors in  $\mathbb{R}^2$ , which have been introduced in chapter 2. The central point is the harmonic decomposition which allows to express elasticity tensors according to their symmetry properties. This setting naturally induces a parameterisation of the tensor field  $\mathbf{\Gamma}$  and its invariants. The Christoffel tensor field will be constructed from the parameterisation  $\mathbf{C}^{\text{hom}} = \varphi(\mathbf{H}, \mathbf{h}, \alpha_2, \alpha_0)$  following the definition (4.2.4).

### Harmonic parameterisation of the Christoffel tensor field

Let us return to the definition of the Christoffel tensor field,

$$\mathbf{\Gamma}(\mathbf{n}; \mathbf{C}^{\text{hom}}) = \mathbf{n} \cdot \mathbf{C}^{\text{hom}} \cdot \mathbf{n} \quad (4.2.8)$$

in which the unit vector  $\mathbf{n}$  indicates the direction of propagation. This vector will be parameterised by an angle  $\theta$ , as expressed in equation (4.2.5), which will represent the angle between the direction of the wave propagation and the horizontal axis of the reference frame. Such setting is of particular interest since each direction of propagation will define a Christoffel tensor, activating specific components of  $\mathbf{C}^{\text{hom}}$ . Consequently, all the information about the apparent medium in the LW-LF regime is retrieved by propagating waves in different directions. From the harmonic decomposition of the elasticity tensor  $\mathbf{C}^{\text{hom}} = \varphi(\mathbf{H}, \mathbf{h}, \alpha_2, \alpha_0)$ , we obtain the following parameterisation of the Christoffel tensor field:

$$\mathbf{\Gamma}(\mathbf{n}_\theta; \mathbf{C}^{\text{hom}}) = (\mathbf{H} + \alpha_0 \mathbf{P}^2) \hat{\cdot} (\mathbf{n}_\theta \otimes \mathbf{n}_\theta) + \mathbf{h} + \left( \mathbf{h} \hat{\cdot} (\mathbf{n}_\theta \otimes \mathbf{n}_\theta) + \frac{1}{4} (\alpha_2 + 2\alpha_0) \right) \mathbf{I} \quad (4.2.9)$$

in which  $\hat{\cdot}$  denotes the twisted double contraction defined as

$$\mathbf{C} \hat{\cdot} (\mathbf{n} \otimes \mathbf{n}) = \mathbf{n} \cdot \mathbf{C} \cdot \mathbf{n}.$$

The intrinsic expression 4.2.9 is highly insightful, making almost straightforward the following deviatoric and spheric decomposition

$$\mathbf{\Gamma}(\mathbf{n}_\theta; \mathbf{C}^{\text{hom}}) = \frac{1}{2} \text{tr} [\mathbf{\Gamma}(\mathbf{n}_\theta; \mathbf{C}^{\text{hom}})] \mathbf{I} + \mathbf{\Gamma}^{\text{dev}}(\mathbf{n}_\theta; \mathbf{C}^{\text{hom}}), \quad (4.2.10)$$

with

$$\begin{cases} \text{tr} [\mathbf{\Gamma}(\mathbf{n}_\theta; \mathbf{C}^{\text{hom}})] = 2\mathbf{h} \hat{\cdot} (\mathbf{n}_\theta \otimes \mathbf{n}_\theta) + \frac{1}{2} (\alpha_2 + 2\alpha_0); \\ \mathbf{\Gamma}^{\text{dev}}(\mathbf{n}_\theta; \mathbf{C}^{\text{hom}}) = (\mathbf{H} + \alpha_0 \mathbf{P}^2) \hat{\cdot} (\mathbf{n}_\theta \otimes \mathbf{n}_\theta) + \mathbf{h}. \end{cases} \quad (4.2.11)$$

### Invariants of the Christoffel tensor field

As the orientation of a tensor varies over a manifold (here  $\mathcal{S}^1$ ), it is interesting to substitute its study for that of a collection of scalar fields over the same manifold. These scalar fields will be given by the elementary polynomial invariants of the Christoffel tensor as  $\theta$  varies. As we shall see, these fields contain all the information needed

to identify the elasticity tensor. Since  $\mathbf{\Gamma}(\theta)$  is a second-order symmetric tensor, its fundamental invariants are:

$$\mathcal{I}_1(\theta) = \text{tr}(\mathbf{\Gamma}), \quad \mathcal{K}_2(\theta) = \mathbf{\Gamma}^{\text{dev}} : \mathbf{\Gamma}^{\text{dev}} \quad (4.2.12)$$

There are many different possibilities for choosing the quadratic invariant, the one we retain here conduct to the simplest expression. Further has a strong physical content since its vanishing is associated with the equality of the wave velocities <sup>2</sup>. The invariants  $\mathcal{I}_1$  and  $\mathcal{K}_2$  can be expressed in terms of propagation speeds as follows

$$\begin{cases} \mathcal{I}_1(\theta) = \rho^{\text{hom}} (v_1^2(\theta) + v_2^2(\theta)) \\ \mathcal{K}_2(\theta) = \frac{1}{2} (\rho^{\text{hom}})^2 (v_1^2(\theta) - v_2^2(\theta))^2 \end{cases} \quad (4.2.13)$$

in which  $v_1(\theta)$  and  $v_2(\theta)$  are the phase velocities of the two waves propagating along the direction  $\theta$ , with  $v_1(\theta) \leq v_2(\theta)$ . Furthermore, expressing the invariants in terms of phase velocities (equation (4.2.13)) opens a wide range opportunities for identification. For instance, phase velocities can be obtained by solving the eigenvalue problem (4.2.6), or by means of experimental measures. In order to characterize the symmetry properties of  $\mathbf{\Gamma}(\mathbf{n}_\theta, \mathbf{C}^{\text{hom}})$ , the previous invariants need to be expressed in a explicit form. By using the harmonic parametrisation equation (4.2.11), these invariant functions can be expressed in terms of the harmonic decomposition of  $\mathbf{C}^{\text{hom}}$ :

$$\begin{cases} \mathcal{I}_1(\theta) = 2\mathbf{h} \hat{\cdot} (\mathbf{n}_\theta \otimes \mathbf{n}_\theta) + \frac{1}{2} (\alpha_2 + 2\alpha_0) \\ \mathcal{K}_2(\theta) = 2\alpha_0 \mathbf{H} :: (\mathbf{n}_\theta \otimes \mathbf{n}_\theta \otimes \mathbf{n}_\theta \otimes \mathbf{n}_\theta) + 2 \left( (\mathbf{H} + \alpha_0 \mathbf{P}^2) : \mathbf{h} \right) : (\mathbf{n}_\theta \otimes \mathbf{n}_\theta) + \frac{1}{4} (4i_2 + j_2 + 2\alpha_0^2), \end{cases} \quad (4.2.14)$$

where  $i_2$  and  $j_2$  are the invariants  $\mathbf{C}^{\text{hom}}$  as defined in equation (2.2.22). It can be observed that, as soon as  $\mathbf{C}^{\text{hom}}$  is, at least, tetragonal,  $\mathcal{I}_1(\theta)$  becomes an isotropic function. In other words, the sum of the square of phase velocities is independent of the direction of propagation<sup>3</sup>. The detailed expressions of these quantities are

$$\begin{aligned} \mathcal{I}_1(\theta) &= \alpha_0 + \frac{\alpha_2}{2} + 2h_1 \cos(2\theta) + 2h_2 \sin(2\theta) \\ \mathcal{K}_2(\theta) &= \left( 2(h_1^2 + h_2^2) + 2(H_1^2 + H_2^2) + \frac{\alpha_0^2}{2} \right) \\ &\quad + 2(2(h_1 H_1 + h_2 H_2) + h_1 \alpha_0) \cos(2\theta) + 2(2(h_1 H_2 - h_2 H_1) + h_2 \alpha_0) \sin(2\theta) \\ &\quad + 2H_1 \alpha_0 \cos(4\theta) + 2H_2 \alpha_0 \sin(4\theta) \end{aligned} \quad (4.2.15)$$

The previous expressions are given in the case of the complete anisotropic, and they take a much simpler form for higher symmetry classes. More precisely, if  $[\mathbf{G}_{\mathbf{C}^{\text{hom}}}]$  is

(1) Orthotropic:  $[\mathbf{D}_2]$

$$\begin{cases} \mathcal{I}_1(\theta) &= \alpha_0 + \frac{\alpha_2}{2} + 2h_1 \cos(2\theta) \\ \mathcal{K}_2(\theta) &= \left( 2h_1^2 + 2H_1^2 + \frac{\alpha_0^2}{2} \right) + 2(2h_1 H_1 + h_1 \alpha_0) \cos(2\theta) + 2H_1 \alpha_0 \cos(4\theta) \end{cases}$$

<sup>2</sup>Indeed, the nullity of  $\mathcal{K}_2(\theta)$  is associated with the equality of the wave velocities, and thus has a strong physical content.

<sup>3</sup>A direct consequence of that is that for tetragonal material, to the maximal value of  $v_2(\theta)$  corresponds the minimal value of  $v_1(\theta)$ .

(2) Tetragonal:  $[D_4]$

$$\begin{cases} \mathcal{I}_1(\theta) &= \alpha_0 + \frac{\alpha_2}{2} \\ \mathcal{K}_2(\theta) &= \left(2H_1^2 + \frac{\alpha_0^2}{2}\right) + 2H_1\alpha_0 \cos(4\theta) \end{cases}$$

(3) Isotropic:  $[O(2)]$

$$\begin{cases} \mathcal{I}_1(\theta) &= \alpha_0 + \frac{\alpha_2}{2} \\ \mathcal{K}_2(\theta) &= \frac{\alpha_0^2}{2} \end{cases}$$

We can also mention the shape for the  $R_0$ -orthotropy, an exotic set of elastic materials [Mou et al., 2023]

$$\begin{cases} \mathcal{I}_1(\theta) &= \alpha_0 + \frac{\alpha_2}{2} + 2h_1 \cos(2\theta) \\ \mathcal{K}_2(\theta) &= \left(2h_1^2 + \frac{\alpha_0^2}{2}\right) + 2h_1\alpha_0 \cos(2\theta) \end{cases}$$

In the following section, the parametrisation of the invariants 4.2.14 will be exploited to implement different algorithms for the identification of effective elastodynamic properties in the LW-LF regime. The application areas of these algorithms will be compared and then evaluated on synthetic data in the section 4.4.

### 4.3 Elastodynamic identification approaches of apparent properties

The aim of the present section is to introduce strategies to identify the effective elastodynamic properties of periodic architected material in the LW-LF regime. Although considered here from a theoretical point of view, these strategies are intended to be used in experimental settings.

Two situations will be successively considered corresponding to two different scenarios:

1. In the first scenario, we assume that mode shapes and wave velocities are available as input data for the identification algorithm. Although experimentally challenging, modal deformation measurement techniques are nevertheless possible. And this is a very active field of research with a significant development of field measurement techniques applied to the dynamic context.
2. The second scenario involves a more realistic data set limited to measurements of phase velocities for different propagation directions.

The starting point of both method is the harmonic decomposition of the effective elasticity tensor  $\mathbf{C}^{\text{hom}}$ :

$$\mathbf{C}^{\text{hom}} = \varphi(\mathbf{H}, \mathbf{h}, \alpha_2, \alpha_0).$$

In this approach no assumption is made regarding the symmetry class of  $\mathbf{C}^{\text{hom}}$ . Then, the Christoffel tensor field is expressed following the previous decomposition:

$$\mathbf{\Gamma}(\theta; \mathbf{C}^{\text{hom}}) = \mathbf{\Gamma}(\theta; \mathbf{H}, \mathbf{h}, \alpha_2, \alpha_0).$$

### 4.3.1 Polarisation-Velocity Based Approach (PVBA)

The method consists in reconstructing explicitly Christoffel tensors for several directions of propagation in order to obtain a linear system with respect to the harmonic components of  $\mathbf{C}^{\text{hom}}$ . The central formula exploited by this method is the spectral decomposition of the Christoffel tensor in the direction  $\theta$ :

$$\mathbf{\Gamma}(\theta; \mathbf{C}^{\text{hom}}) = \rho^{\text{hom}} \left( v_1^2(\theta) \hat{\mathbf{s}}_1 \otimes \hat{\mathbf{s}}_1 + v_2^2(\theta) \hat{\mathbf{s}}_2 \otimes \hat{\mathbf{s}}_2 \right) \quad (4.3.1)$$

in which  $\hat{\mathbf{s}}_i$  is the unit wave polarisation vector for the  $i$ -th mode. The knowledge of both velocities and polarisations gives then access to the complete Christoffel tensor. To identify  $\mathbf{C}^{\text{hom}}$  we use the following explicit parametrisation of  $\mathbf{\Gamma}$  in terms of the harmonic parameters of  $\mathbf{C}$ :

$$\mathbf{\Gamma}(\theta; \mathbf{C}^{\text{hom}}) = \mathbf{\Gamma}^{\text{sph}}(\theta; \mathbf{C}^{\text{hom}}) + \mathbf{\Gamma}^{\text{dev}}(\theta; \mathbf{C}^{\text{hom}}), \quad (4.3.2)$$

with

$$\left[ \mathbf{\Gamma}^{\text{sph}}(\theta; \mathbf{C}^{\text{H}}) \right] = \begin{bmatrix} \frac{\alpha_0}{2} + \frac{\alpha_2}{4} + h_1 \cos(2\theta) + h_2 \sin(2\theta) & 0 \\ 0 & \frac{\alpha_0}{2} + \frac{\alpha_2}{4} + h_1 \cos(2\theta) + h_2 \sin(2\theta) \end{bmatrix}_{\mathcal{B}} \quad (4.3.3)$$

and

$$\left[ \mathbf{\Gamma}^{\text{dev}}(\theta; \mathbf{C}^{\text{H}}) \right] = \begin{bmatrix} h_1 + \left( \frac{\alpha_0}{2} + H_1 \right) \cos(2\theta) + H_2 \sin(2\theta) & h_2 + H_2 \cos 2\theta - \left( \frac{\alpha_0}{2} - H_1 \right) \sin 2\theta \\ h_2 + H_2 \cos 2\theta - \left( \frac{\alpha_0}{2} - H_1 \right) \sin 2\theta & - \left( h_1 + \left( \frac{\alpha_0}{2} + H_1 \right) \cos(2\theta) + H_2 \sin(2\theta) \right) \end{bmatrix}_{\mathcal{B}} \quad (4.3.4)$$

#### PVBA identification algorithm

The identification problem consists in identifying the 6 unknowns  $(\alpha_0, \alpha_2, h_1, h_2, H_1, H_2)$ . Using the intermediate parameter  $\beta_0$ , the problem can be divided in two linear ones:

1. a first linear system in the unknown  $(\beta_0, h_1, h_2)$  and exploiting the first invariant given by 4.2.15 and 4.2.13 ;
2. a second linear system in the remaining unknown  $(\alpha_2, H_1, H_2)$  and exploiting the components of 4.3.2.

The set of angles to use should ensures the invertibility of both linear systems, this condition is generally satisfied if  $\theta_i \in [0, \pi[$ . These directions of propagation could be different from symmetry axes, which might be unknown. Without loss of generality, in this work we will use  $\theta = \{0, \frac{\pi}{4}, \frac{\pi}{2}\}$ . In this case  $\beta_0$  can be easily determined from the expression of the first invariant 4.2.15, and reads:

$$(S_0) : \beta_0 = \frac{1}{2} \left( \mathcal{I}_1(0) + \mathcal{I}_1\left(\frac{\pi}{2}\right) \right) \quad (4.3.5)$$

After computing  $\beta_0$ , the harmonic elements of  $\mathbf{h}$  are obtained

$$(S_{\mathbf{h}}) : \begin{cases} h_1 &= \frac{1}{4} \left( \mathcal{I}_1(0) - \mathcal{I}_1\left(\frac{\pi}{2}\right) \right) \\ h_2 &= \frac{1}{2} \left( \mathcal{I}_1\left(\frac{\pi}{4}\right) - \beta_0 \right) = \frac{1}{4} \left( -\mathcal{I}_1(0) + 2\mathcal{I}_1\left(\frac{\pi}{4}\right) - \mathcal{I}_1\left(\frac{\pi}{2}\right) \right) \end{cases} \quad (4.3.6)$$

Once the first sub-system is solved,  $\beta_0$ ,  $h_1$  and  $h_2$  can be substituted in the second sub-system 4.3.7. In the following, and for sake of simplicity, the component  $ij$  of  $\mathbf{\Gamma}(\theta; \mathbf{C}^{\text{hom}})$  will be denoted by  $\Gamma_{ij}(\theta)$ :

$$(S_{\mathbf{H}}) : \begin{cases} \Gamma_{11}\left(\frac{\pi}{2}\right) &= \frac{\alpha_2}{4} - H_1; \\ \Gamma_{12}\left(\frac{\pi}{4}\right) &= h_2 - H_1 - \frac{1}{2} \left( \beta_0 - \frac{1}{2}\alpha_2 \right); \\ \Gamma_{12}\left(\frac{\pi}{2}\right) &= h_2 - H_2. \end{cases} \quad (4.3.7)$$

Hence

$$(S_{\mathbf{H}}) : \begin{cases} \alpha_2 &= 2h_2 + \beta_0 - 2 \left( \Gamma_{12}\left(\frac{\pi}{4}\right) - \Gamma_{11}\left(\frac{\pi}{2}\right) \right); \\ H_1 &= \frac{\alpha_2}{4} - \Gamma_{11}\left(\frac{\pi}{2}\right); \\ H_2 &= h_2 - \Gamma_{12}\left(\frac{\pi}{2}\right); \end{cases} \quad (4.3.8)$$

Then, a direct expression of the harmonic decomposition of the apparent elasticity tensor has been obtained. The identification has required a complete set of data (velocity and polarisation) obtained for three directions of wave propagation. It is important to remark that no assumption has been necessary on the symmetry class of  $\mathbf{C}^{\text{hom}}$ . If more data are available, or in case of noisy-data set, this direct approach can be substituted by solving numerically two least-square identification problems.

### 4.3.2 Velocity-Based Approaches (VBA)

In this subsection the procedure introduced in the first subsection will be adapted to a situation in which we suppose that polarisation vectors are not available. As will be seen, the parameter identification problem is still solvable, but now it involves to solve a quadratic polynomial system. The solution of this system will be sought using two different approaches: a direct approach, introduced in section 4.3.2.1, and a Fourier based approach, in section 4.3.2.2. This last Fourier based formulation is very helpful in case of noise corrupted data since it allows to filter out high-frequency noise from the signal.

#### 4.3.2.1 Direct approach (VBA-D)

Without measuring the polarisation vectors, we cannot have access to the complete Christoffel tensor as in the previous subsection. Since the only information available are the measures of velocities for various directions of propagation, the Christoffel tensor field is only observable through its fields of invariants  $\mathcal{I}_1$  and  $\mathcal{K}_2$ .

### Identification algorithm

The approach is similar to the previous case and proceed in two steps by solving a waterfall system of equations:

1. the first system is linear, and identical to the first step of the PVBA method (4.3.5-4.3.6);
2. the second system, is fully constructed from the second invariant  $\mathcal{K}_2(\theta)$ . its resolution requires to find the roots of a  $2^{nd}$  degree polynomial system:

$$(S_{\mathbf{H}}) : \begin{cases} \mathcal{K}_2(0) &= 2(h_2 + H_2)^2 + 2\left(H_1 + h_1 + \frac{\alpha_0}{2}\right)^2 \\ \mathcal{K}_2\left(\frac{\pi}{4}\right) &= 2(h_1 + H_2)^2 + 2\left(H_1 - h_2 - \frac{\alpha_0}{2}\right)^2 \\ \mathcal{K}_2\left(\frac{\pi}{2}\right) &= 2(h_2 - H_2)^2 + 2\left(H_1 - h_1 + \frac{\alpha_0}{2}\right)^2 \end{cases} \quad (4.3.9)$$

Replacing  $h_1$  and  $h_2$  by their values in  $(S_{\mathbf{H}})$ , the resolution leads to the identification of the remaining components  $\alpha_0$ ,  $H_1$  and  $H_2$ . The use of a Gröbner basis [Cox et al., 2013] shows that this system is generically soluble<sup>4</sup>. For a generic elasticity tensor, we obtain a Gröbner basis comprising 10 polynomials of degree 2 in  $\mathbb{R}[H_2, H_1, \alpha_0]$ . The first polynomial of which is:

$$a_2(h_1, h_2)H_2^2 + b_2(h_1, h_2)H_2 + c_2(h_1, h_2) = 0$$

with

$$\begin{cases} a_2(h_1, h_2) = 64(h_1^2 + h_2^2) \\ b_2(h_1, h_2) = 16h_2\left(\mathcal{K}_2\left(\frac{\pi}{2}\right) - \mathcal{K}_2(0)\right) \\ c_2(h_1, h_2) = 64h_1^4 + 6h_1^2(4h_2^2 - \mathcal{K}_2(0) - \mathcal{K}_2\left(\frac{\pi}{2}\right)) + (\mathcal{K}_2(0) - \mathcal{K}_2\left(\frac{\pi}{2}\right))^2. \end{cases}$$

It can be observed that in section 4.3.2.1 the unknowns  $(H_1, \alpha_0)$  have been eliminated, hence it can be solved for  $H_2$  only. The solution is then used to determine  $H_1$ , using the second polynomial

$$a_1(h_1, h_2)H_1^2 + b_1(h_1, h_2)H_1 + c_1(h_1, h_2) = 0$$

with

$$\begin{cases} a_1(h_1, h_2) = 16h_1 \\ b_1(h_1, h_2) = 16h_2(H_2 - h_1) + 2\mathcal{K}_2\left(\frac{\pi}{2}\right) - 2\mathcal{K}_2(0) \\ c_1(h_1, h_2) = 8H_2(h_1^2 - h_2^2) + h_1\left(\mathcal{K}_2(0) + \mathcal{K}_2\left(\frac{\pi}{2}\right) - 2\mathcal{K}_2\left(\frac{\pi}{4}\right)\right) + h_2\left(\mathcal{K}_2(0) - \mathcal{K}_2\left(\frac{\pi}{2}\right)\right), \end{cases}$$

---

<sup>4</sup>Gröbner basis can be viewed as a non-linear extension of Gaussian elimination. The method is used here using Lexicographic order and ordering the variable as  $(H_2, H_1, \alpha_0)$ . The measured values  $\mathcal{K}_2(\theta_i)$ , are truncated and hence considered as elements of  $\mathbb{Q}$ .

the solution is then used to determine the remaining unknown  $\alpha_0$ . It can also be noticed that the coefficient of the leading terms vanish for elasticity tensor that are at least tetragonal. In such a degenerated situation, an alternate system should be used. In the case of noisy data, the analytical approach may have no solution at all, one should therefore solve a minimization problem with physical constraints such as the positive-definiteness of the apparent elasticity tensor.

#### 4.3.2.2 Fourier-series approach (VBA-F)

An alternative method consists in exploiting the periodicity of the fields of Christoffel's invariants. The idea behind this approach is to collect a large dataset of velocity measurements for various directions of propagation, with a given sampling interval. These measurements are then used to approximate the two invariants  $\mathcal{I}_1$  and  $\mathcal{K}_2$ . Since  $\mathcal{I}_1$  and  $\mathcal{K}_2$  are  $\pi$ -periodic functions of  $\theta$ , they can be represented by the following Fourier series expansions:

$$\mathcal{I}_1(\theta) = \sum_{n \in \mathbb{N}} (a_n \cos(2n\theta) + a'_n \sin(2n\theta)), \quad \mathcal{K}_2(\theta) = \sum_{n \in \mathbb{N}} (b_n \cos(2n\theta) + b'_n \sin(2n\theta)),$$

in which  $a_n$  and  $b_n$  are, respectively, the Fourier coefficients, given by

$$\begin{cases} a_n &= \frac{1}{\pi} \int_{-\pi/2}^{\pi/2} \mathcal{I}_1(\theta) \cos(2n\theta) d\theta, \\ a'_n &= \frac{1}{\pi} \int_{-\pi/2}^{\pi/2} \mathcal{I}_1(\theta) \sin(2n\theta) d\theta, \end{cases} \quad \begin{cases} b_n &= \frac{1}{\pi} \int_{-\pi/2}^{\pi/2} \mathcal{K}_2(\theta) \cos(2n\theta) d\theta, \\ b'_n &= \frac{1}{\pi} \int_{-\pi/2}^{\pi/2} \mathcal{K}_2(\theta) \sin(2n\theta) d\theta. \end{cases}$$

Projecting the expressions of  $\mathcal{I}_1$  and  $\mathcal{K}_2$  given by onto the the cosine and sine Fourier basis, one identifies the Fourier coefficients of each function

$$(S_{\mathcal{I}_1}) : \begin{cases} a_0 &= \alpha_0 + \frac{\alpha_2}{2} \\ a_1 &= 2h_1 \\ a'_1 &= 2h_2 \end{cases}, \quad (S_{\mathcal{I}_2}) : \begin{cases} b_0 &= 2(h_1^2 + h_2^2) + 2(H_1^2 + H_2^2) + \frac{\alpha_0^2}{2} \\ b_1 &= 2(2(h_1 H_1 + h_2 H_2) + h_1 \alpha_0) \\ b'_1 &= 2(2(h_1 H_2 - h_2 H_1) + h_2 \alpha_0) \\ b_2 &= 2H_1 \alpha_0 \\ b'_2 &= 2H_2 \alpha_0 \end{cases} \quad (4.3.10)$$

with

$$a_n = a'_n = 0, \forall n > 1 \quad \text{and} \quad b_n = b'_n = 0, \forall n > 2.$$

The previous invariant functions can be rewritten as

$$\begin{cases} \mathcal{I}_1(\theta) &= a_0 + a_1 \cos(2\theta) + a'_1 \sin(2\theta), \\ \mathcal{K}_2(\theta) &= b_0 + b_1 \cos(2\theta) + b'_1 \sin(2\theta) + b_2 \cos(4\theta) + b'_2 \sin(4\theta). \end{cases}$$

### Identification algorithm

The main point of this approach is the calculation of the Fourier series coefficients of  $\mathcal{I}_1$  and  $\mathcal{K}_2$  from the data set. For this purpose, the interval  $[0, \pi]$  must be sampled, and the wave velocities measured for each of the sample points. From a numerical point of view, the finer the sampling, the better the evaluation of the coefficients. Let  $N$  be the number of samples per period  $T = \pi$ , the minimum-sampling rate required to reconstruct properly  $\mathcal{I}_1$  and  $\mathcal{K}_2$  is given by the Nyquist–Shannon sampling theorem

$$N \geq \frac{2\max\{f_{1,\max}, f_{2,\max}\}}{T},$$

where  $f_{1,\max} = 1/\pi$  and  $f_{2,\max} = 2/\pi$  are, respectively, the highest spatial frequencies of  $\mathcal{I}_1$  and  $\mathcal{K}_2$ . Taking into account the condition above, The number of minimally required measures need is at least  $N_{\min} = 4$ . Let us now consider a sampling of  $\mathcal{I}_1$  and  $\mathcal{K}_2$  on the interval  $[0, \pi]$  and let us denote by  $\mathcal{I}_{1,i}$  and  $\mathcal{K}_{2,i}$ , respectively, the discrete values of the function in the  $i$  direction:

$$\mathcal{I}_{1,i} = \mathcal{I}_1(\theta_i), \quad \mathcal{K}_{2,i} = \mathcal{K}_2(\theta_i), \text{ with } i \in \llbracket 0, N - 1 \rrbracket,$$

where  $\{\theta_i = \frac{2i\pi}{N}\}_{i \in [0, N-1]}$  is a set of  $N$  equally spaced points corresponding to the directions of propagation, with  $N \geq 4$ . One can write,

$$\begin{cases} a_n \approx \frac{1}{N} \sum_{j=0}^{N-1} \mathcal{I}_1(\theta_j) \cos(2n\theta_j), \\ a'_n \approx \frac{1}{N} \sum_{j=0}^{N-1} \mathcal{I}_1(\theta_j) \sin(2n\theta_j), \end{cases} \quad \begin{cases} b_n \approx \frac{1}{N} \sum_{j=0}^{N-1} \mathcal{K}_2(\theta_j) \cos(2n\theta_j), \\ b'_n \approx \frac{1}{N} \sum_{j=0}^{N-1} \mathcal{K}_2(\theta_j) \sin(2n\theta_j). \end{cases}$$

The mean value of  $\mathcal{I}_1$  corresponds to the isotropic parameter  $\beta_0$ . Further, the components  $h_1$  and  $h_2$  are directly obtained from the above Discrete Fourier Transform (DFT) of  $\mathcal{I}_1$ . Once these coefficients are computed, as well as in the first approach, one can set a system of equations for identifying the remaining parameters. Now, for a generic elasticity tensor, we use the expression of  $a_1$ ,  $a'_1$ ,  $b_1$  and  $b'_1$  given by equation (4.3.10), to recast the expression of  $b_0$  into the following second order equation in  $\alpha_0^2$

$$\alpha_0^4 - 2 \left( b_0 - (a_1^2 + a_1'^2) \right) \alpha_0^2 + (b_2^2 + b_2'^2) = 0. \quad (4.3.11)$$

The latter equation admits 4 solutions but only one solution is retained. The solution must satisfy the condition of definite-positiveness of the apparent elasticity tensor and must be positive since  $\alpha_0$  is an isotropic parameter. Finally,  $H_1$  and  $H_2$  are then directly obtained for this solution using the expression of  $b_1$  and  $b'_1$  in equation (4.3.10).

The Fourier-series based identification approach offers a significant advantage by projecting the discrete Fourier series of the invariants  $\mathcal{I}_1$  and  $\mathcal{K}_2$  onto the cosine and sine Fourier basis. This projection process efficiently eliminates and filters out any potential noise that could compromise the accuracy of the measured data. As a result, the method naturally filters the data by removing higher-order harmonic contributions present in the signals, specifically those above order 2 in the signals of  $\mathcal{I}_1$  and above order 4 in the signals of  $\mathcal{K}_2$ . This noise-filtering property of the approach allows for the identification of the harmonic decomposition elements with an improved accuracy and reliability.

## 4.4 Numerical validation

The identification procedure presented in section 4.3 requires the knowledge of the phase velocities (for VBA-D and VBA-F) and polarizations (for PBA), of plane waves propagating within the architected material towards different directions. In the present work, in order to give a first validation of the methods, the procedure will be tested using data from Finite Elements Method (FEM) simulations. However, it is important to remark that the procedure is general, and can be also implemented experimentally, for instance using dynamic Digital Image Correlation (DIC) [Schaeffer et al., 2017].

### 4.4.1 Methodology

In this section, the methodology used to implement the identification procedure will be sketched. The details about each step, as well as an example of implementation, will be given in the next subsection. The first step of the procedure is the choice of the input, which consists in the geometry of the unit cell, complemented by the constitutive properties of the materials. The microstructure may contain several different phases, one of which may describe the void. The only restriction is that the phase describing the void cannot be connected. Then, once these parameters have been fixed, a FEM code is used to compute the propagation characteristics, i.e. phase velocities and polarizations, needed to provide data for the identification procedure. The computation is performed on the unit cell, considering periodic Floquet-Bloch boundary conditions. Then, the three different approaches are used to retrieve the invariants of  $\mathbf{C}$ , as well as an orientation angle, thus identifying the apparent material  $\mathbf{C}^{\text{app}}$ . Subsequently, a validation procedure is performed to ensure the correctness of the results. This consists in injecting  $\mathbf{C}^{\text{app}}$  in the Christoffel equation for the homogeneous material (equation (4.2.5)) and comparing to the results for full field FEM simulation. In case the validation fails, the computation of the propagation characteristics can be repeated, for instance by considering a different set of propagation directions for the plane waves. If the validation succeeds, the final output is given by considering that  $\mathbf{C}^{\text{eff}} = \mathbf{C}^{\text{app}}$ . The procedure is schematically presented in figure 4.1.

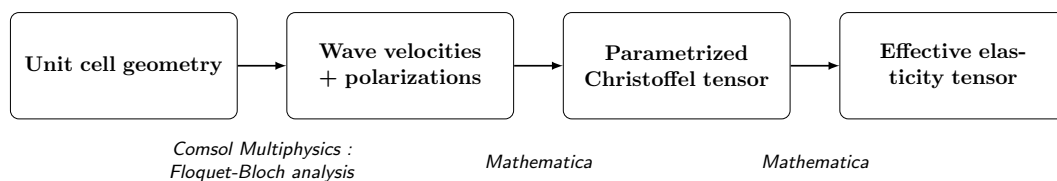


Figure 4.1: Schematic of elastodynamic homogenisation method

### 4.4.2 Results

In this subsection, we perform the procedure using the three approaches for the specific set of periodic architected materials introduced in chapter 3. As mentioned before in chapter 2, the choice of the unit cells is performed in order to explore the different symmetry classes of the constitutive tensor  $\mathbf{C}^{\text{app}}$ .

If we consider the point group  $G_{\mathcal{M}}$  of an infinite periodic material, i.e. the set of vectorial isometries that let the material invariant, the Curie-Neumann's principle can be stated as follows

$$G_{\mathcal{M}} \subset G_{\mathbf{C}^{\text{app}}}. \quad (4.4.1)$$

The meaning of equation (4.4.1) is that a transformation  $\mathbf{g}$  that let  $\mathcal{M}$  invariant is a symmetry transformation of  $\mathbf{C}^{\text{app}}$ . As a result, we can map the different symmetry classes of the periodic architected material into those of the continuum equivalent material. At this stage, and as already pointed out, it is important to note that the framework of Cauchy elasticity does not allow to investigate the effects related to the chirality, or lack of centrosymmetry. In order to account for these characteristics, a generalised continuum framework such as SGE should be considered [Auffray et al., 2015, Auffray et al., 2018].

| Name                            | Digonal               | Orthotropic | Tetragonal     | Isotropic                    |
|---------------------------------|-----------------------|-------------|----------------|------------------------------|
| $[G_{\mathcal{M}}]$             | $[\mathbf{1}], [Z_2]$ | $[D_2]$     | $[Z_4], [D_4]$ | $[Z_3], [D_3], [Z_6], [D_6]$ |
| $[G_{\mathbf{C}^{\text{hom}}}]$ | $[Z_2]$               | $[D_2]$     | $[D_4]$        | $[O(2)]$                     |

Table 4.1: Symmetry classes

In this work, we investigate representative lattice geometries belonging to each subgroup of  $G_{\mathcal{M}}$ . These PAMs are presented in figure 4.2. The unit cell of each PAM is a two-dimensional solid modelled under plane strain hypothesis. In terms of constitutive materials, each lattice is modelled as a linear elastic and isotropic material, with the properties corresponding to the aluminium (Young's modulus  $E = 70$  GPa, Poisson ratio  $\nu = 0.33$  and volume mass density  $\rho = 2700$  kg/m<sup>3</sup>). All unit cells have the same size ( $a = 1$  mm). In a first time we consider the same volume fraction ( $\approx 33\%$ , as in figure 2.8), but later in this work a parametric study with respect to this volume fraction will be also presented. For chiral geometries, the dimensionless geometrical parameter related to the thickness of the ligaments and the radius of the rings, as defined in [Spadoni et al., 2009], is fixed to  $\beta = 0.38$ .

We briefly recall here that the main idea of Floquet-Bloch analysis consists in computing the propagation characteristics (phase velocities and polarizations) by solving the elastodynamic problem over the unit cell. Periodic boundary conditions, namely Floquet-Bloch boundary conditions, are used to take into account the infinite nature of the lattice. It allows to impose on the boundaries of the unit cell a displacement that corresponds to a Bloch wave and solving the equation (2.3.25) for a given wavevector  $\mathbf{k}$ . Consider for instance, the translation vectors  $\mathbf{v}_1 = a\mathbf{e}_1$  and  $\mathbf{v}_2 = a\mathbf{e}_2$  respectively, in the two directions of the lattice  $\mathbf{e}_1$  and  $\mathbf{e}_2$ , with  $a$  the size of the unit cell, the Floquet-Bloch boundary condition reads <sup>5</sup> :

$$\mathbf{u}_{\mathbf{k}}(\mathbf{x} + \mathbf{v}_i, t) = \mathcal{R} \left( \tilde{\mathbf{u}}_{\mathbf{k}}(\mathbf{x} + \mathbf{v}_i) e^{i(\omega t - \mathbf{k} \cdot (\mathbf{x} + \mathbf{v}_i))} \right) = \mathbf{u}_{\mathbf{k}}(\mathbf{x}, t) \mathcal{R} \left( e^{i(\omega t - \mathbf{k} \cdot \mathbf{v}_i)} \right) \quad (4.4.2)$$

This condition shows that the displacement is phase-shift between two homologous points on opposite boundaries of the unit cell. However, under the LW-LF hypothesis, 4.4.2 degenerates into standard periodic boundary conditions and reads

<sup>5</sup>This result derives from using born-Von-Karman conditions, the methodology followed by Bloch rigorously detailed in [Gazalet et al., 2013]

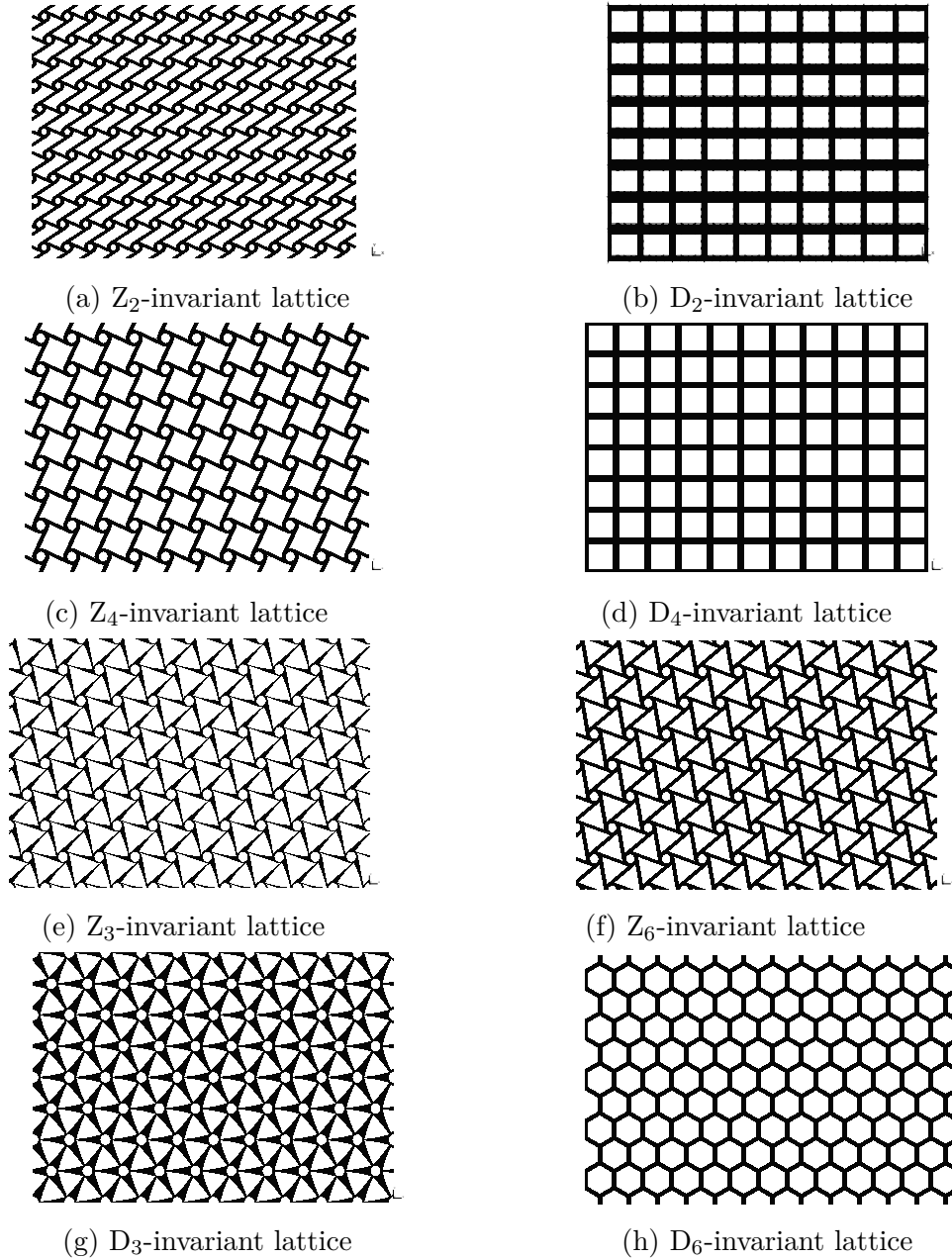


Figure 4.2: Studied PAMs geometries

$$\mathbf{u}(\mathbf{x}+\mathbf{v}_i) = \mathbf{u}(\mathbf{x}) \quad (4.4.3)$$

In order to ensure the LW-LF regime, the problem is solved for large values of the wavelength with respect to the size of the unit cell. In this work we considered a scale separation of

$$\eta = \frac{\lambda_l}{a} = 200, \quad (4.4.4)$$

where  $\lambda_l$  is the loading wavelength. This corresponds to a wavelength 200 times the size of the unit cell. In the case of a unit cell size of  $a = 1 \text{ mm}$ , this corresponds to a wavenumber  $\|\mathbf{k}\| \approx 31.41 \text{ m}^{-1}$ . We solved the wave propagation problem for  $\theta = \{0^\circ, 30^\circ, 45^\circ, 90^\circ\}$ . It should be noted that the choice of an origin for the angle measurement is arbitrary and may or may not correspond to a symmetry element of

the mesostructure.

The software COMSOL MULTIPHYSICS 5.4 has been used to solve the eigenvalue problem for each direction of propagation of the plane wave. The first two eigenfrequencies, divided by the norm of the wavevector, give the phase velocities. The corresponding polarisation fields  $\hat{\mathbf{s}}_i$  are subsequently identified by averaging the displacement vector over the unit cell:

$$\hat{\mathbf{s}}_i = \frac{\langle \tilde{\mathbf{u}} \rangle_i}{\|\langle \tilde{\mathbf{u}} \rangle_i\|}, \quad i = 1, 2, \quad \text{with} \quad \langle \tilde{\mathbf{u}} \rangle = \frac{1}{|\mathcal{T}|} \int_{\mathcal{T}} \tilde{\mathbf{u}}(\mathbf{x}) d\mathbf{x}. \quad (4.4.5)$$

This calculation is performed for an appropriate set of propagation directions, depending on the approach considered. The inversion procedure is then carried out using the commercial software WOLFRAM MATHEMATICA, and gives the set of invariants of  $\mathbf{T}$  and an orientation angle. In order to validate the results, the phase velocities for the apparent material are calculated as follow

$$v_1(\theta) = \sqrt{\frac{1}{2\rho^{\text{hom}}} \left( \mathcal{I}_1(\theta) - \sqrt{\mathcal{K}_2(\theta)} \right)}, \quad v_2(\theta) = \sqrt{\frac{1}{2\rho^{\text{hom}}} \left( \mathcal{I}_1(\theta) + \sqrt{\mathcal{K}_2(\theta)} \right)}. \quad (4.4.6)$$

and represented in polar plots compared with the results obtained from the Floquet-Bloch analysis. It is important to remark that, given the fact that we used noiseless numerical data to feed the identification procedure, all approaches gave quantitatively the same results. These results are summarised in figure 4.3. At these stage, some comments can be done:

- The results of the identification are in excellent agreement with the full-field Floquet-Bloch computation, as the polar plots of the phases velocities are superposed for every symmetry class;
- The apparent elastic behaviour of  $Z_3$ ,  $D_3$ ,  $Z_6$  and  $D_6$  lattices, as anticipated, is isotropic;
- In the LF-LW regime, chirality and lack of centrosymmetry play no role;
- In the case of the square and the orthotropic lattices, respectively  $D_4$  and  $D_2$ , wave propagation is, again as expected, highly anisotropic. The overall behaviour exhibits the same symmetry as the unit cell, as the symmetry lines of the polar plot are aligned with those of the unit cell in the reference frame;
- In the case of chiral materials, we can observe that phase velocities of shear and longitudinal waves are closer. This is due to the auxetic nature of these architectures;
- More interesting, and less trivial, is the behaviour of the tetrachiral lattice  $Z_4$ . From table 4.1 we expect this architecture to be identified as a tetragonal material. This means that the identified  $\mathbf{C}^{\text{app}}$  has more symmetries than the unit cell, and the symmetry lines observed in figure 4.3(a) are not *material* but *mathematical* symmetries. Moreover, these symmetry lines are tilted with respect to the reference frame, and the angle cannot be predicted in advance just by analysing the symmetries of the unit cell, showing the importance of an identification procedure that does not formulate assumptions on the symmetry classes of  $\mathbf{C}^{\text{app}}$ .

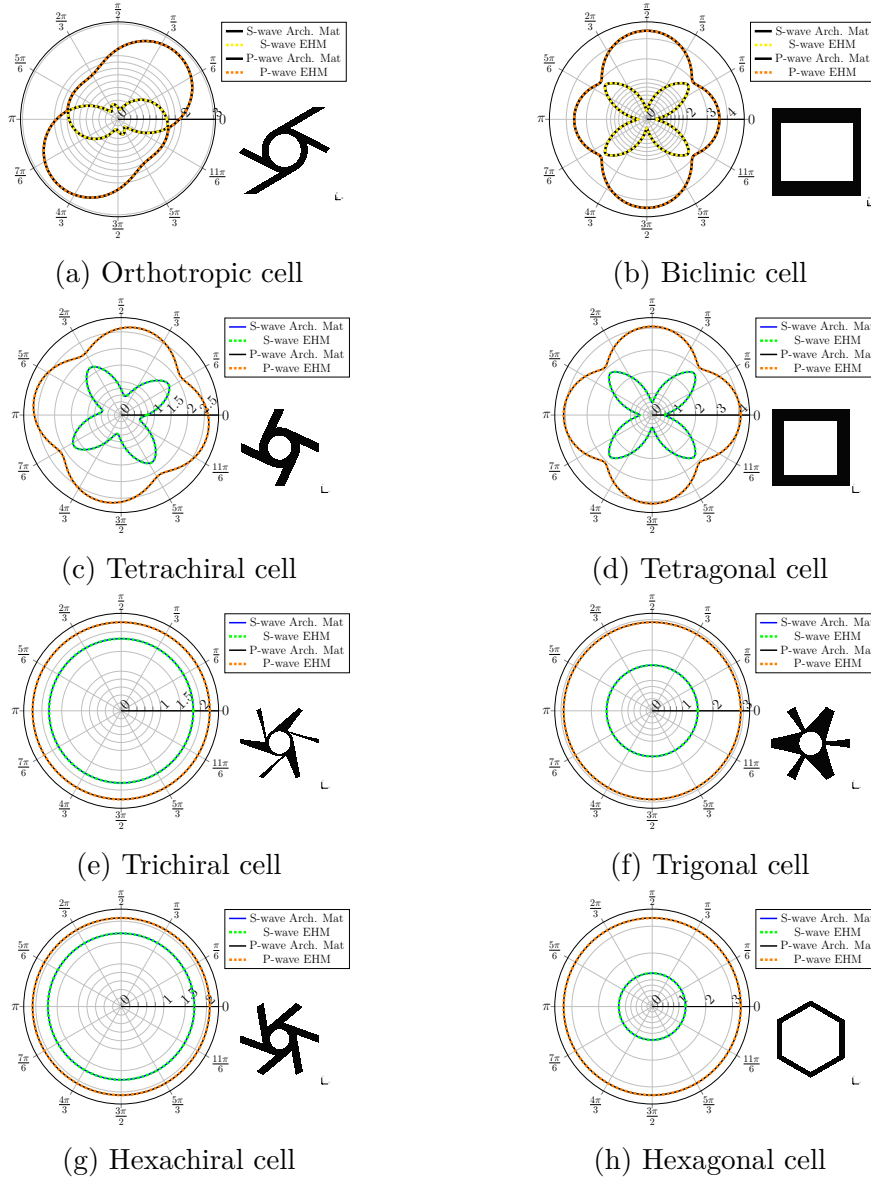


Figure 4.3: Polar plots of phase velocities for different symmetry classes

In a second time, a parametric study for different volume fractions has been performed, and the results obtained by means of the proposed identification procedure compared to those obtained from a elastostatic homogenization (details in Appendix). In figure 4.4 the coefficients of  $\mathbf{C}^{\text{hom}}$  expressed in the reference frame, are plotted for each architecture. The results are in excellent agreement for each symmetry class. It is important to remark that the tetrachiral cell is still cubic, but the fact that its symmetry lines slightly tilted explains why the coefficients  $c_{1112}$  and  $c_{2212}$  are different from zero. Moreover, the fact that  $c_{1112} = -c_{2212}$  confirms that this remark.

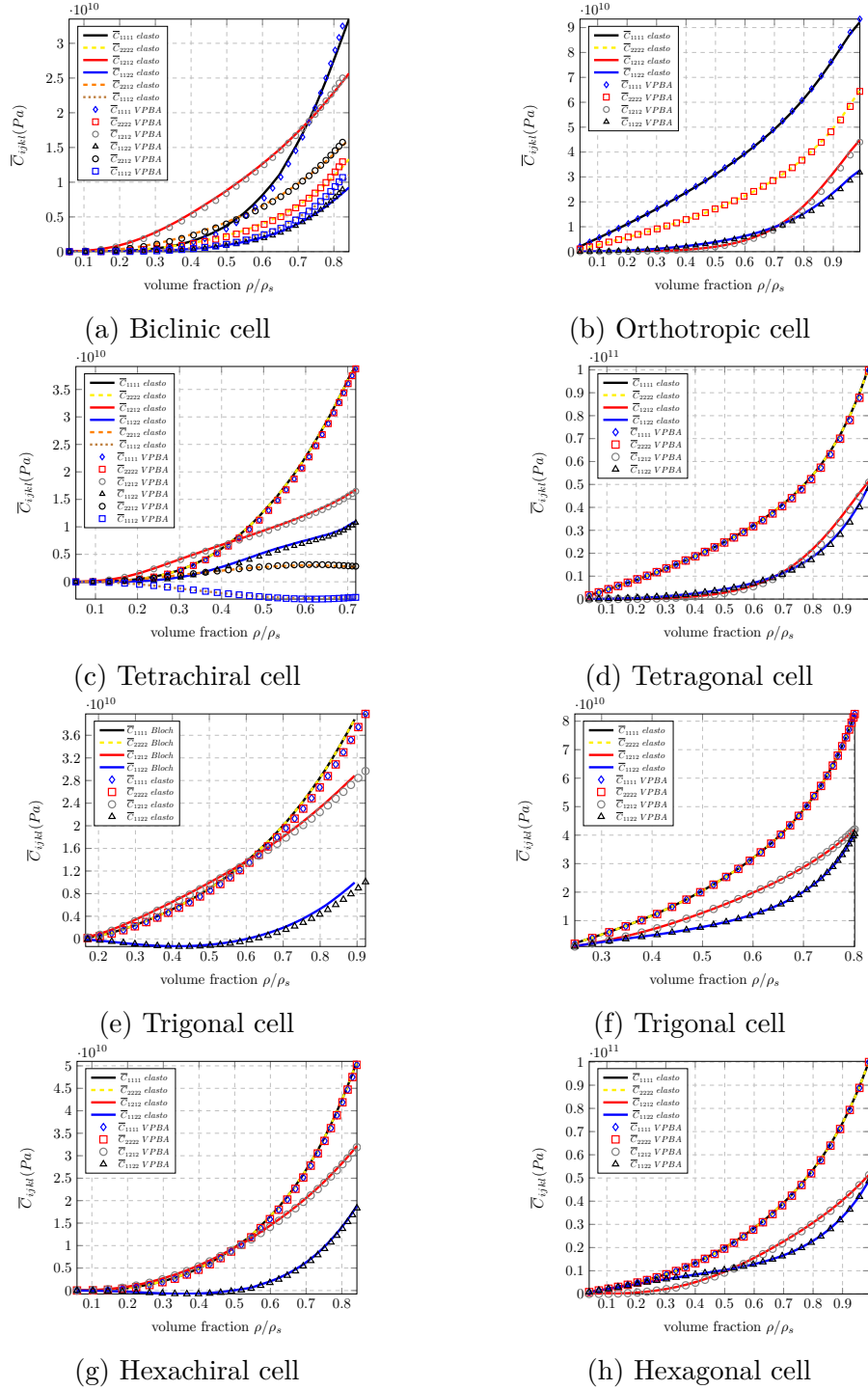


Figure 4.4: Evolution of effective elastic moduli with respect to the volume fraction  $\rho/\rho_s$

## 4.5 Synthesis

In this chapter a novel identification procedure for computing the effective constitutive tensors of an architected material in the LW-LF regime was introduced. The procedure is based on the computation of the invariants of the Christoffel tensor, parameterized with respect to the harmonic decomposition of the elasticity tensor. In the methodology, wave propagation characteristics, such as phase velocities and polarizations, corresponding to plane waves propagating to different directions are processed

to retrieve the effective quantities. No assumptions are made on the symmetry class of the effective tensor.

Three approaches are proposed to implement the procedure: PVBA, which uses both phase velocities and polarizations; VBA, which uses only phase velocities; and VBAF, which is still based on phase velocities, but uses a Fourier series approach. These three strategies are formally equivalent, but they have complementing features and characteristics, as described in table 4.2.

| Approach                          | PVBA                      | VBA                           | VBA-F           |
|-----------------------------------|---------------------------|-------------------------------|-----------------|
| Nature of measurements            | Velocity + Polarisation   | Velocity                      | Velocity        |
| Minimal $N^\circ$ of measurements | 3                         | 3                             | 4               |
| Number of equation                | 3 (5)                     | 3 (5)                         | 3 (?)           |
| Nature of system to solve         | linear ( $1^{st}$ -order) | non-linear ( $2^{nd}$ -order) | $2^{nd}$ -order |
| Computational robustness          | Good                      | Fair                          | Good            |
| Sensitivity to noise              | Good                      | Fair                          | Good            |

Table 4.2: Comparison of the features of the different approaches

From the point of view of computational performance, the PVBA is for certain the best choice, as it requires a minimal number of measures, and the solution of a linear first order system. However, it requires the access to wave polarization, which can be straightforward in the case of numerical simulations, but quite complex and unconventional when concerning experiments. To this end, dynamic DIC methods can be used, as well as the use of 3D laser measurements. The three procedures also exhibit different sensitivity with respect to the presence of noise in the input data. This point is especially interesting when working with real data from experiments. In this case, the Fourier based procedure VBAF is the most performing, while the VBA, since it is based on the solution of a nonlinear  $2^{nd}$  order system, is the less performing. A more comprehensive study of the robustness of the different methods will be the object of a forthcoming work. Concerning the limits of the approach, it is important to remark that the procedure is limited to the LW-LF regime. In this sense, the choice of the scale separation ratio equation (4.4.4) is crucial. Indeed, if the algorithms are applied to data corresponding to wave with a smaller wavelength, they can fail to correctly identify the apparent properties. In particular, it is known that smaller values of  $\eta$  would trigger dispersive effects caused by scattering or internal resonance phenomena. For those classes whose anisotropy is well captured by  $\mathbf{C}^{\text{hom}}$ , like  $D_4$  and  $D_2$  the the difference in the results may not be so remarkable. However, for those classes that are seen as isotropic in classic continuum elasticity, the procedure could give results that are completely wrong, as it can be observed in [Rosi and Auffray, 2019, Rosi et al., 2020]. In this case, a richer EHM able to account for chiral or dispersive effects should be used. It has been shown in the literature that generalized continua, such as Strain Gradient Elasticity (SGE) or Cosserat Elasticity are a suitable choice [Auffray et al., 2015, Rosi and Auffray, 2019].

## 4.6 Appendix: Elastostatic homogenization

In this subsection, we recall some theoretical elements of computational homogenization to predict the effective properties of architected materials in the context of linear elasticity. The elastostatic homogenisation method will be performed, its results will be used as the reference for comparison results the results of the Bloch-wave identification approach. First, the Representative Elementary Volume will be presented. Then, the localisation problem will be posed with appropriate static boundary conditions. Finally, the effective quantities will be defined

### 4.6.1 Introduction

The materials and structures modeling in mechanical systems are generally based on the assumption of materials homogeneity. However, there is a scale below which many materials present a high density of heterogeneities, and whose phases are often randomly distributed. The influence of heterogeneities on the macroscopic behavior behaviour of the structure can be highlighted by representing the mechanisms involved, at a sufficiently small-scale; the characteristic scale of interest becomes the scale of the heterogeneities. However, taking into account these fine-scales often leads to ill-conditioned problems and the numerical cost would be prohibitively expensive (in the context of a finite element simulation for example). Homogenization techniques are based on a decomposition in different levels of the heterogeneous microstructure of the material. They allow, through a multi-scale approach, to provide an equivalent homogeneous model guaranteeing the conservation of a certain number of physical properties of the original medium, which means an identical behavior behaviour "on average". The objective of this section is to present the basic concepts of computational homogenization to predict the effective properties of architected materials in the context of linear elasticity. First, the notion of Representative Volume Element (RVE) is introduced. Then, the localization problems are posed and the effective properties are defined (the effective stress and strain fields and the effective fourth-order elasticity tensor). Finally, a numerical procedure based on Finite Element Method (FEM) is presented to compute the effective properties using different types of boundary conditions.

### Methodology

According to [Bornert et al., 2001], the homogenization procedure is carried out in 3 main steps:

- Representation: Definition of the representative elementary volume (REV);
- Localization: Definition of a localization operator for stress and strain fields;
- Homogenization: Calculation of the effective properties;

### 4.6.2 Representative elementary volume

One basic notion in homogenization and more specifically in computational homogenization is the Representative Elementary Volume (REV). An REV is a domain of finite size that carries all the information about the microstructure, i.e., it describes the microstructure: the different phases geometries and their local distributions. In addition to that, the REV must represent the macroscopic behavior behaviour behaviour

at the microscopic scale, which means that it should contain enough information for effective properties to be calculated on the sole basis of this volume, under some conditions of scale-separation.

The principle of scale-separation involves a comparison between different characteristic lengths. If we denote " $l$ " the characteristic size of the microstructure (size of the considered REV), " $L$ " the characteristic size of the macrostructure and " $d$ " the size of microstructural heterogeneities, the condition " $l \ll L$ " guarantees the continuity of the medium, while " $d \gg l$ " allows to assign to the REV a homogeneous macroscopic behavior behaviour.

The previous conditions can be summarized as follows

$$d \ll l \ll L$$

It is worth noting that, the choice of the REV depends on the specific investigated properties<sup>6</sup>. In addition to that, the computed effective properties will depend on the type of boundary conditions applied over the boundary of the REV [Yvonnet, 2019]. To summarize, the step of representation consists in describing the inner structure : the internal composition of the different phases (local material properties are assumed to be known), their local distribution in the REV (when it's possible) as well as their respective volume fractions. A rich and realistic representation contributes to a reliable estimation of the effective behavior behaviour.

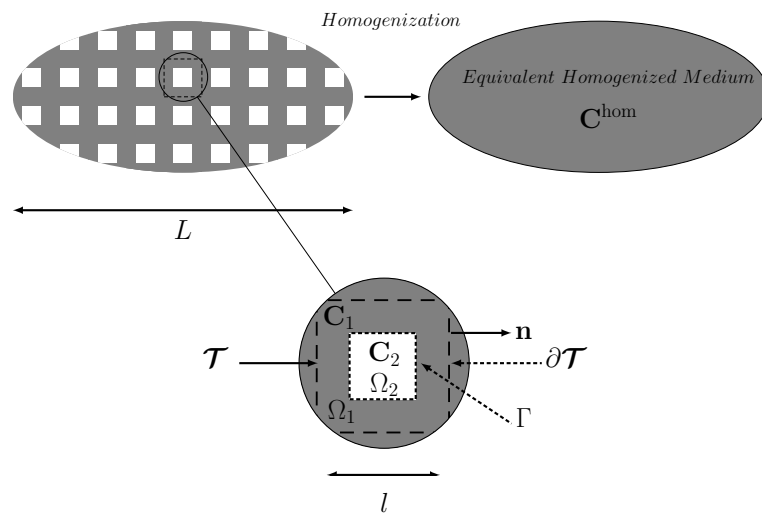


Figure 4.5: **a)** Periodic microstructure; **b)** Representative Elementary Volume (REV) as a unit periodic cell

Since the medium is periodic and deterministic, the REV can be reduced to a single unit cell which must carry all the information about the microstructure and the effective properties to be calculated. In addition to that, the computed effective properties will depend on the type of boundary conditions applied over the boundaries of the REV. Thus, it is more appropriate to choose Periodic Boundary Conditions (PBC) since the convergence macroscopic quantities is ensured just with a single periodic cell. To do so, a localisation problem using strain approach for instance, need to be solved.

<sup>6</sup>The size of the REV for thermal conductivity would be *a priori* different from the REV for a elastic moduli

### 4.6.3 Localization problem

We consider a heterogeneous material composed of  $N$  phases as shown in the figure figure 4.5.a. An REV as defined in figure 4.5.b is associated with a domain  $\Omega \in \mathbb{R}^2$ . The boundary of the domain  $\Omega$  will be denoted by  $\partial\Omega$  and the interface between phases will be supposed perfect and denoted by  $\Gamma$ . The properties are supposed to be known, and given by the fourth-order elastic tensor which also is supposed to be constant within each phase. Hence, we have

$$\mathbf{C}(\mathbf{x}) = \sum_{i=1}^N \chi^i(\mathbf{x}) \mathbf{C}^i \quad , \quad \forall \mathbf{x} \in \Omega \quad (4.6.1)$$

where  $\mathbf{C}^i$  denote the elasticity tensor associated with the  $i$ -th phase, and  $\chi^i(\mathbf{x})$  is the indicator function. The indicator function, called also the characteristic function  $\chi^i(\mathbf{x})$  takes the value of 1 for any point  $\mathbf{x}$  of the domain  $\Omega^i$  associated with the  $i$ -th phase, and 0 elsewhere. The main objective is to define the effective elasticity tensor over the equivalent homogeneous medium as shown in the figure 4.5

The localization of strains is based on the resolution of a boundary value problem called ‘‘Strains localization’’. Assuming that the REV is subjected to homogeneous strain field, the localization problem can be stated as follows :

#### Definition : Strains localization problem

For a given macroscopic strain field  $\bar{\varepsilon}$ , find the displacement field  $\mathbf{u}(\underline{x})$  in  $\Omega$  such that :

$$\nabla \cdot \boldsymbol{\sigma}(\mathbf{x}) = \mathbf{0} \quad , \quad \forall \mathbf{x} \in \Omega; \quad (4.6.2)$$

with

$$\boldsymbol{\sigma}(\mathbf{x}) = \mathbf{C}(\mathbf{x}) : \boldsymbol{\varepsilon}(\mathbf{x}) \quad (4.6.3)$$

$$\boldsymbol{\varepsilon}(\mathbf{x}) = \frac{1}{2} [\mathbf{u}(\mathbf{x}) \otimes \nabla + \nabla \otimes \mathbf{u}(\mathbf{x})] \quad (4.6.4)$$

and verifying

$$\langle \boldsymbol{\varepsilon}(\mathbf{x}) \rangle = \bar{\varepsilon} \quad (4.6.5)$$

Where  $\langle \cdot \rangle = \frac{1}{|\Omega|} \int_{\Omega} \cdot d\Omega$  denotes the spatial averaging operator. There is an alternative localization problem based on stress, assuming that the REV is subjected to a homogeneous stress field. The formulation of the latter problem can be found in the book of [Yvonnet, 2019].

#### Boundary conditions

Before homogenization process, it is necessary to set boundary conditions to  $\Omega$  in order to solve the problem equation (4.6.2) – equation (4.6.4). Hence, the condition equation (4.6.5) can be satisfied by using appropriate boundary conditions.

Assuming that the local strain field is the superposition of a constant macroscopic strain field  $\bar{\varepsilon}$  and a microscopic fluctuation  $\tilde{\varepsilon}(\mathbf{x})$ , we shall write

$$\boldsymbol{\varepsilon}(\mathbf{x}) = \bar{\varepsilon} + \tilde{\varepsilon}(\mathbf{x}) \quad (4.6.6)$$

After applying the spatial averaging operator to equation (4.6.6), and using Green theorem, we have

$$\langle \boldsymbol{\varepsilon}(\mathbf{x}) \rangle = \bar{\boldsymbol{\varepsilon}} + \frac{1}{2|\Omega|} \int_{\partial\Omega} (\tilde{\mathbf{u}}(\mathbf{x}) \otimes \mathbf{n} + \mathbf{n} \otimes \tilde{\mathbf{u}}(\mathbf{x})) d\Gamma \quad (4.6.7)$$

Where  $\tilde{\mathbf{u}}$  is a fluctuating displacement field such that  $\tilde{\mathbf{u}} = \mathbf{u} - \bar{\boldsymbol{\varepsilon}} \cdot \mathbf{x}$ . Therefore, the condition 4.6.5 is satisfied if the second term on the right side of equation (4.6.7) is equal to zero, which leads to the following conditions :

1.  $\tilde{\mathbf{u}}(\mathbf{x}) = 0$  on  $\partial\Omega$ ;
2.  $\tilde{\mathbf{u}}(\mathbf{x})$  is periodic on  $\Omega$ .

The corresponding bounding conditions are obtained by integrating equation (4.6.6) with respect to  $\mathbf{x}$ . In the present framework, only two type of boundary conditions are considered : *Kinematic Uniform Boundary Conditions - KUBC* and *Periodic Boundary Condition - PBC*; For the case of *Static uniform boundary conditions - SUBC* and stress localization problem bases, the interested reader is referred to the book of [Yvonnet, 2019].

#### Definition : Kinematic Uniform Boundary Conditions - KUBC

The displacement  $\mathbf{u}(\mathbf{x})$  is prescribed for any material point  $\mathbf{x} \in \partial\Omega$  such that :

$$\mathbf{u}(\mathbf{x}) = \bar{\boldsymbol{\varepsilon}} \cdot \mathbf{x} \quad , \quad \forall \mathbf{x} \in \partial\Omega \quad (4.6.8)$$

#### Definition : Periodic Boundary Condition - PBC

The displacement  $\mathbf{u}(\mathbf{x})$  over the boundary  $\partial\Omega$  takes the form :

$$\mathbf{u}(\mathbf{x}) = \bar{\boldsymbol{\varepsilon}} \cdot \mathbf{x} + \tilde{\mathbf{u}}(\mathbf{x}) \quad , \quad \forall \mathbf{x} \in \Omega \quad (4.6.9)$$

Where  $\tilde{\mathbf{u}}(\mathbf{x})$  is the fluctuating displacement field which is periodic over  $\Omega$ . In other words,  $\tilde{\mathbf{u}}(\mathbf{x})$  takes the same value on two homologous points  $\mathbf{x}^+$  and  $\mathbf{x}^-$  on opposite faces of the REV  $\Omega$

### 4.6.4 Averaging fields

Let first define the spatial average of a kinematically compatible strain field  $\boldsymbol{\varepsilon}(\mathbf{x})$ . Without loss of generality, we consider the REV of two phases represented in the figure figure 4.5.b, we have

$$\begin{aligned} \langle \boldsymbol{\varepsilon}(\mathbf{x}) \rangle &= \frac{1}{|\Omega|} \int_{\Omega} \varepsilon_{ij} d\Omega = \frac{1}{2|\Omega|} \int_{\Omega} (u_{i,j} + u_{j,i}) d\Omega \\ &= \frac{1}{2|\Omega|} \int_{\partial\Omega} (u_i^1 n_j + u_j^1 n_i) d\Gamma + \frac{1}{2|\Omega|} \int_{\Gamma} (u_i^1 n_j + u_j^1 n_i) ds - \frac{1}{2|\Omega|} \int_{\Gamma} (u_i^2 n_j + u_j^2 n_i) ds \end{aligned} \quad (4.6.10)$$

The interfaces  $\Gamma$  are supposed perfect, hence the red-coloured terms are equals to zero. Then, using equation (4.6.8) and Green theorem , we shall write

$$\langle \boldsymbol{\varepsilon}(\mathbf{x}) \rangle = \frac{1}{2|\Omega|} \int_{\partial\Omega} (u_i n_j + u_j n_i) d\Gamma = \frac{1}{|\Omega|} \int_{\Omega} \bar{\varepsilon}_{ij} d\Omega = \bar{\varepsilon}_{ij} \quad (4.6.11)$$

Consider now the spatial average of a statically admissible stress field  $\boldsymbol{\sigma}(\mathbf{x})$  , i.e.  $\sigma_{ij,j} = 0$ , it yields:

$$\begin{aligned} \langle \boldsymbol{\sigma}(\mathbf{x}) \rangle &= \frac{1}{|\Omega|} \int_{\Omega} \sigma_{ij} d\Omega = \frac{1}{|\Omega|} \int_{\Omega} \sigma_{ik} \delta_{kj} d\Omega \\ &= \frac{1}{|\Omega|} \int_{\Omega^1} \sigma_{ik}^1 \delta_{kj} d\Omega + \frac{1}{|\Omega|} \int_{\Omega^2} \sigma_{ik}^2 \delta_{kj} d\Omega \\ &= \frac{1}{|\Omega|} \int_{\Omega^1} (\sigma_{ik}^1 x_j)_{,k} d\Omega + \frac{1}{|\Omega|} \int_{\Omega^2} (\sigma_{ik}^2 x_j)_{,k} d\Omega \\ &= \frac{1}{|\Omega|} \int_{\partial\Omega} \sigma_{ik}^1 n_k x_j d\Gamma + \frac{1}{|\Omega|} \int_{\Gamma} \sigma_{ik}^1 n_k x_j ds - \frac{1}{|\Omega|} \int_{\Gamma} \sigma_{ik}^2 n_k x_j ds \end{aligned} \quad (4.6.12)$$

As mentioned before, when the interfaces  $\Gamma$  are perfect, the previous relation is simply reduced to

$$\langle \boldsymbol{\sigma}(\mathbf{x}) \rangle = \frac{1}{|\Omega|} \int_{\Omega} \sigma_{ij} d\Omega = \frac{1}{|\Omega|} \int_{\partial\Omega} \sigma_{ik} n_k x_j d\Gamma \quad (4.6.13)$$

### Hill-Mandel lemma

The Hill-Mandel lemma expresses the relation of equivalence in terms of mechanical energies between the macroscopic and the microscopic description of the same medium [Hill, 1963]. Let  $\boldsymbol{\sigma}$  be a statically admissible stress field and  $\boldsymbol{\varepsilon}$  kinematically admissible strain field<sup>7</sup>. Then it holds

$$\langle \boldsymbol{\sigma}(\mathbf{x}) : \boldsymbol{\varepsilon}(\mathbf{x}) \rangle = \langle \boldsymbol{\sigma}(\mathbf{x}) \rangle : \langle \boldsymbol{\varepsilon}(\mathbf{x}) \rangle \quad (4.6.14)$$

The demonstration of thee Hill-Mandel lemma is provided in the reference [Yvonnet, 2019]

### Effective properties

In the strains localization problem equation (4.6.2) - equation (4.6.4), the spatial distribution of different phases are given by the fourth-order tensor  $\mathbf{A}$ , which expresses the relation between micro and macroscopic strain, such that

$$\boldsymbol{\varepsilon}(\mathbf{x}) = \mathbf{A}(\mathbf{x}) : \bar{\boldsymbol{\varepsilon}} \quad (4.6.15)$$

$\mathbf{A}(\mathbf{x})$  is the concentraion (or the localization) strain tensor, verifying

$$\begin{cases} \frac{1}{|\Omega|} \int_{\Omega} A_{ijkl} d\Omega = I_{ijkl}; \\ A_{ijkl} = A_{jikl} = A_{ijlk} \end{cases} \quad (4.6.16)$$

Applying the constitutive law, we obtain

$$\boldsymbol{\sigma} = \mathbf{C}(\mathbf{x}) : \mathbf{A}(\mathbf{x}) : \bar{\boldsymbol{\varepsilon}} \quad (4.6.17)$$

<sup>7</sup>Or  $\boldsymbol{\sigma}$  and  $\boldsymbol{\varepsilon}$  both verifies the periodic boundary conditions.

Then, the macroscopic constitutive relationship is obtained by averaging equation (4.6.17)

$$\bar{\boldsymbol{\sigma}} = \bar{\mathbf{C}} : \bar{\boldsymbol{\varepsilon}} \quad (4.6.18)$$

with

$$\bar{\mathbf{C}} = \langle \mathbf{C}(\mathbf{x}) : \mathbf{A}(\mathbf{x}) \rangle$$

The problem equation (4.6.2) - equation (4.6.4) being linear, its solution can be expanded using the superposition principle as a linear combination of the three independent components of the strain tensor in 2D as

$$\mathbf{u}(\mathbf{x}) = \mathbf{u}^{(11)}(\mathbf{x})\bar{\varepsilon}_{11} + \mathbf{u}^{(22)}(\mathbf{x})\bar{\varepsilon}_{22} + \mathbf{u}^{(12)}(\mathbf{x})\bar{\varepsilon}_{12}$$

where  $\mathbf{u}(\mathbf{x})$  denotes the solution of the problem localisation problem equation (4.6.2) - equation (4.6.4) when prescribing a macroscopic strain field  $\bar{\boldsymbol{\varepsilon}}$ , i.e., the micro-displacement due to prescribed macroscopic strain tensor  $\bar{\varepsilon}_{ij}$  defined by

$$\bar{\varepsilon}_{ij} = \tilde{\mathbf{e}}_i \otimes \tilde{\mathbf{e}}_j, \quad (i, j) = \{(1, 1), (2, 2), (1, 2)\}$$

In other words,  $\mathbf{u}^{(11)}(\mathbf{x})\bar{\varepsilon}_{11}$ ,  $\mathbf{u}^{(22)}(\mathbf{x})\bar{\varepsilon}_{22}$  and  $\mathbf{u}^{(12)}(\mathbf{x})\bar{\varepsilon}_{12}$  are obtained by solving the strain localisation problem with, respectively:

$$\bar{\boldsymbol{\varepsilon}}^{(11)} = \begin{bmatrix} 1 & 0 \\ 0 & 0 \end{bmatrix}, \quad \bar{\boldsymbol{\varepsilon}}^{(22)} = \begin{bmatrix} 0 & 0 \\ 0 & 1 \end{bmatrix}, \quad \bar{\boldsymbol{\varepsilon}}^{(12)} = \frac{1}{2} \begin{bmatrix} 0 & \sqrt{2} \\ \sqrt{2} & 0 \end{bmatrix}, \quad (4.6.19)$$

By setting  $\boldsymbol{\varepsilon}^{(ij)}(\mathbf{x}) = \boldsymbol{\varepsilon}(\mathbf{u}^{(ij)}(\mathbf{x}))$ , one can write

$$\boldsymbol{\varepsilon}(\mathbf{x}) = \boldsymbol{\varepsilon}^{(11)}(\mathbf{x})\bar{\varepsilon}_{11} + \boldsymbol{\varepsilon}^{(22)}(\mathbf{x})\bar{\varepsilon}_{22} + \boldsymbol{\varepsilon}^{(12)}(\mathbf{x})\bar{\varepsilon}_{12},$$

and thus have the following compact form

$$\boldsymbol{\varepsilon}(\mathbf{x}) = \mathbf{A} : \bar{\boldsymbol{\varepsilon}} \quad \text{with} \quad A_{ijkl}(\mathbf{x}) = \varepsilon_{ij}^{(kl)}(\mathbf{x}).$$

Then, taking into the Hooke's law, the macroscopic constitutive relationship is obtained by averaging (4.6.17)<sup>8</sup>

$$\bar{\boldsymbol{\sigma}} = \mathbf{C}^{\text{hom}} : \bar{\boldsymbol{\varepsilon}} \quad \text{with} \quad \mathbf{C}^{\text{hom}} = \langle \mathbf{C}(\mathbf{x}) : \mathbf{A}(\mathbf{x}) \rangle \quad (4.6.20)$$

---

<sup>8</sup>An alternative definition can be obtained from Hill-Mandel lemma.

# Chapter 5

## Asymptotic homogenization: Application to strain-gradient elasticity

### Contents

---

|       |   |     |
|-------|---|-----|
| 5.1   | INTRODUCTION . . . . .  | 136 |
| 5.2   | TWO-SCALE HOMOGENIZATION FRAMEWORK . . . . .  | 137 |
| 5.2.1 | SCALE SEPARATION . . . . .  | 137 |
| 5.2.2 | GOVERNING EQUATIONS . . . . .   | 139 |
| 5.2.3 | TWO-SCALE ASYMPTOTIC EXPANSIONS . . . . .   | 139 |
| 5.2.4 | HOMOGENIZATION PROCEDURE . . . . .  | 140 |
| 5.3   | SECOND ORDER HOMOGENIZATION OF THE 2D WAVE EQUATIONS  | 141 |
| 5.3.1 | COMPUTATION OF $\tilde{\mathbf{u}}_0$ . . . . .   | 142 |
| 5.3.2 | COMPUTATION OF $\tilde{\mathbf{u}}_1$ AND FIRST CELL PROBLEM . . . . .                                    | 143 |
| 5.3.3 | COMPUTATION OF FIRST-ORDER HOMOGENIZED TENSORS  | 144 |
| 5.3.4 | COMPUTATION OF $\tilde{\mathbf{u}}_2$ AND SECOND CELL PROBLEM . . . . .                                   | 146 |
| 5.3.5 | COMPUTATION OF THE SECOND-ORDER HOMOGENIZED COU-<br>PLING TENSORS . . . . .                               | 147 |
| 5.3.6 | COMPUTATION OF $\tilde{\mathbf{u}}_3$ AND THIRD CELL PROBLEM . . . . .                                    | 149 |
| 5.3.7 | COMPUTATION OF SECOND-ORDER HOMOGENIZED TENSORS   | 151 |
| 5.4   | RECIPROCITY RELATIONSHIPS . . . . .   | 152 |
| 5.4.1 | RELATIONSHIP BETWEEN TENSORS $\boldsymbol{\varrho}_1^H$ AND $\mathbf{C}_1^H$ . . . . .                    | 153 |
| 5.4.2 | RELATIONSHIP BETWEEN TENSORS $\boldsymbol{\varrho}_1^H$ , $\mathbf{C}_1^H$ AND $\mathbf{C}_2^H$ . . . . . | 154 |
| 5.5   | MEAN FIELDS, HOMOGENIZED EQUATIONS AND LINK WITH STRAIN-<br>GRADIENT ELASTICITY . . . . .                 | 157 |
| 5.5.1 | DERIVATION OF A FOURTH-ORDER EFFECTIVE TIME-HARMONIC<br>WAVE EQUATION . . . . .                           | 157 |
| 5.5.2 | TRANSIENT FOURTH-ORDER EFFECTIVE WAVE EQUATION  | 160 |
| 5.6   | SYNTHESIS . . . . .   | 160 |

---

## 5.1 Introduction

Homogenization theory, as mentioned previously, focuses on studying the macroscopic behavior of systems that exhibit microscopic heterogeneities. The main idea is to replace such system with an equivalent homogeneous medium that serves as a reliable approximation of the original one, preserving its the macroscopic behavior within a certain range of parameters. In the context of wave propagation in periodic media, scale effects emerge due to nature of the problem and the distinct characteristics of the architected material. At least two scales can be distinguished: the microscopic and macroscopic scales.

Homogenization can be approached in various ways. From the physical, or mechanical point of view, the idea is to identify a characteristic length-scale over which the average of the microscopic fields is computed. The definition of homogenized or effective properties is then derived from these averaged quantities. This characteristic length-scale is often referred to as the REV, which represents the unit cell in the case of periodic media. On the other hand, from the mathematical point view, the homogeneous model is defined as the limit of a sequence of heterogeneous problems, known as auxiliary problems or cell problems, depending on a small parameter  $\epsilon$  going to zero, called the scale separation ratio. The homogenized or effective properties are defined as the resulting properties of this limit problem.

The first developments of asymptotic homogenization for periodic media were made [San70, San71, Bab76], where the term 'homogenization' was first used in a mathematical context. Subsequently, numerous asymptotic models were developed to provide a homogenized description of wave propagation phenomena. In the low-wavelength and low-frequency (LW-LF) regime, Bensoussan et al. [ref] introduced a well-established homogenization theory based on two-scale asymptotic expansions. This theory addresses static and quasi-static behaviors, offering an asymptotic description of wave dispersion. However, it has limitations in capturing internal length scales and dispersion phenomena. To overcome these limitations, higher order terms (in terms of Taylor expansions) were introduced, enabling the models to accurately capture dispersive effects. This improvement is explored in [Bakhvalov and Panasenko, 1989, Santosa and Symes, 1991, Boutin and Auriault, 1993, Smyshlyaev and Cherednichenko, 2000, Fish et al., 2002, Bacigalupo and Gambarotta, 2014b, Wautier and Guzina, 2015, Allaire et al., 2016, Abdulle and Pouchon, 2020, Cornaggia and Guzina, 2020, Cornaggia and Bellis, 2020] for scalar waves in 1D, 2D, 3D and also elastic waves. Two-scale homogenization of the wave equation in periodic media is nowadays well understood, particularly in terms of higher-order contributions that involve higher gradients of the macroscopic strain. However, these results have not been extended to strain-gradient theory. This has motivated a different approach towards constructing a strain-gradient model of the EHM based on two-scale asymptotic expansions. The primary objective of this approach is to define and compute the high-order tensors of the SGE's constitutive law, as introduced in Chapter 3, in order to approximate the acoustic branches in both the LW-LF and the SW-LF regimes.

This chapter is organized as follows. First, we present the formal homogenization framework introduced in [Boutin and Auriault, 1993] for the wave propagation problem in Section 1. Here, the displacement field is expressed in terms of the solutions

of cell problems called correctors. In Section 2, we describe in detail the procedure for using the asymptotic expansion method to compute high-order elastic and inertial homogenized tensors of the medium with respect to the scale parameter  $\epsilon$ . In this framework,  $\epsilon$  represents the ratio between the wavelength of the wave traveling in the medium and the size of its periodic unit cell. We explain how the cell problems are obtained and solved, providing weak form and example of implementation. Next, in section 3, we establish two reciprocity identities between the correctors<sup>1</sup> which are one of the major contributions of this chapter. These relationships, of great practical interest, allow us to reduce the number of cell problems that need to be solved. Finally, in Section 4, we will propose the homogenized wave equations as well as the intrinsic expressions of the homogenized higher-order tensors of the strain-gradient constitutive law derived from the asymptotic homogenization process, which is the second major contribution of this chapter.

The work described in this chapter has been realized in collaboration with Marc Bonnet (POEMS, ENSTA Paris).

## 5.2 Two-scale homogenization framework

The objective of this section is to present the mathematical framework for the higher-order homogenization method, which is based on asymptotic expansions. This framework allows for the computation of essential correctors necessary to define the homogenized high-order tensors for wave propagation in periodic media. We will provide a concise description of the scales involved, the equations employed, and outline the overall procedure followed in this approach.

### 5.2.1 Scale separation

Let us consider a 2D periodic microstructured medium  $\Omega$ , generated by translating the elementary cell  $\mathcal{Y}^\epsilon$  using a set of two lattice vectors  $\mathbf{v}_1$  and  $\mathbf{v}_2$ . The constituent materials, denoted by  $\Omega_1$  and  $\Omega_2$ , are assumed to be linear, elastic and modeled as Cauchy-type continua. Due to its periodicity, the medium can be fully characterized by the elementary unit cell  $\mathcal{Y}^\epsilon$ , which carries all the necessary information about the medium, including its symmetry properties. For illustrative purposes, we consider the example of square periodic media. In this specific case, the unit cell is defined as  $\mathcal{Y}^\epsilon = [0, l]^2$ , as depicted in figure 5.1b, where  $l$  is the size of the unit cell (characteristic length) and  $\mathcal{R}$  the lattice periodicity. As already pointed out in chapter 2, both the elasticity tensor and the mass density are  $\mathcal{Y}^\epsilon$ -periodic, meaning that

$$\begin{cases} \mathbf{C}^\epsilon(\mathbf{x}+\mathbf{v}_i) &= \mathbf{C}^\epsilon(\mathbf{x}) \\ \rho^\epsilon(\mathbf{x}+\mathbf{v}_i) &= \rho^\epsilon(\mathbf{x}) \end{cases}, \forall \mathbf{x} \in \Omega, \mathbf{v}_i \in \mathcal{R}, i = 1, 2 \quad (5.2.1)$$

We study elastic waves in heterogeneous, unbounded, periodic media with characteristic wavelength  $\lambda$  significantly longer than unit cell size. The condition for scale separation is given by the scale parameter  $\epsilon$ , defined as:

$$\epsilon = \frac{l}{\lambda} \ll 1.$$

---

<sup>1</sup>It is worth noting that the first reciprocity identity was previously established in [Boutin and Auriault, 1993], while the second one was partially developed in [Fish et al., 2002] and further completed in this work.

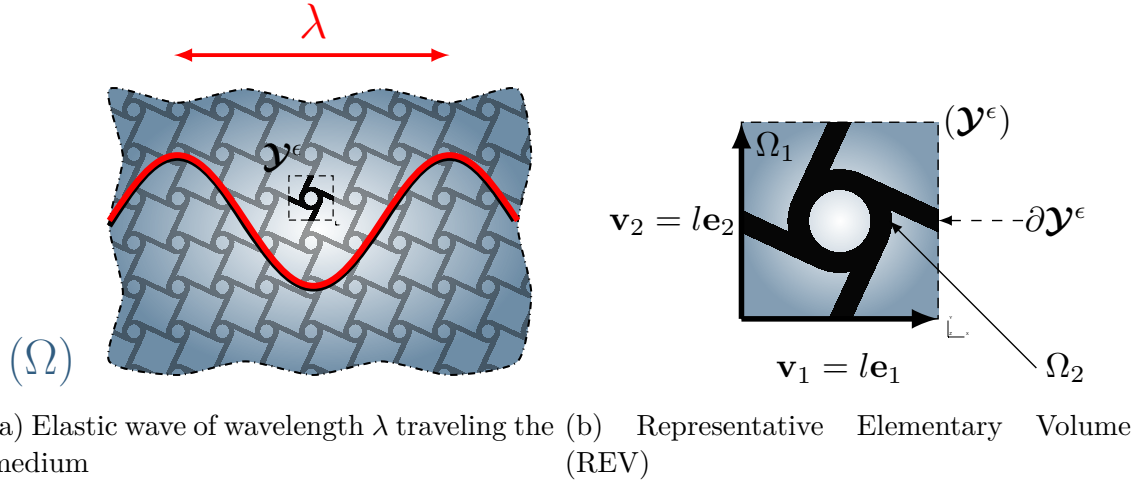


Figure 5.1: Schematics of an infinite heterogeneous periodic media and its unit cell

Therefore, we need to consider two scales: the macroscopic scale  $\mathcal{O}(\lambda)$  and the microscopic scale  $\mathcal{O}(l) \ll \lambda$ . The scale parameter  $\epsilon$  allows to represent both scales by introducing a macroscopic spatial variable  $\mathbf{x} \in \Omega$  (slow variable) and a microscopic spatial variable  $\mathbf{y} = \mathbf{x}/\epsilon - \lfloor \mathbf{x}/\epsilon \rfloor \in \mathcal{Y}^{\epsilon^2}$  (fast variable that describes local fluctuations), as depicted in section 5.2.1

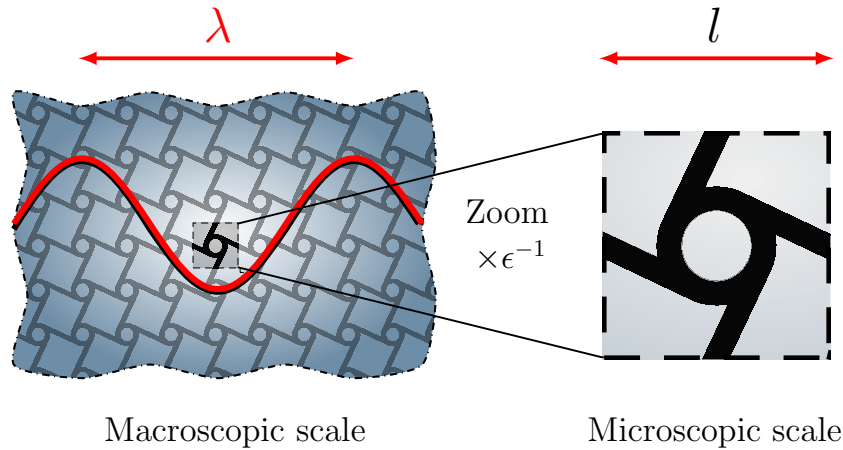


Figure 5.2: Two well distinct scales are considered: the macro-scale, described by  $\mathbf{x}$ , and the micro-scale, described by  $\mathbf{y}$

The medium being assumed to be macroscopically homogeneous, we then have

$$\begin{cases} \mathbf{C}^\epsilon(\mathbf{x}) = \mathbf{C}(\mathbf{y}) \\ \rho^\epsilon(\mathbf{x}) = \rho(\mathbf{y}) \end{cases}, \quad \text{with } \mathbf{y} = \mathbf{x}/\epsilon - \lfloor \mathbf{x}/\epsilon \rfloor \quad (5.2.2)$$

This means that the elasticity tensor  $\mathbf{C}$  and the mass density  $\rho$  are both  $\mathcal{Y}^\epsilon$ -periodic in  $\mathbf{y}$ .

<sup>2</sup>The notation  $\lfloor \cdot \rfloor$  denotes the closest lattice point chosen so that  $\mathbf{x}/\epsilon - \lfloor \mathbf{x}/\epsilon \rfloor$  always belong to the reference cell  $\mathcal{Y}^\epsilon$ .

## 5.2.2 Governing equations

Let us denote by  $\mathbf{u}(\mathbf{x}, t)$  the displacement at time  $t$  of the material point of the medium located at  $\mathbf{x}$ . The local elastodynamic equations written at the cell scale read

$$\boldsymbol{\varepsilon}(\mathbf{x}, t) := \frac{1}{2} [\mathbf{u}(\mathbf{x}, t) \otimes \boldsymbol{\nabla} + \boldsymbol{\nabla} \otimes \mathbf{u}(\mathbf{x}, t)] =: \mathbf{u}(\mathbf{x}, t) \otimes^s \boldsymbol{\nabla}, \quad \forall \mathbf{x} \in \Omega \quad (5.2.3)$$

$$\boldsymbol{\sigma}(\mathbf{x}, t) = \mathbf{C}^e(\mathbf{x}) : \boldsymbol{\varepsilon}(\mathbf{x}, t), \quad \forall \mathbf{x} \in \Omega \quad (5.2.4)$$

$$\boldsymbol{\nabla} \cdot \boldsymbol{\sigma}(\mathbf{x}, t) + \mathbf{f}(\mathbf{x}, t) = \rho^e(\mathbf{x}) \ddot{\mathbf{u}}(\mathbf{x}, t), \quad \forall \mathbf{x} \in \Omega \quad (5.2.5)$$

in which  $\mathbf{f}$  is the body force density. Using the constitutive equation 5.2.4 and the compatibility equation 5.2.3, the linear momentum balance equation 5.2.5 takes the following form

$$\boldsymbol{\nabla} \cdot \{ \mathbf{C}(\mathbf{x}) : (\mathbf{u}(\mathbf{x}, t) \otimes^s \boldsymbol{\nabla}) \} = \rho(\mathbf{x}) \ddot{\mathbf{u}}(\mathbf{x}, t) - \mathbf{f}(\mathbf{x}, t) \quad (5.2.6)$$

As said earlier, we will follow the approach introduced in [Boutin and Auriault, 1993], which consists of considering the propagation of time-harmonic waves of wavelength  $\lambda$ , under the hypothesis of small deformations<sup>3</sup>. Accordingly, applying the Fourier transform to 5.2.6 with respect to the time variable yields the local motion equation in the frequency domain:

$$\boldsymbol{\nabla} \cdot \{ \mathbf{C}(\mathbf{x}) : (\tilde{\mathbf{u}}(\mathbf{x}) \otimes^s \boldsymbol{\nabla}) \} + \omega^2 \rho(\mathbf{x}) \tilde{\mathbf{u}}(\mathbf{x}) = -\tilde{\mathbf{f}}(\mathbf{x}) \quad (5.2.7)$$

## 5.2.3 Two-scale asymptotic expansions

After introducing the slow and fast variables  $\mathbf{x}$  and  $\mathbf{y}$ , the (scalar, vector or tensor) fields are sought as functions of both variables, e.g.  $\mathbf{u}(\mathbf{x}) = \tilde{\mathbf{u}}(\mathbf{x}, \mathbf{y})$ ,  $\boldsymbol{\varepsilon}(\mathbf{x}) = \tilde{\boldsymbol{\varepsilon}}(\mathbf{x}, \mathbf{y}) \dots$ . We furthermore assume that all fields admit a multiscale expansion along powers of the scale parameter  $\epsilon$ . For instance, the displacement field is sought in the form

$$\tilde{\mathbf{u}}_\epsilon(\mathbf{x}) = \sum_{n=0}^{\infty} \epsilon^n \tilde{\mathbf{u}}_n(\mathbf{x}, \mathbf{y}) = \tilde{\mathbf{u}}_0(\mathbf{x}, \mathbf{y}) + \epsilon \tilde{\mathbf{u}}_1(\mathbf{x}, \mathbf{y}) + \epsilon^2 \tilde{\mathbf{u}}_2(\mathbf{x}, \mathbf{y}) + \epsilon^3 \dots, \quad (5.2.8)$$

where each coefficient  $\tilde{\mathbf{u}}_n(\mathbf{x}, \mathbf{y})$  is a function of the two variables  $\mathbf{x}$  and  $\mathbf{y}$  that is  $\mathcal{Y}$ -periodic with respect to the microscopic variable  $\mathbf{y}$ . Accordingly, the stress and strain fields admit the same kind of expansion:

$$\tilde{\boldsymbol{\sigma}}_\epsilon(\mathbf{x}) = \sum_{n=0}^{\infty} \epsilon^n \tilde{\boldsymbol{\sigma}}_n(\mathbf{x}, \mathbf{y}), \quad \tilde{\boldsymbol{\varepsilon}}_\epsilon(\mathbf{x}) = \sum_{n=0}^{\infty} \epsilon^n \tilde{\boldsymbol{\varepsilon}}_n(\mathbf{x}, \mathbf{y}). \quad (5.2.9)$$

One way to understand this ansatz is that, at each macroscopic point  $\mathbf{x}$ , the field  $\tilde{\mathbf{u}}_k(\mathbf{x}, \bullet)$  undergoes modulation as a result of the presence of intermediate small scales in the problem at the point  $\mathbf{x}$ . The modulation is incorporated and expressed through the component  $\tilde{\mathbf{u}}_k(\bullet, \mathbf{y})$  of the function  $\tilde{\mathbf{u}}_k$ .

---

<sup>3</sup>It is important to mention that the choice of the frequency regime is purely strategic in this study. The same analysis in the space-time regime has also been explored in [Fish et al., 2002]. It is merely a choice of notation, except for the definition of the reference wavelength  $\lambda$  which is easier for time-harmonic waves.

### 5.2.4 Homogenization procedure

In order to compute the coefficients  $\tilde{\mathbf{u}}_n(\mathbf{x}, \mathbf{y})$ , as said above, we insert 5.2.8 into 5.2.7 without the body force terms. The spatial differentiation operators  $\tilde{\mathbf{u}}_n(\mathbf{x}, \mathbf{y})$  must account for both scales, and thus have the form

$$\operatorname{div}(\bullet) := \{\nabla_x + \epsilon^{-1}\nabla_y\} \cdot (\bullet), \quad \operatorname{grad}(\bullet) := (\bullet) \otimes \{\nabla_x + \epsilon^{-1}\nabla_y\}.$$

This process leads to a cascade of equations, to be solved successively in increasing order of the power of  $\epsilon$ . Using the two-scale differential operators, the strain of  $\mathbf{u}$  is given by

$$\begin{aligned} \tilde{\mathbf{u}}_\epsilon(\mathbf{x}) \otimes^s \nabla &= \sum_{n=0}^{\infty} \epsilon^n \tilde{\mathbf{u}}_n \otimes^s \nabla_x + \epsilon^{-1} \sum_{n=0}^{\infty} \epsilon^n \tilde{\mathbf{u}}_n \otimes^s \nabla_y \\ &= \sum_{n=0}^{\infty} \epsilon^n \tilde{\mathbf{u}}_n \otimes^s \nabla_x + \sum_{n=0}^{\infty} \epsilon^{n-1} \tilde{\mathbf{u}}_n \otimes^s \nabla_y \\ &= \sum_{n=0}^{\infty} \epsilon^n \tilde{\mathbf{u}}_n \otimes^s \nabla_x + \sum_{n=1}^{\infty} \epsilon^{n-1} \tilde{\mathbf{u}}_n \otimes^s \nabla_y + \epsilon^{-1} \tilde{\mathbf{u}}_0 \otimes \nabla_y \\ &= \sum_{n=0}^{\infty} \epsilon^n (\tilde{\mathbf{u}}_n \otimes^s \nabla_x + \tilde{\mathbf{u}}_{n+1} \otimes^s \nabla_y) + \epsilon^{-1} \tilde{\mathbf{u}}_0 \otimes \nabla_y. \end{aligned} \tag{5.2.10}$$

By incorporating the expression above into the left-hand-side of the equation (5.2.7), we obtain

$$\begin{aligned} \nabla \cdot \{\mathbf{C}(\mathbf{y}) : (\tilde{\mathbf{u}} \otimes^s \nabla)\} &= \{\nabla_x + \epsilon^{-1}\nabla_y\} \cdot \left\{ \mathbf{C}(\mathbf{y}) : \sum_{n=0}^{\infty} \epsilon^n \tilde{\mathbf{u}}_n \otimes^s \{\nabla_x + \epsilon^{-1}\nabla_y\} \right\} \\ &= \epsilon^{-2} \nabla_y \cdot \{\mathbf{C}(\mathbf{y}) : (\tilde{\mathbf{u}}_0 \otimes^s \nabla_y)\} \\ &\quad + \epsilon^{-1} \nabla_x \cdot \{\mathbf{C}(\mathbf{y}) : (\tilde{\mathbf{u}}_0 \otimes^s \nabla_y)\} \end{aligned} \tag{5.2.11}$$

$$+ \epsilon^{-1} \nabla_y \cdot \{\mathbf{C}(\mathbf{y}) : (\tilde{\mathbf{u}}_0 \otimes^s \nabla_x + \tilde{\mathbf{u}}_1 \otimes^s \nabla_y)\} \tag{5.2.12}$$

$$\begin{aligned} &+ \sum_{n=0}^{\infty} \epsilon^n \nabla_x \cdot \{\mathbf{C}(\mathbf{y}) : (\tilde{\mathbf{u}}_{n+1} \otimes^s \nabla_x + \tilde{\mathbf{u}}_n \otimes^s \nabla_y)\} \\ &+ \sum_{n=0}^{\infty} \epsilon^n \nabla_y \cdot \{\mathbf{C}(\mathbf{y}) : (\tilde{\mathbf{u}}_{n+2} \otimes^s \nabla_x + \tilde{\mathbf{u}}_{n+1} \otimes^s \nabla_y)\} \end{aligned} \tag{5.2.13}$$

while the inertial term of 5.2.7 becomes

$$\omega^2 \rho^\epsilon(\mathbf{x}) \tilde{\mathbf{u}}(\mathbf{x}) = \omega^2 \rho(\mathbf{y}) \sum_{n=0}^{\infty} \epsilon^n \tilde{\mathbf{u}}_n. \tag{5.2.14}$$

By substituting the expansions 5.2.13 and 5.2.14 into the equation of motion 5.2.7, the latter becomes a power series in  $\epsilon$ . Setting each coefficient of that expansion to zero yields a cascade of differential equations. To make this cascade of equations explicit, we introduce the following operators [Gambin and Kröner, 1989]:

$$\begin{cases} \boldsymbol{\varepsilon}_x(\bullet) & := (\bullet) \otimes^s \nabla_x & \boldsymbol{\varepsilon}_y(\bullet) & := (\bullet) \otimes^s \nabla_y \\ \boldsymbol{\eta}_x(\bullet) & := \boldsymbol{\varepsilon}_x(\bullet) \otimes \nabla_x & \boldsymbol{\eta}_y(\bullet) & := \boldsymbol{\varepsilon}_y(\bullet) \otimes \nabla_y \\ \boldsymbol{\kappa}_x(\bullet) & := \boldsymbol{\eta}_x(\bullet) \otimes \nabla_x & \boldsymbol{\kappa}_y(\bullet) & := \boldsymbol{\eta}_y(\bullet) \otimes \nabla_y \end{cases} \tag{5.2.15}$$

$$\begin{cases} \mathcal{L}_{yy}\{\bullet\} & := -\nabla_y \cdot \{\mathbf{C}(\mathbf{y}) : (\bullet) \otimes^s \nabla_y\} \\ \mathcal{L}_{xy}\{\bullet\} & := -\nabla_x \cdot \{\mathbf{C}(\mathbf{y}) : (\bullet) \otimes^s \nabla_y\} - \nabla_y \cdot \{\mathbf{C}(\mathbf{y}) : (\bullet) \otimes^s \nabla_x\} \\ \mathcal{L}_{xx}\{\bullet\} & := -\nabla_x \cdot \{\mathbf{C}(\mathbf{y}) : (\bullet) \otimes^s \nabla_x\} \end{cases} \quad (5.2.16)$$

As a result, the functions  $\tilde{\mathbf{u}}_n(\mathbf{x}, \mathbf{y})$  satisfy the following cascade of equations:

$$\begin{cases} / \epsilon^{-2} : & \mathcal{L}_{yy}\{\tilde{\mathbf{u}}_0\} = 0 \\ / \epsilon^{-1} : & \mathcal{L}_{yy}\{\tilde{\mathbf{u}}_1\} + \mathcal{L}_{xy}\{\tilde{\mathbf{u}}_0\} = 0 \\ / \epsilon^0 : & \mathcal{L}_{yy}\{\tilde{\mathbf{u}}_2\} + \mathcal{L}_{xy}\{\tilde{\mathbf{u}}_1\} + \mathcal{L}_{xx}\{\tilde{\mathbf{u}}_0\} = \omega^2 \rho(\mathbf{y}) \tilde{\mathbf{u}}_0 \\ / \epsilon^1 : & \mathcal{L}_{yy}\{\tilde{\mathbf{u}}_3\} + \mathcal{L}_{xy}\{\tilde{\mathbf{u}}_2\} + \mathcal{L}_{xx}\{\tilde{\mathbf{u}}_1\} = \omega^2 \rho(\mathbf{y}) \tilde{\mathbf{u}}_1 \\ / \epsilon^n : & \mathcal{L}_{yy}\{\tilde{\mathbf{u}}_{n+2}\} + \mathcal{L}_{xy}\{\tilde{\mathbf{u}}_{n+1}\} + \mathcal{L}_{xx}\{\tilde{\mathbf{u}}_n\} = \omega^2 \rho(\mathbf{y}) \tilde{\mathbf{u}}_n \quad , \quad n \geq 2 \end{cases} \quad (5.2.17)$$

where in each problem of order  $\epsilon^{j-2}$ , the main unknown is the displacement field  $\tilde{\mathbf{u}}_j$ , while the fields  $\tilde{\mathbf{u}}_{j-1}$  and  $\tilde{\mathbf{u}}_{j-2}$  are considered as inputs to the problem. Solving the above system therefore allows to compute iteratively the terms of the two-scale expansion 5.2.8, which will be the subject of the next section. We will notably exhibit specific *cell problems*, whose solutions are a family of tensor fields  $\{\chi^j(\mathbf{y})\}_{j>0}$  called cell-functions or correctors, each of these tensors being a tensor of order  $j+2$ .

### 5.3 Second order homogenization of the 2D wave equations

In this section we will provide a detailed explanation of the homogenization process. First, we will present the main results, then the methodology to obtain formally the successive cell problems, their formulation and resolution in order to compute the corrector fields. Subsequently, we will provide the corresponding weak form and example of implementation, and give the definition of the homogenized tensors at each order. Our study will be restricted to the first four equations of 5.2.17, which involves considering the following ansatz for the displacement field expansion

$$\tilde{\mathbf{u}}_\epsilon(\mathbf{x}) = \tilde{\mathbf{u}}_0(\mathbf{x}, \mathbf{y}) + \epsilon \tilde{\mathbf{u}}_1(\mathbf{x}, \mathbf{y}) + \epsilon^2 \tilde{\mathbf{u}}_2(\mathbf{x}, \mathbf{y}) + \epsilon^3 \tilde{\mathbf{u}}_3(\mathbf{x}, \mathbf{y}) + o(\epsilon^3) \quad (5.3.1)$$

We will establish that solving 5.2.17 up to the  $\epsilon^1$ -order leads to the following separated variables solutions:

$$\begin{cases} / \epsilon^{-2} : & \tilde{\mathbf{u}}_0(\mathbf{x}, \mathbf{y}) = \bar{\mathbf{U}}_0(\mathbf{x}) \\ / \epsilon^{-1} : & \tilde{\mathbf{u}}_1(\mathbf{x}, \mathbf{y}) = \bar{\mathbf{U}}_1(\mathbf{x}) + \chi^1(\mathbf{y}) : \varepsilon_x(\bar{\mathbf{U}}_0(\mathbf{x})) \\ / \epsilon^0 : & \tilde{\mathbf{u}}_2(\mathbf{x}, \mathbf{y}) = \bar{\mathbf{U}}_2(\mathbf{x}) + \chi^1(\mathbf{y}) : \varepsilon_x(\bar{\mathbf{U}}_1(\mathbf{x})) + \chi^2(\mathbf{y}) : \eta_x(\bar{\mathbf{U}}_0(\mathbf{x})) \\ / \epsilon^1 : & \tilde{\mathbf{u}}_3(\mathbf{x}, \mathbf{y}) = \bar{\mathbf{U}}_3(\mathbf{x}) + \chi^1(\mathbf{y}) : \varepsilon_x(\bar{\mathbf{U}}_2(\mathbf{x})) + \chi^2(\mathbf{y}) : \eta_x(\bar{\mathbf{U}}_1(\mathbf{x})) \\ & \quad + \chi^3(\mathbf{y}) : \kappa_x(\bar{\mathbf{U}}_0(\mathbf{x})) \end{cases} \quad (5.3.2)$$

where  $\bar{\mathbf{U}}_n(\mathbf{x})$  are the macroscopic fields, depends only on the macroscopic variable  $\mathbf{x}$  and defined as the mean displacement fields over the cell

$$\bar{\mathbf{U}}_n(\mathbf{x}) = \langle \tilde{\mathbf{u}}_n(\mathbf{x}, \mathbf{y}) \rangle_{\mathcal{Y}^\epsilon} := \frac{1}{|\mathcal{Y}^\epsilon|} \int_{\mathcal{Y}^\epsilon} \tilde{\mathbf{u}}_n(\mathbf{x}, \mathbf{y}) d\mathbf{y};$$

and  $\chi^1(\mathbf{y}), \chi^2(\mathbf{y}), \chi^3(\mathbf{y})$  are the so-called cell functions, periodic and zero-mean over  $\mathcal{Y}^\epsilon$ , representing solutions of the first three cell problems<sup>4</sup>.

To obtain this result, we first observe that the equations in 5.2.17 have the form

$$\mathcal{L}_{yy}\{\tilde{\mathbf{u}}_n\} = \mathbf{g}_n(\mathbf{x}, \mathbf{y}),$$

where the right-hand side  $\mathbf{g}_n(\mathbf{x}, \mathbf{y})$  depends on  $\tilde{\mathbf{u}}_0, \dots, \tilde{\mathbf{u}}_{n-1}$ . Thus, each  $\tilde{\mathbf{u}}_n$  is sought as a  $\mathcal{Y}^\epsilon$ -periodic function of the fast variable  $\mathbf{y}$  that is parameterized (through the right-hand side) by the slow variable  $\mathbf{x}$ . The ensuing cascade of equations 5.2.17 is solved successively using the following lemma 3.1, which is a form of *Fredholm's alternative* [Allaire et al., 1997].

To establish a proper mathematical formalism before entering the detail of the iterative resolution, let us introduce the Sobolev space in which the solutions are defined. This definition will help us accurately formulate and present subsequent cell-problems.

### Definition : Sobolev spaces of periodic functions

We denote by  $H_{\text{per}}^1(\mathcal{Y}^\epsilon; \mathbb{R}^d)$  the closure of  $C_{\text{per}}^\infty(\mathcal{Y}^\epsilon; \mathbb{R}^d)$  for the  $H^1(\mathcal{Y}^\epsilon)$  norm (where  $C_{\text{per}}^\infty(\mathcal{Y}^\epsilon; \mathbb{R}^d)$  is the set of all vector  $C^\infty(\mathbb{R}^d)$  functions that are  $\mathcal{Y}^\epsilon$ -periodic). Then,  $H_{\#}^1(\mathcal{Y}^\epsilon; \mathbb{R}^d)$  is the subspace of all zero-mean vector functions in  $H_{\text{per}}^1(\mathcal{Y}^\epsilon)$ :

$$H_{\#}^1(\mathcal{Y}^\epsilon; \mathbb{R}^d) = \left\{ \mathbf{w} \in H_{\text{per}}^1(\mathcal{Y}^\epsilon), \langle \mathbf{w} \rangle_{\mathcal{Y}^\epsilon} = \mathbf{0} \right\}$$

### Lemma 3.1: Fredholm's alternative

For given  $\mathbf{g}(\mathbf{y}) \in L^2(\mathcal{Y}^\epsilon)$ , the problem

$$\mathcal{L}_{yy}\mathbf{w} = \mathbf{g} \quad \text{in } \mathcal{Y}^\epsilon, \quad \mathbf{w} \text{ } \mathcal{Y}^\epsilon\text{-periodic} \quad (5.3.3)$$

has a unique solution  $\mathbf{w} \in H_{\#}^1(\mathcal{Y}^\epsilon; \mathbb{R}^d)$  if and only if the right hand side satisfies the compatibility condition

$$\int_{\mathcal{Y}^\epsilon} \mathbf{g}(\mathbf{y}) d\mathbf{y} = \mathbf{0}. \quad (5.3.4)$$

In other words, the solution of 5.3.3 is unique up to an additive constant field, which is fixed by the zero-mean requirement featured in  $\mathbf{w} \in H_{\#}^1(\mathcal{Y}^\epsilon)$ .

## 5.3.1 Computation of $\tilde{\mathbf{u}}_0$

It follows from 5.2.17 that the  $\epsilon^{-2}$  order problem is of the form 5.3.3 with  $\mathbf{g} = \mathbf{0}$  and with  $\mathbf{x}$  a parameter. By virtue of the previous Lemma, the only  $\mathcal{Y}^\epsilon$ -periodic solution

<sup>4</sup>It is important to note that selecting zero-mean solutions over the unit cell is a strategic choice, but alternative options are also available. For instance, one can choose to either fix or not fix a non-null mean.

$\tilde{\mathbf{u}}_0(\mathbf{x}, \mathbf{y})$  of the problem

$$\mathcal{L}_{yy}\{\tilde{\mathbf{u}}_0\} = 0 \quad (5.3.5)$$

is constant with respect to  $\mathbf{y}$ , and hence is for some function  $\bar{\mathbf{U}}_0$  of the form

$$\tilde{\mathbf{u}}_0(\mathbf{x}, \mathbf{y}) = \bar{\mathbf{U}}_0(\mathbf{x}). \quad (5.3.6)$$

From a physical point of view, the macroscopic field  $\bar{\mathbf{U}}_0$  can be seen as large scale modulations of translatory rigid body motions, associated with a "zero-th" order constant cell solution  $\boldsymbol{\chi}^0 = \mathbf{I}$ .

### 5.3.2 Computation of $\tilde{\mathbf{u}}_1$ and first cell problem

The first-order term of the displacement expansion  $\tilde{\mathbf{u}}_1$  is obtained by solving the  $\mathcal{O}(\epsilon^{-1})$  problem in 5.2.17. Since  $\tilde{\mathbf{u}}_0$  is of the form 5.3.6, the governing problem for  $\tilde{\mathbf{u}}_1$  reads

$$\mathcal{L}_{yy}\{\tilde{\mathbf{u}}_1\} = \mathbf{g}_1, \quad \tilde{\mathbf{u}}_1 \text{ } \mathcal{Y}^\epsilon\text{-periodic, with } \mathbf{g}_1 = -\mathcal{L}_{xy}\{\bar{\mathbf{U}}_0\} = \nabla_y \cdot \{\mathbf{C}(\mathbf{y}) : \boldsymbol{\varepsilon}_x(\bar{\mathbf{U}}_0)\} \quad (5.3.7)$$

Being the gradient of an  $\mathbf{y}$ -periodic function, the source term  $\mathbf{g}_1$  immediately satisfies the compatibility condition 5.3.4. Equation 5.3.7 is hence, by Lemma 3.1, solvable in  $H_{\#}^1(\mathcal{Y}^\epsilon; \mathbb{R}^d)$  and its general solution can by linearity be written in the form

$$\tilde{\mathbf{u}}_1(\mathbf{x}, \mathbf{y}) = \bar{\mathbf{U}}_1(\mathbf{x}) + \boldsymbol{\chi}^1(\mathbf{y}) : \boldsymbol{\varepsilon}_x(\bar{\mathbf{U}}_0(\mathbf{x})) \quad (5.3.8)$$

where the third-order tensor  $\boldsymbol{\chi}^1$  is the first corrector, solution of the following problem:

#### First cell problem ( $/\epsilon^{-1}$ )

We call "first cell problem" the following PDE system with prescribed periodic boundary conditions

$$-\nabla_y \cdot \{\mathbf{C}(\mathbf{y}) : \boldsymbol{\varepsilon}_y(\boldsymbol{\chi}^{1\{kl\}})\} = \nabla_y \cdot \{\mathbf{C}(\mathbf{y}) : (\tilde{\mathbf{e}}_k \otimes \tilde{\mathbf{e}}_l)\} \quad \text{in } \mathcal{Y}^\epsilon \quad (5.3.9)$$

where  $\boldsymbol{\chi}^{1\{kl\}}(\mathbf{y}) \in H_{\#}^1(\mathcal{Y}^\epsilon)$  and  $\{kl\} = \{11, 22, 12\}$

The first cell problem can be viewed as a family of 3 elementary 2D problems posed on the unit cell  $\mathcal{Y}^\epsilon$  and indexed by  $\{kl\}$ , in which the loading is encoded by the second member. Hence,  $\boldsymbol{\chi}^{1\{kl\}}$  corresponds to the response of the unit cell, which means the displacement field due to prescribed macroscopic strain tensor  $\bar{\boldsymbol{\varepsilon}}^{(kl)} = \tilde{\mathbf{e}}_k \otimes \tilde{\mathbf{e}}_l$ , i.e.

$$\bar{\boldsymbol{\varepsilon}}^{(11)} = \begin{bmatrix} 1 & 0 \\ 0 & 0 \end{bmatrix}_{\mathcal{K}}, \quad \bar{\boldsymbol{\varepsilon}}^{(22)} = \begin{bmatrix} 0 & 0 \\ 0 & 1 \end{bmatrix}_{\mathcal{K}}, \quad \bar{\boldsymbol{\varepsilon}}^{(12)} = \frac{1}{2} \begin{bmatrix} 0 & \sqrt{2} \\ \sqrt{2} & 0 \end{bmatrix}_{\mathcal{K}}. \quad (5.3.10)$$

These problems are solved in a FEM code using the following weak form<sup>5</sup>.

<sup>5</sup>The constraints associated with the zero-mean value and periodicity of the solution can be enforced through the use of Lagrange multipliers. Interested readers can find further details on the implementation of these constraints in [Yvonnet, 2019].

### Weak form of the first cell problem

For each macroscopic loading  $\tilde{\mathbf{e}}_k \otimes \tilde{\mathbf{e}}_l$ , the weak of the first cell problem indexed by  $\{kl\}$  is : Find  $\chi^{1\{kl\}} \in H_{\#}^1(\mathcal{Y}^\epsilon)$  such that

$$\int_{\mathcal{Y}^\epsilon} \boldsymbol{\varepsilon}_y(\chi^{1\{kl\}}) : \mathbf{C} : \boldsymbol{\varepsilon}_y(\mathbf{v}) dy = - \int_{\mathcal{Y}^\epsilon} (\tilde{\mathbf{e}}_k \otimes^s \tilde{\mathbf{e}}_l) : \mathbf{C} : \boldsymbol{\varepsilon}_y(\mathbf{v}) dy \quad \forall \mathbf{v} \in H_{\#}^1(\mathcal{Y}^\epsilon) \quad (5.3.11)$$

Using index notation, we have more explicitly

$$\int_{\mathcal{Y}^\epsilon} \chi_{i,j}^{1\{kl\}} C_{ijpq} v_{p,q} dy = - \int_{\mathcal{Y}^\epsilon} C_{\{kl\}pq} v_{p,q} dy \quad (5.3.12)$$

*Remark:* In this chapter, the indices of the loadings will be represented using curly braces  $\{..\}$ . In cases where the loading is symmetric, such as in the first cell problem, it will be denoted within parentheses  $(..)$  for simplicity. It is important to note that this index symmetry of the loadings will thus be consistently interpreted as a tensorial symmetry, as introduced in Section 2 of Chapter 2.

After computing the first corrector, we now go back to the  $\epsilon^{-1}$  order problem 5.3.7. Replacing  $\tilde{\mathbf{u}}_1$  by the solution 5.3.8, it takes the form

$$\nabla_y \cdot \{ \mathbf{C}(\mathbf{y}) : [\bar{\mathbf{U}}_1 + \chi^1 : \boldsymbol{\varepsilon}_x(\bar{\mathbf{U}}_0)] \otimes \nabla_y \} + \nabla_y \cdot \{ \mathbf{C}(\mathbf{y}) : \boldsymbol{\varepsilon}_x(\bar{\mathbf{U}}_0) \} = 0,$$

i.e.

$$\nabla_y \cdot \{ \mathbf{C}(\mathbf{y}) : ([\boldsymbol{\varepsilon}_y(\chi^1) + \mathbf{1}] : \boldsymbol{\varepsilon}_x(\bar{\mathbf{U}}_0)) \} = 0 \quad (5.3.13)$$

or, in components :

$$\{ C_{ijpq} \left[ \chi_{p,q}^{1(kl)} + \frac{1}{2} (\delta_{pk} \delta_{ql} + \delta_{pl} \delta_{qk}) \right] \bar{U}_{0k,l} \}_{,j} = 0$$

From this order, and for the sake of clarity, we introduce the cell stress  $\mathbf{S}_0$  given by

$$\mathbf{S}_0(\mathbf{y}) = \mathbf{C}(\mathbf{y}) : [\boldsymbol{\varepsilon}_y(\chi^1(\mathbf{y})) + \mathbf{1}], \quad \mathcal{S}_{0ij}^{(kl)} = C_{ijpq} \chi_{p,q}^{1(kl)} + C_{ijkl}, \quad (5.3.14)$$

and equation 5.3.13 expresses that this cell stress is self-equilibrated:

$$\nabla_y \cdot \{ \mathbf{S}_0(\mathbf{y}) : \boldsymbol{\varepsilon}_x(\bar{\mathbf{U}}_0) \} = 0, \quad \text{i.e.} \quad \{ \mathcal{S}_{0ij}^{(kl)} \bar{U}_{0k,l} \}_{,j} = 0.$$

And since  $\bar{\mathbf{U}}_0$  does not depend on  $\mathbf{y}$ , this equation can be simply written as

$$\nabla_y \cdot \mathbf{S}_0(\mathbf{y}) = 0, \quad \text{i.e.} \quad \mathcal{S}_{0ij,j}^{(kl)} = 0$$

### 5.3.3 Computation of first-order homogenized tensors

Next,  $\tilde{\mathbf{u}}_2$  is to be found by solving the  $\mathcal{O}(\epsilon^0)$  equation of 5.2.17, which reads

$$\mathcal{L}_{yy} \{ \tilde{\mathbf{u}}_2 \} = \mathbf{g}_2, \quad \tilde{\mathbf{u}}_2 \text{ } \mathcal{Y}^\epsilon\text{-periodic,} \quad (5.3.15)$$

with

$$\begin{aligned} \mathbf{g}_2 &= -\mathcal{L}_{xy}\{\tilde{\mathbf{u}}_1\} - \mathcal{L}_{xx}\{\tilde{\mathbf{u}}_0\} + \omega^2 \rho(\mathbf{y}) \tilde{\mathbf{u}}_0 \\ &= \nabla_y \cdot \{\mathbf{C}(\mathbf{y}) : \varepsilon_x(\tilde{\mathbf{u}}_1)\} + \nabla_x \cdot \{\mathbf{C}(\mathbf{y}) : \varepsilon_y(\tilde{\mathbf{u}}_1)\} + \nabla_x \cdot \{\mathbf{C}(\mathbf{y}) : \varepsilon_x(\tilde{\mathbf{u}}_0)\} \end{aligned} \quad (5.3.16)$$

$$+ \omega^2 \rho(\mathbf{y}) \tilde{\mathbf{u}}_0 \quad (5.3.17)$$

From the expression of  $\tilde{\mathbf{u}}_1$  5.3.8, we have

$$\varepsilon_y(\tilde{\mathbf{u}}_1) = \varepsilon_y(\boldsymbol{\chi}^1) : \varepsilon_x(\bar{\mathbf{U}}_0), \quad \varepsilon_x(\tilde{\mathbf{u}}_1) = \varepsilon_x(\bar{\mathbf{U}}_1) + \boldsymbol{\chi}^1 : \boldsymbol{\eta}_x(\bar{\mathbf{U}}_0), \quad (5.3.18)$$

while  $\tilde{\mathbf{u}}_0 = \bar{\mathbf{U}}_0$  (see 5.3.6). This allows to recast 5.3.17 as

$$\begin{aligned} \mathbf{g}_2 &= \nabla_y \cdot \{\mathbf{C}(\mathbf{y}) : [\varepsilon_x(\bar{\mathbf{U}}_1) + \boldsymbol{\chi}^1 : \boldsymbol{\eta}_x(\bar{\mathbf{U}}_0)]\} \\ &\quad + \nabla_x \cdot \{\mathbf{C}(\mathbf{y}) : [\varepsilon_y(\boldsymbol{\chi}^1) + \mathbf{1}] : \varepsilon_x(\bar{\mathbf{U}}_0)\} + \omega^2 \rho(\mathbf{y}) \bar{\mathbf{U}}_0 \\ &= \nabla_y \cdot \{\mathbf{C}(\mathbf{y}) : [\varepsilon_x(\bar{\mathbf{U}}_1) + \boldsymbol{\chi}^1 : \boldsymbol{\eta}_x(\bar{\mathbf{U}}_0)]\} + \nabla_x \cdot \{\boldsymbol{\mathcal{S}}_0 : \varepsilon_x(\bar{\mathbf{U}}_0)\} + \omega^2 \rho(\mathbf{y}) \bar{\mathbf{U}}_0 \end{aligned} \quad (5.3.19)$$

Since, in addition, the integral of  $\nabla_y \cdot \{\mathbf{H}_1(\mathbf{x}, \mathbf{y})\}$  over  $\mathcal{Y}^\epsilon$  vanishes because the quantity  $\mathbf{H}_1(\mathbf{x}, \mathbf{y}) = \mathbf{C}(\mathbf{y}) : [\varepsilon_x(\bar{\mathbf{U}}_1) + \boldsymbol{\chi}^1 : \boldsymbol{\eta}_x(\bar{\mathbf{U}}_0)]$  is  $\mathcal{Y}^\epsilon$ -periodic, the compatibility condition 5.3.4 for  $\mathbf{g}_2$  becomes

$$\int_{\mathcal{Y}^\epsilon} \nabla_x \cdot \{\boldsymbol{\mathcal{S}}_0(\mathbf{y}) : \varepsilon_x(\bar{\mathbf{U}}_0)\} \mathrm{d}\mathbf{y} + \omega^2 \left( \int_{\mathcal{Y}^\epsilon} \rho(\mathbf{y}) \mathrm{d}\mathbf{y} \right) \bar{\mathbf{U}}_0 = 0 \quad (5.3.20)$$

We thus obtain the macroscopic balance equation at order  $\epsilon^0$

$$\nabla_x \cdot \{\mathbf{C}_0^H : \varepsilon_x(\bar{\mathbf{U}}_0)\} + \omega^2 \varrho_0^H \bar{\mathbf{U}}_0 = 0, \quad (5.3.21)$$

Where  $\mathbf{C}_0^H$  and  $\varrho_0^H$  are respectively, the effective elasticity tensor and the effective mass density.

### Definition : First-order homogenized tensor

The first-order homogenized elasticity tensor  $\mathbf{C}_0^H$  and mass density  $\varrho_0^H$  are defined by

$$\mathbf{C}_0^H = \langle \boldsymbol{\mathcal{S}}_0 \rangle_{\mathcal{Y}^\epsilon} = \frac{1}{|\mathcal{Y}^\epsilon|} \int_{\mathcal{Y}^\epsilon} \mathbf{C}(\mathbf{y}) : [\varepsilon_y(\boldsymbol{\chi}^1(\mathbf{y})) + \mathbf{1}] \mathrm{d}\mathbf{y} \quad , \quad \varrho_0^H = \frac{1}{|\mathcal{Y}^\epsilon|} \int_{\mathcal{Y}^\epsilon} \rho(\mathbf{y}) \mathrm{d}\mathbf{y}.$$

Using component notation, the tensor  $\mathbf{C}_0^H$  is thus given by

$$C_{0ijkl}^H = \langle \mathcal{S}_{0ij}^{(kl)} \rangle_{\mathcal{Y}^\epsilon} = \frac{1}{|\mathcal{Y}^\epsilon|} \int_{\mathcal{Y}^\epsilon} (C_{ijpq} \chi_{p,q}^{1(kl)} + C_{ijkl}) \mathrm{d}\mathbf{y}.$$

This tensor satisfy the following index permutation symmetry

$$C_{0ijkl}^H = C_{0jikl}^H = C_{0ijlk}^H = C_{0klij}^H,$$

hence, its space vector is given by

$$\mathbf{C}_0^H \in \{\mathbf{T} \in \mathbb{S}^2(\mathbb{S}^2(\mathbb{R}^2)) \mid \mathbf{T}_{(ij) \ (kl)}\}$$

*Proof of the index symmetry of  $\mathbf{C}_0^H$ .* (i) *Minor symmetry* Due to the symmetry of the elasticity tensor and the loading, it is evident that the homogenized tensor  $\mathbf{C}_0^H$  possesses naturally the minor symmetry. We have :

$$C_{0ijkl}^H = \langle C_{ijpq} \chi_{p,q}^{1(kl)} + C_{ijkl} \rangle_{\mathcal{Y}^\epsilon} = \langle C_{jipq} \chi_{p,q}^{1(kl)} + C_{jikl} \rangle_{\mathcal{Y}^\epsilon} = \langle C_{ijpq} \chi_{p,q}^{1(lk)} + C_{ijlk} \rangle_{\mathcal{Y}^\epsilon}$$

i.e.

$$C_{0ijkl}^H = C_{0jikl}^H = C_{0ijlk}^H$$

(ii) *Major symmetry* The major symmetry is proven using a first reciprocity identity between the components of the cell problem. Let's recall the weak form of the first cell problem

$$\int_{\mathcal{Y}^\epsilon} \chi_{p,q}^{1(ij)} C_{pqrs} v_{r,s} dy = - \int_{\mathcal{Y}^\epsilon} C_{rs(ij)} v_{r,s} dy$$

By setting  $v_r = \chi_r^{1(kl)}$  as the trial field in the weak form associated with  $\chi^{1(ij)}$ , and vice versa,  $v_r = \chi_r^{1(ij)}$  in the weak form associated with  $\chi^{1(kl)}$ , we obtain:

$$\begin{aligned} (a) \quad & \int_{\mathcal{Y}^\epsilon} \chi_{p,q}^{1(ij)} C_{pqrs} \chi_{r,s}^{1(kl)} dy = - \int_{\mathcal{Y}^\epsilon} C_{rs(ij)} \chi_{r,s}^{1(kl)} dy \\ (b) \quad & \int_{\mathcal{Y}^\epsilon} \chi_{p,q}^{1(kl)} C_{pqrs} \chi_{r,s}^{1(ij)} dy = - \int_{\mathcal{Y}^\epsilon} C_{rs(kl)} \chi_{r,s}^{1(ij)} dy \end{aligned} \quad (5.3.22)$$

Due to the symmetry of the left-hand-side bilinear forms and taking into account the symmetry of  $\mathbf{C}$ , we obtain

$$\int_{\mathcal{Y}^\epsilon} C_{(ij)rs} \chi_{r,s}^{1(kl)} dy = \int_{\mathcal{Y}^\epsilon} C_{(kl)rs} \chi_{r,s}^{1(ij)} dy,$$

which implies

$$C_{0ijkl}^H = \langle C_{(ij)rs} \chi_{r,s}^{1(kl)} + C_{ijkl} \rangle_{\mathcal{Y}^\epsilon} = \langle C_{(kl)rs} \chi_{r,s}^{1(ij)} + C_{kl ij} \rangle_{\mathcal{Y}^\epsilon} = C_{0kl ij}^H.$$

□

### 5.3.4 Computation of $\tilde{\mathbf{u}}_2$ and second cell problem

We now return to the governing problem 5.3.15 for  $\tilde{\mathbf{u}}_2$ . The relation 5.3.21, which ensures its solvability, may now be used to simplify its right-hand side  $\mathbf{g}_2$ . From 5.3.21, we deduce

$$\omega^2 \rho(\mathbf{y}) \bar{\mathbf{U}}_0 = -\beta(\mathbf{y}) \nabla_x \cdot \{ \mathbf{C}_0^H : \boldsymbol{\varepsilon}_x(\bar{\mathbf{U}}_0) \},$$

where  $\beta(\mathbf{y}) = \rho(\mathbf{y})/\varrho_0^H$ . Putting this expression of  $\bar{\mathbf{U}}_0$  in 5.3.19, equation 5.3.15 becomes

$$\mathcal{L}_{yy} \{ \tilde{\mathbf{u}}_2 \} = \nabla_y \cdot \{ \mathbf{C}(\mathbf{y}) : [\boldsymbol{\varepsilon}_x(\bar{\mathbf{U}}_1) + \boldsymbol{\chi}^1 : \boldsymbol{\eta}_x(\bar{\mathbf{U}}_0)] \} + \nabla_x \cdot \{ (\boldsymbol{\mathcal{S}}_0 - \beta(\mathbf{y}) \mathbf{C}_0^H) : \boldsymbol{\varepsilon}_x(\bar{\mathbf{U}}_0) \}. \quad (5.3.23)$$

In view of the above form of its right-hand side, the general  $\mathcal{Y}^\epsilon$ -periodic solution of problem 5.3.23 can be written in the form

$$\tilde{\mathbf{u}}_2(\mathbf{x}, \mathbf{y}) = \bar{\mathbf{U}}_2(\mathbf{x}) + \boldsymbol{\chi}^1(\mathbf{y}) : \boldsymbol{\varepsilon}_x(\bar{\mathbf{U}}_1(\mathbf{x})) + \boldsymbol{\chi}^2(\mathbf{y}) : \boldsymbol{\eta}_x(\bar{\mathbf{U}}_0(\mathbf{x})), \quad (5.3.24)$$

where  $\bar{\mathbf{U}}_2(\mathbf{x})$  is the average of  $\tilde{\mathbf{u}}_2(\mathbf{x}, \mathbf{y})$  over  $\mathcal{Y}^\epsilon$ ;  $\boldsymbol{\chi}^1$  solves the first cell problem; and the fourth order tensor  $\boldsymbol{\chi}^2(\mathbf{y})$  is the second cell-function. Before setting up the second cell problem, some simplifications need to be made on the equation 5.3.23. From the ansatz 5.3.24, we have

$$\boldsymbol{\varepsilon}_y(\tilde{\mathbf{u}}_2) = \boldsymbol{\varepsilon}_y(\boldsymbol{\chi}^1) : \boldsymbol{\varepsilon}_x(\bar{\mathbf{U}}_1) + \boldsymbol{\varepsilon}_y(\boldsymbol{\chi}^2) : \boldsymbol{\eta}_x(\bar{\mathbf{U}}_0). \quad (5.3.25)$$

On using the above expression and taking into account 5.3.13, equation 5.3.23 becomes  $-\nabla_y \cdot \{\mathbf{C}(\mathbf{y}) : [\boldsymbol{\varepsilon}_y(\boldsymbol{\chi}^2) : \boldsymbol{\eta}_x(\bar{\mathbf{U}}_0) + \boldsymbol{\chi}^1 : \boldsymbol{\eta}_x(\bar{\mathbf{U}}_0)]\} = \nabla_x \cdot \{(\mathbf{S}_0 - \beta(\mathbf{y})\mathbf{C}_0^H) : \boldsymbol{\varepsilon}_x(\bar{\mathbf{U}}_0)\}$

### Second cell problem ( $/\epsilon^0$ )

We call “second cell problem” the following PDE system with prescribed periodic boundary conditions

$$-\nabla_y \cdot \{\mathbf{C}(\mathbf{y}) : \boldsymbol{\varepsilon}_y(\boldsymbol{\chi}^{2\{(kl)m\}})\} = \nabla_x \cdot \{\mathbf{S}_{0\{m\}} - \beta(\mathbf{y})\mathbf{C}_{0\{(kl)m\}}^H\} + \nabla_y \cdot \{\mathbf{C}(\mathbf{y}) \cdot \boldsymbol{\chi}^{1\{(kl)\}}\} \quad , \quad \text{in } \mathcal{Y}^\epsilon \quad (5.3.26)$$

where  $\boldsymbol{\chi}^{1\{(kl)m\}}(\mathbf{y}) \in H_{\#}^1(\mathcal{Y}^\epsilon)$  and  $\{(kl)m\} = \{111, 221, 122, 222, 112, 121\}$

The corresponding weak form can be written as follows:

### Weak form of the second cell problem

For each macroscopic loading indexed by  $\{(kl)m\}$ , the weak of the second cell problem is: Find  $\boldsymbol{\chi}^{2\{(kl)m\}} \in H_{\#}^1(\mathcal{Y}^\epsilon)$  such that

$$\begin{aligned} & \int_{\mathcal{Y}^\epsilon} \boldsymbol{\varepsilon}_y(\boldsymbol{\chi}^{2\{(kl)m\}}) : \mathbf{C} : \boldsymbol{\varepsilon}_y(\mathbf{v}) \, dy \\ &= \underbrace{\int_{\mathcal{Y}^\epsilon} (\mathbf{S}_{0\{m\}} - \beta(\mathbf{y})\mathbf{C}_{0\{(kl)m\}}^H) \cdot \mathbf{v} \, dy}_{\text{loading terms}} - \int_{\mathcal{Y}^\epsilon} (\mathbf{C}_{\{m\}} \cdot \boldsymbol{\chi}^{1\{(kl)\}}) : \boldsymbol{\varepsilon}_y(\mathbf{v}) \, dy \quad \forall \mathbf{v} \in H_{\#}^1(\mathcal{Y}^\epsilon). \end{aligned}$$

Using index notation, we have more explicitly

$$\int_{\mathcal{Y}^\epsilon} \chi_{p,q}^{2\{(kl)m\}} C_{pqrs} v_{r,s} \, dy = \int_{\mathcal{Y}^\epsilon} (\mathbf{S}_{0\{m\}r}^{(kl)} - \beta(\mathbf{y})C_{0\{(kl)\{m\}r}^H) v_r \, dy - \int_{\mathcal{Y}^\epsilon} \chi_p^{1\{(kl)\}} C_{p\{m\}rs} v_{r,s} \, dy$$

Similarly to what was said for the first cell problem, the tensor-valued cell solution  $\boldsymbol{\chi}^{2\{(kl)m\}}$  may be seen as a collection of six solutions corresponding to elementary loads defined in terms of the previous cell solutions  $\boldsymbol{\chi}^{1\{(kl)\}}$  and  $\mathbf{S}_{0\{m\}r}^{(kl)}$  and the material fields  $\mathbf{C}$  and  $\rho$ .

## 5.3.5 Computation of the second-order homogenized coupling tensors

Next,  $\tilde{\mathbf{u}}_3$  is to be found by solving the  $\mathcal{O}(\epsilon)$  equation of 5.2.17, which reads

$$\mathcal{L}_{yy}\{\tilde{\mathbf{u}}_3\} = \mathbf{g}_3, \quad \tilde{\mathbf{u}}_3 \text{ } \mathcal{Y}^\epsilon\text{-periodic,} \quad (5.3.27)$$

with

$$\begin{aligned} \mathbf{g}_3 &= -\mathcal{L}_{xy}\{\tilde{\mathbf{u}}_2\} - \mathcal{L}_{xx}\{\tilde{\mathbf{u}}_1\} + \omega^2 \rho(\mathbf{y}) \tilde{\mathbf{u}}_1 \\ &= \nabla_y \cdot \{\mathbf{C}(\mathbf{y}) : \boldsymbol{\varepsilon}_x(\tilde{\mathbf{u}}_2)\} + \nabla_x \cdot \{\mathbf{C}(\mathbf{y}) : \boldsymbol{\varepsilon}_y(\tilde{\mathbf{u}}_2)\} + \nabla_x \cdot \{\mathbf{C}(\mathbf{y}) : \boldsymbol{\varepsilon}_x(\tilde{\mathbf{u}}_1)\} \end{aligned} \quad (5.3.28)$$

$$+ \omega^2 \rho(\mathbf{y}) \tilde{\mathbf{u}}_1 \quad (5.3.29)$$

From the expression of  $\tilde{\mathbf{u}}_2$  5.3.24, we have

$$\begin{aligned} \boldsymbol{\varepsilon}_y(\tilde{\mathbf{u}}_2) &= \boldsymbol{\varepsilon}_y(\boldsymbol{\chi}^1) : \boldsymbol{\varepsilon}_x(\bar{\mathbf{U}}_1) + \boldsymbol{\varepsilon}_y(\boldsymbol{\chi}^2) : \boldsymbol{\eta}_x(\bar{\mathbf{U}}_0), \\ \boldsymbol{\varepsilon}_x(\tilde{\mathbf{u}}_2) &= \boldsymbol{\varepsilon}_x(\bar{\mathbf{U}}_2) + \boldsymbol{\chi}^1 : \boldsymbol{\eta}_x(\bar{\mathbf{U}}_1) + \boldsymbol{\chi}^2 : \boldsymbol{\kappa}_x(\bar{\mathbf{U}}_0) \end{aligned} \quad (5.3.30)$$

which, used together with 5.3.18 and the ansatz 5.3.8 in the summands of 5.3.29, yields

$$\begin{aligned} \mathbf{g}_3 &= \nabla_y \cdot \{\mathbf{C}(\mathbf{y}) : [\boldsymbol{\varepsilon}_x(\bar{\mathbf{U}}_2) + \boldsymbol{\chi}^1 : \boldsymbol{\eta}_x(\bar{\mathbf{U}}_1) + \boldsymbol{\chi}^2 : \boldsymbol{\kappa}_x(\bar{\mathbf{U}}_0)]\} \\ &\quad + \nabla_x \cdot \{\mathbf{C}(\mathbf{y}) : [\boldsymbol{\varepsilon}_y(\boldsymbol{\chi}^1) : \boldsymbol{\varepsilon}_x(\bar{\mathbf{U}}_1) + \boldsymbol{\varepsilon}_y(\boldsymbol{\chi}^2) : \boldsymbol{\eta}_x(\bar{\mathbf{U}}_0)]\} \\ &\quad + \nabla_x \cdot \{\mathbf{C}(\mathbf{y}) : [\boldsymbol{\varepsilon}_x(\bar{\mathbf{U}}_1) + \boldsymbol{\chi}^1 : \boldsymbol{\eta}_x(\bar{\mathbf{U}}_0)]\} \end{aligned} \quad (5.3.31)$$

$$\begin{aligned} &\quad + \omega^2 \rho(\mathbf{y}) [\bar{\mathbf{U}}_1(\mathbf{x}) + \boldsymbol{\chi}^1(\mathbf{y}) : \boldsymbol{\varepsilon}_x(\bar{\mathbf{U}}_0(\mathbf{x}))] \\ &= \nabla_y \cdot \{\mathbf{C}(\mathbf{y}) : [\boldsymbol{\varepsilon}_x(\bar{\mathbf{U}}_2) + \boldsymbol{\chi}^1 : \boldsymbol{\eta}_x(\bar{\mathbf{U}}_1) + \boldsymbol{\chi}^2 : \boldsymbol{\kappa}_x(\bar{\mathbf{U}}_0)]\} \\ &\quad + \nabla_x \cdot \{\boldsymbol{\mathcal{S}}_0 : \boldsymbol{\varepsilon}_x(\bar{\mathbf{U}}_1) + \boldsymbol{\mathcal{S}}_1 : \boldsymbol{\eta}_x(\bar{\mathbf{U}}_0)\} \end{aligned} \quad (5.3.32)$$

$$+ \omega^2 \rho(\mathbf{y}) [\bar{\mathbf{U}}_1(\mathbf{x}) + \boldsymbol{\chi}^1(\mathbf{y}) : \boldsymbol{\varepsilon}_x(\bar{\mathbf{U}}_0(\mathbf{x}))] \quad (5.3.33)$$

wherein  $\boldsymbol{\mathcal{S}}_1$  is the second-order cell stress, introduced here for the sake of clarity

$$\boldsymbol{\mathcal{S}}_1 = \mathbf{C}(\mathbf{y}) : [\boldsymbol{\varepsilon}_y(\boldsymbol{\chi}^2(\mathbf{y})) + \boldsymbol{\chi}^1(\mathbf{y}) \hat{\otimes} \mathbf{I}], \quad \mathcal{S}_{1ij}^{\{(kl)m\}} = C_{ijpq} (\chi_{p,q}^{2\{(kl)m\}} + \chi_p^{1(kl)} \delta_{q\{m\}}).$$

Since, in addition, the integral of  $\nabla_y \cdot \{\mathbf{H}_2(\mathbf{x}, \mathbf{y})\}$  vanishes because the quantity  $\mathbf{H}_2(\mathbf{x}, \mathbf{y}) = \mathbf{C}(\mathbf{y}) : [\boldsymbol{\varepsilon}_x(\bar{\mathbf{U}}_2) + \boldsymbol{\chi}^1 : \boldsymbol{\eta}_x(\bar{\mathbf{U}}_1) + \boldsymbol{\chi}^2 : \boldsymbol{\kappa}_x(\bar{\mathbf{U}}_0)]$  is  $\mathcal{Y}^\epsilon$ -periodic, the compatibility condition 5.3.4 for  $\mathbf{g}_3$  becomes

$$\begin{aligned} &\int_{\mathcal{Y}^\epsilon} (\nabla_x \cdot \{\boldsymbol{\mathcal{S}}_0 : \boldsymbol{\varepsilon}_x(\bar{\mathbf{U}}_1) + \boldsymbol{\mathcal{S}}_1 : \boldsymbol{\eta}_x(\bar{\mathbf{U}}_0)\}) \, d\mathbf{y} \\ &\quad + \omega^2 \int_{\mathcal{Y}^\epsilon} (\rho(\mathbf{y}) [\bar{\mathbf{U}}_1(\mathbf{x}) + \boldsymbol{\chi}^1(\mathbf{y}) : \boldsymbol{\varepsilon}_x(\bar{\mathbf{U}}_0(\mathbf{x}))]) \, d\mathbf{y} = 0. \end{aligned} \quad (5.3.34)$$

This provides the sought macroscopic balance equation at order  $\epsilon^1$

$$\nabla_x \{\mathbf{C}_0^H : \boldsymbol{\varepsilon}_x(\bar{\mathbf{U}}_1)\} + \omega^2 \varrho_0 \bar{\mathbf{U}}_1 = -\nabla_x \{\mathbf{C}_1^H : \boldsymbol{\eta}_x(\bar{\mathbf{U}}_0)\} - \omega^2 \boldsymbol{\varrho}_1^H : \boldsymbol{\varepsilon}_x(\bar{\mathbf{U}}_0), \quad (5.3.35)$$

where the homogenized elastic and inertial coupling tensors, denoted as  $\mathbf{C}_1^H$  and  $\boldsymbol{\varrho}_1^H$  respectively, are given by

$$\begin{aligned} \mathbf{C}_1^H &= \langle \boldsymbol{\mathcal{S}}_1 \rangle_{\mathcal{Y}^\epsilon} = \frac{1}{|\mathcal{Y}^\epsilon|} \int_{\mathcal{Y}^\epsilon} \mathbf{C}(\mathbf{y}) : [\boldsymbol{\varepsilon}_y(\boldsymbol{\chi}^2(\mathbf{y})) + \boldsymbol{\chi}^1(\mathbf{y}) \hat{\otimes} \mathbf{I}] \, d\mathbf{y} \\ \text{i.e. } \mathcal{C}_{1ijklm}^H &= \langle \mathcal{S}_{1ij}^{\{(kl)m\}} \rangle_{\mathcal{Y}^\epsilon} = \frac{1}{|\mathcal{Y}^\epsilon|} \int_{\mathcal{Y}^\epsilon} C_{(ij)pq} (\chi_{p,q}^{2\{(kl)m\}} + \chi_p^{1(kl)} \delta_{q\{m\}}) \, d\mathbf{y} \end{aligned}$$

and:

$$\begin{aligned} \boldsymbol{\varrho}_1^H &= \frac{1}{|\mathcal{Y}^\epsilon|} \int_{\mathcal{Y}^\epsilon} \rho(\mathbf{y}) \boldsymbol{\chi}^1(\mathbf{y}) d\mathbf{y} \\ \text{i.e. } \varrho_{1pkl}^H &= \frac{1}{|\mathcal{Y}^\epsilon|} \int_{\mathcal{Y}^\epsilon} \rho \chi_p^{1(kl)} d\mathbf{y} \end{aligned}$$

These tensors satisfy the following index permutation symmetry

$$C_{1ijklm}^H = C_{1jiklm}^H = C_{1ijlkm}^H \quad , \quad \varrho_{1pkl}^H = \varrho_{1plk}^H.$$

Therefore, the corresponding tensor space for these tensors can be defined as follows:

$$\mathbf{C}_1^H \in \{\mathbf{T} \in \mathbb{S}^2(\mathbb{S}^2(\mathbb{R}^2)) \otimes \mathbb{R}^2 \mid \mathbf{T}_{(ij)p(kl)}\}, \quad \boldsymbol{\varrho}_1^H \in \{\mathbf{T} \in \mathbb{S}^2(\mathbb{R}^2) \otimes \mathbb{R}^2 \mid \mathbf{T}_{(kl)m}\}$$

### 5.3.6 Computation of $\tilde{\mathbf{u}}_3$ and third cell problem

We now return to the governing problem 5.3.27 for  $\tilde{\mathbf{u}}_3$ , whose solvability is ensured by relation 5.3.35. The latter may now be used to simplify the right-hand side  $\mathbf{g}_3$  of problem 5.3.27. Equation 5.3.35 multiplied by  $\beta$  produces

$$\omega^2 \rho(\mathbf{y}) \bar{\mathbf{U}}_1(\mathbf{x}) = -\beta(\mathbf{y}) \left[ \nabla_x \cdot \{ \mathbf{C}_0^H : \boldsymbol{\varepsilon}_x(\bar{\mathbf{U}}_1) + \mathbf{C}_1^H : \boldsymbol{\eta}_x(\bar{\mathbf{U}}_0) \} + \omega^2 \boldsymbol{\varrho}_1^H : \boldsymbol{\varepsilon}_x(\bar{\mathbf{U}}_0) \right] \quad (5.3.36)$$

which, inserted in 5.3.33, allows to reformulate  $\mathbf{g}_3$  as

$$\begin{aligned} \mathbf{g}_3 &= \nabla_y \cdot \{ \mathbf{C}(\mathbf{y}) : [\boldsymbol{\varepsilon}_x(\bar{\mathbf{U}}_2) + \boldsymbol{\chi}^1 : \boldsymbol{\eta}_x(\bar{\mathbf{U}}_1) + \boldsymbol{\chi}^2 : \boldsymbol{\kappa}_x(\bar{\mathbf{U}}_0)] \} \\ &\quad + \nabla_x \cdot \{ (\mathcal{S}_0 - \beta(\mathbf{y}) \mathbf{C}_0^H) : \boldsymbol{\varepsilon}_x(\bar{\mathbf{U}}_1) \} \\ &\quad + \nabla_x \cdot \{ (\mathcal{S}_1 - \beta(\mathbf{y}) \mathbf{C}_1^H) : \boldsymbol{\eta}_x(\bar{\mathbf{U}}_0) \} \end{aligned} \quad (5.3.37)$$

$$+ \omega^2 \left( \rho(\mathbf{y}) \boldsymbol{\chi}^1(\mathbf{y}) - \beta(\mathbf{y}) \boldsymbol{\varrho}_1^H \right) : \boldsymbol{\varepsilon}_x(\bar{\mathbf{U}}_0(\mathbf{x})) \quad (5.3.38)$$

Moreover, the inertial term in the above expression can be reformulated using the macroscopic balance equation 5.3.21 at order  $\epsilon^0$ , which provides

$$-\omega^2 \boldsymbol{\varepsilon}_x(\bar{\mathbf{U}}_0) = \frac{1}{\varrho_0^H} \left( \nabla_x \cdot \{ \mathbf{C}_0^H : \boldsymbol{\varepsilon}_x(\bar{\mathbf{U}}_0) \} \right) \otimes \nabla_x \quad (5.3.39)$$

Substituting this expression into 5.3.38, equation 5.3.27 becomes

$$\begin{aligned} \mathcal{L}_{yy} \{ \tilde{\mathbf{u}}_3 \} &= \nabla_y \cdot \{ \mathbf{C}(\mathbf{y}) : [\boldsymbol{\varepsilon}_x(\bar{\mathbf{U}}_2) \\ &\quad + \boldsymbol{\chi}^1 : \boldsymbol{\eta}_x(\bar{\mathbf{U}}_1) + \boldsymbol{\chi}^2 : \boldsymbol{\kappa}_x(\bar{\mathbf{U}}_0)] \} \\ &\quad + \nabla_x \cdot \{ (\mathcal{S}_0 - \beta(\mathbf{y}) \mathbf{C}_0^H) : \boldsymbol{\varepsilon}_x(\bar{\mathbf{U}}_1) \} + \nabla_x \cdot \{ (\mathcal{S}_1 - \beta(\mathbf{y}) \mathbf{C}_1^H) : \boldsymbol{\eta}_x(\bar{\mathbf{U}}_0) \} \\ &\quad + \beta(\mathbf{y}) \left( \frac{\boldsymbol{\varrho}_1^H}{\varrho_0^H} - \boldsymbol{\chi}^1 \right) : \left( \nabla_x \cdot \{ \mathbf{C}_0^H : \boldsymbol{\varepsilon}_x(\bar{\mathbf{U}}_0) \} \right) \otimes \nabla_x \end{aligned} \quad (5.3.40)$$

Since its right-hand side satisfies the compatibility condition 5.3.4, equation 5.3.40 has  $\mathcal{Y}^\epsilon$ -periodic solutions which, by linearity, can be written in the form

$$\tilde{\mathbf{u}}_3(\mathbf{x}, \mathbf{y}) = \bar{\mathbf{U}}_3(\mathbf{x}) + \boldsymbol{\chi}^1(\mathbf{y}) : \boldsymbol{\varepsilon}_x(\bar{\mathbf{U}}_2(\mathbf{x})) + \boldsymbol{\chi}^2(\mathbf{y}) : \boldsymbol{\eta}_x(\bar{\mathbf{U}}_1(\mathbf{x})) + \boldsymbol{\chi}^3(\mathbf{y}) : \boldsymbol{\kappa}_x(\bar{\mathbf{U}}_0(\mathbf{x})), \quad (5.3.41)$$

where  $\bar{\mathbf{U}}_3(\mathbf{x})$  is the average of  $\tilde{\mathbf{u}}_3(\mathbf{x}, \mathbf{y})$  over  $\mathcal{Y}^\epsilon$  and  $\boldsymbol{\chi}^3(\mathbf{y})$  is a 5<sup>th</sup> order tensor, solution of the third cell problem. By substituting the expression of  $\tilde{\mathbf{u}}_3$  from 5.3.41 into equation (5.3.40), and considering both macroscopic balance equations 5.3.21 and 5.3.35 at orders  $\epsilon^0$  and  $\epsilon^1$  respectively, equation (5.3.40) simplifies to

$$-\nabla_{\mathbf{y}} \cdot \{ [\mathbf{C}(\mathbf{y}) : \boldsymbol{\varepsilon}_{\mathbf{y}}(\boldsymbol{\chi}^3) + \mathbf{C}(\mathbf{y}) \cdot \boldsymbol{\chi}^2] :: \boldsymbol{\kappa}_x(\bar{\mathbf{U}}_0) \} = \quad (5.3.42)$$

$$\nabla_x \cdot \{ (\boldsymbol{\mathcal{S}}_1(\mathbf{y}) - \beta(\mathbf{y})\mathbf{C}_1^H(\mathbf{y})) :: \boldsymbol{\eta}_x(\bar{\mathbf{U}}_0) \} \quad (5.3.43)$$

$$+ \beta(\mathbf{y}) \left( \frac{\boldsymbol{\varrho}_1^H}{\varrho_0^H} - \boldsymbol{\chi}^1 \right) : \left( \nabla_x \cdot \{ \mathbf{C}_0^H : \boldsymbol{\varepsilon}_x(\bar{\mathbf{U}}_0(\mathbf{x})) \} \right) \otimes \nabla_x \quad (5.3.44)$$

After these simplifications, one can set up the third cell-problem as follows:

### Third cell problem ( $/\epsilon^0$ )

We call third cell problem" the following PDE system with prescribed periodic boundary conditions

$$-\nabla_{\mathbf{y}} \cdot \{ \mathbf{C}(\mathbf{y}) : \boldsymbol{\varepsilon}_{\mathbf{y}}(\boldsymbol{\chi}^{3\{(klmn)\}}) \} = \nabla_{\mathbf{y}} \cdot \{ \mathbf{C}(\mathbf{y}) \cdot \boldsymbol{\chi}^{2\{(kl)m\}} \} + (\boldsymbol{\mathcal{S}}_{1\{n\}} - \beta(\mathbf{y})\mathbf{C}_{1\{n\}\{(kl)m\}}^H) \\ + \beta(\mathbf{y}) \left( \frac{\boldsymbol{\varrho}_{1\{n\}}^H}{\varrho_0^H} - \boldsymbol{\chi}^{1\{n\}} \right) \cdot \mathbf{C}_{0\{(kl)m\}}^H \quad \text{in } \mathcal{Y}^\epsilon \quad (5.3.45)$$

Where  $\boldsymbol{\chi}^{1\{(kl)mn\}}(\mathbf{y}) \in H_{\#}^1(\mathcal{Y}^\epsilon)$  and  $\{(kl)mn\} = \begin{cases} 1111, 2211, 1221, 2221, 1121, 1211 \\ 1112, 2212, 1222, 2222, 1122, 1212 \end{cases}$

The corresponding weak form can be written as follows:

### Weak form of the third cell problem

For each macroscopic loading indexed by  $\{(kl)mn\}$ , the weak of the third cell problem is: Find  $\boldsymbol{\chi}^{3\{(kl)mn\}} \in H_{\#}^1(\mathcal{Y}^\epsilon)$  such that

$$\int_{\mathcal{Y}^\epsilon} \boldsymbol{\varepsilon}(\boldsymbol{\chi}^{3\{(kl)mn\}}) : \mathbf{C} : \boldsymbol{\varepsilon}(\mathbf{v}) \, d\mathbf{y} = - \int_{\mathcal{Y}^\epsilon} (\mathbf{C}_{\{n\}} \cdot \boldsymbol{\chi}^{2\{(kl)m\}}) : \boldsymbol{\varepsilon}(\mathbf{v}) \, d\mathbf{y} \quad (5.3.46)$$

$$- \int_{\mathcal{Y}^\epsilon} (\beta(\mathbf{y})\mathbf{C}_{1\{n\}\{(kl)\{m\}}^H - \boldsymbol{\mathcal{S}}_{1\{n\}}) \cdot \mathbf{v} \, d\mathbf{y} \quad (5.3.47)$$

$$+ \int_{\mathcal{Y}^\epsilon} \left[ \beta(\mathbf{y}) \left( \frac{\boldsymbol{\varrho}_{1\{n\}}^H}{\varrho_0^H} - \boldsymbol{\chi}^{1\{n\}} \right) \cdot \mathbf{C}_{0\{m\}\{(kl)\}}^H \right] \cdot \mathbf{v} \, d\mathbf{y} \quad \forall \mathbf{v} \in H_{\#}^1(\mathcal{Y}^\epsilon). \quad (5.3.48)$$

Using index notation, we have more explicitly

$$\int_{\mathcal{Y}^\epsilon} \chi_{p,q}^{3\{(kl)mn\}} C_{pqrs} v_{r,s} dy = - \int_{\mathcal{Y}^\epsilon} \chi_p^{2\{(kl)m\}} C_{p\{n\}rs} v_{r,s} dy \quad (5.3.49)$$

$$- \int_{\mathcal{Y}^\epsilon} \left( \beta(\mathbf{y}) C_{1r\{n\}\{(kl)m\}}^H - \mathcal{S}_{1r\{n\}}^{\{(kl)m\}} \right) v_r dy \quad (5.3.50)$$

$$+ \int_{\mathcal{Y}^\epsilon} \left[ \beta \left( \frac{\varrho_{1r\{n\}p}^H}{\varrho_0^H} - \chi_r^{1\{n\}p} \right) \cdot C_{0p\{m\}\{(kl)\}}^H \right] v_r dy \quad (5.3.51)$$

### 5.3.7 Computation of second-order homogenized tensors

Finally,  $\tilde{\mathbf{u}}_4$  is to be found by solving the  $\mathcal{O}(\epsilon^2)$  equation of 5.2.17, which reads

$$\mathcal{L}_{yy}\{\tilde{\mathbf{u}}_4\} = \mathbf{g}_4, \quad \tilde{\mathbf{u}}_4 \text{ } \mathcal{Y}^\epsilon\text{-periodic,} \quad (5.3.52)$$

with

$$\begin{aligned} \mathbf{g}_4 &= -\mathcal{L}_{xy}\{\tilde{\mathbf{u}}_3\} - \mathcal{L}_{xx}\{\tilde{\mathbf{u}}_2\} + \omega^2 \rho(\mathbf{y}) \tilde{\mathbf{u}}_2 \\ &= \nabla_y \cdot \{\mathbf{C}(\mathbf{y}) : \boldsymbol{\varepsilon}_x(\tilde{\mathbf{u}}_3)\} + \nabla_x \cdot \{\mathbf{C}(\mathbf{y}) : \boldsymbol{\varepsilon}_y(\tilde{\mathbf{u}}_3)\} + \nabla_x \cdot \{\mathbf{C}(\mathbf{y}) : \boldsymbol{\varepsilon}_x(\tilde{\mathbf{u}}_2)\} \end{aligned} \quad (5.3.53)$$

$$+ \omega^2 \rho(\mathbf{y}) \tilde{\mathbf{u}}_2 \quad (5.3.54)$$

This time, we do not need to solve problem 5.3.52, and are only interested in formulating the compatibility condition 5.3.4 on  $\mathbf{g}$  that ensures its solvability. Since  $\mathbf{C}$  is  $\mathcal{Y}^\epsilon$ -periodic, the integral of  $\nabla_y \cdot \{\mathbf{C}(\mathbf{y}) : \boldsymbol{\varepsilon}_x(\tilde{\mathbf{u}}_2)\}$  vanishes, and the sought condition is

$$\begin{aligned} &\underbrace{\int_{\mathcal{Y}^\epsilon} \nabla_x \cdot \{\mathbf{C}(\mathbf{y}) : \boldsymbol{\varepsilon}_y(\tilde{\mathbf{u}}_3)\} dy}_{(b_1)} + \underbrace{\int_{\mathcal{Y}^\epsilon} \nabla_y \cdot \{\mathbf{C}(\mathbf{y}) : \boldsymbol{\varepsilon}_x(\tilde{\mathbf{u}}_3)\} dy}_{(b_2)=0} \\ &\quad + \underbrace{\int_{\mathcal{Y}^\epsilon} \nabla_x \cdot \{\mathbf{C}(\mathbf{y}) : \boldsymbol{\varepsilon}_x(\tilde{\mathbf{u}}_2)\} dy}_{(b_3)} + \underbrace{\int_{\mathcal{Y}^\epsilon} \omega^2 \rho(\mathbf{y}) \tilde{\mathbf{u}}_2 dy}_{(b_4)} = 0 \end{aligned} \quad (5.3.55)$$

From the expression of  $\tilde{\mathbf{u}}$  5.3.41, we have

$$\boldsymbol{\varepsilon}_x(\tilde{\mathbf{u}}_3) = \boldsymbol{\varepsilon}_y(\boldsymbol{\chi}^1) : \boldsymbol{\varepsilon}_x(\bar{\mathbf{U}}_2) + \boldsymbol{\varepsilon}_y(\boldsymbol{\chi}^2) \cdot \boldsymbol{\eta}_x(\bar{\mathbf{U}}_1) + \boldsymbol{\varepsilon}_y(\boldsymbol{\chi}^3) \cdot \boldsymbol{\kappa}_x(\bar{\mathbf{U}}_0) \quad (5.3.56)$$

which, used together with 5.3.25 and the ansatz 5.3.8 in the summands of 5.3.54, yields

$$\begin{cases} (b_1) &= \nabla_x \cdot \left( \int_{\mathcal{Y}^\epsilon} \mathbf{C}(\mathbf{y}) : \left[ \boldsymbol{\varepsilon}_y(\boldsymbol{\chi}^1) : \boldsymbol{\varepsilon}_x(\bar{\mathbf{U}}_2) + \boldsymbol{\varepsilon}_y(\boldsymbol{\chi}^2) \cdot \boldsymbol{\eta}_x(\bar{\mathbf{U}}_1) + \boldsymbol{\varepsilon}_y(\boldsymbol{\chi}^3) \cdot \boldsymbol{\kappa}_x(\bar{\mathbf{U}}_0) \right] dy \right) \\ (b_3) &= \nabla_x \cdot \left( \int_{\mathcal{Y}^\epsilon} \mathbf{C}(\mathbf{y}) : \left[ \boldsymbol{\varepsilon}_x(\bar{\mathbf{U}}_2) + \boldsymbol{\chi}^1 \cdot \boldsymbol{\eta}_x(\bar{\mathbf{U}}_1) + \boldsymbol{\chi}^2 \cdot \boldsymbol{\kappa}_x(\bar{\mathbf{U}}_0) \right] dy \right) \\ (b_4) &= \omega^2 \int_{\mathcal{Y}^\epsilon} \left( \rho(\mathbf{y}) \bar{\mathbf{U}}_2 + \rho(\mathbf{y}) \boldsymbol{\chi}^1 : \boldsymbol{\varepsilon}_x(\bar{\mathbf{U}}_1) + \rho(\mathbf{y}) \boldsymbol{\chi}^2 \cdot \boldsymbol{\eta}_x(\bar{\mathbf{U}}_0) \right) dy \end{cases}$$

The compatibility requirement  $(b_1) + (b_3) + (b_4) = 0$  then provides the sought macroscopic balance equation at order  $\epsilon^2$ :

$$\begin{aligned}
& \nabla_x \cdot \left( \int_{\mathcal{Y}^\epsilon} \mathbf{S}_0(\mathbf{y}) : \boldsymbol{\varepsilon}_x(\bar{\mathbf{U}}_2) \, d\mathbf{y} \right) + \omega^2 \int_{\mathcal{Y}^\epsilon} \rho(\mathbf{y}) \bar{\mathbf{U}}_2(\mathbf{x}) \, d\mathbf{y} \\
& + \nabla_x \cdot \left( \int_{\mathcal{Y}^\epsilon} \mathbf{S}_1(\mathbf{y}) :: \boldsymbol{\eta}_x(\bar{\mathbf{U}}_1) \, d\mathbf{y} \right) + \omega^2 \int_{\mathcal{Y}^\epsilon} \rho(\mathbf{y}) \boldsymbol{\chi}^1 : \boldsymbol{\varepsilon}_x(\bar{\mathbf{U}}_1) \, d\mathbf{y} \\
& + \nabla_x \cdot \left( \int_{\mathcal{Y}^\epsilon} \mathbf{S}_2(\mathbf{y}) :: \boldsymbol{\kappa}_x(\bar{\mathbf{U}}_0) \, d\mathbf{y} \right) + \omega^2 \int_{\mathcal{Y}^\epsilon} \rho(\mathbf{y}) \boldsymbol{\chi}^2 :: \boldsymbol{\eta}_x(\bar{\mathbf{U}}_0) \, d\mathbf{y} = 0,
\end{aligned}$$

i.e.

$$\begin{aligned}
& \nabla_x \cdot \{ \mathbf{C}_0^H : \boldsymbol{\varepsilon}_x(\bar{\mathbf{U}}_2) \} + \omega^2 \varrho_0 \bar{\mathbf{U}}_2 \\
& = -\nabla_x \{ \mathbf{C}_1^H :: \boldsymbol{\eta}_x(\bar{\mathbf{U}}_1) \} - \omega^2 \boldsymbol{\varrho}_1^H : \boldsymbol{\varepsilon}_x(\bar{\mathbf{U}}_1) - \nabla_x \cdot \{ \mathbf{C}_2^H :: \boldsymbol{\kappa}_x(\bar{\mathbf{U}}_0) \} - \omega^2 \boldsymbol{\varrho}_2^H :: \boldsymbol{\eta}_x(\bar{\mathbf{U}}_0),
\end{aligned} \tag{5.3.57}$$

wherein  $\mathbf{S}_2$  is the second-order cell stress, introduced here for the sake of clarity

$$\mathbf{S}_2 = \mathbf{C} : \left[ \boldsymbol{\varepsilon}_y(\boldsymbol{\chi}^3) + \boldsymbol{\chi}^2 \hat{\otimes} \mathbf{I} \right], \quad \mathbf{S}_{1ij}^{\{(kl)mn\}} = C_{ijpq} \left( \chi_{p,q}^{3\{(kl)mn\}} + \chi_p^{2\{(kl)m\}} \delta_{q\{n\}} \right).$$

and the second-order homogenized elastic and inertial tensors, denoted as  $\mathbf{C}_2^H$  and  $\boldsymbol{\varrho}_2^H$  respectively, are given by

$$\mathbf{C}_2^H = \langle \mathbf{S}_2 \rangle_{\mathcal{Y}^\epsilon} = \frac{1}{|\mathcal{Y}^\epsilon|} \int_{\mathcal{Y}^\epsilon} \mathbf{C}(\mathbf{y}) : \left[ \boldsymbol{\varepsilon}_y(\boldsymbol{\chi}^3(\mathbf{y})) + \boldsymbol{\chi}^2(\mathbf{y}) \hat{\otimes} \mathbf{I} \right] \, d\mathbf{y} \tag{5.3.58}$$

$$\text{i.e.} \quad C_{2ijnklm}^H = \langle \mathbf{S}_{2ij}^{\{(kl)mn\}} \rangle_{\mathcal{Y}^\epsilon} = \frac{1}{|\mathcal{Y}^\epsilon|} \int_{\mathcal{Y}^\epsilon} C_{ijpq} \left( \chi_{p,q}^{3\{(kl)mn\}} + \chi_p^{1\{(kl)m\}} \delta_{q\{n\}} \right) \, d\mathbf{y} \tag{5.3.59}$$

and:

$$\boldsymbol{\varrho}_2^H = \frac{1}{|\mathcal{Y}^\epsilon|} \int_{\mathcal{Y}^\epsilon} \rho(\mathbf{y}) \boldsymbol{\chi}^2(\mathbf{y}) \, d\mathbf{y} \tag{5.3.60}$$

$$\text{i.e.} \quad \varrho_{2pklm}^H = \frac{1}{|\mathcal{Y}^\epsilon|} \int_{\mathcal{Y}^\epsilon} \rho \chi_p^{2\{(kl)m\}} \, d\mathbf{y} \tag{5.3.61}$$

These tensors satisfy the following index permutation symmetry

$$C_{2ijnklm}^H = C_{2jinklm}^H = C_{2ijnlkm}^H, \quad \varrho_{2pklm}^H = \varrho_{2plkm}^H.$$

Therefore, the corresponding tensor space for these tensors can be defined as follows:

$$\mathbf{C}_2^H \in \{ \mathbf{T} \in (\mathbb{S}^2(\mathbb{R}^2) \otimes \mathbb{R}^2)^2 | \mathbf{T}_{(ij)n(kl)m} \}, \quad \boldsymbol{\varrho}_2^H \in \{ \mathbf{T} \in \mathbb{S}^2(\mathbb{R}^2) \otimes^2 \mathbb{R}^2 | \mathbf{T}_{p(kl)m} \}$$

## 5.4 Reciprocity relationships

The purpose of this section is to establish relationships between the homogenized elastic and inertial high-order tensors, known as the “*Reciprocity Identities.*” These identities directly arise from the weak forms satisfied by the first three cell solutions, “tested” against other solutions. As mentioned earlier in this chapter, these identities hold significant practical interest as they establish a direct link between the correctors. Consequently, the homogenized tensors derived from the  $n^{\text{th}} > 2$  cell problem can be

entirely computed using those obtained from the preceding  $(n - 1)^{th}$  problem. This reduction in the number of cell problems that need to be solved eliminates the need to solve the last cell-problem, which in this case is the third one. Instead, it becomes possible to compute the second-order homogenized tensors solely using the first two correctors and the so-called reciprocity identities.

To this end, two new tensors,  $\mathbf{D}_1$  and  $\mathbf{D}_2$ , will be introduced, and will also serve in the last Section of this chapter.

### 5.4.1 Relationship between tensors $\varrho_1^H$ and $\mathbf{C}_1^H$

**Proposition 4.1: First reciprocity identity [Boutin and Auriault, 1993]**

The homogenized coupling tensors  $\varrho_1^H$  and  $\mathbf{C}_1^H$  satisfy the following “reciprocity relationship”:

$$C_{1ijklm}^H - \frac{\varrho_{1p(ij)}^H}{\varrho_0^H} C_{0(kl)\{m\}p}^H = D_{1ijklm} \quad (5.4.1)$$

where the fifth-order tensor  $\mathbf{D}_1$  is defined by

$$D_{1ijklm} = \int_{\mathcal{Y}^\epsilon} \left( \mathcal{S}_{0\{m\}p}^{(ij)} \chi_p^{1(kl)} - \mathcal{S}_{0\{m\}p}^{(kl)} \chi_p^{1(ij)} \right) dy.$$

□

*Proof.* • Let’s recall the weak form of the first cell problem

$$\int_{\mathcal{Y}^\epsilon} \chi_{p,q}^{1(ij)} C_{pqrs} v_{r,s} dy = - \int_{\mathcal{Y}^\epsilon} C_{rs(ij)} v_{r,s} dy$$

By setting  $v_r = \chi_r^{2\{(kl)m\}}$  as trial field in the weak form associated to  $\chi^{1(ij)}$ , we obtain

$$\int_{\mathcal{Y}^\epsilon} \chi_{p,q}^{1(ij)} C_{pqrs} \chi_{r,s}^{2\{(kl)m\}} dy = - \underbrace{\int_{\mathcal{Y}^\epsilon} C_{rs(ij)} \chi_{r,s}^{2\{(kl)m\}} dy}_{(a)} \quad (5.4.2)$$

Considering the definition of  $\mathbf{C}_1^H$

$$C_{1ijklm}^H = \int_{\mathcal{Y}^\epsilon} \left( C_{(ij)rs} \chi_{r,s}^{2\{(kl)m\}} + C_{(ij)\{m\}p} \chi_p^{1(kl)} \right) dy$$

one yields to the following relationships linking the components of  $\mathbf{C}_1^H$  and the second member (a)

$$\underbrace{\int_{\mathcal{Y}^\epsilon} C_{(ij)rs} \chi_{r,s}^{2\{(kl)m\}} dy}_{(-a)} = \underbrace{C_{1ijklm}^H - \int_{\mathcal{Y}^\epsilon} C_{(ij)\{m\}p} \chi_p^{1(kl)} dy}_{(b)} \quad (5.4.3)$$

• Now, let’s recall the weak form of the second cell problem

$$\int_{\mathcal{Y}^\epsilon} \chi_{r,s}^{2\{(kl)m\}} C_{rspq} v_{p,q} dy = - \int_{\mathcal{Y}^\epsilon} \left( \frac{\rho}{\varrho_0^H} C_{0(kl)\{m\}p}^H - \mathcal{S}_{0\{m\}p}^{(kl)} \right) v_p dy - \int_{\mathcal{Y}^\epsilon} \chi_s^{1(kl)} C_{s\{m\}pq} v_{p,q} dy$$

Similarly setting  $v_p = \chi_p^{1(ij)}$  as trial field in the weak form associated to  $\chi^{2\{(kl)m\}}$

$$\int_{\mathcal{Y}^\epsilon} \chi_{r,s}^{2\{(kl)m\}} C_{rspq} \chi_{p,q}^{1(ij)} dy = - \int_{\mathcal{Y}^\epsilon} \left( \frac{\rho}{\varrho_0^H} C_{0(kl)\{m\}p}^H - \mathcal{S}_{0\{m\}p}^{(kl)} \right) \chi_p^{1(ij)} dy - \int_{\mathcal{Y}^\epsilon} \chi_s^{1(kl)} C_{s\{m\}pq} \chi_{p,q}^{1(ij)} dy$$

taking into account the symmetry of  $\mathbf{C}$ , we obtain

$$\int_{\mathcal{Y}^\epsilon} \chi_{p,q}^{1(ij)} C_{pqr} \chi_{r,s}^{2\{(kl)m\}} dy = \underbrace{- \int_{\mathcal{Y}^\epsilon} \left( \frac{\rho}{\varrho_0^H} C_{0(kl)\{m\}p}^H - \mathcal{S}_{0\{m\}p}^{(kl)} \right) \chi_p^{1(ij)} dy - \int_{\mathcal{Y}^\epsilon} \chi_s^{1(kl)} C_{s\{m\}pq} \chi_{p,q}^{1(ij)} dy}_{(c)} \quad (5.4.4)$$

- Finally, due to the symmetry of the bilinear forms 5.4.2, 5.4.4 and taking into account 5.4.3, the corresponding linear forms are hence equal which implies that their respective second members are equal  $(b) = -(c)$ , it yields

$$C_{1ijklm}^H - \int_{\mathcal{Y}^\epsilon} C_{(ij)\{m\}s} \chi_s^{1(kl)} dy = \frac{C_{0(kl)\{m\}p}^H}{\varrho_0^H} \int_{\mathcal{Y}^\epsilon} \rho \chi_p^{1(ij)} dy - \int_{\mathcal{Y}^\epsilon} \mathcal{S}_{0\{m\}p}^{(kl)} \chi_p^{1(ij)} dy + \int_{\mathcal{Y}^\epsilon} \chi_s^{1(kl)} C_{s\{m\}pq} \chi_{p,q}^{1(ij)} dy$$

We establish the following identity

$$C_{1ijklm}^H - \frac{C_{0(kl)\{m\}p}^H}{\varrho_0^H} \varrho_{1p(ij)}^H = D_{1ijklm} = \int_{\mathcal{Y}^\epsilon} \left( \mathcal{S}_{0\{m\}p}^{(ij)} \chi_p^{1(kl)} - \mathcal{S}_{0\{m\}p}^{(kl)} \chi_p^{1(ij)} \right) dy \quad \square$$

We note that the tensor  $\mathbf{D}_1$  defined by 5.4.1 has respectively, the following symmetry and skew-symmetry properties

$$D_{1ijklm} = D_{1jiklm}, \quad D_{1ijklm} = D_{1ijklm}, \quad D_{1ijklm} = -D_{1kljim}. \quad (5.4.5)$$

Hence, its corresponding vector space is given by

$$\mathbf{D}_1 \in \{ \mathbf{T} \in \Lambda^2(\mathcal{S}^2(\mathbb{R}^2)) \otimes \mathbb{R}^2 | \mathbf{T}_{(ij)(kl)m} \},$$

in which the notation  $\dots$  indicates antisymmetry with respect to block permutation.

## 5.4.2 Relationship between tensors $\varrho_1^H$ , $\mathbf{C}_1^H$ and $\mathbf{C}_2^H$

In the previous work of [Fish et al., 2002], the second reciprocity identity was introduced in the simplified case of materials with uniform density. In this subsection, our contribution lies in presenting a complete and refined version of this relationship, ensuring its clarity and conciseness.

### Proposition 4.2: Second reciprocity identity

Let the sixth-order tensor  $\mathbf{D}_2$  be defined by

$$D_{2ijnklm} := C_{2ijnklm}^H - \frac{\varrho_{1p(ij)}^H}{\varrho_0^H} \left( D_{1pnklm} - \frac{\varrho_p^\# \{n\}s}{\varrho_0^H} C_{0s\{m\}(kl)}^H \right) - C_{0(ij)\{n\}a}^H \frac{\varrho_{2aklm}^H}{\varrho_0^H} \quad (5.4.6)$$

with the third-order tensor  $\varrho^\sharp$  defined by

$$\varrho_{1ikl}^\sharp := \varrho_{1ikl}^H - \varrho_{1kil}^H. \quad (5.4.7)$$

Then, the homogenized tensors  $\varrho_1^H$ ,  $\mathbf{C}_1^H$  and  $\mathbf{C}_2^H$  satisfy the following “reciprocity relationship”

$$\begin{aligned} D_{2ijnklm} &= \int_{\mathcal{Y}^\epsilon} \chi_{p,q}^{2(ijn)} C_{pqab} \chi_{a,b}^{2\{(kl)m\}} dy - \int_{\mathcal{Y}^\epsilon} \chi_p^{1(ij)} C_{p\{n\}a\{m\}} \chi_a^{1(kl)} dy \\ &\quad + \int_{\mathcal{Y}^\epsilon} \beta \chi_p^{1(ij)} \chi_p^{1\{n\}s} C_{0s\{m\}(kl)}^H dy \end{aligned} \quad (5.4.8)$$

□

*Proof.* • Let’s recall the weak form of the first cell problem

$$\int_{\mathcal{Y}^\epsilon} \chi_{p,q}^{1(ij)} C_{pqrs} v_{r,s} dy = - \int_{\mathcal{Y}^\epsilon} C_{rs(ij)} v_{r,s} dy$$

By setting  $v_r = \chi_r^{3(klmn)}$  as trial field in the weak form associated to  $\chi^{1(ij)}$ , we obtain

$$\int_{\mathcal{Y}^\epsilon} \chi_{p,q}^{1(ij)} C_{pqrs} \chi_{r,s}^{3(klmn)} dy = - \underbrace{\int_{\mathcal{Y}^\epsilon} C_{rs(ij)} \chi_{r,s}^{3(klmn)} dy}_{(a)} \quad (5.4.9)$$

Considering the definition of  $\mathbf{C}_2^H$

$$C_{2ijnklm}^H = \int_{\mathcal{Y}^\epsilon} \left( C_{(ij)rs} \chi_{r,s}^{2\{(kl)m\}} + C_{(ij)\{m\}p} \chi_p^{1(kl)} \right) dy$$

one yields to the following relationships linking the components of  $\mathbf{C}_1^H$  and the second member (a)

$$\underbrace{\int_{\mathcal{Y}^\epsilon} C_{(ij)rs} \chi_{r,s}^{3(klmn)} dy}_{(-a)} = \underbrace{C_{2ijnklm}^H - \int_{\mathcal{Y}^\epsilon} C_{(ij)\{n\}p} \chi_p^{2\{(kl)m\}} dy}_{(b)} \quad (5.4.10)$$

• Now, let’s recall the weak form of the third cell problem

$$\begin{aligned} \int_{\mathcal{Y}^\epsilon} \chi_{p,q}^{3(klmn)} C_{pqij} v_{i,j} dy &= - \int_{\mathcal{Y}^\epsilon} \chi_p^{2\{(kl)m\}} C_{p\{n\}ij} v_{i,j} dy \\ &\quad - \int_{\mathcal{Y}^\epsilon} \left( \beta(\mathbf{y}) C_{1i\{n\}\{(kl)m\}}^H - \mathcal{S}_{1i\{n\}}^{\{(kl)m\}} \right) v_i dy \\ &\quad + \int_{\mathcal{Y}^\epsilon} \left[ \beta \left( \frac{\varrho_{1i\{n\}p}^H}{\varrho_0^H} - \chi_i^{1\{n\}p} \right) \cdot C_{0p\{m\}(kl)}^H \right] v_i dy \end{aligned}$$

Similarly setting  $v_p = \chi_p^{1(ij)}$  as trial field in the weak form associated to  $\chi^{3(klmn)}$

$$\begin{aligned} \int_{\mathcal{Y}^\epsilon} \chi_{r,s}^{3(klmn)} C_{rspq} \chi_{p,q}^{1(ij)} dy &= - \int_{\mathcal{Y}^\epsilon} \chi_s^{2\{(kl)m\}} C_{s\{n\}pq} \chi_{p,q}^{1(ij)} dy \\ &\quad - \int_{\mathcal{Y}^\epsilon} \left( \beta(\mathbf{y}) C_{1p\{n\}\{(kl)m\}}^H - \mathcal{S}_{1p\{n\}}^{\{(kl)m\}} \right) \chi_p^{1(ij)} dy \\ &\quad + \int_{\mathcal{Y}^\epsilon} \left[ \beta \left( \frac{\varrho_{1p\{n\}s}^H}{\varrho_0^H} - \chi_p^{1\{n\}s} \right) \cdot C_{0s\{m\}(kl)}^H \right] \chi_p^{1(ij)} dy \end{aligned} \quad (5.4.11)$$

taking into account the symmetry of  $\mathbf{C}$ , we obtain

$$\begin{aligned} \int_{\mathcal{Y}^\epsilon} \chi_{p,q}^{1(ij)} C_{pqrs} \chi_{r,s}^{3(klmn)} dy &= + \underbrace{\int_{\mathcal{Y}^\epsilon} \left[ \beta \left( \frac{\varrho_{1p\{n\}s}^H}{\varrho_0^H} - \chi_p^{1\{n\}s} \right) \cdot C_{0s\{m\}(kl)}^H \right] \chi_p^{1(ij)} dy}_{(c_1)} \\ &\quad - \underbrace{\int_{\mathcal{Y}^\epsilon} \chi_s^{2\{(kl)m\}} C_{s\{n\}pq} \chi_{p,q}^{1(ij)} dy - \int_{\mathcal{Y}^\epsilon} \left( \beta(\mathbf{y}) C_{1p\{n\}\{(kl)m\}}^H - \mathcal{S}_{1p\{n\}}^{\{(kl)m\}} \right) \chi_p^{1(ij)} dy}_{(c_0)} \end{aligned} \quad (5.4.12)$$

- Finally, Due to the symmetry of the bilinear forms 5.4.9, 5.4.11 and taking into account 5.4.10, the linear corresponding linear forms are hence equals which implies that their respective second members are equal  $(b) = -(c_0 + c_1)$ , it yields

$$\begin{aligned} C_{2ijnklm}^H - \int_{\mathcal{Y}^\epsilon} C_{(ij)\{n\}s} \chi_s^{2\{(kl)m\}} dy &= \int_{\mathcal{Y}^\epsilon} \chi_s^{2\{(kl)m\}} C_{s\{n\}pq} \chi_{p,q}^{1(ij)} dy \\ &\quad + \int_{\mathcal{Y}^\epsilon} \left( \beta(\mathbf{y}) C_{1p\{n\}\{(kl)m\}}^H - \mathcal{S}_{1p\{n\}}^{\{(kl)m\}} \right) \chi_p^{1(ij)} dy \\ &\quad - \int_{\mathcal{Y}^\epsilon} \left[ \beta \left( \frac{\varrho_{1p\{n\}s}^H}{\varrho_0^H} - \chi_p^{1\{n\}s} \right) \cdot C_{0s\{m\}(kl)}^H \right] \chi_p^{1(ij)} dy \end{aligned}$$

regrouping the terms,

$$\begin{aligned} C_{2ijnklm}^H &= \int_{\mathcal{Y}^\epsilon} C_{(ij)\{n\}s} \chi_s^{2\{(kl)m\}} dy + \int_{\mathcal{Y}^\epsilon} \chi_s^{2\{(kl)m\}} C_{s\{n\}pq} \chi_{p,q}^{1(ij)} dy + \frac{\varrho_{1p(ij)}^H}{\varrho_0^H} C_{1p\{n\}\{(kl)m\}}^H \\ &\quad - \int_{\mathcal{Y}^\epsilon} \mathcal{S}_{1p\{n\}}^{\{(kl)m\}} \chi_p^{1(ij)} dy - \frac{\varrho_{1p(ij)}^H}{\varrho_0^H} \frac{\varrho_{1p\{n\}s}^H}{\varrho_0^H} C_{0s\{m\}(kl)}^H + \int_{\mathcal{Y}^\epsilon} \beta \chi_p^{1(ij)} \chi_p^{1\{n\}s} C_{0s\{m\}(kl)}^H dy \end{aligned}$$

We establish the following identity:

$$\begin{aligned} C_{2ijnklm}^H - \frac{\varrho_{1p(ij)}^H}{\varrho_0^H} \left( D_{1pnklm} - \frac{\varrho_{ps\{n\}}^\#}{\varrho_0^H} C_{0s\{m\}(kl)}^H \right) \\ = \int_{\mathcal{Y}^\epsilon} \left( \mathcal{S}_{0\{n\}s}^{(ij)} \chi_s^{2\{(kl)m\}} - \chi_p^{1(ij)} \mathcal{S}_{1p\{n\}}^{\{(kl)m\}} \right) dy + \int_{\mathcal{Y}^\epsilon} \beta \chi_p^{1(ij)} \chi_p^{1\{n\}s} C_{0s\{m\}(kl)}^H dy \end{aligned} \quad (5.4.13)$$

$$\begin{aligned} \int_{\mathcal{Y}^\epsilon} \chi_{p,q}^{2(ijn)} C_{pqab} \chi_{a,b}^{2\{(kl)m\}} dy &= - \int_{\mathcal{Y}^\epsilon} \chi_p^{1(ij)} C_{p\{n\}ab} \chi_{a,b}^{2\{(kl)m\}} dy - \int_{\mathcal{Y}^\epsilon} \left( \beta(\mathbf{y}) C_{0(ij)\{n\}a}^H - \mathcal{S}_{0\{n\}a}^{(ij)} \right) \chi_a^{2\{(kl)m\}} dy \\ &= - \int_{\mathcal{Y}^\epsilon} \chi_p^{1(ij)} C_{p\{n\}ab} \chi_{a,b}^{2\{(kl)m\}} dy - C_{0(ij)\{n\}a}^H \frac{\varrho_{2aklm}^H}{\varrho_0^H} + \int_{\mathcal{Y}^\epsilon} \mathcal{S}_{0\{n\}a}^{(ij)} \chi_a^{2\{(kl)m\}} dy \\ &= \int_{\mathcal{Y}^\epsilon} \left( \mathcal{S}_{0\{n\}a}^{(ij)} \chi_a^{2\{(kl)m\}} - \chi_p^{1(ij)} \mathcal{S}_{1p\{n\}}^{\{(kl)m\}} \right) dy + \int_{\mathcal{Y}^\epsilon} \chi_p^{1(ij)} C_{p\{n\}a\{m\}} \chi_a^{1(kl)} dy \\ &\quad - C_{0(ij)\{n\}a}^H \frac{\varrho_{2aklm}^H}{\varrho_0^H} \end{aligned}$$

Therefore

$$\begin{aligned} & \int_{\mathcal{Y}^\epsilon} \left( \mathcal{S}_{0\{n\}a}^{(ij)} \chi_a^{2\{(kl)m\}} - \chi_p^{1(ij)} \mathcal{S}_{1p\{n\}}^{\{(kl)m\}} \right) dy \\ &= \int_{\mathcal{Y}^\epsilon} \chi_{p,q}^{2(ijn)} C_{pqab} \chi_{a,b}^{2\{(kl)m\}} dy - \int_{\mathcal{Y}^\epsilon} \chi_p^{1(ij)} C_{p\{n\}a\{m\}} \chi_a^{1(kl)} dy + C_{0(ij)\{n\}a}^H \frac{\varrho_{2aklm}^H}{\varrho_0^H} \end{aligned} \quad (5.4.14)$$

which, used in 5.4.13, provides

$$D_{2ijnklm} = \int_{\mathcal{Y}^\epsilon} \chi_{p,q}^{2(ijn)} C_{pqab} \chi_{a,b}^{2\{(kl)m\}} dy - \int_{\mathcal{Y}^\epsilon} \chi_p^{1(ij)} C_{p\{n\}a\{m\}} \chi_a^{1(kl)} dy \quad (5.4.15)$$

$$+ \int_{\mathcal{Y}^\epsilon} \beta \chi_p^{1(ij)} \chi_p^{1\{n\}s} C_{0s\{m\}(kl)}^H dy. \quad (5.4.16)$$

The proof of the reciprocity identity is complete.  $\square$

## 5.5 Mean fields, homogenized equations and link with strain-gradient elasticity

The objective of this section is to establish the connection between the higher-order homogenized tensors derived from the asymptotic analysis and the constitutive law of the strain-gradient model introduced at the end of Chapter 3. As observed in the previous section, the tensors obtained through asymptotic expansion do not possess the same symmetries as those in the strain-gradient model. Therefore, it is difficult to compare the two models. The contribution of this work lies in constructing the appropriate tensors that satisfy the constitutive law while respecting all the properties of the model, including index symmetries and positive definiteness of the tensors. To achieve this, we propose establishing the homogenized balance equations at different orders and utilizing the reciprocity identities established in the preceding section to construct these tensors. Subsequently, we will present a transient form of the effective wave equation, along with its corresponding weak form.

### 5.5.1 Derivation of a fourth-order effective time-harmonic wave equation

We define the second-order approximation  $\overline{\mathbf{U}}_\epsilon(\mathbf{x})$  of the macroscopic displacement field as:

$$\overline{\mathbf{U}}_\epsilon(\mathbf{x}) = \overline{\mathbf{U}}_0(\mathbf{x}) + \epsilon \overline{\mathbf{U}}_1(\mathbf{x}) + \epsilon^2 \overline{\mathbf{U}}_2(\mathbf{x}) + o(\epsilon^2), \quad (5.5.1)$$

whose coefficients  $\overline{\mathbf{U}}_0(\mathbf{x})$ ,  $\overline{\mathbf{U}}_1(\mathbf{x})$  and  $\overline{\mathbf{U}}_2(\mathbf{x})$  satisfy the macroscopic balance equations 5.3.21, 5.3.35 and 5.3.57 at the first three orders derived in Section ???. These equations, recalled for convenience, read:

$$\begin{aligned} O(\epsilon^0): \quad & \nabla_x \{ \mathbf{C}_0^H : \boldsymbol{\varepsilon}_x(\overline{\mathbf{U}}_0) \} + \omega^2 \varrho_0^H \overline{\mathbf{U}}_0 = 0 \\ O(\epsilon^1): \quad & \nabla_x \{ \mathbf{C}_0^H : \boldsymbol{\varepsilon}_x(\overline{\mathbf{U}}_1) \} + \omega^2 \varrho_0^H \overline{\mathbf{U}}_1 = -\nabla_x \{ \mathbf{C}_1^H : \boldsymbol{\eta}_x(\overline{\mathbf{U}}_0) \} - \omega^2 \varrho_1^H : \boldsymbol{\varepsilon}_x(\overline{\mathbf{U}}_0) \\ O(\epsilon^2): \quad & \nabla_x \{ \mathbf{C}_0^H : \boldsymbol{\varepsilon}_x(\overline{\mathbf{U}}_2) \} + \omega^2 \varrho_0^H \overline{\mathbf{U}}_2 = -\nabla_x \{ \mathbf{C}_1^H : \boldsymbol{\eta}_x(\overline{\mathbf{U}}_1) \} - \omega^2 \varrho_1^H : \boldsymbol{\varepsilon}_x(\overline{\mathbf{U}}_1) \\ & \quad - \nabla_x \{ \mathbf{C}_2^H : \boldsymbol{\kappa}_x(\overline{\mathbf{U}}_0) \} - \omega^2 \varrho_2^H : \boldsymbol{\eta}_x(\overline{\mathbf{U}}_0) \end{aligned}$$

or, in component notation:

$$\begin{aligned}
(a) \quad 0 &= C_{0ijkl}^H U_{0k,\ell j} + \omega^2 \varrho_0^H U_{0i} \\
(b) \quad 0 &= C_{0ijkl}^H U_{1k,\ell j} + \omega^2 \varrho_0^H U_{1i} + C_{1ijklm}^H U_{0k,\ell mj} + \omega^2 \varrho_{1ipq}^H U_{0p,q} \\
(c) \quad 0 &= C_{0ijkl}^H U_{2k,\ell j} + \omega^2 \varrho_0^H U_{2i} + C_{1ijklm}^H U_{1k,\ell mj} + \omega^2 \varrho_{1ipq}^H U_{1p,q} \\
&\quad + C_{2ijnklm}^H U_{0k,\ell mnj} + \omega^2 \varrho_{2ipqr}^H U_{0p,qr}.
\end{aligned} \tag{5.5.2}$$

The effective wave equation for  $\overline{\mathbf{U}}_\epsilon(\mathbf{x})$  is to be obtained from the combination of the macroscopic balance equations (5.5.2a)+(5.5.2b)+ $\epsilon^2$ (5.5.2c), keeping in mind that the resulting PDE needs only be satisfied at order  $O(\epsilon^2)$ . Before effecting the above combination, we will recast equations (5.5.2b) and (5.5.2c) into equivalent forms that take advantage of the reciprocity identities.

(a) *Reformulation of the  $O(\epsilon)$  balance equation.* We write  $\mathbf{C}_1^H$  as

$$C_{1ijklm}^H = D_{1ijklm} + \frac{\varrho_{1pij}^H}{\varrho_0^H} C_{0pmkl}^H, \tag{5.5.3}$$

in (b), with the reciprocity residual tensor  $\mathbf{D}_1$  given by 5.4.1, which allows to recast the  $O(\epsilon)$  macroscopic balance equation (5.5.2b) as

$$0 = C_{0ijkl}^H U_{1k,\ell j} + \omega^2 \varrho_0^H U_{1i} + D_{1ijklm} U_{0k,\ell mj} + \omega^2 \varrho_{1ikl}^\# U_{0k,\ell}, \tag{5.5.4}$$

where  $\varrho_1^\#$  is defined by 5.4.7.

(b) *Reformulation of the  $O(\epsilon^2)$  balance equation.* To this aim, we first express  $\mathbf{C}_2^H$  as

$$C_{2ijnklm}^H = D_{2ijnklm} + \frac{\varrho_{1pij}^H}{\varrho_0^H} D_{1pnklm} + \frac{\varrho_{2pklm}^H}{\varrho_0^H} C_{0pmij}^H - \frac{\varrho_{1p(ij)}^H}{\varrho_0^H} \frac{\varrho_{psn}^\#}{\varrho_0^H} C_{0s\{m\}(kl)}^H, \tag{5.5.5}$$

(with the reciprocity residual tensor  $\mathbf{D}_2$  given by 5.4.8) and use again the representation 5.5.3 of  $\mathbf{C}_1^H$ , to find

$$\begin{aligned}
0 &= C_{0ijkl}^H U_{2k,\ell j} + \omega^2 \varrho_0^H U_{2i} + D_{1ijklm} U_{1k,\ell mj} + \frac{\varrho_{1pij}^H}{\varrho_0^H} C_{0pmkl}^H U_{1k,\ell mj} + \omega^2 \varrho_{1ipq}^H U_{1p,q} \\
&+ \left( D_{2ijnklm} + \frac{\varrho_{1pij}^H}{\varrho_0^H} D_{1pnklm} + \frac{\varrho_{2pklm}^H}{\varrho_0^H} C_{0pmij}^H - \frac{\varrho_{1p(ij)}^H}{\varrho_0^H} \frac{\varrho_{psn}^\#}{\varrho_0^H} C_{0s\{m\}(kl)}^H \right) U_{0k,\ell mnj} + \omega^2 \varrho_{2iklm}^H U_{0k,\ell m}.
\end{aligned} \tag{5.5.6}$$

We next observe that, by combining 5.5.4 and (5.5.2a), we have

$$\begin{aligned}
&\frac{\varrho_{1pij}^H}{\varrho_0^H} \left( D_{1pnklm} U_{0k,\ell mnj} - \frac{\varrho_{psn}^\#}{\varrho_0^H} C_{0s\{m\}(kl)}^H U_{0k,\ell mnj} + C_{0pmkl}^H U_{1k,\ell mj} \right) + \omega^2 \varrho_{1ipq}^H U_{1p,q} \\
&= \omega^2 \left( \varrho_{1ikl}^H - \varrho_{1klj}^H \right) U_{1k,\ell} - \frac{\varrho_{1pij}^H}{\varrho_0^H} \left( \varrho_{1psn}^\# C_{0s\{m\}(kl)}^H U_{0k,\ell mnj} + \omega^2 \varrho_{1pkl}^\# U_{0k,\ell j} \right) \\
&= \omega^2 \varrho_{1ikl}^\# U_{1p,j},
\end{aligned} \tag{5.5.7}$$

while we also have

$$\begin{aligned}
&\varrho_{2pklm}^H C_{0pmij}^H U_{0k,\ell mnj} + \omega^2 \varrho_0^H \varrho_{2iklm}^H U_{0k,\ell m} \\
&= \left( \varrho_{2pklm}^H C_{0pmij}^H + \varrho_{2pijn}^H C_{0pmkl}^H \right) U_{0k,\ell mnj} - \varrho_{2pijn}^H C_{0pmkl}^H U_{0k,\ell mnj} + \omega^2 \varrho_0^H \varrho_{2iklm}^H U_{0k,\ell m} \\
&= \left( \varrho_{2pklm}^H C_{0pmij}^H + \varrho_{2pijn}^H C_{0pmkl}^H \right) U_{0k,\ell mnj} + \omega^2 \varrho_0^H \left( \varrho_{2iklm}^H + \varrho_{2kilm}^H \right) U_{0k,\ell m}.
\end{aligned} \tag{5.5.8}$$

Using identities 5.5.7 and 5.5.8 in 5.5.6 allows to recast the latter into

$$\begin{aligned} & C_{0ijkl}^H U_{2k,\ell j} + \omega^2 \varrho_0^H U_{2i} + D_{1ijklm} U_{1k,\ell mj} + \omega^2 \varrho_{1ik\ell}^\# U_{1k,\ell} \\ & + \left( D_{2ijnklm} + \frac{\varrho_{2pk\ell m}^H}{\varrho_0^H} C_{0pni j}^H + \frac{\varrho_{2pijn}^H}{\varrho_0^H} C_{0pmk\ell}^H \right) U_{0k,\ell mnj} + \omega^2 \left( \varrho_{2ik\ell m}^H + \varrho_{2kil m}^H \right) U_{0k,\ell m} = 0 \end{aligned} \quad (5.5.9)$$

Now, we recall expression 5.4.6 of  $\mathbf{D}_2$  and notice that we have

$$\left( \int_{\mathcal{Y}^\epsilon} \beta \chi_p^{1(ij)} \chi_p^{1\{n\}s} dy \right) C_{0s\{m\}(kl)}^H U_{0k,\ell mnj} = -\omega^2 \left( \int_{\mathcal{Y}^\epsilon} \rho \chi_p^{1(i\ell)} \chi_p^{1km} dy \right) U_{0k,\ell m}$$

thanks to equation (5.5.2a). Consequently, we have

$$\begin{aligned} D_{2ijnklm} U_{0k,\ell mnj} & = \left( \int_{\mathcal{Y}^\epsilon} \chi_{p,q}^{2(ijn)} C_{pqab} \chi_{a,b}^{2\{(kl)m\}} dy - \int_{\mathcal{Y}^\epsilon} \chi_p^{1(ij)} C_{p\{n\}a\{m\}} \chi_a^{1(kl)} dy \right) U_{0k,\ell mnj} \\ & \quad - \omega^2 \left( \int_{\mathcal{Y}^\epsilon} \rho \chi_p^{1(i\ell)} \chi_p^{1km} dy \right) U_{0k,\ell m} \end{aligned} \quad (5.5.10)$$

Finally, thanks to equation (5.5.2a), we also have

$$C_{0pmk\ell}^H C_{0pni j}^H U_{0k,\ell mnj} + \varrho_0^H \omega^2 C_{0imk\ell}^H U_{0k,\ell m} = 0 \quad (5.5.11)$$

We then use 5.5.10 in 5.5.9 and *add to the resulting equality a scalar multiple of equality 5.5.11*, with an arbitrary weight parameter denoted  $\eta^2$ , which yields the final form of the  $O(\epsilon^2)$  macroscopic balance equation (5.5.2c):

$$\begin{aligned} & C_{0ijkl}^H U_{2k,\ell j} + D_{1ijklm} U_{1k,\ell mj} - E_{ijnklm} U_{0k,\ell mnj} \\ & \quad + \omega^2 \left( \varrho_0^H U_{2i} + \varrho_{1ik\ell}^\# U_{1k,\ell} - G_{ik\ell m} U_{0k,\ell m} \right) = 0 \end{aligned} \quad (5.5.12)$$

where the fourth-order tensor  $\mathbf{G}$  and the sixth-order tensor  $\mathbf{E}$  are defined by

$$G_{ik\ell m} = \int_{\mathcal{Y}^\epsilon} \rho \chi_p^{1(i\ell)} \chi_p^{1km} dy - \varrho_{2ik\ell m}^H - \varrho_{2kil m}^H + \eta^2 C_{0imk\ell}^H \quad (5.5.13)$$

$$\begin{aligned} E_{ijnklm} & = \int_{\mathcal{Y}^\epsilon} \chi_p^{1(ij)} C_{p\{n\}a\{m\}} \chi_a^{1(kl)} dy - \int_{\mathcal{Y}^\epsilon} \chi_{p,q}^{2(ijn)} C_{pqab} \chi_{a,b}^{2\{(kl)m\}} dy \\ & \quad - \frac{\varrho_{2pk\ell m}^H}{\varrho_0^H} C_{0pni j}^H - \frac{\varrho_{2pijn}^H}{\varrho_0^H} C_{0pmk\ell}^H + \eta^2 C_{0pmk\ell}^H C_{0pni j}^H \end{aligned} \quad (5.5.14)$$

We observe that a suitable selection of the adjustable parameter  $\eta$  will ensure positivity of both tensors  $\mathbf{J}$  and  $\mathbf{A}$  (in the sense of the symmetric quadratic forms  $D_{2ijnklm} Q_{ijn} Q_{klm}$  and  $G_{ik\ell m} R_{im} R_{kl}$ , respectively).

(c) *Effective strain-gradient wave equation.* We finally formulate the combination (5.5.2a) +  $\epsilon$ 5.5.4 +  $\epsilon^2$ 5.5.12, i.e.:

$$\begin{aligned} o(\epsilon^2) & = C_{0ijkl}^H U_{0k,\ell j} + \omega^2 \varrho_0^H U_{0i} \\ & \quad + \epsilon \left[ C_{0ijkl}^H U_{1k,\ell j} + \omega^2 \varrho_0^H U_{1i} + D_{1ijklm} U_{0k,\ell mj} + \omega^2 \varrho_{1ik\ell}^\# U_{0k,\ell} \right] \\ & \quad + \epsilon^2 \left[ C_{0ijkl}^H U_{2k,\ell j} + D_{1ijklm} U_{1k,\ell mj} - E_{ijnklm} U_{0k,\ell mnj} \right. \\ & \quad \quad \left. + \omega^2 \left( \varrho_0^H U_{2i} + \varrho_{1ik\ell}^\# U_{1k,\ell} - G_{ik\ell m} U_{0k,\ell m} \right) \right] \end{aligned} \quad (5.5.15)$$

$$= C_{0ijkl}^H U_{\epsilon k,\ell j} + M_{ijklm} U_{\epsilon k,\ell mj} - A_{ijnklm} U_{\epsilon k,\ell mnj} \quad (5.5.16)$$

$$+ \omega^2 \left( \varrho_0^H U_{\epsilon i} + K_{ik\ell} U_{\epsilon k,\ell} - J_{ik\ell m} U_{\epsilon k,\ell m} \right) \quad (5.5.17)$$

where the correspondance between the strain-gradient notation and the previously defined tensors are:

$$K_{ikl} := \epsilon \varrho_{1ikl}^{\sharp}, \quad J_{iklm} := \epsilon^2 G_{iklm}, \quad M_{ijklm} := \epsilon D_{1ijklm}, \quad A_{ijnklm} := \epsilon^2 E_{ijnklm}$$

### 5.5.2 Transient fourth-order effective wave equation

A transient version of the effective wave equation can be derived following the same steps as in the time-harmonic case. The transient effective motion hence satisfies

$$o(\epsilon^2) = C_{0ijkl}^{\text{H}} U_{ek,lj} + M_{ijklm} U_{ek,lmj} - A_{ijnklm} U_{ek,lmnj} - \varrho_0^{\text{H}} U_{ei}'' - K_{ikl} U_{ek,\ell}'' + J_{iklm} U_{ek,lm}'' \quad (5.5.18)$$

the prime symbol denoting a time derivative.

## 5.6 Synthesis

In this chapter, the classical second-order asymptotic expansion for the elastic wave equation is recalled. Reciprocity relationship are recalled (for the first one) and completed (for the second one). These identities enable to (i) reduce the number of cell problems necessary to compute the effective properties and (ii) reformulate the effective wave equation in the strain-gradient formalism, ensuring expected symmetries and sign of higher-order tensors thanks to an arbitrary adjustable parameter. These properties are crucial to establish the well-posedness of this model in the time domain<sup>6</sup>. An article in collaboration with M. Bonnet is in preparation, and numerical application and illustrations are provided in the next Chapter.

---

<sup>6</sup>M. Bonnet, private communication

# Chapter 6

## Computation of high-order homogenized tensors : numerical examples

### Contents

---

|       |  |     |
|-------|--|-----|
| 6.1   | NUMERICAL VALIDATION . . . . .                           | 161 |
| 6.1.1 | CONVERGENCE OF THE HOMOGENIZATION SCHEME . . . . .       | 165 |
| 6.1.2 | INFLUENCE OF THE HETEROGENITIES/UNIT-CELL SIZE . . . . . | 168 |
| 6.1.3 | TRANSLATION INVARIANCE . . . . .                         | 169 |

---

The purpose of this chapter is to set the numerical framework of the homogenized high-order tensors provided by the two-scale homogenization method for periodic media, as presented in chapter 5. We begin recalling the numerical implementation of the cell-problems. Next, the heterogeneities' size effects will be highlighted by computing the effective parameters for a two-phase unit cell, by varying the size of the heterogeneity. Finally, we investigate the influence of translation/rotational invariance of the medium, in the sens of symmetry groups, on the homogenized tensors for a given geometry.

### 6.1 Numerical validation

In order to identify the effective high-order tensors, the variational problems ?? and ?? need to be solved numerically by the finite element method in order to compute the cell-functions  $\chi^1$  and  $\chi^2$ . It is worth noting that, thanks to the reciprocity identities, there is no need to compute the 3<sup>th</sup> cell function. Let's recall the variational formulation corresponding to each cell functions, and the definition of the homogenized tensors.

**Cell functions:** The first two cell functions  $\chi^1$  and  $\chi^2$  are solutions of the cell problems consisting of the differential equations over the unit cell  $\mathcal{Y}^1$ :

$$\begin{aligned}
 \text{(a)} \quad & -\nabla_y \cdot \{ \mathbf{C}(\mathbf{y}) : \varepsilon_y (\chi^{1(ij)}) \} = \nabla_y \cdot \{ \mathbf{C}(\mathbf{y}) : (\mathbf{e}_i \otimes^s \mathbf{e}_j) \} \\
 \text{(b)} \quad & -\nabla_y \cdot \{ \mathbf{C}(\mathbf{y}) : \varepsilon_y (\chi^{2\{(kl)m\}}) + \mathbf{C}(\mathbf{y}) \cdot \chi^{1(kl)} \} = \nabla_x \cdot \{ \mathcal{S}_{0\{m\}} - \beta(\mathbf{y}) \mathbf{C}_{0\{(kl)m\}}^H \} \\
 & \hspace{15em} (6.1.1)
 \end{aligned}$$

With the requirements

$$\langle \boldsymbol{\chi}^i \rangle_{\mathcal{Y}^1} = 0, \quad \boldsymbol{\chi}^i \text{ is } \mathcal{Y}^1 - \text{periodic} \quad (i = 1, 2, 3).$$

As shown in the figure (??), the correctors  $\boldsymbol{\chi}^1$  and  $\boldsymbol{\chi}^2$  need to be computed, by solving respectively, the first and the second cell problems using periodic boundary conditions over the unit cell. The corresponding variational formulations, using index notation, are written as follows :

### Variational formulation

For each macroscopic loading indexed by  $(i, j)$ , respectively by  $(k, l, m)$ , solve the following variational problems: find  $\boldsymbol{\chi}^{1(ij)}$  and  $\boldsymbol{\chi}^{2\{(kl)m\}} \in H_{\#}^1(\mathcal{Y}^1)$  such that

$$\begin{aligned} \text{(a)} \quad & \int_{\mathcal{Y}^1} \chi_{i,j}^{1(kl)} C_{ijpq} v_{p,q} dy = - \int_{\mathcal{Y}^1} C_{(kl)pq} v_{p,q} dy \\ \text{(b)} \quad & \int_{\mathcal{Y}^1} \chi_{p,q}^{2\{(kl)m\}} C_{pqrs} v_{r,s} dy = - \int_{\mathcal{Y}^1} \chi_p^{1(kl)} C_{p\{m\}rs} v_{r,s} dy - \int_{\mathcal{Y}^1} \left( \beta(\mathbf{y}) C_{0(kl)\{m\}r}^H - \mathcal{S}_{0\{m\}r}^{(kl)} \right) v_r dy \end{aligned} \quad (6.1.2)$$

Where  $(ij) = \{11, 22, 12\}$  and  $(k, l, m) = \{111, 221, 122, 222, 112, 121\}$

In total, there are 9 variational problem in 2D to be solved, 3 for the first corrector  $\boldsymbol{\chi}^1$  and 6 for  $\boldsymbol{\chi}^2$ . Once these cell-functions are computed, the high-order homogenized tensors that appear in 5.5.18 can be calculated using following the definition given in chapter 5.

$$1^{st}\text{-cell pb.} \quad \begin{cases} \varrho_0^H & = \langle \rho \rangle_{\mathcal{Y}^1} \\ C_{0ijkl}^H & = \langle C_{ijpq} \chi_p^{1(kl)} + C_{ijkl} \rangle_{\mathcal{Y}^1} \\ \epsilon K_{ikl}^{H\#} & = \langle \rho \left( \chi_i^{1(kl)} - \chi_k^{1(il)} \right) \rangle_{\mathcal{Y}^1} \\ \epsilon M_{ijklm}^{H\#} & = \langle \mathcal{S}_{0\{m\}p}^{(ij)} \chi_p^{1(kl)} - \mathcal{S}_{0\{m\}p}^{(kl)} \chi_p^{1(ij)} \rangle_{\mathcal{Y}^1}. \end{cases} \quad (6.1.3)$$

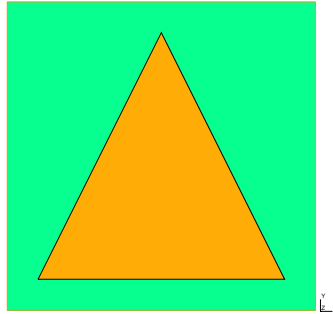
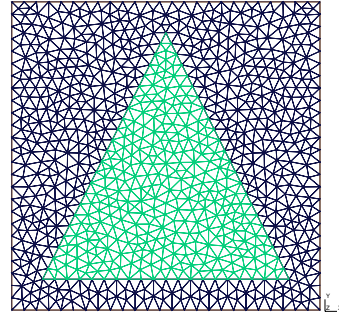
$$2^{nd}\text{-cell pb.} \quad \begin{cases} \epsilon^2 J_{iklm}^H & = \langle \rho \chi_p^{1(il)} \chi_p^{1(km)} \rangle_{\mathcal{Y}^1} - \varrho_{2ikm}^H - \varrho_{2kilm}^H + \eta^2 C_{0imkl}^H \\ \epsilon^2 A_{ijnklm}^H & = \langle \chi_p^{1(ij)} C_{p(n)a\{m\}} \chi_a^{1(kl)} - \chi_{p,q}^{2(ijn)} C_{pqab} \chi_{a,b}^{2\{(kl)m\}} \rangle_{\mathcal{Y}^1} \\ & - \frac{\varrho_{2pklm}^H}{\varrho_0^H} C_{0pnij}^H - \frac{\varrho_{2pijn}^H}{\varrho_0^H} C_{0pmkl}^H + \eta^2 C_{0pmkl}^H C_{0pnij}^H \end{cases} \quad (6.1.4)$$

Where the skew-symmetric 3<sup>th</sup>-order and the 5<sup>th</sup>-order dynamic tensors, are defined as follows

$$K_{ikl}^{H\#} = \epsilon^{-1} \left( \varrho_{0ikl}^H - \varrho_{0kil}^H \right), \quad M_{0ijklm}^{H\#} = M_{ijklm}^H - M_{0klijm}^H$$

The second-order homogenization model described in the previous chapter is implemented in the open-source code FreeFem++ with quadratic shape' functions. The computational tool includes FreeFem++ script for solving cell-problems with the finite element method and provides the solutions fields, and COMSOL Multiphysics software/Gmsh for the parametric modelling of the unit-cells and generating mesh files with triangular elements for each geometry. The homogenization procedure is summarized in Fig. (XX). In order to illustrate steps of implementation, we provide

in the following, a first 2D numerical example of the computed cell-functions and the homogenized high-order tensors for a two-phase square unit cell with a triangular inclusion of size  $a = 1 \text{ mm}$ , shown in the figure ?? . An example of mesh is given in Figure ?? as well as the nodes used for applying the boundary conditions<sup>1</sup>.

(a)  $Z_2^\pi$  unit cell

(b) 2D mesh of the unit cell with periodic boundary conditions : Homologous edges has the same color

| Phase     | $E$ (GPa) | $\nu$ | $\rho$ ( $kg/m^3$ ) | volume fraction |
|-----------|-----------|-------|---------------------|-----------------|
| Matrix    | 70        | 0.33  | 2700                | 68 %            |
| Inclusion | 200       | 0.3   | 7850                | 32 %            |

Table 6.1: The material properties

The size of the unit cell is  $a = 1 \text{ mm}$  and the material properties for both phases (matrix and inclusion) are shown in Table ?? :  $E$  Young's modulus,  $\nu$  Poisson's ratio,  $\rho$  mass density, and volume fraction. We first solve the cell-problem (6.1.2.a) to compute the first three cell-functions  $\chi^{1(kl)}$  for each unit macroscopic loading (macroscopic strain  $\mathbf{e}_k \otimes^s \mathbf{e}_l$ ). The figure 6.2 presents the solutions of the first three cell problems. Then we solve the second-cell problem (6.1.2.b) to compute the cell-functions  $\chi^{2\{(kl)m\}}$  for each macroscopic strain-gradient loading.

<sup>1</sup>For each opposite two opposite boundaries of the cell, homologous nodes are coloured the same

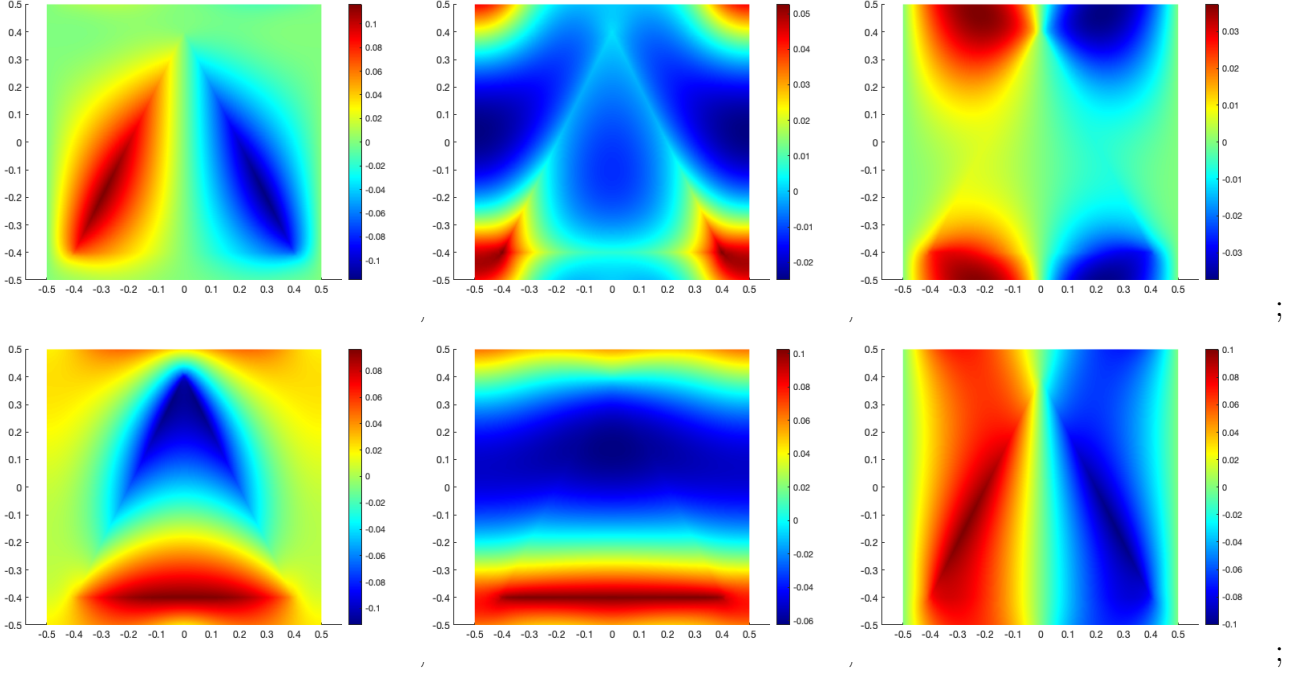


Figure 6.2: Cell-functions  $\chi^{1(11)}$ ,  $\chi^{1(22)}$  and  $\chi^{1(12)}$  produced by each macroscopic strain loading

Hereforth, the homogenized tensors will be represented by its matrix form in the kelvin Basis with the following notation convention  $C_{ijkl}^H = C_{IJ}^H$ ,  $K_{ikl}^{H\sharp} = K_{iI}^{H\sharp}$ ,  $M_{ijklm}^{H\sharp} = M_{I\alpha}^{H\sharp}$ ,  $J_{ijkl}^H = J_{IJ}^H$  and  $A_{ijnklm}^H = A_{\alpha\beta}^H$  such as <sup>2</sup>

| $I$  | 1  | 2  | 3  |
|------|----|----|----|
| $ij$ | 11 | 22 | 12 |

Table 6.2: Kelvin notation used for 2D strain tensors

| $\alpha$ | 1   | 2   | 3   | 4   | 5   | 6   |
|----------|-----|-----|-----|-----|-----|-----|
| $klm$    | 111 | 221 | 122 | 222 | 112 | 121 |

Table 6.3: Kelvin notation used for 2D strain-gradient tensors

Hence, one can write [Auffray et al., 2015]

$$[\mathbf{C}_0^H] = \begin{pmatrix} C_{11}^H & C_{12}^H & C_{13}^H \\ * & C_{22}^H & C_{23}^H \\ * & * & C_{33}^H \end{pmatrix}_{\kappa}, \quad [\mathbf{K}^{H\sharp}] = \begin{pmatrix} 0 & K_{12}^{H\sharp} \\ K_{21}^{H\sharp} & 0 \\ 0 & K_{32}^{H\sharp} \end{pmatrix}_{\kappa}, \quad [\mathbf{J}^H] = \begin{pmatrix} J_{11}^H & J_{12}^H & J_{13}^H \\ * & J_{22}^H & J_{23}^H \\ * & * & J_{33}^H \end{pmatrix}_{\kappa},$$

$$[\mathbf{M}^{H\sharp}] = \begin{pmatrix} 0 & M_{12}^{H\sharp} & M_{13}^{H\sharp} & M_{14}^{H\sharp} & 0 & M_{16}^{H\sharp} \\ -M_{12}^{H\sharp} & 0 & M_{23}^{H\sharp} & 0 & -M_{14}^{H\sharp} & M_{26}^{H\sharp} \\ M_{16}^{H\sharp} & M_{26}^{H\sharp} & 0 & M_{23}^{H\sharp} & M_{13}^{H\sharp} & 0 \end{pmatrix}_{\kappa},$$

and

<sup>2</sup>see Auffray for the construction

$$[\mathbf{A}^H] = \begin{pmatrix} A_{11}^H & A_{12}^H & A_{13}^H & A_{14}^H & A_{15}^H & A_{16}^H \\ * & A_{22}^H & A_{23}^H & A_{24}^H & A_{25}^H & A_{26}^H \\ * & * & A_{33}^H & A_{34}^H & A_{35}^H & A_{36}^H \\ * & * & * & A_{44}^H & A_{45}^H & A_{46}^H \\ * & * & * & * & A_{55}^H & A_{56}^H \\ * & * & * & * & * & A_{66}^H \end{pmatrix}_{\mathcal{K}}.$$

At this order, one can compute the  $\mathbf{C}_0^H$  et  $\varrho_0^H$ . the homogenized tensor  $\mathbf{M}^{H\sharp}$  and  $\mathbf{K}^{H\sharp}$  can be obtained using the 1st reciprocity identity. We give the value of the computed homogenized tensors defined by 6.1.3 and 6.1.4

$$[\mathbf{C}_0^H] \simeq \begin{pmatrix} 134.9 & 62.1 & 0 \\ 62.1 & 137.20 & \\ 0 & 0 & 69.09 \end{pmatrix}_{\mathcal{K}} \text{ GPa}, \quad \epsilon^1 [\mathbf{K}^{H\sharp}] \simeq \begin{pmatrix} 0 & -4.882 \\ 1.613 * 10^{-4} & 0 \\ 0 & 6.905 \end{pmatrix}_{\mathcal{K}} \text{ GPa}\cdot\text{m}$$

$$\epsilon^1 [\mathbf{M}^{H\sharp}] \simeq \begin{pmatrix} 0 & -0.023 & 0.083 & 0 & 0 & 0 \\ 0.023 & 0 & 0.21 & 0 & 0 & 0 \\ 0 & 0 & 0 & -0.21 & -0.083 & 0 \end{pmatrix}_{\mathcal{K}} \text{ GPa}\cdot\text{m}, \quad \epsilon^2 [\mathbf{J}^H] \simeq \begin{pmatrix} 91.5 & 76.2 & 0 \\ 76.2 & 92.91 & 0 \\ 0 & 0 & 98.83 \end{pmatrix}_{\mathcal{K}} \text{ GPa}\cdot\text{m}^2$$

$$\epsilon^2 [\mathbf{A}^H] \simeq \begin{pmatrix} 1.195 & 0.782 & 0.950 & 0 & 0 & 0 \\ 0.782 & 0.251 & 0.210 & 0 & 0 & 0 \\ 0.950 & 0.210 & 0.614 & 0 & 0 & 0 \\ 0 & 0 & 0 & 1.437 & 1.006 & 1.168 \\ 0 & 0 & 0 & 1.006 & 0.316 & 0.278 \\ 0 & 0 & 0 & 1.168 & 0.278 & 0.625 \end{pmatrix}_{\mathcal{K}} \text{ GPa}\cdot\text{m}^2,$$

with the homogenized mass density  $\varrho_0^H \simeq 4348 \text{ kg}\cdot\text{m}^{-3}$ . Note that All cell-functions in figure 6.2 has the symmetry of the unit cell. One can notice that  $\mathbf{C}_0^H$  and  $\mathbf{J}^H$ , have respectively 4 independant components,  $\mathbf{K}^{H\sharp}$  and  $\mathbf{M}^{H\sharp}$  respectively on depends on 3 independant components, while the 6<sup>th</sup>-order tensor  $\mathbf{A}^H$  includes 12 independant components. As expected, the homogenized tensors exhibit the  $Z_2^\pi$  symmetry, and have the same shape as the constitutive tensors of a material havin  $Z_2^\pi$  symmetry, which is in agreement with the theoretically matrix shapes predicted in [Auff,Dir,Ro]. In order to compare and validate the results, the convergence with respect to the mesh quality, the influence of translation/rotation of the unit cell and the size of heterogeneities will be investigated in the next subsections.

### 6.1.1 Convergence of the homogenization scheme

Now we compute the homogenized tensors in order to study the convergence of the effective properties with respect to the mesh, for a number of elements ranging from 70 to 26000. To investigate to size effect, it would be interesting to consider a new square unit-cell with square inclusion (see Figure 6.3) for which, one would expect that the homogenized tensors exhibit the  $D_4$  symmetry. In this case, we know that the 4<sup>th</sup>-order tensors  $\mathbf{C}_0^H$  and  $\mathbf{J}^H$  depend, respectively only on 3 independant components, and the 6<sup>th</sup>-order tensor  $\mathbf{A}^H$  depend on 6 independant components, such as

$$C_{11}^{H,D_4} = C_{22}^{H,D_4}, \quad J_{11}^{H,D_4} = J_{22}^{H,D_4}, \quad (6.1.5)$$

and

$$\begin{aligned} A_{11}^{\text{H},\text{D}_4} &= A_{44}^{\text{H},\text{D}_4}, & A_{22}^{\text{H},\text{D}_4} &= A_{55}^{\text{H},\text{D}_4}, & A_{33}^{\text{H},\text{D}_4} &= A_{66}^{\text{H},\text{D}_4}, \\ A_{23}^{\text{H},\text{D}_4} &= A_{56}^{\text{H},\text{D}_4}, & A_{13}^{\text{H},\text{D}_4} &= A_{46}^{\text{H},\text{D}_4}, & A_{12}^{\text{H},\text{D}_4} &= A_{45}^{\text{H},\text{D}_4}. \end{aligned} \quad (6.1.6)$$

It is worth noting that, due to the centrosymmetry of the unit cell, the 3<sup>th</sup>-order tensor  $\mathbf{K}^{\text{H}\sharp}$  and the 5<sup>th</sup>-order  $\mathbf{M}^{\text{H}\sharp}$  are, respectively vanishing (see. Auff,Dir,Ro).

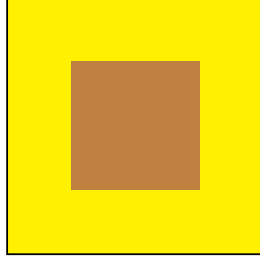


Figure 6.3:  $\text{D}_4$  unit-cell with a square inclusion

The convergence analysis consists in computing the relative errors related to the relationships 6.1.5 and 6.1.6, such as

$$\begin{aligned} \delta_{C_{11}^{\text{H},\text{D}_4}}(n_e) &= \frac{|C_{11}^{\text{H},\text{D}_4} - C_{22}^{\text{H},\text{D}_4}|}{C_{11}^{\text{H},\text{D}_4}}, & \delta_{J_{11}^{\text{H},\text{D}_4}}(n_e) &= \frac{|J_{11}^{\text{H},\text{D}_4} - J_{22}^{\text{H},\text{D}_4}|}{J_{11}^{\text{H},\text{D}_4}}, \\ \delta_{A_{11}^{\text{H},\text{D}_4}}(n_e) &= \frac{|A_{11}^{\text{H},\text{D}_4} - A_{44}^{\text{H},\text{D}_4}|}{A_{11}^{\text{H},\text{D}_4}}, \dots, & \delta_{A_{33}^{\text{H},\text{D}_4}}(n_e) &= \frac{|A_{33}^{\text{H},\text{D}_4} - A_{66}^{\text{H},\text{D}_4}|}{A_{33}^{\text{H},\text{D}_4}} \end{aligned} \quad (6.1.7)$$

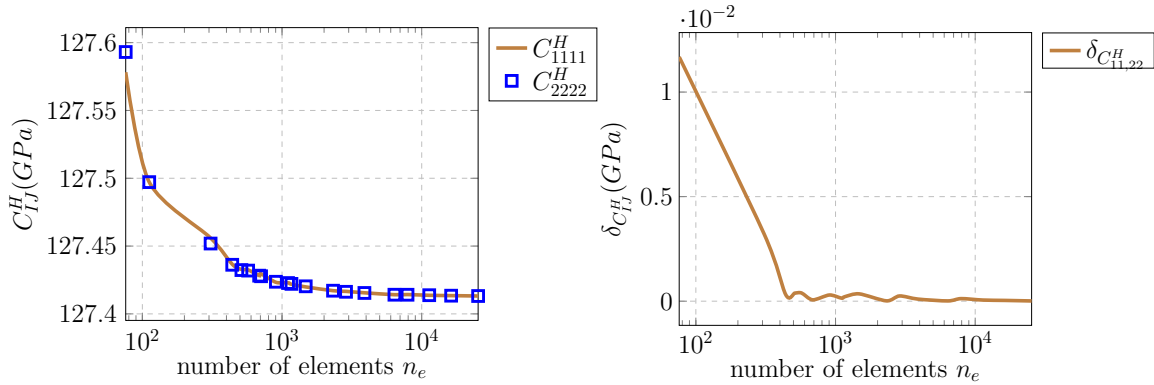


Figure 6.4: Mesh convergence : Evolution of the homogenized components of the elasticity tensor  $\mathbf{C}^{\text{H}}$  with respect to the number of elements

the figures 6.4 and 6.5 show the convergence of the homogenized components and the errors as a function of the mesh size. for  $n_e=100$ , we can see that the relative errors made on  $C_{11}^{\text{H}}$  and  $J_{11}^{\text{H}}$ , are respectively about 0,003 % and 0,008%. For  $n_e > 1000$ , it appears that those errors become very negligible (smaller than 0.0001 %). Similar observation can be made on figure 6.6 about the errors made on the components of  $\mathbf{A}^{\text{H}}$ , THE homogenized second order elasticity tensor. The overall errors are much larger : about 0.1 % for  $n_e = 100$ , 0,05 for  $n_e = 500$ , and 0,01 for  $n_e = 900$ . It becomes

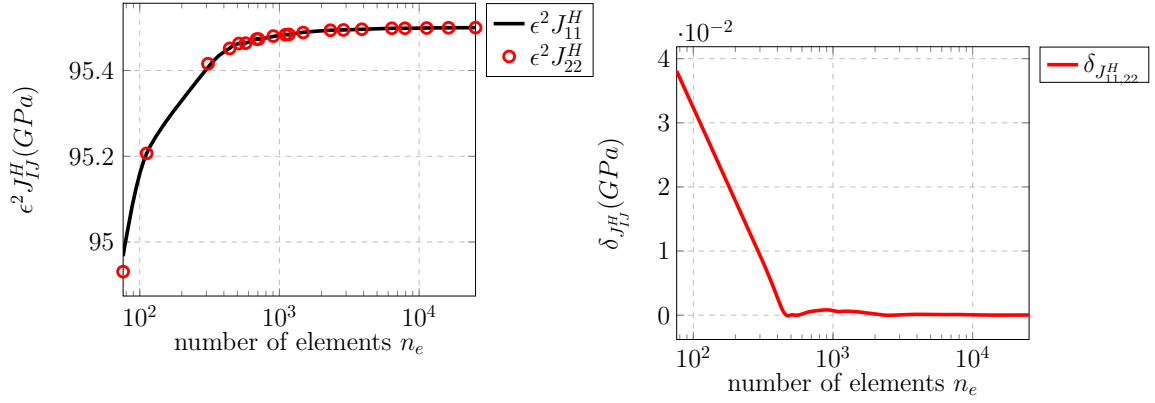


Figure 6.5: Mesh convergence : Evolution of the homogenized components of the homogenized micro-inertia tensor  $\mathbf{J}^H$  with respect to the number of elements

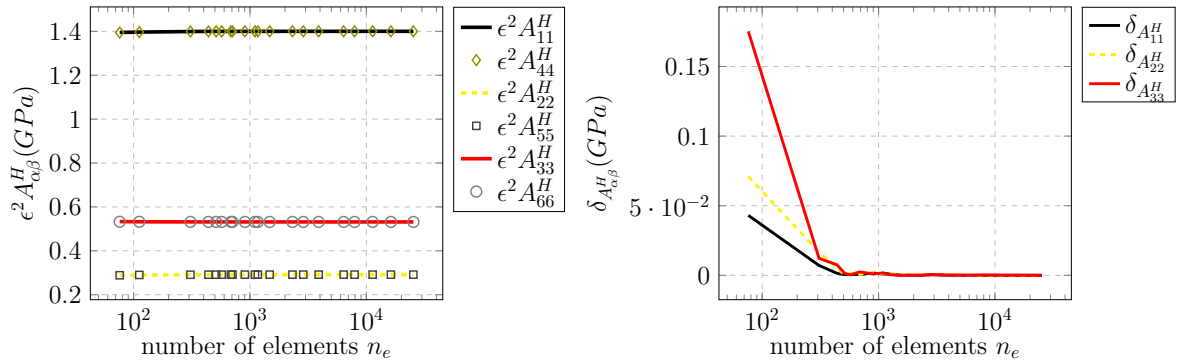


Figure 6.6: Mesh convergence : Evolution of the homogenized components of the homogenized second order elasticity tensor  $\mathbf{A}^H$  with respect to the number of elements

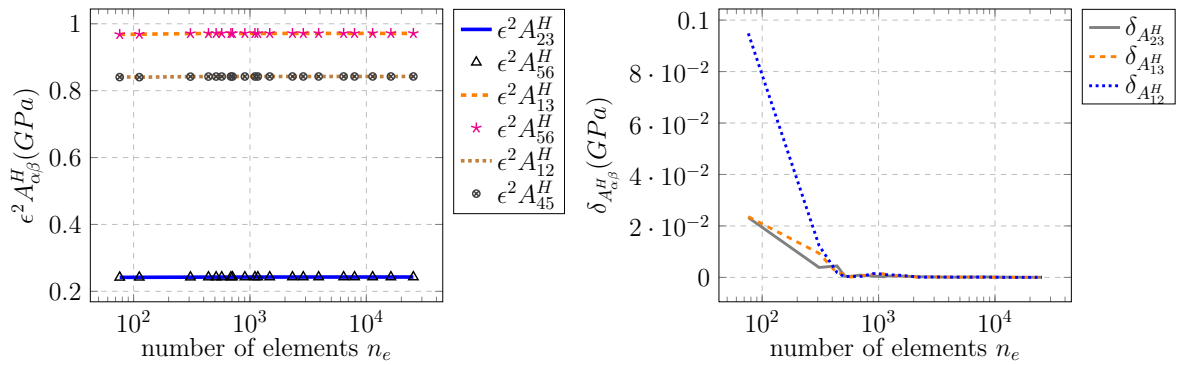


Figure 6.7: Mesh convergence : Evolution of the homogenized components with respect to the number of elements

acceptable from  $n_e = 1000$ , for which the relative errors are smaller than 0.0008 %. Hence, We can see that the mesh size has almost no effect on the accuracy of the values of homogenized components for  $n_e > 1000$ . Finally, the numerical values<sup>3</sup> of components of the coupling tensors  $\mathbf{K}^{H\sharp}$  and  $\mathbf{M}^{H\sharp}$ , are found to be less than  $10^{-6}$  GPa · m which are negligible as compared to the values of the non-centrosymmetric case  $Z_2^\pi$ .

<sup>3</sup>Not reported here

These results, as expected, comply with the expected symmetric.

### 6.1.2 Influence of the heterogeneities/unit-cell size

In this subsection, the effect of 2 parameters on the effective properties are quantitatively investigated quantitatively: the size of the heterogeneity (inclusion) and the size of the unit cell. The first study focuses on the effect of the volume fraction of the inclusion, while the second focuses on the scale ratio. Without loss of generality, we choose to consider the previous unit cell with same material properties and a volume fraction varying as a function of the size of the thickness of the matrix and the length of the unit cell, such as

$$V_f = 1 - \frac{(a - 2t)^2}{a^2}.$$

The thickness of the matrix  $t$  varies from 0.005 mm to 0.4842 mm, leading to a change of the volume fraction  $V_f$  of the matrix from 2 to 0.99 % as indicated in Table (XX). The homogenized components are plotted on figure ?? as the functions of volume fraction of matrix,

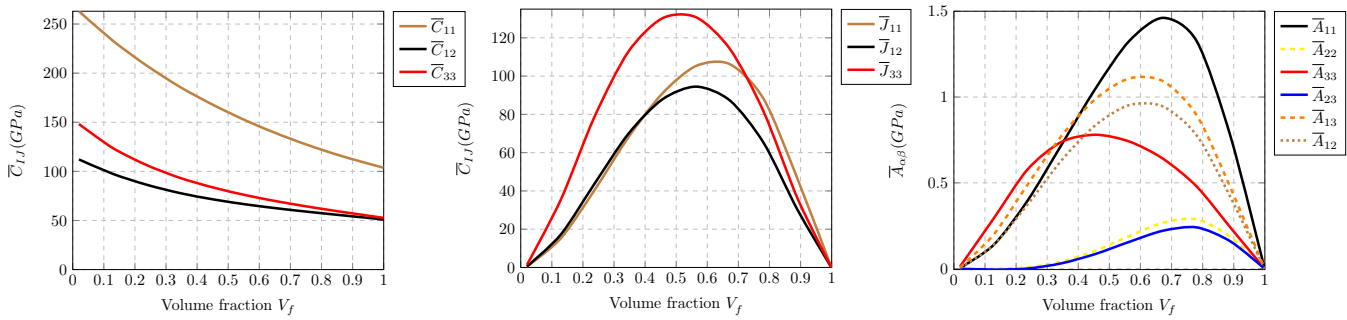


Figure 6.8: Evolution of the homogenized components with respect to the volume fraction of heterogeneities

It can be noticed that the volume fraction  $V_f$  has more effect on the homogenized components of the sixth-order tensor  $\mathbf{A}^H$  than those of  $\mathbf{C}_0^H$  and  $\mathbf{J}^H$ . We observe that the strain-gradient homogenized components increase at first, then decrease. Strain-gradient effects only appears when the material is heterogeneous at the local scale. However, when the volume fraction is near to 0 or to 100 %, the unit cell can be viewed as a homogeneous single phase and thus, the strain-gradient effects vanishes.

As mentioned before, the homogenized high-order tensor are defined independently of the scale ratio, i.e. the size of the unit cell. One would like to check this property numerically. To do so, we compute the homogenized components over the same previous unit cell, while varying its size from 0.1 mm to 1 mm, which is equivalent to consider the initial unit-cell ( $a=1\text{mm}$ ) with multiple irreducible unit cells such that the volume fraction remains the same. It is expected that, for each configuration, the homogenization process provides the same value of the homogenized tensors. The results are shown in figure ??,

One can notice that, the homogenized components of the first order elasticity tensor remains unchanged as expected since it does not depends on the scale ratio. However,

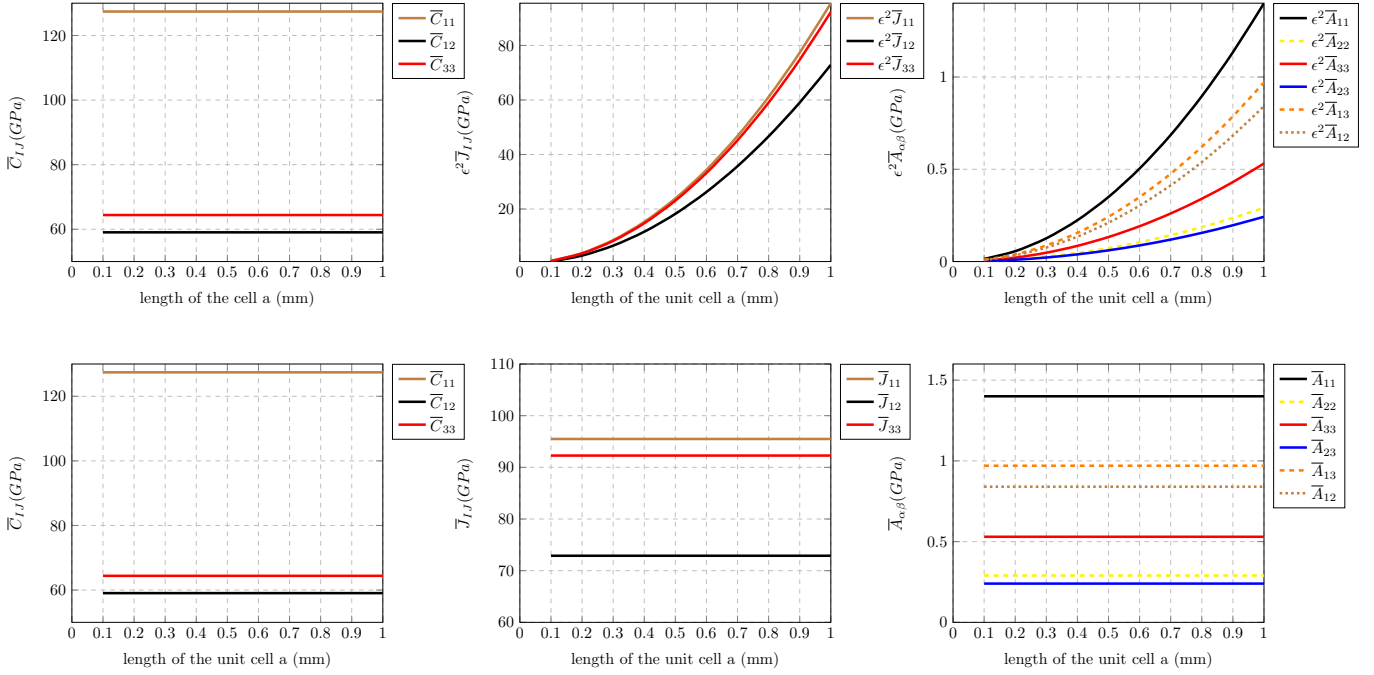


Figure 6.9: Evolution of the homogenized components with respect to the unit cell size

the high-order homogenized components depend linearly on the scale ration  $\epsilon$  which, in this cas, is taken to be equal to  $a^2$ . As a consequence, the latter are independent of the number of on the unit cell-size/scale ratio,. i.e. the number periods. Hence, it can be determined by considering only one irreducible unit cell, with an suitable scale separation ratio  $\epsilon$ .

### 6.1.3 Translation invariance

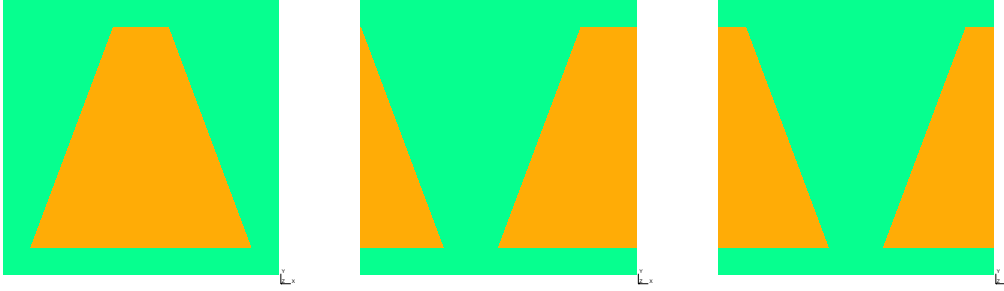
As said in chapter 2, A medium is periodic if the space is filled from a set of independent translations of the unit cell. Thus, the medium exhibits translational invariance of the effective properties with respect to the Bravais lattice' basis vectors. Furthermore, in the case where the elementary cell has some rotational invariance, or mirror lines for example, it is expected that the homogenized properties will also have this invariance. One would like to check numerically those invariance properties. To this end, we consider 2  $Z_2^{\pi}$ -invariant unit cells  $\mathcal{Y}_1$  and  $\mathcal{Y}_2$ , as obtained by translation of the reference unit cell  $\mathcal{Y}_0$  (shifted by a distance  $d < a$ ) in the direction  $\mathbf{e}_1$  as shown in figures ??, such as

$$\mathcal{Y}_{\text{ref}} = (0, a) \times (0, a), \quad \mathcal{Y}_1 = \mathcal{Y}_{\text{ref}} + \{(2a/5, 0)\}, \quad \mathcal{Y}_2 = \mathcal{Y}_{\text{ref}} + \{(a/2, 0)\}.$$

Then we compute the relative errors of homogenized tensors with respect to the reference configuration (non-shifted), defined as

$$\begin{aligned} \epsilon(\mathbf{C}^{\text{H}}) &= \frac{\|\mathbf{C}_{\text{ref}}^{\text{H}} - \mathbf{C}^{\text{H}}\|}{\|\mathbf{C}_{\text{ref}}^{\text{H}}\|}, & \epsilon(\mathbf{J}^{\text{H}}) &= \frac{\|\mathbf{J}_{\text{ref}}^{\text{H}} - \mathbf{J}^{\text{H}}\|}{\|\mathbf{J}_{\text{ref}}^{\text{H}}\|}, & \epsilon(\mathbf{K}^{\text{H}\sharp}) &= \frac{\|\mathbf{K}_{\text{ref}}^{\text{H}\sharp} - \mathbf{K}^{\text{H}\sharp}\|}{\|\mathbf{K}_{\text{ref}}^{\text{H}\sharp}\|} \\ \epsilon(\mathbf{M}^{\text{H}\sharp}) &= \frac{\|\mathbf{M}_{\text{ref}}^{\text{H}\sharp} - \mathbf{M}^{\text{H}\sharp}\|}{\|\mathbf{M}_{\text{ref}}^{\text{H}\sharp}\|}, & \epsilon(\mathbf{A}^{\text{H}}) &= \frac{\|\mathbf{A}_{\text{ref}}^{\text{H}} - \mathbf{A}^{\text{H}}\|}{\|\mathbf{A}_{\text{ref}}^{\text{H}}\|} \end{aligned}$$

where  $\|\bullet\|$  stands for the frobunius norm.



(a)  $\mathcal{Y}_{\text{ref}}$  :  $Z_2^\pi$  reference unit cell (b)  $\mathcal{Y}_1$  : Shifted cell n° 1 (c)  $\mathcal{Y}_2$  : Shifted cell n° 2

Thus one would expect that for each of these configurations, the homogenization procedure provides the same homogenized tensors. The results for each tensor are shown in the table 6.4

| $\epsilon$      | $\mathbf{C}^{\text{H}}$  | $\mathbf{J}^{\text{H}}$  | $\mathbf{K}^{\text{H}}$  | $\mathbf{M}^{\text{H}}$  | $\mathbf{A}^{\text{H}}$  |
|-----------------|--------------------------|--------------------------|--------------------------|--------------------------|--------------------------|
| $\mathcal{Y}_1$ | $1.70064 \times 10^{-6}$ | $4.35424 \times 10^{-6}$ | $1.49992 \times 10^{-4}$ | $5.96706 \times 10^{-5}$ | $9.37738 \times 10^{-6}$ |
| $\mathcal{Y}_2$ | $1.35382 \times 10^{-6}$ | $3.35399 \times 10^{-6}$ | $1.44675 \times 10^{-4}$ | $5.86591 \times 10^{-5}$ | $8.08951 \times 10^{-6}$ |

Table 6.4

This shows that the invariance of homogenized tensors with respect to the unit cell choice is numerically satisfied. Furthermore, the unit cell exhibits a mirror line symmetry, we would like to check the property of rotational/inversion invariance of the homogenized tensors with respect to unit cell. We choose a configuration in which the unit cell is rotated with an angle of  $\pi/2$ , then we compute homogenized tensors for a transformed unit cell under the action of the orthogonal group. Let consider the previous refence unit-cell, which exhibits a symmetry plane with respect to  $\mathbf{e}_2$ . The coupling inertia tensor has the following form

$$\mathbf{K}_{(\mathbf{e}_2)}^{\text{H}} = \begin{pmatrix} 0 & \mathbf{K}_{211} \\ 0 & \mathbf{K}_{222} \\ \sqrt{2}\mathbf{K}_{112} & 0 \end{pmatrix}_{\mathcal{K}}, \quad \mathbf{K}_{(\mathbf{e}_2)}^{\text{H}\sharp} = \begin{pmatrix} 0 & \mathbf{K}_{211} - \mathbf{K}_{112} \\ 0 & 0 \\ \sqrt{2}(\mathbf{K}_{112} - \mathbf{K}_{211}) & 0 \end{pmatrix}_{\mathcal{K}} \quad (6.1.8)$$

The homogenized coupling inertia tensor for the reference cell is given by

$$\mathbf{K}_{\mathcal{Y}_{\text{ref}}}^{\text{H}\sharp}(\mathbf{e}_2) = \begin{pmatrix} 0 & 7.554448186 \\ 0 & -5.697746155 \times 10^{-8} \\ -10.6836030 & 0 \end{pmatrix}$$

Let  $\mathbf{Q}(\mathbf{e}_2)$  be the reflection tensor in the normal axis to  $\mathbf{e}_2$ . The invariance of  $\overline{\mathbf{K}}_{Z_2^\pi(\mathbf{e}_2)}$  under the action of  $\mathbf{Q}(\mathbf{e}_2)$  if equivalent to

$$\mathbf{K}^{\text{H}\sharp\star} = \mathbf{Q}(\mathbf{e}_2) \star \mathbf{K}_{\mathcal{Y}_{\text{ref}}}^{\text{H}\sharp}(\mathbf{e}_2) = \mathbf{K}_{\mathcal{Y}_{\text{ref}}}^{\text{H}\sharp}(\mathbf{e}_2)$$

Numerically, we obtain

$$\epsilon(\mathbf{K}^{\text{H}\sharp}) = \frac{\|\mathbf{K}^{\text{H}\sharp\star} - \mathbf{K}_{\mathcal{Y}_{\text{ref}}}^{\text{H}\sharp}(\mathbf{e}_2)\|}{\|\mathbf{K}_{\mathcal{Y}_{\text{ref}}}^{\text{H}\sharp}(\mathbf{e}_2)\|} = 1.13955 \times 10^{-7}$$

This shows, as expected, that the invariance of the coupling inertia tensor with respect to a mirror line transformation is numerically satisfied.

## Synthesis

In this chapter, the cell problems defined in Chapter 5 were implemented and solved using the finite element method, utilizing the open-source FreeFem++ code. It should be noted that, thanks to the reciprocity identities established in Chapter 5, only the first two cell problems were considered for the calculation of the homogenized tensors.

Subsequently, we numerically validated these codes through a few numerical tests for convergence, verifying the form of the obtained tensors as well as their properties.



# Chapter 7

## Conclusion and Perspectives

### Conclusion

The research work presented in this manuscript has allowed us to characterize the elastodynamic behaviour of periodic architected materials. This endeavor was pursued via two key approaches: Firstly, through the characterization and identification of effective properties through wave propagation, and secondly, through the computation of these effective properties using the method of asymptotic homogenization.

Through a systematic investigation, the study has highlighted the influence of local architecture - the geometry of the elementary cell - on the overall elastodynamic behaviour of the architected material. We have established an elastodynamic signature via Bloch analysis, leading to a proposed method for identifying apparent properties from information gleaned from wave propagation. This approach, while phenomenological in nature, provided critical insights into the inherent characteristics of architected materials. Simultaneously, a mathematical avenue was also explored, aimed at calculating the effective properties of the medium, which offered an interesting contrast to the phenomenological method. By implementing the asymptotic homogenization method in elastodynamics, the study has contributed to the establishment of some important reciprocity relations and the construction of a Strain-gradient type model using the method of asymptotic development.

However, as is often the case in scientific exploration, each answer we found opened the door to new questions. How the local architecture influences the overall behaviour of architected materials is a question that has been frequently addressed in various ways. Future studies might delve deeper into the influences of different architectural geometries on the material's elastodynamic behaviour, refining the identification methods for apparent properties. Additionally, the mathematical approach could be further extended and refined to account for more complex or different types of materials.

Further work could also be directed towards refining the numerical models and validation tests. The robustness and versatility of the finite element code developed for the construction of the tensors of the Strain-gradient model could be further enhanced, and more extensive validation could strengthen our trust in the results it provides.

## Perspectives

Looking forward, there are several promising avenues for further research and exploration. Firstly, a natural extension of this study is to extend the method of identification in the low-frequency and long-wavelength regime to 3D situations. This progression can greatly enhance the versatility and applicability of the methods presented herein.

Secondly, an extension of the identification method to the short-wavelength and low-frequency regime could be considered. This would involve the construction of invariants of the generalized Christoffel tensors and would further broaden the scope and potential applications of our work.

Thirdly, carrying out a sensitivity study related to noise would be an interesting next step to test the robustness of our identification methods. This will provide valuable insight into the effectiveness of our methods under less than ideal or variable conditions.

The fourth point for future exploration is a more profound investigation and design of anisotropic multi-inertial networks. This investigation can potentially lead to the development of materials with custom-designed, unique properties.

Finally, another promising direction is the construction of models based on topological optimization, homogenization, and dehomogenization. This would provide a way to achieve optimal control, such as controlling wave propagation, for instance. This could lead to the development of new materials with remarkable characteristics that can be fine-tuned for specific applications. This represents an exciting and challenging direction for future research.

# Bibliography

- [Abdoul-Anziz and Seppecher, 2018] Abdoul-Anziz, H. and Seppecher, P. (2018). Strain gradient and generalized continua obtained by homogenizing frame lattices. *Mathematics and mechanics of complex systems*, 6(3):213–250.
- [Abdulle and Pouchon, 2020] Abdulle, A. and Pouchon, T. (2020). Effective models and numerical homogenization for wave propagation in heterogeneous media on arbitrary timescales. *Foundations of Computational Mathematics*, 20(6):1505–1547.
- [Abud and Sartori, 1983] Abud, M. and Sartori, G. (1983). The geometry of spontaneous symmetry breaking. *Annals of Physics*, 150(2):307–372.
- [Addressi et al., 2013] Addressi, D., De Bellis, M. L., and Sacco, E. (2013). Micromechanical analysis of heterogeneous materials subjected to overall cosserat strains. *Mechanics Research Communications*, 54:27–34.
- [Alderson et al., 2010] Alderson, A., Alderson, K. L., Attard, D., Evans, K. E., Gatt, R., Grima, J. N., Miller, W., Ravirala, N., Smith, C., and Zied, K. (2010). Elastic constants of 3-, 4- and 6-connected chiral and anti-chiral honeycombs subject to uniaxial in-plane loading. *Composites Science and Technology*, 70(7):1042–1048.
- [Allaire et al., 1997] Allaire, G., Bonnetier, E., Francfort, G., and Jouve, F. (1997). Shape optimization by the homogenization method. *Numerische Mathematik*, 76:27–68.
- [Allaire et al., 2016] Allaire, G., Briane, M., and Vanninathan, M. (2016). A comparison between two-scale asymptotic expansions and bloch wave expansions for the homogenization of periodic structures. *SEMA journal*, 73:237–259.
- [Allaire et al., 2002] Allaire, G., Jouve, F., and Toader, A.-M. (2002). A level-set method for shape optimization. *Comptes rendus. Mathématique*, 334(12):1125–1130.
- [Allaire and Yamada, 2018] Allaire, G. and Yamada, T. (2018). Optimization of dispersive coefficients in the homogenization of the wave equation in periodic structures. *Numerische Mathematik*, 140:265–326.
- [Alomar and Concli, 2020] Alomar, Z. and Concli, F. (2020). A review of the selective laser melting lattice structures and their numerical models. *Advanced Engineering Materials*, 22(12):2000611.
- [Amstutz and Andrä, 2006] Amstutz, S. and Andrä, H. (2006). A new algorithm for topology optimization using a level-set method. *Journal of computational physics*, 216(2):573–588.

- [Amstutz et al., 2010] Amstutz, S., Giusti, S. M., Novotny, A. A., and De Souza Neto, E. A. (2010). Topological derivative for multi-scale linear elasticity models applied to the synthesis of microstructures. *International Journal for Numerical Methods in Engineering*, 84(6):733–756.
- [Armstrong, 1997] Armstrong, M. A. (1997). *Groups and symmetry*. Springer Science & Business Media.
- [Ashby, 2013] Ashby, M. (2013). Designing architected materials. *Scripta Materialia*, 68(1):4–7.
- [Ashby and Bréchet, 2003a] Ashby, M. and Bréchet, Y. J. (2003a). Designing hybrid materials. *Acta materialia*, 51(19):5801–5821.
- [Ashby and Bréchet, 2003b] Ashby, M. F. and Bréchet, Y. J. (2003b). Designing hybrid materials. *Acta materialia*, 51(19):5801–5821.
- [Ashby and Gibson, 1997] Ashby, M. F. and Gibson, L. J. (1997). Cellular solids: structure and properties. *Press Syndicate of the University of Cambridge, Cambridge, UK*, pages 175–231.
- [Ashcroft and Mermin, 2022] Ashcroft, N. W. and Mermin, N. D. (2022). *Solid state physics*. Cengage Learning.
- [Askes and Aifantis, 2011] Askes, H. and Aifantis, E. C. (2011). Gradient elasticity in statics and dynamics: an overview of formulations, length scale identification procedures, finite element implementations and new results. *International Journal of Solids and Structures*, 48(13):1962–1990.
- [Auffray, 2017] Auffray, N. (2017). *Géométrie des espaces de tenseurs, application à l'élasticité anisotrope classique et généralisée*. Hdr thesis, Université Paris-Est.
- [Auffray et al., 2021] Auffray, N., Abdoul-Anziz, H., and Desmorat, B. (2021). Explicit harmonic structure of bidimensional linear strain-gradient elasticity. *European Journal of Mechanics-A/Solids*, 87:104202.
- [Auffray et al., 2015] Auffray, N., Dirrenberger, J., and Rosi, G. (2015). A complete description of bi-dimensional anisotropic strain-gradient elasticity. *International Journal of Solids and Structures*, 69:195–206.
- [Auffray et al., 2023] Auffray, N., El Ouafa, S., Rosi, G., and Desmorat, B. (2023). Anisotropic structure of two-dimensional linear cosserat elasticity. *Mathematics and Mechanics of Complex Systems*, 10(4):321–356.
- [Auffray et al., 2018] Auffray, N., He, Q., and Le Quang, H. (2018). Complete symmetry classification and compact matrix representations for 3D strain gradient elasticity. *International Journal of Solids and Structures*, 159(Journal of the Mechanics and Physics of Solids 99 2017):197–210.
- [Auffray et al., 2017] Auffray, N., Kolev, B., and Olive, M. (2017). Handbook of bi-dimensional tensors: Part i: Harmonic decomposition and symmetry classes. *Mathematics and Mechanics of Solids*, 22(9):1847–1865.

- [Auffray et al., 2014] Auffray, N., Koley, B., and Petitot, M. (2014). On anisotropic polynomial relations for the elasticity tensor. *Journal of Elasticity*, 115(1):77–103.
- [Auffray and Ropars, 2016] Auffray, N. and Ropars, P. (2016). Invariant-based reconstruction of bidimensional elasticity tensors. *International Journal of Solids and Structures*, 87:183–193.
- [Babae et al., 2013] Babae, S., Shim, J., Weaver, J. C., Chen, E. R., Patel, N., and Bertoldi, K. (2013). 3d soft metamaterials with negative poisson’s ratio. *Advanced Materials*, 25(36):5044–5049.
- [Bacigalupo and Gambarotta, 2014a] Bacigalupo, A. and Gambarotta, L. (2014a). Homogenization of periodic hexa- and tetrachiral cellular solids. *Composite Structures*, 116:461–476.
- [Bacigalupo and Gambarotta, 2014b] Bacigalupo, A. and Gambarotta, L. (2014b). Second-gradient homogenized model for wave propagation in heterogeneous periodic media. *International Journal of Solids and Structures*, 51(5):1052–1065.
- [Bakhvalov and Panasenko, 1989] Bakhvalov, N. and Panasenko, G. (1989). Homogenisation: averaging processes in periodic media, volume 36 of mathematics and its applications (soviet series).
- [Barthelat, 2015] Barthelat, F. (2015). Architected materials in engineering and biology: fabrication, structure, mechanics and performance. *International Materials Reviews*, 60(8):413–430.
- [Bendsoe, 1988] Bendsoe, M. (1988). General optimal topologies in structural design using a homogenization method. *Computer methods in applied mechanics and engineering*, 93:291–318.
- [Bendsøe and Kikuchi, 1988] Bendsøe, M. P. and Kikuchi, N. (1988). Generating optimal topologies in structural design using a homogenization method. *Computer methods in applied mechanics and engineering*, 71(2):197–224.
- [Bertoldi et al., 2010] Bertoldi, K., Reis, P. M., Willshaw, S., and Mullin, T. (2010). Negative poisson’s ratio behavior induced by an elastic instability. *Advanced materials*, 22(3):361–366.
- [Biswas et al., 2020] Biswas, R., Poh, L. H., and Shedbale, A. S. (2020). A micromorphic computational homogenization framework for auxetic tetra-chiral structures. *Journal of the Mechanics and Physics of Solids*, 135:103801.
- [Bornert et al., 2001] Bornert, M., Bretheau, T., and Gilormini, P. (2001). *Homogénéisation en mécanique des matériaux, Tome 1: Matériaux aléatoires élastiques et milieux périodiques*. Hermes science.
- [Bouaziz et al., 2008] Bouaziz, O., Bréchet, Y., and Embury, J. D. (2008). Heterogeneous and architected materials: a possible strategy for design of structural materials. *Advanced Engineering Materials*, 10(1-2):24–36.
- [Boutin, 1996] Boutin, C. (1996). Microstructural effects in elastic composites. *International Journal of Solids and Structures*, 33(7):1023–1051.

- [Boutin and Auriault, 1993] Boutin, C. and Auriault, J. (1993). Rayleigh scattering in elastic composite materials. *International journal of engineering science*, 31(12):1669–1689.
- [Brillouin, 1930] Brillouin, L. (1930). Les électrons libres dans les métaux et le rôle des réflexions de bragg. *Journal de Physique et le Radium*, 1(11):377–400.
- [Brillouin, 1953] Brillouin, L. (1953). *Wave propagation in periodic structures: electric filters and crystal lattices*, volume 2. Dover publications.
- [Bückmann et al., 2015] Bückmann, T., Kadic, M., Schittny, R., and Wegener, M. (2015). Mechanical cloak design by direct lattice transformation. *Proceedings of the National Academy of Sciences*, 112(16):4930–4934.
- [Budiansky, 1999] Budiansky, B. (1999). On the minimum weights of compression structures. *International Journal of Solids and Structures*, 36(24):3677–3708.
- [Cheng et al., 2020] Cheng, Q., Guo, H., Yuan, T., Sun, P., Guo, F., and Wang, Y. (2020). Topological design of square lattice structure for broad and multiple band gaps in low-frequency range. *Extreme Mechanics Letters*, 35:100632.
- [Clausen et al., 2015] Clausen, A., Wang, F., Jensen, J. S., Sigmund, O., and Lewis, J. A. (2015). Topology optimized architectures with programmable poisson’s ratio over large deformations. *Adv. Mater*, 27(37):5523–5527.
- [Cornaggia and Bellis, 2020] Cornaggia, R. and Bellis, C. (2020). Tuning effective dynamical properties of periodic media by fft-accelerated topological optimization. *International Journal for Numerical Methods in Engineering*, 121(14):3178–3205.
- [Cornaggia and Guzina, 2020] Cornaggia, R. and Guzina, B. B. (2020). Second-order homogenization of boundary and transmission conditions for one-dimensional waves in periodic media. *International Journal of Solids and Structures*, 188:88–102.
- [Cosserat and Cosserat, 1909] Cosserat, E. M. P. and Cosserat, F. (1909). *Théorie des corps déformables*. A. Hermann et fils.
- [Cox et al., 2013] Cox, D., Little, J., and O’Shea, D. (2013). *Ideals, varieties, and algorithms: an introduction to computational algebraic geometry and commutative algebra*. Springer Science & Business Media.
- [Cummer et al., 2016] Cummer, S. A., Christensen, J., and Alù, A. (2016). Controlling sound with acoustic metamaterials. *Nature Reviews Materials*, 1(3):1–13.
- [Czech et al., 2015] Czech, C., Guarneri, P., Thyagaraja, N., and Fadel, G. (2015). Systematic design optimization of the metamaterial shear beam of a nonpneumatic wheel for low rolling resistance. *Journal of Mechanical Design*, 137(4):041404.
- [Deshpande et al., 2001a] Deshpande, V., Ashby, M., and Fleck, N. (2001a). Foam topology: bending versus stretching dominated architectures. *Acta materialia*, 49(6):1035–1040.
- [Deshpande et al., 2001b] Deshpande, V. S., Fleck, N. A., and Ashby, M. F. (2001b). Effective properties of the octet-truss lattice material. *Journal of the Mechanics and Physics of Solids*, 49(8):1747–1769.

- [Desmorat and Auffray, 2019] Desmorat, B. and Auffray, N. (2019). Space of 2d elastic materials: a geometric journey. *Continuum Mechanics and Thermodynamics*, 31:1205–1229.
- [Desmorat et al., 2020] Desmorat, B., Olive, M., Auffray, N., Desmorat, R., and Kolev, B. (2020). Computation of minimal covariants bases for 2d coupled constitutive laws. *arXiv preprint arXiv:2007.01576*.
- [Dirrenberger, 2012] Dirrenberger, J. (2012). *Propriétés effectives de matériaux architecturés*. PhD thesis, Ecole Nationale Supérieure des Mines de Paris.
- [Dirrenberger, 2018] Dirrenberger, J. (2018). *Towards an integrated approach for the development of architected materials*. PhD thesis, Sorbonne Université.
- [Dirrenberger et al., 2011] Dirrenberger, J., Forest, S., Jeulin, D., and Colin, C. (2011). Homogenization of periodic auxetic materials. In *11th International Conference on the Mechanical Behavior of Materials (ICM11)*, volume 10, pages 1847–1852. Elsevier.
- [Durand et al., 2022] Durand, B., Lebée, A., Seppecher, P., and Sab, K. (2022). Predictive strain-gradient homogenization of a pantographic material with compliant junctions. *Journal of the Mechanics and Physics of Solids*, 160:104773.
- [Eremeyev et al., 2013] Eremeyev, V. A., Lebedev, L. P., Altenbach, H., Eremeyev, V. A., Lebedev, L. P., and Altenbach, H. (2013). Kinematics of micropolar continuum. *Foundations of Micropolar Mechanics*, pages 11–13.
- [Eringen, 1968] Eringen, A. (1968). Theory of micropolar elasticity, volume ii, chapter 7, fracture, edited by h. liebowitz.
- [Eringen, 2001] Eringen, A. C. (2001). *Microcontinuum field theories: II. Fluent media*, volume 2. Springer Science & Business Media.
- [Eringen, 2012] Eringen, A. C. (2012). *Microcontinuum field theories: I. Foundations and solids*. Springer Science & Business Media.
- [Faure, 2017] Faure, A. (2017). *Optimisation de forme de matériaux et structures architecturés par la méthode des lignes de niveaux avec prise en compte des interfaces graduées*. PhD thesis, Université Grenoble Alpes (ComUE).
- [Fish et al., 2002] Fish, J., Chen, W., and Nagai, G. (2002). Non-local dispersive model for wave propagation in heterogeneous media: one-dimensional case. *International Journal for Numerical Methods in Engineering*, 54(3):331–346.
- [Fleck and Deshpande, 2004] Fleck, N. and Deshpande, V. (2004). The resistance of clamped sandwich beams to shock loading. *J. Appl. Mech.*, 71(3):386–401.
- [Fleck et al., 2010] Fleck, N. A., Deshpande, V. S., and Ashby, M. F. (2010). Micro-architected materials: past, present and future. *Proceedings of the Royal Society A: Mathematical, Physical and Engineering Sciences*, 466(2121):2495–2516.
- [Floquet, 1883] Floquet, G. (1883). Sur les équations différentielles linéaires à coefficients périodiques. *Annales scientifiques de l'École normale supérieure*, 12:47–88.

- [Forest, 2005] Forest, S. (2005). Mechanics of cosserat media—an introduction. *Ecole des Mines de Paris, Paris*, pages 1–20.
- [Forest, 2006] Forest, S. (2006). *Milieux continus généralisés et matériaux hétérogènes*. Presses des MINES.
- [Forest et al., 2001] Forest, S., Pradel, F., and Sab, K. (2001). Asymptotic analysis of heterogeneous cosserat media. *International Journal of Solids and Structures*, 38(26-27):4585–4608.
- [Forest and Sievert, 2006] Forest, S. and Sievert, R. (2006). Nonlinear microstrain theories. *International journal of solids and structures*, 43(24):7224–7245.
- [Forte and Vianello, 2014] Forte, S. and Vianello, M. (2014). A unified approach to invariants of plane elasticity tensors. *Meccanica*, 49:2001–2012.
- [François, 1995] François, M. L. M. (1995). *Identification des symétries matérielles de matériaux anisotropes*. PhD thesis, Université Pierre et Marie Curie-Paris VI.
- [Gambin and Kröner, 1989] Gambin, B. and Kröner, E. (1989). Higher-order terms in the homogenized stress-strain relation of periodic elastic media. *physica status solidi (b)*, 151(2):513–519.
- [Gazalet et al., 2013] Gazalet, J., Dupont, S., Kastelik, J.-C., Rolland, Q., and Djafari-Rouhani, B. (2013). A tutorial survey on waves propagating in periodic media: Electronic, photonic and phononic crystals. perception of the bloch theorem in both real and fourier domains. *Wave Motion*, 50(3):619–654.
- [Germain, 1973] Germain, P. (1973). The method of virtual power in continuum mechanics. part 2: Microstructure. *SIAM Journal on Applied Mathematics*, 25(3):556–575.
- [Gibson and Ashby, 1997] Gibson, L. J. and Ashby, M. F. (1997). *Cellular Solids: Structure and Properties*. Cambridge Solid State Science Series: i-vi. Cambridge University Press, 2 edition.
- [Giorgio et al., 2022] Giorgio, I., Hild, F., Gerami, E., Dell’Isola, F., and Misra, A. (2022). Experimental verification of 2d cosserat chirality with stretch-micro-rotation coupling in orthotropic metamaterials with granular motif. *Mechanics Research Communications*, 126:104020.
- [Glacet et al., 2019] Glacet, A., Tanguy, A., and Réthoré, J. (2019). Vibrational properties of quasi-periodic beam structures. *Journal of Sound and Vibration*, 442:624–644.
- [Gonella and Ruzzene, 2008] Gonella, S. and Ruzzene, M. (2008). Analysis of in-plane wave propagation in hexagonal and re-entrant lattices. *Journal of Sound and Vibration*, 312(1-2):125–139.
- [Goyos-Ball et al., 2017] Goyos-Ball, L., Garcia-Tunon, E., Fernandez-Garcia, E., Diaz, R., Fernandez, A., Prado, C., Saiz, E., and Torrecillas, R. (2017). Mechanical and biological evaluation of 3d printed 10cetzp-al2o3 structures. *Journal of the European Ceramic Society*, 37(9):3151–3158.

- [Green and Rivlin, 1964] Green, A. E. and Rivlin, R. S. (1964). Multipolar continuum mechanics. *Archive for rational mechanics and analysis*, 17:113–147.
- [Grima et al., 2008] Grima, J. N., Gatt, R., and Farrugia, P.-S. (2008). On the properties of auxetic meta-tetrachiral structures. *physica status solidi (b)*, 245(3):511–520.
- [Grünbaum and Shephard, 1987] Grünbaum, B. and Shephard, G. C. (1987). *Tilings and patterns*. Courier Dover Publications.
- [He and Zheng, 1996] He, Q. C. and Zheng, Q. S. (1996). On the symmetries of 2d elastic and hyperelastic tensors. *Journal of elasticity*, 43:203–225.
- [Hermann, 1934] Hermann, C. (1934). Tensoren und kristallsymmetrie. *Zeitschrift für Kristallographie-Crystalline Materials*, 89(1-6):32–48.
- [Hestenes and Holt, 2007] Hestenes, D. and Holt, J. W. (2007). Crystallographic space groups in geometric algebra. *Journal of Mathematical Physics*, 48(2):023514.
- [Hewage et al., 2016] Hewage, T. A., Alderson, K. L., Alderson, A., and Scarpa, F. (2016). Double-negative mechanical metamaterials displaying simultaneous negative stiffness and negative poisson’s ratio properties. *Advanced Materials*, 28(46):10323–10332.
- [Hild and Roux, 2012] Hild, F. and Roux, S. (2012). Comparison of local and global approaches to digital image correlation. *Experimental mechanics*, 52(9):1503–1519.
- [Hill, 1963] Hill, R. (1963). Elastic properties of reinforced solids: some theoretical principles. *Journal of the Mechanics and Physics of Solids*, 11(5):357–372.
- [Kadic et al., 2013] Kadic, M., Bückmann, T., Schittny, R., and Wegener, M. (2013). On anisotropic versions of three-dimensional pentamode metamaterials. *New Journal of Physics*, 15(2):023029.
- [Kadic et al., 2012] Kadic, M., Bückmann, T., Stenger, N., Thiel, M., and Wegener, M. (2012). On the practicability of pentamode mechanical metamaterials. *Applied Physics Letters*, 100(19).
- [Kadic et al., 2019] Kadic, M., Milton, G. W., van Hecke, M., and Wegener, M. (2019). 3d metamaterials. *Nature Reviews Physics*, 1(3):198–210.
- [Khakalo et al., 2018] Khakalo, S., Balobanov, V., and Niiranen, J. (2018). Modelling size-dependent bending, buckling and vibrations of 2d triangular lattices by strain gradient elasticity models: applications to sandwich beams and auxetics. *International Journal of Engineering Science*, 127:33–52.
- [Lakes and Benedict, 1982] Lakes, R. S. and Benedict, R. L. (1982). Noncentrosymmetry in micropolar elasticity. *International Journal of Engineering Science*, 20(10):1161–1167.
- [Landy et al., 2008] Landy, N. I., Sajuyigbe, S., Mock, J. J., Smith, D. R., and Padilla, W. J. (2008). Perfect metamaterial absorber. *Physical review letters*, 100(20):207402.

- [Lemkalli et al., 2023] Lemkalli, B., Kadic, M., El Badri, Y., Guenneau, S., Bouzid, A., and Achaoui, Y. (2023). Mapping of elastic properties of twisting metamaterials onto micropolar continuum using static calculations. *International Journal of Mechanical Sciences*, 254:108411.
- [Lepidi and Bacigalupo, 2017] Lepidi, M. and Bacigalupo, A. (2017). Asymptotic approximation of the band structure for tetrachiral metamaterials. *Procedia engineering*, 199:1460–1465.
- [Li et al., 2017] Li, T., Hu, X., Chen, Y., and Wang, L. (2017). Harnessing out-of-plane deformation to design 3d architected lattice metamaterials with tunable poisson’s ratio. *Scientific Reports*, 7(1):8949.
- [Li et al., 2018] Li, X., Lu, Z., Yang, Z., and Yang, C. (2018). Anisotropic in-plane mechanical behavior of square honeycombs under off-axis loading. *Materials & Design*, 158:88–97.
- [Liu et al., 2008] Liu, N., Guo, H., Fu, L., Kaiser, S., Schweizer, H., and Giessen, H. (2008). Three-dimensional photonic metamaterials at optical frequencies. *Nature materials*, 7(1):31–37.
- [Liu et al., 2012] Liu, X., Huang, G., and Hu, G. (2012). Chiral effect in plane isotropic micropolar elasticity and its application to chiral lattices. *Journal of the Mechanics and Physics of Solids*, 60(11):1907–1921.
- [Malgrange et al., 2014] Malgrange, C., Ricolleau, C., and Schlenker, M. (2014). *Symmetry and physical properties of crystals*. Springer.
- [McGee et al., 2019] McGee, O., Jiang, H., Qian, F., Jia, Z., Wang, L., Meng, H., Chronopoulos, D., Chen, Y., and Zuo, L. (2019). 3d printed architected hollow sphere foams with low-frequency phononic band gaps. *Additive Manufacturing*, 30:100842.
- [McWeeny, 2002] McWeeny, R. (2002). *Symmetry: An introduction to group theory and its applications*. Courier Corporation.
- [Meena and Singamneni, 2019] Meena, K. and Singamneni, S. (2019). A new auxetic structure with significantly reduced stress concentration effects. *Materials & Design*, 173:107779.
- [Milton and Cherkaev, 1995] Milton, G. W. and Cherkaev, A. V. (1995). Which elasticity tensors are realizable?
- [Mindlin, 1964] Mindlin, R. (1964). Micro-structure in linear elasticity, archs. ration mech. *Analysis*, 1(4):16.
- [Mindlin, 1965] Mindlin, R. D. (1965). Second gradient of strain and surface-tension in linear elasticity. *International Journal of Solids and Structures*, 1(4):417–438.
- [Mindlin and Eshel, 1968] Mindlin, R. D. and Eshel, N. (1968). On first strain-gradient theories in linear elasticity. *International Journal of Solids and Structures*, 4(1):109–124.

- [Molitch-Hou, 2018] Molitch-Hou, M. (2018). Overview of additive manufacturing process. In *Additive manufacturing*, pages 1–38. Elsevier.
- [Mou et al., 2023] Mou, G., Desmorat, B., Turlin, R., and Auffray, N. (2023). On exotic linear materials: 2d elasticity and beyond. *International Journal of Solids and Structures*, page 112103.
- [Mousanezhad et al., 2016] Mousanezhad, D., Haghpanah, B., Ghosh, R., Hamouda, A. M., Nayeb-Hashemi, H., and Vaziri, A. (2016). Elastic properties of chiral, anti-chiral, and hierarchical honeycombs: A simple energy-based approach. *Theoretical and Applied Mechanics Letters*, 6(2):81–96.
- [Nassar, 2015] Nassar, H. (2015). *Elastodynamic homogenization of periodic media*. PhD thesis, Université Paris-Est.
- [Nassar et al., 2020] Nassar, H., Chen, Y., and Huang, G. (2020). Polar metamaterials: a new outlook on resonance for cloaking applications. *Physical review letters*, 124(8):084301.
- [Nassar et al., 2022] Nassar, H., Lebée, A., and Werner, E. (2022). Strain compatibility and gradient elasticity in morphing origami metamaterials. *Extreme Mechanics Letters*, 53:101722.
- [Nowacki, 1972] Nowacki, W. (1972). *Theory of micropolar elasticity*, volume 494. Springer.
- [Nunziato and Cowin, 1979] Nunziato, J. W. and Cowin, S. C. (1979). A nonlinear theory of elastic materials with voids. *Archive for Rational Mechanics and Analysis*, 72:175–201.
- [Passman, 1984] Passman, S. L. (1984). Stress relaxation, creep, failure and hysteresis in a linear elastic material with voids. *Journal of elasticity*, 14(2):201–212.
- [Placidi et al., 2017] Placidi, L., Andreaus, U., and Giorgio, I. (2017). Identification of two-dimensional pantographic structure via a linear d4 orthotropic second gradient elastic model. *Journal of Engineering Mathematics*, 103(1):1–21.
- [Poncelet et al., 2018] Poncelet, M., Somera, A., Morel, C., Jailin, C., and Auffray, N. (2018). An experimental evidence of the failure of cauchy elasticity for the overall modeling of a non-centro-symmetric lattice under static loading. *International Journal of Solids and Structures*, 147:223–237.
- [Prall and Lakes, 1997] Prall, D. and Lakes, R. (1997). Properties of a chiral honeycomb with a Poisson’s ratio of - 1. *International Journal of Mechanical Sciences*, 39(3):305–314.
- [Rafsanjani and Pasini, 2016] Rafsanjani, A. and Pasini, D. (2016). Bistable auxetic mechanical metamaterials inspired by ancient geometric motifs. *Extreme Mechanics Letters*, 9:291–296.
- [Reis et al., 2015] Reis, P. M., Jaeger, H. M., and Van Hecke, M. (2015). Designer matter: A perspective. *Extreme Mechanics Letters*, 5:25–29.

- [Réthoré et al., 2015] Réthoré, J., Kaltenbrunner, C., Dang, T. B. T., Chaudet, P., and Kuhn, M. (2015). Gradient-elasticity for honeycomb materials: Validation and identification from full-field measurements. *International Journal of Solids and Structures*, 72:108–117.
- [Rosi and Auffray, 2016] Rosi, G. and Auffray, N. (2016). Anisotropic and dispersive wave propagation within strain-gradient framework. *Wave Motion*, 63:120–134.
- [Rosi and Auffray, 2019] Rosi, G. and Auffray, N. (2019). Continuum modelling of frequency dependent acoustic beam focussing and steering in hexagonal lattices. *European Journal of Mechanics - A/Solids*, 77:103803.
- [Rosi et al., 2020] Rosi, G., Auffray, N., and Combescure, C. (2020). On the failure of classic elasticity in predicting elastic wave propagation in gyroid lattices for very long wavelengths. *Symmetry*, 12(8):1243.
- [Rosi et al., 2018] Rosi, G., Placidi, L., and Auffray, N. (2018). On the validity range of strain-gradient elasticity: a mixed static-dynamic identification procedure. *European Journal of Mechanics-A/Solids*, 69:179–191.
- [Royer and Dieulesaint, 1999] Royer, D. and Dieulesaint, E. (1999). *Elastic waves in solids I: Free and guided propagation*. Springer Science & Business Media.
- [Rudykh and Boyce, 2014] Rudykh, S. and Boyce, M. C. (2014). Transforming wave propagation in layered media via instability-induced interfacial wrinkling. *Physical review letters*, 112(3):034301.
- [Santosa and Symes, 1991] Santosa, F. and Symes, W. W. (1991). A dispersive effective medium for wave propagation in periodic composites. *SIAM Journal on Applied Mathematics*, 51(4):984–1005.
- [Sasse, 2020] Sasse, V. (2020). Classification of the 17 wallpaper groups. *The University of Chicago, Department of Mathematics*.
- [Schaedler et al., 2014] Schaedler, T. A., Ro, C. J., Sorensen, A. E., Eckel, Z., Yang, S. S., Carter, W. B., and Jacobsen, A. J. (2014). Designing metallic microlattices for energy absorber applications. *Advanced Engineering Materials*, 16(3):276–283.
- [Schaeffer et al., 2017] Schaeffer, M., Trainiti, G., and Ruzzene, M. (2017). Optical measurement of in-plane waves in mechanical metamaterials through digital image correlation. *Scientific Reports*, 7(1):424–37.
- [Schoenflies, 1891] Schoenflies, A. (1891). *Krystallsysteme und Krystallstructur*. Springer.
- [Senechal, 1996] Senechal, M. (1996). *Quasicrystals and geometry*. CUP Archive.
- [Shan et al., 2015] Shan, S., Kang, S. H., Raney, J. R., Wang, P., Fang, L., Candido, F., Lewis, J. A., and Bertoldi, K. (2015). Multistable architected materials for trapping elastic strain energy. *Advanced Materials*, 27(29):4296–4301.

- [Shan et al., 2014] Shan, S., Kang, S. H., Wang, P., Qu, C., Shian, S., Chen, E. R., and Bertoldi, K. (2014). Harnessing multiple folding mechanisms in soft periodic structures for tunable control of elastic waves. *Advanced Functional Materials*, 24(31):4935–4942.
- [Shim et al., 2013] Shim, J., Shan, S., Košmrlj, A., Kang, S. H., Chen, E. R., Weaver, J. C., and Bertoldi, K. (2013). Harnessing instabilities for design of soft reconfigurable auxetic/chiral materials. *Soft Matter*, 9(34):8198–8202.
- [Shiyin et al., 2015] Shiyin, X., Xiuchang, H., and Hongxing, H. (2015). A study on the isolation performance of trichiral lattices with gradient geometry. *Journal of Vibration and Control*, 21(16):3465–3475.
- [Smyshlyaev and Cherednichenko, 2000] Smyshlyaev, V. P. and Cherednichenko, K. D. (2000). On rigorous derivation of strain gradient effects in the overall behaviour of periodic heterogeneous media. *Journal of the Mechanics and Physics of Solids*, 48(6-7):1325–1357.
- [Sokolowski and Zochowski, 1999] Sokolowski, J. and Zochowski, A. (1999). On the topological derivative in shape optimization. *SIAM journal on control and optimization*, 37(4):1251–1272.
- [Somera, 2022] Somera, A. (2022). *On the effective elasticity of quasi-periodic lattice materials: From microscopic foundations to experimental validation*. PhD thesis, École centrale de Nantes.
- [Spadoni and Ruzzene, 2012] Spadoni, A. and Ruzzene, M. (2012). Elasto-static micropolar behavior of a chiral auxetic lattice. *Journal of the Mechanics and Physics of Solids*, 60(1):156–171.
- [Spadoni et al., 2009] Spadoni, A., Ruzzene, M., Gonella, S., and Scarpa, F. (2009). Phononic properties of hexagonal chiral lattices. *Wave motion*, 46(7):435–450.
- [Tamburrino et al., 2018] Tamburrino, F., Graziosi, S., and Bordegoni, M. (2018). The design process of additively manufactured mesoscale lattice structures: a review. *Journal of Computing and Information Science in Engineering*, 18(4):040801.
- [Terroir, 2022] Terroir, A. (2022). *Étude et réalisation de métamatériaux acoustiques architecturés*. PhD thesis, Université de Lille.
- [Toupin, 1962] Toupin, R. (1962). Elastic materials with couple-stresses. *Archive for rational mechanics and analysis*, 11(1):385–414.
- [Trinh et al., 2012] Trinh, D. K., Janicke, R., Auffray, N., Diebels, S., and Forest, S. (2012). Evaluation of generalized continuum substitution models for heterogeneous materials. *International Journal for Multiscale Computational Engineering*, 10(6).
- [Uribe-Lam et al., 2021] Uribe-Lam, E., Treviño-Quintanilla, C. D., Cuan-Urquizo, E., and Olvera-Silva, O. (2021). Use of additive manufacturing for the fabrication of cellular and lattice materials: a review. *Materials and Manufacturing Processes*, 36(3):257–280.
- [Vannucci, 2002] Vannucci, P. (2002). *Journal of Elasticity*, 67(2):81–96.

- [Vianello, 1997] Vianello, M. (1997). An integrity basis for plane elasticity tensors. *Archives of Mechanics*, 49(1):197–208.
- [Voigt, 1910] Voigt, W. (1910). *Lehrbuch der kristallphysik:(mit ausschluss der kristalloptik)*, volume 34. BG Teubner.
- [Wadley, 2006] Wadley, H. N. (2006). Multifunctional periodic cellular metals. *Philosophical Transactions of the Royal Society A: Mathematical, Physical and Engineering Sciences*, 364(1838):31–68.
- [Wadley et al., 2003] Wadley, H. N., Fleck, N. A., and Evans, A. G. (2003). Fabrication and structural performance of periodic cellular metal sandwich structures. *Composites science and technology*, 63(16):2331–2343.
- [Wallach and Gibson, 2001] Wallach, J. and Gibson, L. (2001). Mechanical behavior of a three-dimensional truss material. *International Journal of Solids and Structures*, 38(40-41):7181–7196.
- [Wang and McDowell, 2004] Wang, A.-J. and McDowell, D. (2004). In-plane stiffness and yield strength of periodic metal honeycombs. *J. Eng. Mater. Technol.*, 126(2):137–156.
- [Wang et al., 2003] Wang, M. Y., Wang, X., and Guo, D. (2003). A level set method for structural topology optimization. *Computer methods in applied mechanics and engineering*, 192(1-2):227–246.
- [Wang et al., 2014] Wang, P., Casadei, F., Shan, S., Weaver, J. C., and Bertoldi, K. (2014). Harnessing buckling to design tunable locally resonant acoustic metamaterials. *Physical review letters*, 113(1):014301.
- [Wautier and Guzina, 2015] Wautier, A. and Guzina, B. B. (2015). On the second-order homogenization of wave motion in periodic media and the sound of a chessboard. *Journal of the Mechanics and Physics of Solids*, 78:382–414.
- [Wicks and Hutchinson, 2001] Wicks, N. and Hutchinson, J. W. (2001). Optimal truss plates. *International Journal of Solids and Structures*, 38(30-31):5165–5183.
- [Wojciechowski, 1989] Wojciechowski, K. (1989). Two-dimensional isotropic system with a negative poisson ratio. *Physics Letters A*, 137(1-2):60–64.
- [Xu et al., 2020] Xu, X., Wang, C., Shou, W., Du, Z., Chen, Y., Li, B., Matusik, W., Hussein, N., and Huang, G. (2020). Physical realization of elastic cloaking with a polar material. *Physical review letters*, 124(11):114301.
- [Yang and Müller, 2021] Yang, H. and Müller, W. H. (2021). Size effects of mechanical metamaterials: a computational study based on a second-order asymptotic homogenization method. *Archive of Applied Mechanics*, 91(3):1037–1053.
- [Yeo et al., 2018] Yeo, J., Jung, G. S., Martín-Martínez, F. J., Ling, S., Gu, G. X., Qin, Z., and Buehler, M. J. (2018). Materials-by-design: computation, synthesis, and characterization from atoms to structures. *Physica scripta*, 93(5):053003.
- [Yvonnet, 2019] Yvonnet, J. (2019). *Computational homogenization of heterogeneous materials with finite elements*, volume 258. Springer.

- [Yvonnet et al., 2020] Yvonnet, J., Auffray, N., and Monchiet, V. (2020). Computational second-order homogenization of materials with effective anisotropic strain-gradient behavior. *International Journal of Solids and Structures*, 191:434–448.
- [Zhao et al., 2021] Zhao, S., Zhang, T. F. H., Gao, Y., and Chang, Z. (2021). Elastic wave propagation and bandgaps in finitely stretched soft lattice material. *arXiv preprint arXiv:2106.04063*.
- [Zheng and Boehler, 1994] Zheng, Q. S. and Boehler, J.-P. (1994). The description, classification, and reality of material and physical symmetries. *Acta Mechanica*, 102:73–89.
- [Zhou and Rozvany, 1991] Zhou, M. and Rozvany, G. I. (1991). The coc algorithm, part ii: Topological, geometrical and generalized shape optimization. *Computer methods in applied mechanics and engineering*, 89(1-3):309–336.
- [Zou et al., 2009] Zou, Z., Reid, S., Tan, P., Li, S., and Harrigan, J. (2009). Dynamic crushing of honeycombs and features of shock fronts. *International Journal of Impact Engineering*, 36(1):165–176.